Experimental Study of Sediment Transport and Culvert Capacity

by

Wade J. Barnes, B.S.CE

A Dissertation

In

Civil Engineering

Department of Civil and Environmental Engineering

Submitted to the Graduate Faculty
of Texas Tech University in
Partial Fulfillment of
the Requirements for
the Degree of

Doctor of Philosophy

Approved

Theodore G. Cleveland, Ph.D., P.E.
Chair of Committee

E. Annette Hernandez Uddameri, Ph.D., P.E.

Kenneth A. Rainwater, Ph.D., P.E., BCEE, D.WRE, CFM

Dominick Casadonte
Dean of the Graduate School

May, 2013

Acknowledgments

I am especially grateful to those individuals and groups who have assisted me in achieving this prestigious advanced degree in engineering. Without the financial and moral support, this accomplishment would not be possible.

First, I would like to thank the Texas Department of Transportation for funding this project. Through their funding of project 0–6549, I was given the opportunity to work for two different organizations, Texas Tech University and U.S. Geological Survey, translating into a full time position in research. Research was something I never thought I would be interested in and without this opportunity, I would not have had the challenge to complete this project, nor would I had the chance to apply the research into what is now my dissertation.

Second, I would like to thank my committee members who dedicated their time in assisting me in finish my research and dissertation. Without your input and corrections to my southern backwoods service–man writing skills, I could not have completed a document that qualified for the requirements of a Ph.D education.

Dr. Rainwater, I am very appreciative of the lessons taught in sincerity and humbleness. The classes I have taken with you demonstrated methods in teaching skills that I now try to emulate. I appreciate how you correct mistakes we students often make without belittling or destroying a persons confidence. I hope I can develop this same skill.

Dr. Hernandez, (now Dr. Uddameri), I owe you so much gratitude, for if it was not for your counseling, I would have not ever considered pursuing a Ph.D. To think this once plumber was capable of reaching such a higher level of education is still very mind blowing to me. Your constant encouragement created a belief in me that allowed my success to happen in this field. Your confidence to allow me to substitute teach in your classes helped my decision to pursue a teaching career at the university level.

Dr. Cleveland, my advisor, my friend, from the bottom of my heart, thank you for including me in your move to Texas Tech. If you would have not offered me a position in grad school, I would have never gone back to school after I completed my bachelor's

degree. I am very grateful for the countless fluid seminars, the ear you supplied whether you wanted to or not to allow me to vent, complain, and sometimes just plain cuss. The past five years have been an adventure I will never forget or be able to properly show my appreciation. Words are not a justification for what I have been allowed to accomplish for the past five years. THANK YOU!

Third, I need to thank all of the students who worked so very hard in the laboratory. The countless number of hours in construction, cleaning, and data recognition would not have been possible with you folks. In no particular order, thank you Larissa da Costa, Marla Mauricio, Nicole Frantz Smith, Annabel Ulary, Kirsten Marshall, Holley Murphy Saez, Chelsie Babin, Clark Obermiller, Jeremy Dixon, Nino Mendoza, Stephen Wolf, Jake Irvin, Dakota McDonald, Randy Franks, Michael Blevins, Wesley Kumfer, and Blake Rupert. A special thank you goes out to Devan Glover who turned my hand sketches into professional drawings.

Fourth, I would like to thank all of my friends for their continued support. Friends who continually encouraged me to finish and not quit. A very special thank you to Philip and Karen for the love and never ending support. Also, I would like to thank William Asquith for all of your help in Latex and the editing comments throughout the process of my paper.

Last but not least, my family who has stood by me throughout all of the life changes and emotional roller coasters over the past few years. Without them, I could not have finished this daunting task. The unconditional love given by the Mclaughlins will never be forgotten. And to my wife, Charmyane, who has stood by my side through the good and bad. Who supplied a shoulder to cry on, an ear to listen to all of the complaints and accomplishments, an unmentionable amount of time proof reading and editing, and most of all my rock who knew when to kick me in the pants and when to just listen, THANK YOU for your support and friendship.

I would like to dedicate this paper to the most loving and trusting woman who ever lived . . . Diane Barnes. Mom, I love you.

Table of Contents

APPENDICES

List of Tables

List of Figures

Abstract

Sediment Transport has been a concern to hydraulic engineers for at least the past 200 years. Design methods for conveyance of clear water through culvert systems can be found as far back as the Roman aqua-ducts and the Ming dynasty. There have been few studies performed on the conveyance of water and solids in culverts. Recent studies have started addressing the ability of culverts to pass solids, in response to a need to provide fish passage, and structure serviceability.

This research presented physical modeling to study the interaction of sediment migration and culvert systems. The research conducted was performed in a laboratory, collecting data in an open flume at discharge rates between 12 and 16 cfs. Sediment particles were observed and digitally recorded during the sediment movement in the experimental channel. Velocity profiles near the structure were obtained and analyzed. Solids mass movement were measured. The results support the conclusions that larger open areas convey more sediment solids, flow patterns around structures are less affected by larger open areas, and culvert outlet control has the greatest influence on solids transport through culverts. Furthermore, the results are presented and interpreted to show why common sediment transport equations developed in uniform flows are not applicable for the culvert systems under outlet control.

Chapter 1

Introduction

Advancements in technology, working conditions, and living habits necessitate re-evaluation of transportation infrastructure, in particular the crossing of rivers or streams. Population growth in rural areas and changes in rural economies require greater dependence on the ability to transverse waterways.

Rural low water crossings, in contrast to conventional bridges, are designed for occasional submersion. These crossings are designed in regions of low traffic load, about 200 vehicles per day. A conventional bridge is typically required by the Federal Emergency Management Agency (FEMA) guidance to be serviceable after a 1%-chance (100-year) flood event; low water crossings, typically, are held to a lower standard, but survivability of the structure is an important economic issue.

As the low water crossings age, local watersheds are changing in terms of population, land use (urbanization), and the structures crossing these water ways may become inadequate. This study focuses on structures that are similar to those in Central Texas in the Edwards Plateau (Hill Country) region.

During a flood event, deposited bed load materials may cover or bury the crossing, resulting in a partial or complete operational failure. After flooding, these roads are impassable from the left over sedimentation and debris. Crossing during a flood event often results in loss of vehicles and lives. Closures are a major economic problem for the local residents, restricting everyday life and business, and increasing unpredictable maintenance costs. At

remote locations, repair crews have difficulty reaching the site, increasing costs to maintain these crossings.

This research included a literature review of previous experimental data from that literature. Physical model experiments were performed to assess the hydraulic capacity of culvert systems in mobile bed situations. Experiments were designed to test the ability of the systems to convey both clear-water and solids through the culvert. The knowledge gained will enhance understanding of how to design culvert systems to address the maintainability issue identified herein.

1.1 Background

Culverts are used as a means to convey water flow through a road structure for intermittent or continual everyday water flow. Conventional culvert design considers clear-water discharge only. Recent studies in fish passage through buried culvert systems has recognized consideration of solids flow into and through culverts as an important ecological component of future fish populations (*Bates et al.*, 2003); similarly the drainage engineering community also recognized the importance of solids transport as part of overall drainage.

State transportation departments are concerned with maintenance issues caused by sediment debris obstructions in culvert systems. Maintenance concerns include, but are not limited to: erosion before and after the culvert system, clogging of culvert barrels causing water flow over the road and damage to the road deck, and premature erosion of the side banks from the continued flow over the road.

Gravel bed streams are formed by the gross erosion in the drainage basin surrounding our natural streams and river ways (*Branson and Reid*, 1981). As the water speed diminishes moving downstream, sediment particles fall out of the flow stream and increase the

sediment deposition in the waterways (*Hadley and Schumm*, 1961). *Schumm and Hadley* (1957) performed field observations in Wyoming and New Mexico recording observations of the erosion affects in the streams and found two general gross erosion categories: (1) drainage basins with actively eroding headwaters and rapidly eroding valley reaches or (2) moderate erosion in the headwaters and deep gullies in the valley reaches. The authors further explain how a gulling effect occurs in our stream channels. Headwaters erode the stream banks and beds transporting the debris downstream; then depositing sediment in the drainage basins. The continual flow of streams cut into these deposits in the streams and basins further migrating the sediment downstream causing head cutting creating deeper gullies each time upstream. This generation-transport process is a continuous evolution in the geomorphology of streams and river ways.

Figure 1.1 is an example of a sediment bar deposit in a natural channel. The photograph is of the upstream approach to a low water crossing named Flatrock Crossing near Junction, Texas. The natural stream has migrated around the main sediment bar deposited before the road crossing. Figure 1.1a looks upstream from the road deck, and Figure 1.1b looks downstream towards the road crossing. During high flow events the sediment bar is covered, and water flows over the road deck. During these high flow events, the solids are mobilized and the morphology changes.

1.2 Purpose

Texas Department of Transportation (TxDOT) in cooperation with Lamar University, Texas Tech University, University of Houston, and U.S. Geological Survey initiated a project in 2005 to investigate low water crossing failure. Each partner was responsible for a component of the project. The University of Houston along with Texas Tech University was asked to investigate ways of minimizing the problem.

(a) View from road deck looking upstream

(b) View from upstream looking at the road deck

Figure 1.1. Sediment deposits around a low water crossing

The purpose of this research was to:

1. Test a simplified mobilization theory to predict imminent motion of a gravel bed.
2. Identify hydraulic conditions under which mobilization is likely to occur.
3. Correlate the experimental conditions to geomorphic interpretation, and other experimental work from the literature.
4. Identify (qualitatively) from small models, design elements that can accommodate solids flow.

1.3 Dissertation Structure

1. A summary of prior relevant efforts in bed mobilization are presented in the literature review.
2. A description of a series of physical model experiments, where different culvert systems were examined. These different systems were selected as possible culvert combinations that could have favorable performance features, in particular self-cleansing with respect of solids, or conveying a larger solids flux relative to other configurations.

3. An analysis of the physical model experiments in the context of generalized culvert hydraulics and bed mobilization, and an analysis in the context of the literature derived database.
4. A summary of the findings from the physical model experiments as well as guidance for culvert system designs, and suggestions for future research activities in the topic of liquid-solid transport in culvert systems.

1.4 Scope

The research project was to study the sediment conveyance properties of a multicell or staggered barrel system. A typical staggered barrel system is designed with a large center barrel and two or more smaller outside barrels. The intent is for the center barrel to convey the natural baseflow in the stream. The staggered barrel system design sets the inverts of the outside barrels higher than the center barrel invert elevation. The outside barrels are not engaged in the typical baseflows or small storm events. The outside barrels are designed to convey higher flow rates found in larger storm events. The purpose of the design in a staggered barrel system is to mimic the natural cross sectional shape of the channel at the road crossing as a means to convey baseline flows without disturbing the natural channel. Generally, these systems are designed for locations where construction of larger structures is not economical (*Wargo and Weisman*, 2006).

Two recent studies exit on staggered barrel systems by *Wargo and Weisman* (2006) and *Haderlie and Tullis* (2008). *Wargo and Weisman* (2006) performed laboratory experiments looking at the flow depths in the culvert barrels and scouring effects on the outlet of the culverts. Experiments used a scaled 4% storm event typical to Benson Hollow Tributary in Wyoming County, PA. They compared the water depth and scouring effects in the multi-barrel system to a a single barrel culvert. *Haderlie and Tullis* (2008) study compared the

hydraulics of a staggered barrel system to a single barrel system. Their main study used superposition techniques to predict the head-discharge rate for culverts under inlet control.

This research included small-scale physical model experiments to produce qualitative understanding of bed mobilization and culvert solids accommodation capabilities. In addition, crude but meaningful measurements[1] were also collected, in part to assess the viability of video monitoring for field deployment, and in part to estimate the forces involved in bed mobilization.

This dissertation describes these experiments and presents the geometric and hydraulic data collected in Appendix D. Constructing a simple force-balance model provided a means to predict critical velocities and shear forces at which mobilization could be anticipated. The model predictions were compared to a more complicated model, data from the literature, data from geomorphology surveys, and from experimental results conducted specifically for this research. These predictions were intended to help select appropriate culvert structures in mobile bed systems. The prediction equations overestimated observed values by nearly an order of magnitude and are not recommended for use around culvert structures.

This research compared two staggered barrel configurations along with several more conventional culvert configurations. The two staggered barrel configurations were comprised of three barrels where: (1) the crown elevations of the barrels matched, and 2) the invert elevations of the barrels matched. The individual barrels were two 4–inch diameter circular barrels sandwiching a 6–inch diameter circular barrel. Further experiments provided data for single circular barrels, multiple circular barrels (equal diameters), single rectangular barrel, and multiple rectangular barrels. Studies were conducted to compare different geometries of culvert barrel[s] and the hydraulic conditions to transport sediments through culvert models. The experimental mobile bed was comprised of two sediment size

[1] Semi-quantitative results.

ranges, 1/4 and 1/2–in. The culvert models were tested with two approach flow angles and the approach channel cross section was essentially rectangular with benches at the roadway elevation.

1.5 Contents

The remainder of the dissertation is organized as follows: Chapter 2 is a literature review related to relevant channel hydraulics and a review of solids mobility. Chapter 3 describes the construction of the experimental apparatus. Chapter 4 presents the physical model experiment design in detail, including measuring instruments, and the types of data that were collected. Chapter 5 describes the solids mobility in terms of incipient motion through calculations performed on data collected. Chapter 6 presents a mapping of velocity profiles demonstrating the flow field through the channel with no sediment movement. Chapter 7 compares the physical model mobile sediment yield to known sediment transport equations. Chapter 8 describes the flow field with respect to flow depth with sediment movement. Chapter 9 concludes the dissertation with the findings as interpreted by the author, suggestions for future work, and guidance for design and maintenance of new and existing culvert systems.

Chapter 2

Literature Review

This chapter is a review of prior work related to solids motion in streams, channel hydraulics, and other background relevant for the research. The review and background is grouped by topic; the relevance of each topic is only an introduction into an individual topic as needed to help explain experimental design or results.

2.1 Sediment Movement Classification

Sediment movement is classified by the type or form of movement that occurs during transport. These classifications are referred to as contact load, saltation load, suspended load and laminated load. Movement in terms of bed–load include contact and saltation load (*Chien and Wan*, 1999).

Contact load is the case where particles slide or roll across the top of the sediment bed. The sediment particles extend far enough into the liquid flow pattern exposing enough contact area so that momentum transfer can overcome the stability of the particle. The particles remain in contact with the sediment bed as they slide and roll across the surface.

Saltation load is when the water flow supplies enough lift and drag force to overcome the frictional and gravitational forces and cause the particles to jump temporarily into the flow. The particle travels along a flow path for short distances until the transport momentum is overcome by the particles' weight causing the particle to fall out of the flow pattern.

Suspended load is when the turbulent water flow produces eddies larger than the particles that cause enough lift force to transport the particle downstream. Even if a particle falls out

of an eddy, it may fall into additional eddies that transport the particle further downstream. For the particles to be lifted far enough into the flow pattern to become suspended, the particle must pass through the saltation stage.

Contact, saltation, and suspended loads are interactions between the flow and the top layer of a sediment bed, when the water's shear velocity is large enough to cause sediment particles to move. When the shear forces are even larger, sediment particles from beneath the top layer are also moved. This movement type is called laminated load (*Chien and Wan*, 1999).

2.1.1 Bed–Forms

Migration of sediments downstream changes the topography of the channel bed. Deposit formations of sediment can form ripples, waves, dunes, and anti-dunes as the sediment migrates downstream (*Vanoni*, 1975; *Chien and Wan*, 1999). Figure 2.1 shows various types of sediment formations related to the type of flow and particle size

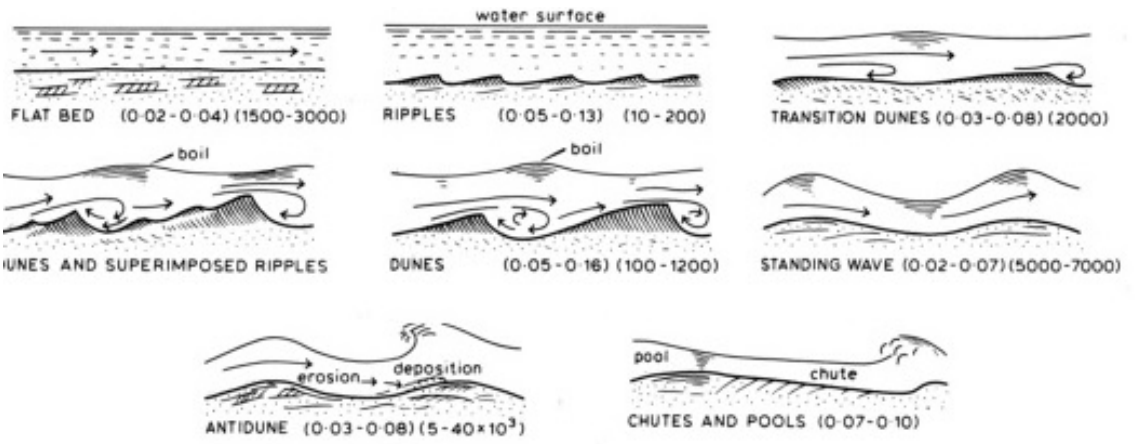

Figure 2.1. Typical sediment formations in fluvial streams (*Richards*, 1982)

A flat bed is a closely packed sediment bed that occurs usually in sand beds. Flat beds are formed by high velocities eroding ripples and dunes in a sweeping fashion. Generally large depths are associated with the high velocities.

Ripples form during low flow rates. The cross sections are generally not symmetrical. The upstream faces are gentle long slopes with sharp short downstream faces. Ripples are usually only 5 cm high and have wave lengths between 1 and 15 cm. Ripples are formed by sediment grains less than 0.6 mm.

Dunes form from increasing flow velocities. Dunes change from a convex upstream face to a concave face as the velocities increase. Wavelengths and depths are greater than those for ripples and heights are higher with a proportional relationship to the depth. Large grain particles tend to migrate downstream in dune formations rather than ripples. Some smaller sediment particles may form ripples on the front faces of dunes in larger depths of flow.

Anti-dunes form in phase with the surface waves. Anti-dunes may move upstream, downstream, or remain stationary depending on the water surface conditions. Shapes approach a near sinusoidal formation and depend on depth and velocities.

2.2 Drag force and Lift force

Figure 2.2 is a sketch of steady flow over a stream bed that shows the basic forces on a grain particle. The driving force is the drag force (F_D) applied by the flowing water. As the drag force overcomes the frictional force (f) supplied by the sediment bed, the particle can start to move. In addition, some researchers feel the lift force (F_L) is also a part of the force balance equation that allows for sediment movement. The lift force must overcome the gravitation force (F_g) of the particle and the hydrostatic pressure forces applied by the fluid. One criticism of Shields' work, is that he did not include the lift force of the particle as a part of the force balance (*Yang*, 1996; *Vanoni*, 1975; *Chien and Wan*, 1999).

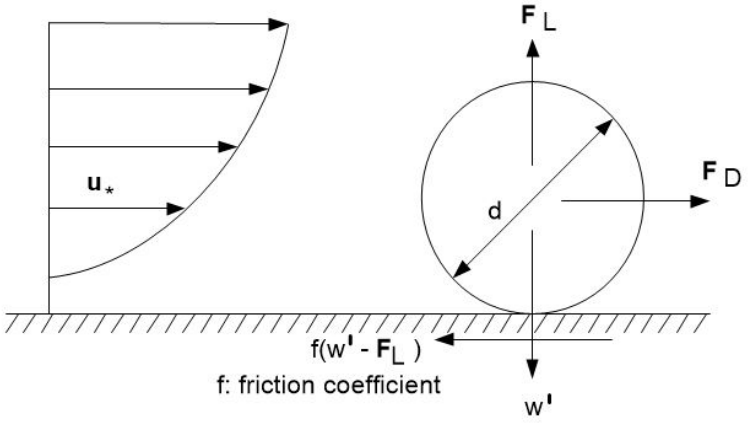

Figure 2.2. A sketch of basic forces acting on a grain particle (adapted from *Liu* (2001))

Drag force caused by pressure and viscous skin friction forces,is typically calculated using a quadratic drag law such as Equation 2.1,

$$F_D = \frac{1}{2}\rho C_D \frac{\pi D^2}{4} V_d^2 \tag{2.1}$$

where ρ is the density of the fluid, C_D is a drag coefficient, D is the particles diameter, and V_d is a local velocity at a distance d above the sediment bed.

Lift force, which is a shear flow caused by the velocity of the flow, is typically calculated by Equation 2.2,

$$F_L = \frac{1}{2}\rho C_L \frac{\pi d^2}{4} V_d^2 \tag{2.2}$$

where C_L is a lift coefficient derived from a balance of buoyant forces (F_B) and gravity forces (F_g).

$$F_B = \frac{\pi}{6} d^3 \rho_w g \tag{2.3}$$

$$F_g = \frac{\pi}{6} d^3 \rho_s g \tag{2.4}$$

where ρ is the density of water or density of solid respectively.

Drag (C_D) and lift coefficients (C_L), depend on the shape and surface roughness of the body and the Reynolds number. They are usually determined experimentally.

2.3 Incipient Motion

Incipient motion is defined as the initiation of particle movement when the moving water forces overcome the static forces of the particle. These forces experienced by the particle from the interaction of water drag forces, static and dynamic frictional forces, gravitational (weight) force, and any buoyant forces. For fine and cohesive materials, an adhesive force is added to the balance.

The Shields' diagram is the most recognized and widely used tool to predict incipient motion. Figure 2.3 is a copy of Shields' original diagram (*Shields*, 1936). Figure 2.4 is a more familiar Shields' diagram as presented by *Rouse* (1939) that shows a curve labeled as Shields curve (*Vanoni*, 1975; *Guo*, 2002). The curve separates the liquid-solids system into movement and non-movement regimes; values above the curve indicate movement while values below the curve indicate stability (no movement).

Shields' work is considered controversial throughout the literature. The graph is considered implicit by some researchers because shear velocity (u_*) is found both in the abscissa and ordinate axises (*Vanoni*, 1975; *Guo*, 2002; *Dey and Raju*, 2002), causing the need for engineers to create iterative calculations to solve for a dimensionless shear stress (τ_*). The ordinate axis generally known as the Shields parameter is calculated by Equation 2.5

$$\tau_* = \frac{\tau_o}{(\gamma_s - \gamma)d} \tag{2.5}$$

where τ_* is the dimensionless tractive force coefficient, τ_o is the shear stress associated with the boundary, γ_s is the specific weight of the grain, γ is the specific weight of fluid, and d is equal to the mean grain size.

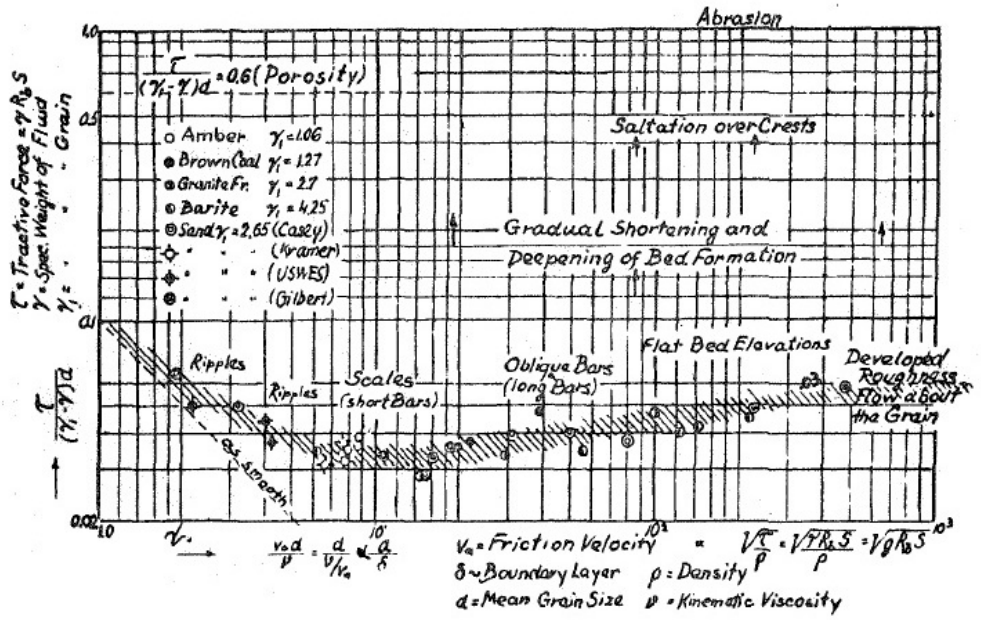

Figure 2.3. Shields original diagram (*Shields*, 1936)

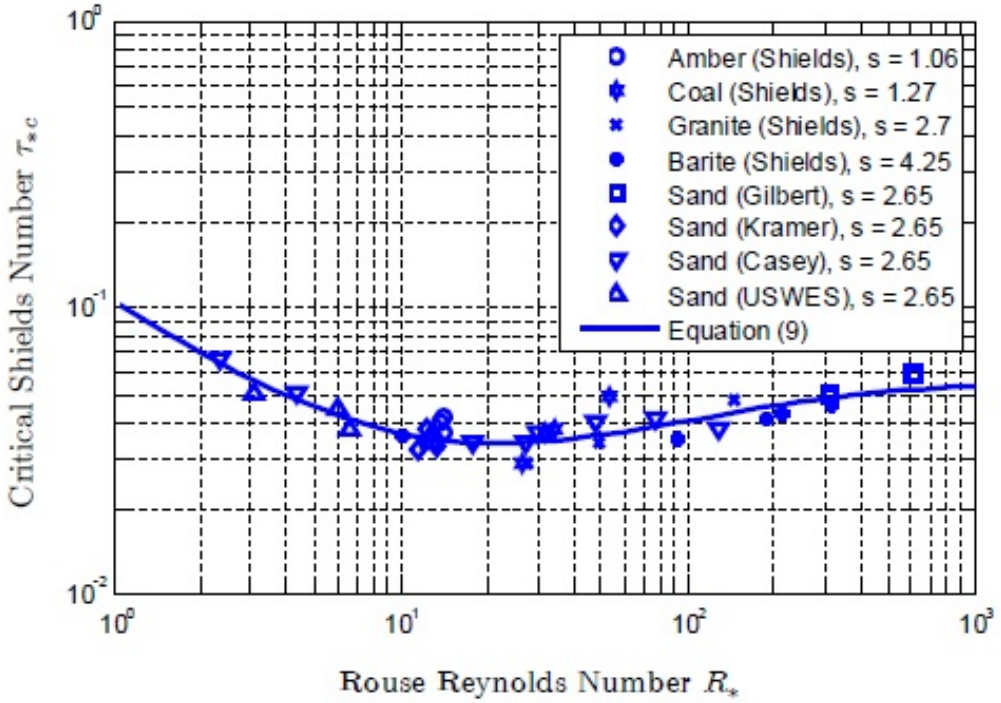

Figure 2.4. Shields diagram as presented by *Rouse* (1939)

The Shields' parameter is the dimensionless value at which particles have a high probability of incipient motion. Shields referred to this value as the critical tractive force coefficient (*Shields*, 1936) at which particles begin to move (incipient motion). An associated critical shear stress can be derived using the dimensionless value (τ_*) from Equation 2.6

$$\tau_c = \tau_*(\gamma_s - \gamma)d \tag{2.6}$$

where τ_c is the critical shear stress expressed in units of $\frac{lbs}{ft^2}$ or $\frac{N}{m^2}$.

The shear stress associated with open channel boundaries can be calculated by Equation 2.7 (*Elliot*, 2002)

$$\tau_o = \gamma_f R' S \tag{2.7}$$

where γ_f is the specific weight of the fluid, R' is the hydraulic radius of the cross–sectional area at a particular location in an open channel (sometimes replaced with D as the depth of flow in wide channels), and S is the slope of the energy grade line.

The abscissa axis on the Shields diagram represents the dimensionless Reynolds number associated with grain size, usually the mean grain diameter. The Reynolds number (R_{e*}) based on grain diameter is calculated by Equation 2.8

$$R_{e*} = \frac{u_* d_s}{\nu} \tag{2.8}$$

where R_{e*} is the Reynolds number based on grain size, u_* is the shear velocity, d_s is the known particle diameter or the mean particle size (d_{50}), and ν is the kinematic viscosity of the fluid.

Shear velocity (u_*) is calculated by using Equation 2.9 when the bed-shear stress is known or with Equation 2.10 if the characteristics of the open channel are known.

$$u_* = \sqrt{\frac{\tau_0}{\rho}} \tag{2.9}$$

$$u_* = \sqrt{g R_h S} \tag{2.10}$$

where g is the gravitational constant, R_h is the hydraulic radius, and S is the bed slope. The detailed derivation of these equations are reported in the literature by many authors (e.g. *Vanoni* (1975); *Guo* (2002); *Mays* (2005)), and these details are omitted herein.

2.3.1 Introduction to the Shields Curve

The introduction of the Shields curve and an equation referenced to as the Shields-Rouse Equation 2.11 (*Guo*, 2002) were first introduced by *Rouse* (1939). Rouse created a parameter that made calculations for the Shields diagram as explicit calculations. *Vanoni* (1975) states that the Rouse parameter, Equation 2.11, may be used if the fluid and sediment properties are known and common units are consistent throughout the equation.

$$R_* = \frac{D\sqrt{0.1(\frac{\rho_s}{\rho}-1)gD}}{\nu} \tag{2.11}$$

where R_* is the Rouse number, D is the sediment particle size (generally the mean grain diameter), ρ_s is the density of the sediment, and ρ is the density of the fluid, and g is the gravitational constant.

2.3.2 Using the Rouse Parameter

This section explains how to use the Rouse parameter to access the Shields Diagram. The first step is to calculate the Rouse number (R_*) using Equation 2.11. Next, find the intersection of R_* and the Shields curve, then project horizontally from this intersection to the y-axis to locate the dimensionless shear stress (τ_*) associated with the grain particle. From here critical values associated with the shear stress, shear velocity, and Reynolds grain number can be recovered from the above listed equations.

The critical values represent the conditions where incipient motion is possible and are used as reference values for comparing stability with known channel characteristics. For instance, when comparing τ_o and τ_C, if τ_o is greater than τ_C then incipient motion is anticipated, whereas if τ_C is greater than τ_o then incipient motion is not anticipated.

2.4 Sediment Transport Equations

Sediment transport equations incorporating various theories have been derived from data collected over the past century in laboratory and field experiments for uniform and non-uniform materials . The theories are based on different types of bed-load movement, as some include total bed movement while others address specific particle movements in suspension or over the bed. The different formulas are further based on empirical equations, semi-theoretical formulas based on physical concepts, probability theory, and dimensional analysis. Some theories are based on water velocities, discharge, shear stress, and bed form, while other theories regression analysis performed on the selected individual parameters. Formulas presented here are concerned with bed-load movement only, and the data collected in the experiments best fit these parameters provided in the formulas.

2.4.1 Du Boys' Equation

Du Boys' work influenced sediment transport work from 1879 to 1949. Du Boys' work assumes that sediment moves in layers along the stream bed and the movement is explained by a balance of tractive and resistance forces. Du Boys created an equation for the relationship between average cross sections of hydraulic parameters and shear stresses; the equation is shown as Equation 2.12 (*Du Boys*, 1879; *Vanoni*, 1975)

$$q_b = K\tau_o(\tau_o - \tau_c)^m \tag{2.12}$$

where q_b is bed–load transport rate in weight per unit time per unit width, τ_o is the hydraulically applied shear stress, τ_c is the critical, or threshold shear stress, for the initiation of movement, K and m are constants found experimentally, m is equal to 1 when τ_o/τ_c. K is related to the particle size, d, as presented in Equation 2.13 by *Straub* (1935),

$$K = \frac{0.173}{d^{3/4}} \tag{2.13}$$

where the units of K are $ft^6/(lb^2 - s)$ in the U.S. customary system.

2.4.2 Shields' Equation

The *Shields* (1936) transport equation is derived from the developed incipient motion parameters. The equation is homogeneous and may be used with any consistent units of measurement, as

$$\frac{q_b \gamma_s}{q\gamma S} = 10\frac{\tau - \tau_c}{(\gamma_s - \gamma)d} \tag{2.14}$$

where q_b is the bed-load per channel width, q is the water discharge per channel width, γ_s is the specific weight of the sediment, γ is the specific weight of water, d is the sediment particle diameter, and τ is the bed shear stress obtained by Equation 2.15,

$$\tau = \gamma H S_o \tag{2.15}$$

where H is the mean flow depth and S_o is the bed slope.

2.4.3 Meyer-Peter's Equation

Meyer-Peter et al. (1934) created an equation from analysis of laboratory experiments. The equation is designed for specific parameters of sediment particles. The equation can be used for coarser grain particles with diameters greater than 3 mm. Equation 2.16 is the Meyer-Peter equation in SI units,

$$\frac{0.4q_b^{2/3}}{d} = \frac{q^{2/3}S}{d} - 17 \tag{2.16}$$

where q_b is the bed-load per channel width, q is the water discharge per channel width, d is sediment particle diameter, and S slope of the energy grade line. The constants in the equation 17 and 0.4 are valid for sand grain particles with a specific gravity of 2.65.

2.4.4 Meyer-Peter and Müller's Equation

Meyer-Peter and Müller (1948) further advanced the work first performed by *Meyer-Peter et al.* (1934) with an additional 14 years of extensive data recorded from laboratory experiments. The laboratory experiments conducted by *Meyer-Peter and Müller* were used to develop relationships for sediment particles with any specific weight, different slopes, and different particle sizes to dimensionless bed load functions and dimensionless shear stress (*Meyer-Peter and Müller*, 1948). Their equation, derived from the original work of Meyer-Peter, is shown as Equation 2.17 in dimensionless form,

$$\left[\frac{q_s(\gamma_s-\gamma)}{\gamma_s}\right]^{2/3}\left(\frac{\gamma}{g}\right)^{1/3}\frac{0.25}{(\gamma_s-\gamma)d_m} = \frac{(\frac{K_s}{K_r})^{3/2}\gamma_s RS'}{(\gamma_s-\gamma)d_m} - 0.47 \tag{2.17}$$

where R is the hydraulic radius, d_m is the mean particle diameter, γ_s is the specific weight of sediment particle, γ is the specific weight of water, q_b is the bed-load rate in underwater weight per unit time and width, K_s/K_r represents a correction factor reducing the shear stress seen on the bed accounting for form drag losses, and S' is the energy slope.

2.4.5 Schoklitsch's Equation

Schoklitsch (1934) pioneered the discharge approach by analyzing experiments conducted in small flumes with well sorted sediment particles by *Gilbert* in 1914 . Schoklitsch

published two formulas, one in 1934 and the second in 1943. The 1943 equation was formulated by plotting a bed-load for a given flow and grain diameter verses slope. Schoklitsch equations are formulated in SI units and for grain particles that have a 2.65 specific gravity. The equation developed by the curve for the given results is shown as equation 2.18,

$$q_b = 2500 S^{3/2}(q - q_c) \tag{2.18}$$

where q_b is bed-load [(kg/s)/m], d is the particle size (mm), q is the water discharge, and q_c is the critical discharge at incipient motion calculated by Equation 2.19

$$q_c = \frac{0.6 d^{3/2}}{S^{7/6}} \tag{2.19}$$

where d is the particle size (m).

2.4.6 Rottner's Equation

The *Rottner* (1959) equation is based on regression analysis of laboratory data. The equation is based on hydraulic parameters and regression analysis. Rottner analyzed work performed by *Johnson* (1943) and created a relationship of bed-load movement to a relative roughness parameter. Rottner's equation is shown as Equation 2.20,

$$\begin{aligned} q_b =& \gamma_s [(\zeta_s - 1) g D^3]^{3/2} \\ & * \left\{ \frac{V}{[\zeta - 1) g D]^{1/2}} \left[0.667 \left(\frac{d_{50}}{D} \right)^{2/3} + 0.14 \right] - 0.778 \left(\frac{d_{50}}{D} \right)^{2/3} \right\}^3 \end{aligned} \tag{2.20}$$

where q_b is the bed-load discharge (in lbs/s per ft of width), γ_s is the specific weight of sediment (lbs/ft^3), ζ_s is the sediment's specific gravity, g is the acceleration of gravity, D is the mean depth (in ft.), V is the mean velocity (ft/s), d_{50} is the mean particle size.

2.4.7 Summary

The equations presented in this literature review are just a few of those available in the literature presented by many authors. These equations were applied to this research because they contain parameters that were collected in the physical model experiments and hence can be used to compare estimated and observed transport. The utility of such a comparison was to select which, if any, equation might be useful to the practicing engineer.

2.5 Open Channel Flow

The staggered barrel system examined exists as a hydraulic structure placed in an open channel. This background section reviews some relevant terminology related to open channel flow, in particular flow regimes and important dimensionless quantities.

The definition of open channel flow is a body of water flowing within a confining structure that has a top boundary exposed to the atmosphere (called the free surface) and solid sides and bottom. Open channels are streams, rivers, canals, ditches, man made structures with defined geometric shapes, and partially full pipe flow (*Sturm*, 2009). Open channels are important in this research because, with the exception of the portion of flow through the staggered barrel culverts (surcharged in these experiments), all experimental flows have a free surface.

Flows in open channels are characterized as either uniform or non-uniform, steady or unsteady, and sometimes as turbulent, transitional, or laminar. Uniform flow means the velocity and depth are constant between two cross sections; non-uniform flow is when the velocity and depth changes between two cross sections. In non-uniform flow, the depth may change from section to section. Non-uniform flow is further classified as gradually varying flow or as rapidly varying flow. Gradually varied flow means the depth changes

over long distances. Rapidly varied flow means the depth changes over short distances, and possibly with abrupt changes in depth in the streams structure. Flow is also classified as steady or unsteady. Steady flow is when the depths, discharge and velocity are constant at a cross-section over the time period of observational considerations. Non-steady flow is when the depth, discharge, and/or velocity changes over the time period of observational considerations (*Henderson*, 1966).

2.5.1 Basic Laws of Fluid flow

Open channel flow models use equations that balance the forces in the flow between the free surface, solid boundary and hydraulic characteristics in the water flow. Basic equations used are conservation of mass (continuity), conservation of energy, and conservation of linear momentum (force-momentum). Some of these expressions can be evaluated with simple 1-D calculations, while others require experimental work, derivations and/or integrations of known empirical equations. Conservation of Mass states that for any closed system, the mass of a system is indestructible as long as matter is not introduced or removed matter between two particles. Conservation of Momentum states as the momentum of a controlled system remains constant if no external forces are not introduced. Conservation of Energy, which is the first law of thermodynamics, states the total amount of energy in an isolated system remains constant over time, energy is neither created nor destroyed (*Potter and Wiggert*, 2002).

The definition of discharge is the product of cross-sectional flow and the mean section velocity as in Equation 2.21,

$$Q = VA \tag{2.21}$$

where Q is flow(discharge), V is mean velocity, and A is cross sectional area.

2.5.2 Flow Types

Two dimensionless properties are important in classifying open channel flows with regards to turbulence and energy; the Reynolds number (*Re*) and the Froude number (*Fr*) (*White*, 1979).

The Reynolds number classifies flow as laminar, turbulent or transitional. Laminar flow is when the fluid flows in parallel streamline layers. Turbulent flow is less organized, and the liquid will exhibit non-zero flow in all available directions of movement. Transitional flow is the change in flow from laminar to turbulent. The difference in types of flow was first described by Oswald Reynolds. Reynolds discovered that flow was a function of speed, depth, and viscosity and created a dimensionless relationship (*Reynolds*, 1883),

$$R_e = \frac{\rho V L}{\mu} \tag{2.22}$$

where ρ is the density of the fluid, V is velocity, L is a characteristic length related to depth, and μ is dynamic viscosity of the fluid.

Reynolds discovered the threshold for flowing fluids changing state between laminar and turbulent flow. Known today as a Reynold's number (R_e), the value is used to describe the flow type in moving fluids in pipes and open channels. Some scientists and engineers think the threshold for open channels is better described by lower values for separate laminar and turbulent flow represented as $R_e/4$. The Reynolds number reflects a ratio of inertial forces to viscous forces and is used in this research to classify the flow as turbulent as well as to examine some resistance models to explain observed behavior (*Potter and Wiggert*, 2002).

The Froude number reflects the ratio of inertial forces to gravity forces and is used in this research to classify the flow as sub-critical (an unanticipated result) or super-critical,

Table 2.1: Reynold's Numbers (R_e)

Flowline	Pipe	Open Channel
Laminar	≤ 2000	≤ 500
Transitional	2000–4000	500–1000
Turbulent	≥ 4000	≥ 1000

and to potentially examine some empirical models that attempt to explain solids transport behavior.

The Froude number is a function of speed and the depth of flow. Froude numbers are calculated by 2.23.

$$Fr = \frac{V}{\sqrt{gD}} \tag{2.23}$$

where V is the mean velocity, D is a length scale related to depth, and g is the gravitational acceleration (32.17 ft/s^2).

Froude values less than one indicate the flow is sub-critical; values greater than 1 the flow is super-critical and the value of one means the flow is critical. The term critical is related to the specific energy in the flow and the depth-energy relationship is unique at critical flow (an energy minimum). The Froude number is nearly proportional to velocity head and as such relates substantial information regarding the speed of flow relative to a particular depth.

Sub–critical flow has a depth greater than critical flow which in turn has a depth greater than supercritical flow for a given cross–section. Froude numbers are used in describing the shape of the surface profile and some other conditions of the channel (*Chow*, 1959).

2.5.3 Water Surface Profile

Water surface profiles can be derived from the energy equation and manipulated algebraically to form equation 2.25.

$$\frac{dy}{dx} = \frac{S_o - S}{1 - Fr^2} \tag{2.24}$$

where y is flow depth, x is flow distance, S_o is the channel slope, S is the energy slope, and Fr is the Froude number. Notice that the equation is undefined at the critical depth (Fr=1).

Graphical representations of water surface profiles developed by *Bakhmeteff* (1932)for gradually varied flow are shown in Figure 2.5. Textbooks in fluid mechanics and open channel hydraulics, and literature journals have provided tables and sketches describing the differences in flow types and the associated equations with very little change since their first development. Table 2.2 is a portion of the complete table available in *Potter and Wiggert* (2002, chap. 10), representing the classifications of surface profiles. In this research the observed profile(s) were all mild, (M_1, M_2, M_3) depending on where in the model the observation was made- details are presented in Chapter 6 of this paper.

$$\frac{dy}{dx} = \frac{S_o - S}{1 - Fr^2} \tag{2.25}$$

where S_o is the channel slope, S is the energy slope, and Fr is the Froude number. Notice that the equation is undefined at the critical depth ($Fr = 1$).

Table 2.2: Classification of Surface Profile

ChannelSlope	*Profile Type*	*Depth Range*	Fr	$\frac{dy}{dx}$	$\frac{dE}{dx}$
Mild	M_1	$y > y_o > y_c$	< 1	> 0	> 0
$S_o < S_c$	M_2	$y_o > y > y_c$	< 1	< 0	< 0
$y_o > y_c$	M_3	$y_o > y_c > y$	> 1	> 0	< 0

2.5.4 Flow Resistance

Flow resistance is caused by frictional forces at the free surface, frictional forces associated with the geometric cross-sectional form and taper, and frictional forces associated

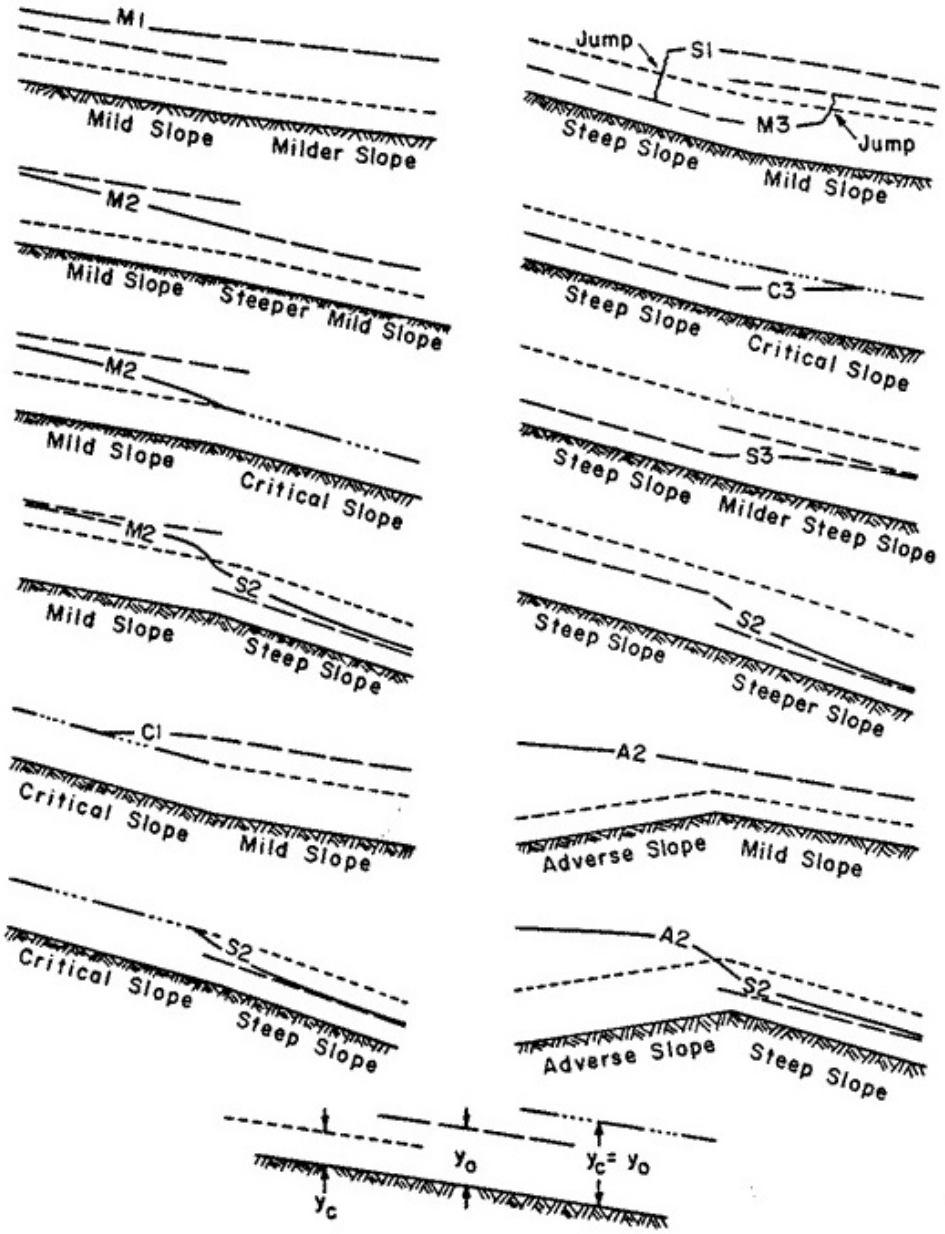

Figure 2.5. Surface Profiles adopted from Bakhmeteff Open Channel Hydraulics (*Bakhmeteff*, 1932)

with roughness of flow boundaries. Surface losses are generally related to shear stresses between the atmosphere and the flowing fluid body. Channels and hydraulic structures resistance factors are generally explained by a single coefficient. These coefficients include the

channel shape, form, and materials which in turn makes it hard to evaluate the coefficient. The problem then lies in the ability to predict velocity profiles (*Bray*, 1982).

Form resistance is related to the shape, size and type of material coming into contact with the liquid at the rigid boundaries.

Some of the earliest work performed on the discovery of flow resistance was done by Antoine de Chézy (1775). Chézy's Equation 2.26 describes the mean velocity in pipe and open channel flow (*Chow*, 1959),

$$U = C\sqrt{RS_o} \tag{2.26}$$

where U is the mean section velocity , C is the Chézy coefficient , R is the hydraulic radius, and S_o is the bottom slope .

Chézy's C coefficients relate to the frictional resistance of solid surfaces in pipes and open channels. The hydraulic radius captures the shape effect (and taper from section to section); the C coefficient captures the surface roughness at the liquid-rigid boundary interface. Chézy's work, which was performed in the 18^{th} century, however it was not published until the 19^{th} century about the same time of Robert Manning (*Rouse and Ince*, 1957). Robert Manning developed frictional relationships known as Manning's roughness coefficients, n. Manning's n values are tabulated in most engineering books and design manuals for fluid flow in pipes and open channels, and are the most widely used values for resistance for fluid flow over solid surfaces. Manning created a mathematical relationship between his roughness values and Chézy's C coefficients as presented in Equation 2.27,

$$C = \frac{c_1}{n} R^{\frac{1}{6}} \tag{2.27}$$

where C is the Chézy coefficient, c_1 is 1.00 for Si units and 1.486 for English units, R is the hydraulic radius, and n is Manning's roughness coefficient. However, Manning

discarded this general relationship of roughness for a more homogeneous equation which is recognized today as Manning's Equation (*Sturm*, 2009)

Like Chézy's resistance model, Manning's model also captures shape using hydraulic radius and surface roughness using the n value. Manning resistance coefficients are empirically developed from experimental measurements in terms of the mean velocity in flowing fluids. The product of this mean velocity and flow area is the channel discharge, Q. Many tabulated values of n were computed from measured discharges, for known water surface or energy slopes, and known cross–sectional areas. These n values are associated with descriptions of surface roughness (i.e. smooth concrete, short grass, etc.). As such, n, is not a directly measurable quantity (nor is Chézy's C), however the descriptive approach has served the hydraulic engineer well. Now known as Manning's Equation, 2.28 mean velocities can be derived for a channel by knowing the geometry of the channel and using a value of n from one of the printed tables,

$$V = \frac{c1}{n} R^{\frac{2}{3}} S_o^{\frac{1}{2}} \tag{2.28}$$

where R is the hydraulic radius, S_o is the energy slope, sometimes replaced with the water surface slope (non-uniform flow), and it is very common to use the channel bottom slope.

An alternate (hybrid) resistance model combines the concept of friction factor from classical flow in pipes as

$$U = \sqrt{\frac{8g}{f}\sqrt{RS}} \tag{2.29}$$

where f is the resistance factor (defined as friction factor by Darcy Weibach).

The friction factor is obtained from the Moody diagram or Jain equation by computing the channel Reynolds number

$$R_e = \frac{VD}{v} \tag{2.30}$$

where D is flow depth,

and the roughness ratio

$$\frac{k_s}{4R} \tag{2.31}$$

where k_s is a roughness height. In natural channels k_s is often taken as D_{50} of the channel material (or d_{84}).

A direct estimate is often made as (*Limerinos*, 1970),

$$f = \frac{1}{1.2 + 2.03\log(R/d_{84})} \tag{2.32}$$

2.6 Velocity Profile Distribution

Velocity profiles are plots of time averaged velocity versus depth or elevation from the rigid boundary (or mobile bed). The shapes of these profiles convey information on resistance and stresses that impact solids transport. In the literature, the velocity profile can be used to calculate the mean velocity. The shape of the profile is a function of the resistance coefficients found in the channel. Resistance equations used to predict the velocity profile are developed in straight uniform flow conditions, and the lack of data for the complexity of non-uniform flow and meandering channel shapes have limited the success to developing equations for these conditions (*Bray*, 1982).

Velocity distributions in turbulent clear water are explained by two regions for pipe flow and open channel flows. The inner turbulent layer which is influenced by the channels roughness, and the outer region that is only effected by shear stresses in the fluid and bed materials (*Coles*, 1956). Open channel flow is not uniformly distributed, nor is the velocity throughout the depth. Velocity profiles are often assumed to be logarithmic distributed in turbulent flows and linearly distributed in laminar flows (*Chow*, 1959; *Henderson*, 1966). Figure 2.6 presents typical velocity profile shapes for turbulent and laminar velocity profiles.

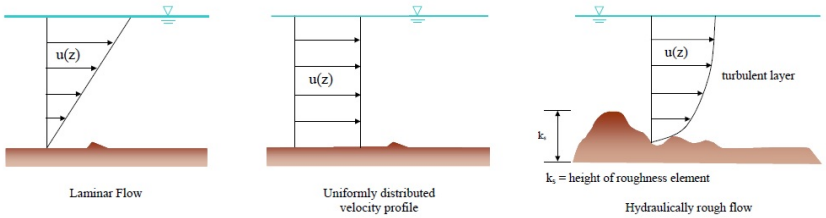

Figure 2.6. Typical velocity profiles in open channels (*Kummu*, 2002)

For turbulent flows, the semi-vertical portion of the velocity profile is logarithmic, the convex curve near the bed is a result of the bed roughness. Generalized assumptions made are the turbulent flow conforms to uniform and steady flow and all of the experimentations allow for fully developed flow regimes. The flow is assumed to be a function of the fluid and channel properties, as in Equation 2.33,

$$Q = \phi(U_*, \tau, \nu, D, S_o, roughness,\ geometry) \tag{2.33}$$

The structure of the function ϕ is mostly unknown, hence the reliance on empirical models and experiments. In culvert systems, the shapes are interpreted to convey the structures' ability to influence solid transport.

2.6.1 Boundary Layer Theory

In open channel flow, most flows are turbulent, but near the liquid-solid interface the velocity drops considerably and a boundary-layer theory is applied to describe stresses of this near-bed (or near-boundary) locations. The boundary layer thickness (δ) is a characteristic length (depth) from the solid boundary to where the velocity reaches 99% of the maximum free stream velocity (*Schlicting*, 1968).

The boundary layer theory divides the flow regime into four layers. Layer I is the uppermost layer and is generally referred to as the outer layer. The outer layer comprises 80–90% of the flow depth. Layer II is the logarithmic layer where the law of the wall holds true

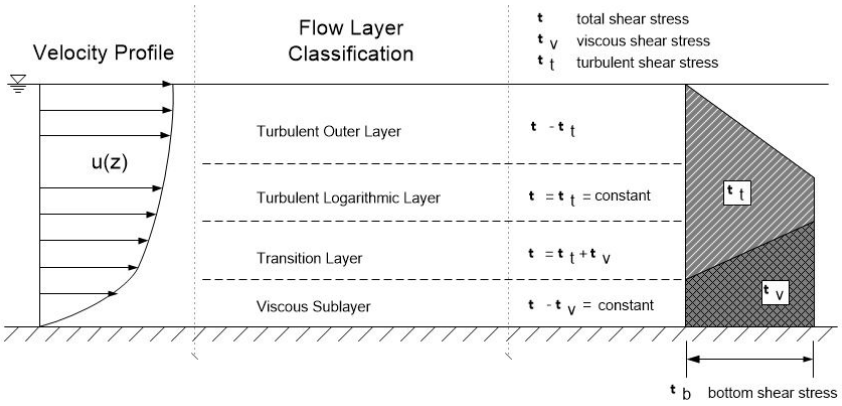

Figure 2.7. Representation of the boundary layers (*Liu*, 2001)

when the velocity distribution is logarithmic. Layer III is the transition layer where the laminar and turbulent layers are joining characteristics. The bottom most layer, Layer IV, is the viscous or laminar sublayer where the shear stress is constant throughout the layer (*Hinze*, 1975). Figure 2.7 is a drawing showing the boundary layers and their associated shear stress relationships. The viscous (laminar) layer is where the boundary roughness influences water flow. The thickness of the viscous layer (δ_s) can be found by Equation 2.34 developed by *Nikuradse* (1933),

$$\delta_s = \frac{11.6\nu}{u_*} \tag{2.34}$$

When the laminar layer thickness is much greater than the grain size, the grain roughness is not affected by the above turbulent flow. Such flow is called hydraulically smooth flow over the sediment bed. If the laminar layer is much thinner than the grain size, the grain roughness can protrude into the turbulent flow. Such flow is called hydraulically rough. Values are shown in the Figure 2.8 demonstrating laminar and turbulent flow with relationship to k_s and δ (*Keulegan*, 1938).

There are several theories on how to calculate the roughness height of the solid boundary. *Nikuradse* (1933) developed a roughness height in pipe flow related to an equivalent

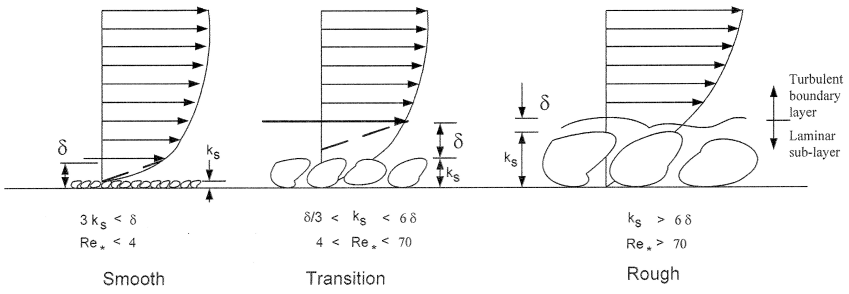

Figure 2.8. Relationship between grain roughness height and flow type near the wall region (adapted from *Bartnik and Struzynski* (1996))

mean height (D_{50}) for a sand grain treated as a sphere. Others have represented k_s as a characteristic height k to represent different relative grain sizes; i.e. d_{65}, d_{84}, and d_{90}.

$$k_s = d_{65} \qquad (\textit{Einstein}, 1950)$$

$$k_s = d_{90} \qquad (\textit{Meyer-Peter and Müller}, 1948)$$

$$k_s = d_{85} \qquad (\textit{Simons and Richardson}, 1966)$$

However, in open channel flow k_s is a representation of the roughness diameter caused by the grain distribution in the sediment bed rather than the height of the grains. In this case, some researchers feel k_s should be determined experimentally. *Bray* (1979, 1982) and *Hey* (1979) have developed relationships to grain sizes of 3.8 d_{84} or 6.8 d_{50} to represent k_s.

In boundary layer theory it is helpful to know where the no-slip boundary is located (height). The no-slip boundary is the constant in the logarithmic velocity laws that normalizes the equations. *Nikuradse* (1933) work produced a relationship between the grain roughness k_s and the height of the no-slip boundary. Different naming conventions exist for the height of the no slip boundary. The terms Z_o and y_o are interchangeable in the meaning of a characteristic height for the no slip boundary.

Nikuradse (1933) used the following relationships to explain Z_o :

$$\mathsf{z}_\mathsf{o} = \begin{cases} 0.11\nu/u_* & \text{Hydraulically smooth} \\ 0.033k_s & \text{Hydraulically rough} \\ 0.11\nu/u_* + 0.033k_s & \text{Transition} \end{cases} \tag{2.35}$$

some investigators think that Z_o has to be found experimentally or though empirical equations. The Law of the Wall is an example of an empirical equation (*Von Karman*, 1934) that can be used to find Z_o.

2.6.2 Distribution Theories

In the turbulent layer, the velocity profile is assumed to follow a logarithmic profile. Two approaches to explain the velocity distribution within the turbulent layer were reported about the same time. In the 1920's and 1930's both Prandtl and Von Karman developed logarithmic equations to explain velocity distributions *Schlicting* (1968),*Von Karman* (1934).

Prandtl developed a logarithmic velocity distribution along with the help of his students Schlichting and Nikuradse, closely related to The Law of the Wall equation developed by Von Karman (*Yang*, 1996). Equation 2.36 is Prandtl's equation,

$$u = A + 5.75log\frac{y}{k_s}U_* \tag{2.36}$$

where u is the velocity at a distance y above the bed, U_* is shear velocity ($\sqrt{gDS}$), D is the depth of flow, S is the slope, ν is the kinematic viscosity, and k_s is equivalent grain roughness defined by *Schlicting* (1968), A is a constant representing rough wall (8.5) or smooth wall (5.5) from Nikuradse.

Von Karman derived the classical theory The Law of the Wall. Equation 2.37 is one of the most recognized equations describing the velocity profile in the turbulent inner layer,

$$u = U_* \frac{1}{k} \ln(Z/Z_o) \tag{2.37}$$

where u is the velocity at a distance above the bed, U_* is the shear velocity, z is depth of flow, and z_o is characteristic depth where velocity is zero, and k is the Von Karman constant (0.41). U_* is derived from the slope of the linear velocity distribution and z_o is the quotient of the intercept divided by the slope $(z_o = B/m)$.

Scientists and students have been comparing their own work or confirming Von Karman's theories for decades. Von Karman believed that shear velocity and Z_o are determined mathematically from the log law equation and one requirement is that the velocity profile in the inner turbulent layer must fit the logarithmic profiles for the first 15-20% of the flow depth above the bed. Some scientists have extrapolated the theory into the outer layers of turbulent flow.

Equation 2.38 is called the Defect Law (*Guo and Julien*, 2001),

$$\frac{U_{max} - \bar{u}}{U_*} = f(\frac{y}{\delta}) \tag{2.38}$$

where U_{max} is the maximum velocity measured at the surface, $\bar{u}$ is the mean velocity, and δ is the thickness of the boundary layer.

The Defect Law is commonly used to explain the velocity distribution in the outer layer. The Defect Law assumes a logarithmic profile in the outer region and creates an overlap region with the log law. The Defect Law states the velocity distribution is strictly a function of depth rather than the effects of the roughness and viscosity.

When the Defect Law deviates away from a logarithmic profile, the deviation can be explained by the Wake Law. *Coles* (1956) developed a function using the law of the wall plus the wake law function that describes the separation point in the time average velocity profiles in the turbulent outer layer,

$$\frac{U}{U_*} = \frac{1}{k}\ln\left(\frac{Z}{Z_o}\right) + B_w + \frac{2\Pi}{k\sin^2(\frac{\pi}{2}\frac{y}{\delta})} \tag{2.39}$$

where U is the mean time velocity average, U_* is the shear velocity, k is Von Karman's constant (0.41), B_w is determined experimentally, Π is the wake strength coefficient calibrated with data in the outer flow region, y is the characteristic depth from the stream bottom, and δ is the boundary layer thickness.

The Wake Law has been proven to improve the accuracy of velocity profiles in open channels by *Coleman* (1981); *Nezu and Nakagawa* (1993), and *Coleman* (1986). For clear water, the Coles' wake strength was discovered to fall between 0–0.2. Although some researchers feel the wake law is applicable, other researchers such as *Guo and Julien* (2001) have found that existing velocity profile equations are not adequate to fit all observed velocity profiles.

2.6.3 Resistance to Flow with a Movable Boundary

Velocity profiles have been described by several methods when a movable boundary is considered. Prandtl's and Von Karman's methods have been applied, Nikurasde equations are often used, *Einstein and Barbarossa* (1952) developed several opinions and equations in their work.

Einstein (1950) expressed the velocity distribution resistance to grain roughness with

$$\frac{U}{U'_*} = 5.75\log(12.27\frac{R'}{k_s}x) \tag{2.40}$$

where U'_* is shear velocity because of grain roughness = $\sqrt{gR'S}$, R' is the hydraulic radius due to skin friction, k_s is the equivalent grain roughness = d_{65}, x is a function of k_s/δ, δ is the boundary layer thickness expressed as

$$\delta_s = \frac{u_* k_s}{\nu} \tag{2.41}$$

where ν is kinematic viscosity.

Engelund and Hansen (1967) developed an approach that expressed the energy loss to the bed form, *Lovera and Kennedy* (1969) and *Alan and Kennedy* (1969) derived a relationship of the Darcy-Weisbach friction factor to the grain roughness and the relative roughness in flumes and natural rivers. *Yang* (1996) developed an empirical technique looking at the unit stream power rather than the bed form.

Power law equations have been derived to explain the velocity distribution in uniform flows; although, most power laws have been developed through pipe flow tests, they are also used in open channel flow. A general form is

$$\frac{u}{u_{max}} = (\frac{y}{h})^{\frac{1}{m}} \tag{2.42}$$

where u is mean velocity, u_{max} is the maximum flow velocity taken at the free surface $(y = h)$, y is the characteristic length of depth above the stream bed (datum), and h is the flow depth. The $1/m$ is the power law exponent. When applying the power law near the bed surface, u_{max} can be replaced with the shear velocity u_*.

The exponent factor has been reported by many researchers as $m = 7$ (*Schlicting*, 1968; *Keulegan*, 1938). Nikuradse reported a $m = 7$ coefficient in his work for smooth walls in pipe flow *Nikuradse* (1933); *Schlicting* (1968). *Hinze* (1975) used $m = 7$ as a power law and reported results performing better than the log-laws,(some assumptions apply). Manning used an exponent $m = 6$ to show proportionality between average velocity and depth. *Chen* (1991) performed linear regression on various power exponents ranging from $m = 4$ to $m = 12$ and concluded each power law exponent was valid for limited range of Reynolds numbers. *Cheng* (2007) did an evaluation on deriving the power law as a first derivative of the log law and concluded that the power law works particularly well in the over-lap region and reasonably well for the majority of the flow field. These findings suggest that the widely acceptable Manning 1/6 power used by engineers should be adjusted to higher

values over rough boundaries.

2.7 Summary

This literature review is an introduction to many relevant subjects in the field of hydraulics and sediment transportation that are important in this research. Understanding what type of sediment movement will occur in our channels will help engineers in predicting erosion and deposition rates in our rivers, streams, and lakes. Different theories of sediment movement apply to suspended loads, bed-loads, and total movement loads. Sediment movement is a function of energy transfered through the flow, type of fluid, and kinetic and potential energy transfer from the flow to the sediment particles. This literature review is only an introduction to some complex topics involving sediment transport and the reader is advised to refer to the literature for a further explanation on the topics presented. The next chapter describes the construction process in developing the physical experimental model.

Chapter 3

Laboratory Model Construction

3.1 East Research Facility Background

Texas Tech University is home to a multi–functional open channel flume. The East Loop Research Laboratory was created to conduct relatively large–scale open channel experiments. The laboratory and open channel flume were funded by the Water Resources Center (WRC), Center for Multidisciplinary Research in Transportation (TechMRT) and Texas Department of Transportation (TxDOT). The research facility is further shared with the U.S.Geological Survey (USGS). Figure 3.1 shows pictures of the laboratory when looking geographically north and south.

(a) Upstream view (north wall in background)

(b) Downstream view (south wall in background)

Figure 3.1. Laboratory facility

The East Loop Research facility also functions as a student teaching laboratory. The main skeleton structure of the flume was built by subcontractors; however, all of the fin-

ished materials, desks, storage bins, and experimental models were designed and built by graduate and undergraduate students under the guidance of the laboratory manager and hosting professors in the Civil and Environmental Engineering (CEE) department. Students were exposed to the finer arts of construction and application of engineering techniques to accomplish various experiments.

The flume structure consists of an aluminum framework and aluminum floor panels welded to the aluminum framework. The flume walls are made of two $4ft \times 8ft \times 0.5in$ bonded glass panels. The see-through panels allow for photography and visual inspections of experimental work. The flume's dimensions are $50ft \times 8ft \times 4ft$.

Water is circulated continuously by two methods; five 2–in parallel submersible pumps (0.2–cfs ea.), or a variable speed controlled axial pump capable of pumping 30 cfs. For low discharge rates, the five 2–in submersible pumps are individually controlled with electrical switches allowing various off and on operational combinations. Combinations of discharge range from 0.2 to 1.0 cfs. For larger discharge rates, the variable speed axial pump is used. The variable speed controller allows for a discharge range of 1 to 30 cfs. The axial pumping system is constructed with 24–in $\varnothing$ PVC pipe on the suction and discharge side of the pump. The pump system circulates water from a 13,000 gallon reservoir to a 4,000 gallon head tank. Water is allowed to free flow from the head tank through a discharge chute into the flume for open channel flow. Flow rates through the head tank are measured using a discharge rating curve for the tank.

The flume is tiltable with slope ranging from a negative 0.3% to a positive 5.0%. The flume is tilted using variable speed electric screw jacks around a center pivoting axis with respect to the flume's length.

3.1.1 Laboratory Instrumentation

The laboratory uses several types of instruments for measuring velocities and flow depth, as well as various video devices for image capture. Velocity and flow measurements are made using several technologies. Mechanical velocity meters such as pygmy meters, axial-flow propeller meters, and drift tracers are used for extreme shallow flows or surface velocities. For flow depths more than 0.2 ft, 2-D and 3-D Acoustic Doppler Velocimeters (MicroADV) are used to measure velocities and compute discharges for varying flow depths, discharge rates, and channel model configurations.

Flow depths in the flume and reservoirs are measured by a series of permanently fixed, or hand held staff gages. Pressure transducers, bubblers, and radar level sensors are also used to measure depths and water-surface levels. Laser surface water technology is being developed and tested during on–going experiments.

Through the cooperation of the USGS, a simulated gaging station has been constructed to monitor the experiments in the flume. Data are transmitted from the radar and bubbler devices through a Satlink Data collector. Using a designated satellite signal, the data are fed live to web servers hosted by the USGS and published over the Internet. During live research operations the data are visible to the public. In addition, the USGS hosts a series of rain gages and varying field calibrating pressure transducers in the laboratory facilities.

Image acquisition is handled by various digital cameras, analog video cameras, digital video cameras, and an underwater video camera. Daily hand-written records and experimental results are collected along with recorded analog or digital data and stored on various computer systems.

Video operations are controlled by three systems. For broad general videoing, cameras manufactured by Swann security captures events around the laboratory and surface water conditions. The cameras have a Med-high-color resolution with an adjustable focal length

of 3.5–8mm. These cameras can record at a rate of 30 frames per second, and the accompanying software allows the video to be slowed to 1/10th of a second for a recorded frame. The analog system is great for capturing video of the drift tracers for surface velocities.

High resolution cameras are positioned around the experimental apparatus to capture live experimental events. The FOR–A VFC 300 is a variable frame rate camera that is capable of capturing images at a variety of frame rates and resolutions. The resolution ranges from 200px $\times$ 200px to 512px $\times$ 512px. Focal lengths are determined by the lens attached to the camera. The laboratory currently operates the cameras with 2 telephoto lenses for long distance recording, 1 semi-wide angle lens for close (2–10 ft) recording, and a fish-eye lens with a set focal length. Cameras are positioned to view through the glass panels or above the channel to capture water surface fluctuations or debris movement within the flow. The accompanying software allows for variable recording rates ranging from 300 FPS to time delay rates of 10 SPF.

The third video camera, a SeaView SeaMaster Pole-Cam System (SMP-50-SYS), features technology that automatically provides an optimal picture in all water conditions. Some of the features include automatic switching between color and Black&White pictures, high intensity infrared lighting assures clear viewing, compact body structure, and easily mounts to telescoping poles for control over mobility. The camera is equipped with RCA cables for recording on any type of monitor, camcorder, VCR, or TV. Operational power is either 110v or 12v DC battery.

3.2 Experimental Channel Construction

The experimental channel was designed and constructed to simulate flooding conditions in low water crossings as found in rural areas throughout central Texas. A rectangular stream channel was constructed out of plywood and dimensional lumber. The channel bed

was elevated off the aluminum flume floor with constructed floor trusses. Floor trusses were constructed in a typical web design used in lumber construction. Floor trusses were framed with 2×4 treated lumber and 2×6 or 2×8 dimensional lumber for top–plates; the 2×6 top–plate trusses were used at the junctions of the plywood floor, and 2×8 top–plate trusses were placed in the location of the flume containing the culvert models. A crawl space was designed in the floor truss' to allow a person to transverse the length of the experimental channel to install experimental equipment or make repairs to the model.

The experimental model floor was covered with 4×8 sheets of plywood for the complete 8–ft width of the flume. Full sheets of plywood were placed longitudinally, parallel to the flume side rails, in the center of the experimental channel. Gaps at the outer flume side walls were filled with cut sheets of plywood allowing for an expansion gap along the flume glass walls.

To simulate a stream channel with embankments, stream banks were constructed with an 8–in depth and a floodplain with 1/3 slope and 1.0–ft width. Stream bank construction allowed for a center stream channel width of 5.8–ft and a total top width of 7.8–ft (glass wall to glass wall). Figure 3.2 is a drawing that depicts a typical cross–section of the experimental channel.

The experimental channel was 40–ft long with the first 8—ft designed for a pooling area to regulate the discharge from the head tank chute. The remaining 32–ft contained the water transport stream channel. The final 10–ft of the flume was used for a sediment catch basin and free fall overflow into the large reservoir tank (Figure 3.3).

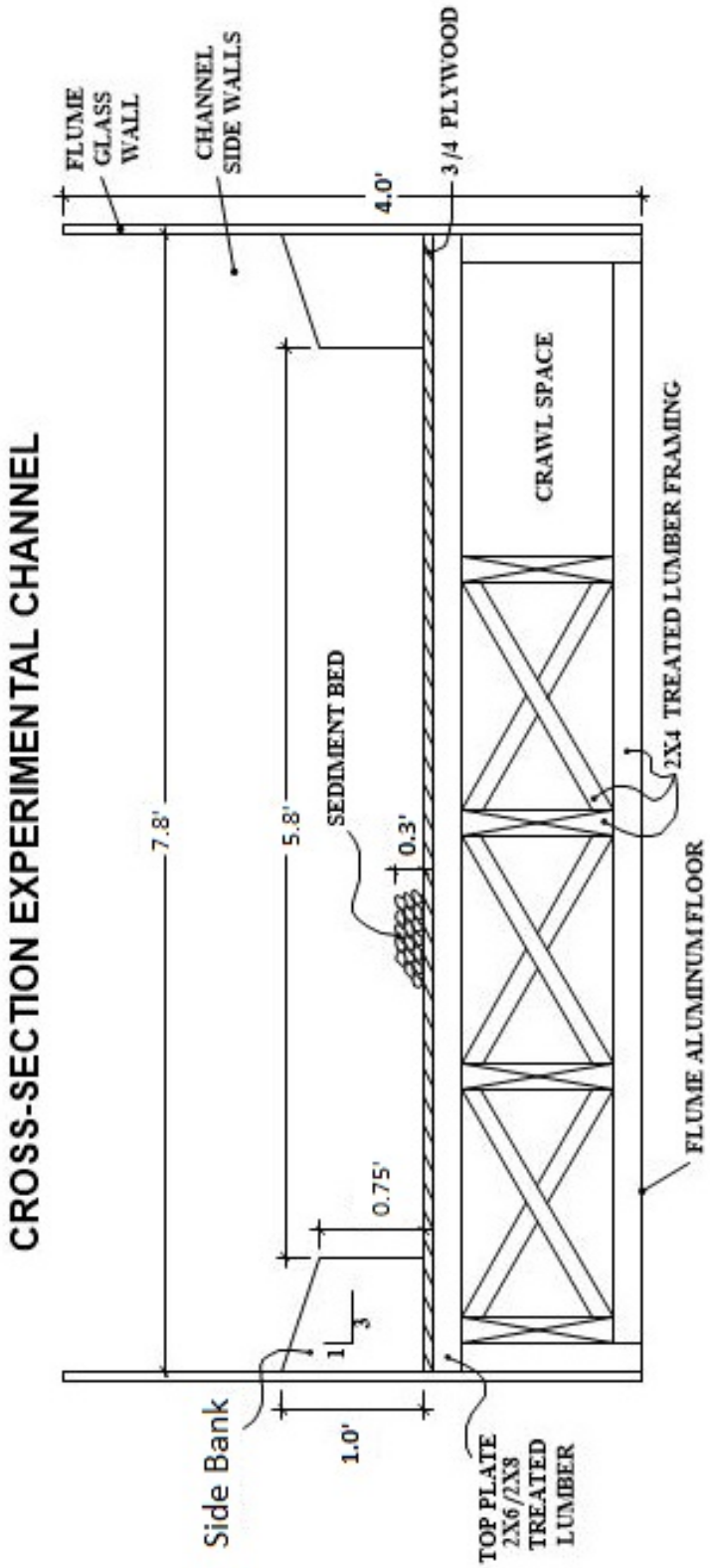

Figure 3.2. Experimental channel cross-section

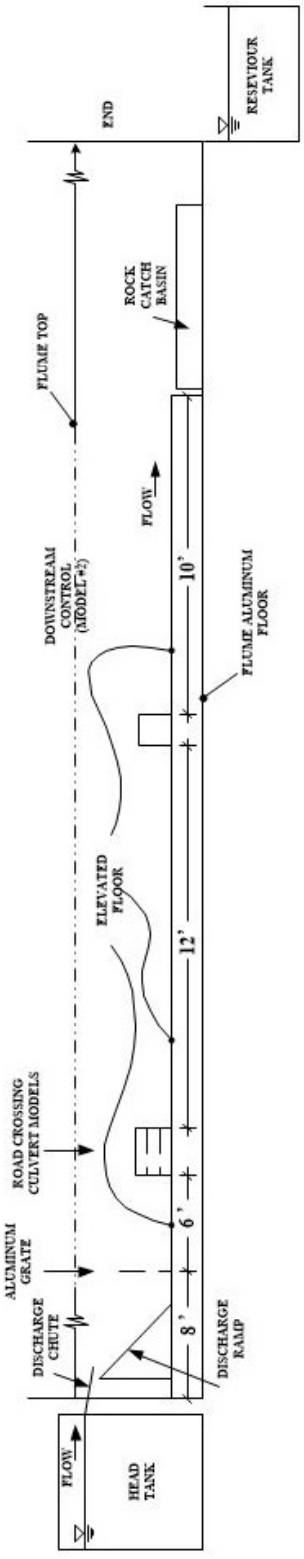

Figure 3.3. Elevation sketch of the flume and experimental channel

3.2.1 Discharge Ramp

In the beginning design stages for the experimental flow rates, water circulation tests demonstrated a large loss in energy in the water flow from the discharge head tank into the flume channel (pool area). The water tumbled into the pool area forming downward and backward (upstream) eddies (Figure 3.4). Starting experimental slopes were relatively low at a 0.3% that produced a water flow downstream by pure pressure flow, resulting into velocities that were too small to generate enough shear stresses to move the sediment particles.

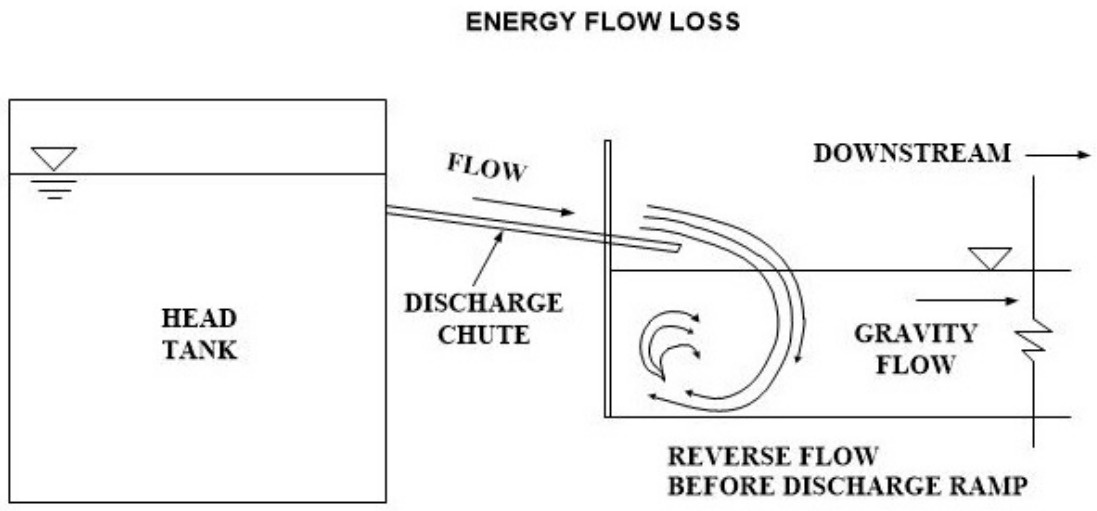

Figure 3.4. Elevation sketch of the flume and experimental channel

To remove the loss in energy, a discharge ramp was designed to direct the discharge from the head tank chute towards the downstream flow direction. The discharge ramp (Figure 3.5) was designed with a slight concave surface to gently introduce the discharge to the downstream direction and eliminate the backward formations of eddies. Momentum losses

Figure 3.5. Discharge ramp

were still experienced through the hydraulic jump formed at the union of the ramp flow and the channel discharge. The intensity of the hydraulic jump decreased as the water depth changed in the channel with increasing discharge rates; however, the upstream eddies and momentum loss were minimized.

A galvanized grate was installed at the beginning of the the stream banks to assist in breaking up the turbulent eddies formed from the merging discharge from the head tank and the channel water. The galvanized grate served two purposes: (1) the grate fins straighten and direct the discharge downstream and (2) created a backstop for the sediment bed formed in the channel. Figure 3.6 shows two pictures of the grate in service: Figure 3.6a is a picture of the grate separating the sediment bed from the discharge chute and Figure 3.6b shows the water flow pattern through the grate towards the sediment bed.

(a) Picture of the galvanized grate. **(b)** Water flow through the grate

Figure 3.6. Dispersion grate

3.2.2 Road Crossing and Culvert Design

Experiments used two types of road crossings that transversed the waterway. One configuration placed the road crossing perpendicular to the water flow and the second placed the roadway skewed 15° to the water flow. Drawings of the two road crossings are shown in Figure 6.13.

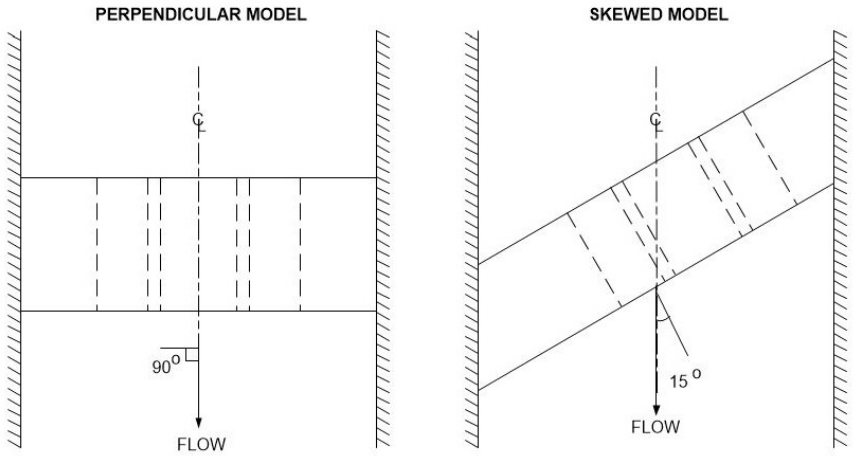

Figure 3.7. Drawing of the two model positions with respect to the flow direction

Two road crossings were placed in different locations down the length of the channel. The first was placed 6–ft from the grate and the second 14–ft downstream of the first

crossing. The first road crossing was placed in the area of interest for the experiments. The second road crossing was used as a downstream control point for the water surface and flow conditions. The dimensions of the road crossings were $7.5ft \times 2.5ft \times 0.92ft$. The road crossings traversed the width of the flume connecting the side banks and floodplain. The design for the road crossings placed the culverts in the center of the channel.

The road crossing and culvert system were constructed as modular sections to create a faster method when changing between the culvert model types. Modules consisted of a base, a center section, and the road top. The center module allowed the different culvert types to be easily interchanged, without the need of replacing the entire road crossing. Figure 3.8 is a photo of the students constructing the road crossing modules.

Figure 3.8. Road crossing under construction

3.2.3 Culvert Design

The research project required different culvert sizes and geometric shapes. Sizes and shapes ranged from 4–in and 6–in circular to a 6×7–in rectangle. Project require-

ments included the study of single and multi-barrel configurations. Culvert modules were designed and constructed in groups of three. The web design between each culvert was set at 50 % of the 6–in ⌀ circular barrels for all culvert designs and offset configurations (*ARM*, 1948, p. 410). Each barrel was built independent of each other to allow swapping of geometric shapes and sizes, increasing the number of combinations of available culverts. The culvert barrels were designed to place the inverts at 1.5 in above the plywood floor and level with the sediment bed.

Single barrel testing was performed by covering the outside barrels with a square plate. The square plates attached to each other by connecting a 2×2 square tube through the culvert. The square plates were then screwed to the 2×2 tubes in order to eliminate extra screw holes in main model.

3.2.3.1 Culvert Model Type

Eight different culvert model configurations were tested throughout the experiments. Culvert sizes included 4 in ⌀, 6 in ⌀, circular, and rectangular 6×7 in. Table 3.1 is a list of the culvert types, sizes, and the coding used in the data files. Culvert model results are described by the listed code in the remainder of the dissertation.

The tested culvert types included single and multiple barrels of the same size and geometric shape. Two exceptions were the staggered barrel configurations. The staggered barrels used two 4–in circular barrels sandwiching a 6–in circular barrel. Two different configurations used the staggered barrel set up, one constructed the inverts at the same level shown in Figure 3.9a and the second configuration was constructed with the crowns matching on each barrel as shown in Figure 3.9b.

Most culvert models were used in both the perpendicular and skewed road crossing model experiments; however, not all models were tested at the three slopes. Drawings

Table 3.1: Culvert Models

Description	*Size* (inch)	*Code*
Single Barrel Circular	4	S4C
Multiple Barrel Circular	4	M4C
Single Barrel Circular	6	S6C
Multiple Barrel Circular	6	M6C
Single Barrel Rectangular	6×7	SR
Single Barrel Rectangular	6×7	MR
Staggered Barrels with Inverts Equal	4–6–4	SB–I
Staggered Barrels with Crowns Equal	4–6–4	SB–C

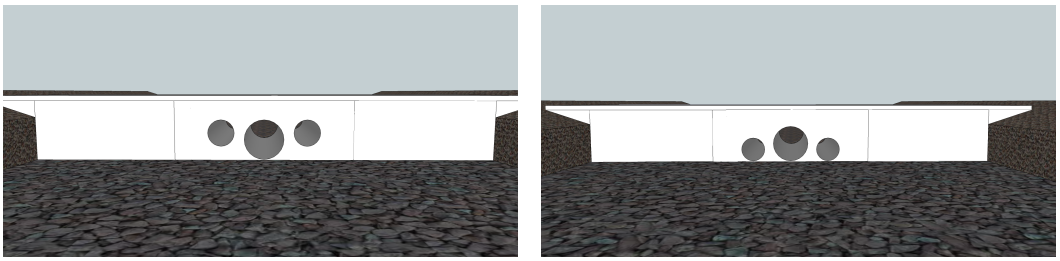

(a) Staggered barrels with the crowns at equal elevations

(b) Staggered barrels with inverts at equal elevations

Figure 3.9. Drawings representing the two staggered barrel configurations

representing the different culvert models are displayed in Appendix C. Original drawings are borrowed from *Dixon* (2011), which was an additional document produced from the research project.

3.3 Channel Form Resistance

Unusual velocity profiles were discovered across the width of the channel during the experimental design sessions. Velocities were much higher along the painted wood surfaces and the glass walls of the flume. To increase the resistance in the channel, outdoor carpeting was added to the stream embankments and 1.5 ft above the channel sides on the glass walls.

To increase roughness factor along the plywood channel floor, a sediment particle bed was created and leveled to a depth of 0.75 in before the first road crossing. An expanded aluminum metal screen was then placed over the top of the sediment bed and fastened to the plywood floor. Figure 3.10 is a photograph of these changes constructed to increase channel flow resistance. Figure 3.10a shows a section of the aluminum screen covering the sediment bed and Figure 3.10b shows the carpet added to the stream banks and glass walls.

(a) Picture of the aluminum screen trapping the lowest layer of sediment particles.

(b) Outdoor carpet applied to stream banks and glass walls.

Figure 3.10. Pictures showing the roughness factor manually increased in the channel

3.4 Sediment Types

Project scope included testing two different sized stones. Seven cubic feet of a nominal 1–in and four cubic feet of a nominal 2–in river bed gravel were purchased from a local rock distributor. Stones were stored in separate masonry bins built by undergraduate students working on the project. The 1–in size rocks were purchased assuming the rocks were of a well graded distribution.

3.4.1 Sediment Geologic Classification

An attempt was made to classify the rock material characteristics for sediment grain size, hardness values, rock classification, color, and specific gravity. Four different types of rocks were present. The types of rocks present in the sediment load were limestone, sandstone, chert, and various igneous rocks. Other characteristics that were examined included the roundness and color of the sediment load. Surface texture was examined visually and compared to standardized GSA rock color charts (*Oberman*, 2011):

- The limestone grain color (around 50%) ranged from very light grey (N8)to medium light grey (N6) to a pale reddish brown (10R 5/4). The limestone had a variety of different textures including a dull mat luster, pitted, curved ridges, and scratches.
- The sandstone grain color (around 25%) ranged from moderate reddish brown (10R 4/6) to moderate yellowish brown (10YR 5/4) to moderate orange pink (10R 7/4). The sandstone was pitted with a dull luster and some grains even displayed liesegang banding.
- The chert grain color (around 24%) ranged from black (N1) to very pale orange (10YR 8/2) to dark reddish brown (10R 3/4). The chert sediment textures varied in structure from pitted, scratched, smooth, conchoidal fractures, and frosted.
- The igneous grain color (about 1%) ranged from grayish black (N2)to moderate reddish orange (10R 6/6) to dark reddish brown (10R 3/4). All were dull in luster and some were foliated, with quartzite, gneiss, and quartz trachyte present.

3.4.2 Sieve Analysis

A laboratory grain size distribution was determined through a sieve separation analysis. A five–gallon sample was collected of each rock size. The 2–in rocks were run through U.S. Standard size sieves ranging from 2–in to 3/4–in. Everything captured on the 3/4–in

sieve was considered pan material for the end of the analysis. The 1–in rocks were run through U.S. Standard sieves ranging from 1-1/4 to 3/8–in. Everything passing the 3/8–in sieve was ignored and not considered as part of the grain distribution, because this material would wash from the model.

The two grain distributions are shown in the Tables 3.2 and 3.3. Figure 3.11 is a graph of the sieve analysis along with the physical rock count distribution. The results for the two distributions showed a poorly graded sediment distribution.

The research team's objective was to test two different size ranges in rocks; after studying the two distributions, the conclusion was drawn that each distribution represented a single rock size instead of a range in sizes. The grain analysis and physical count results showed that 1–in was the dominant size for the large rock range (Table 3.2), and 0.5–in was the dominant size for the smaller rock range (Table 3.3). Since the scope of the work did not include exploring the threshold of incipient motion, the grain size became a non–contributing factor in the overall procedures. Since the research team had some experience with working with a nominal 1/2–in sediment grain, the small rock was loaded into the experimental flume channel to start the experimental design process.

Table 3.2: Sieve Analysis Nominal 2–in Rocks

U.S. Standard	Mass Retained	Percent Retained	Percent Passing	Physical Count	Physical Count
(in)	(g)	(%)	(%)	(#)	(%)
2"	0.00	0.00	100.00	0	0.00
1.75"	0.00	0.00	100.00	0	0.00
1.5"	2251.52	7.18	92.82	6	0.76
1.25"	4329.09	13.81	79.01	81	10.29
1"	22194.78	70.79	8.22	596	75.73
3/4"	2576.98	8.22	0.00	104	13.21

Table 3.3: Sieve Analysis Nominal 1–in Rocks

U.S. Standard	Mass Retained	Percent Retained	Percent Passing	Physical Count	Physical Count
(in)	(g)	(%)	(%)	(#)	(%)
1 1/4"	0.00	0.00	100.00	0	0.00
1"	1056.08	3.40	96.60	35	0.67
7/8"	1717.5	5.53	91.07	85	1.64
3/4"	4825.88	15.53	75.54	337	6.49
5/8"	7048.34	22.68	52.86	803	15.47
1/2"	14043.13	45.20	7.66	3121	60.13
3/8"	2380.35	7.66	0.00	809	15.59

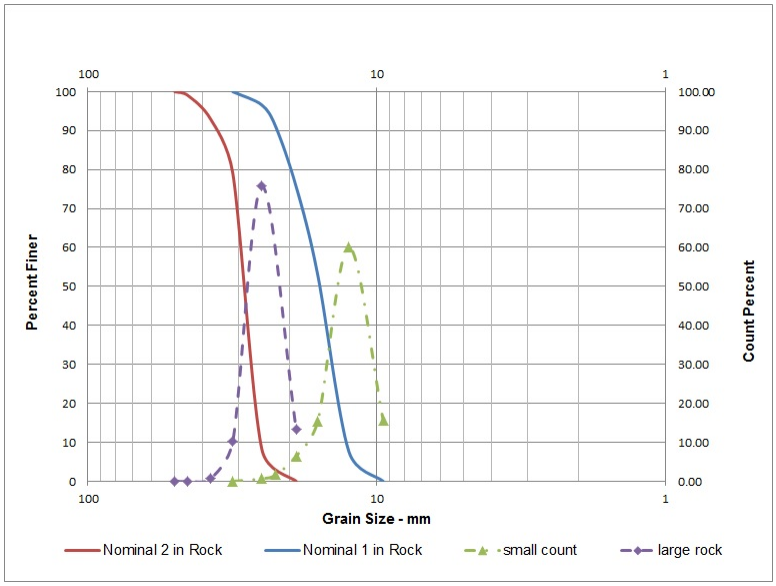

Figure 3.11. Grain size distribution for the nominal 2–in and 1–in rock

3.5 Summary

The experimental channel used in this research was constructed in a large flume operated by TechMRT and WRC. The channel was designed to simulate natural channel flows across a sediment bed. The research studied the affects of flood stages over a road crossing with multiple culvert sizes and barrels. Experimental procedures are presented in the next chapter includes the hydraulic conditions of the experiments.

Chapter 4

Experimental Design

The scope of this chapter is to describe how the experiments were designed. Experimental testing techniques strived for repeatability and redundancy. One of the theoretical questions was to find out if geometric shape, size, or quantity of barrels would affect the amount of sediment passing through a road system with culverts. Experiments were designed to study the interaction of semi–steady sediment bed movement and culverts under water flooding conditions. The experiments listed in this chapter are mentioned as category groups. Sediment transport experiments were conducted in series of three and the velocity profile experiments were conducted with the large grain particles. Not every culvert model was used at every slope, and the small grain particle was tested at only two of the three slopes. Changes were made throughout the project as the learning curve improved and because time was limited to contract time limits for this project.

4.1 Experiment Model Placement

Experimental procedural tasks were concerned with finding a discharge rate that would cause sediment movement at a constant continual rate. The research team expected the sediment downstream of the road crossing to easily move because of higher velocities and supercritical flow on the downstream side of the culvert.

Originally the experimental channel used a broad–crested weir as a means of discharge control and measurements and only contained one road crossing model at a downstream distance of 28 ft from the head tank discharge chute. Several experimental trial runs were

performed at different discharge rates while visually monitoring potential sediment movement. Incipient motion started in a rolling fashion at a discharge rate approximately 5 cfs from the discharge of the weir. Within minutes of beginning incipient motion, the sediment started to achieve an armoring state and further sediment motion stopped. Therefore, the flow rate was increased in small increments in an attempt to achieve continuous movement. The axial pump was operated by a variable frequency controller, so increasing the flow rate was relatively simple by increasing the electrical frequency in 0.1 hz increments. After 6 hours of careful monitoring of sediment movement and increasing flow rates, the sediment movement was occurring in small increments and forming a sediment dune 4 ft from the discharge of the weir (start of the experimental channel), leaving the sediment 14 ft from the desired culvert model. The sediment bed formed a dune that was as high as the stream side embankments. Final discharge rates were estimated at approximately 10 cfs. The only detectable sediment movement was directly in front of the culvert, an approximate 1.0 ft radius of sediment in front of the culvert barrel had been siphoned through the culvert. The remaining sediment in the channel before and after the road crossing had not moved.

In the second set of trials, the flow rate was increased over a shorter time period with shorter time gaps between flow increments. The end results were about the same. To better understand the possible movement of sediment grains, two sets of colored rocks were added to the channel and monitored for movement. A set of green rocks was placed 6 inches wide across the width of the sediment bed and 6 ft downstream of the weir. A second set of pink rocks were placed 14 ft downstream of the weir (6 ft in front of the road crossing). Experimental trials started with the discharge rate at approximately 7 cfs and increased to approximately 12 cfs. Sediment movement results (Figure 4.1) showed the green rocks moved about 4.0 feet from their starting position, however the pink rocks showed virtually no movement (Figure 4.2). An experimental trial was set up to increase

the flow rate rather quickly to approximately 20 cfs to see if full movement would be achieved. A flow rate of 18 cfs and channel depth of 1.5 ft were achieved before discharge started splashing over the back and sides of the channel upstream of the weir. Little to no improvement was achieved at this increased flow rate.

Figure 4.1. Sediment trial movement

A decision was made to remove the upstream weir to increase velocities in the mobile portion. Experimental trials continued with monitoring sediment movement and the water flow in the channel. Studying the water flow and direction showed the discharge from the head tank entered the flume channel and rolled backwards or in an upstream direction forming very powerful upstream eddies. Much of the energy of the water was lost in the first 6 ft of the channel. Flow depths in the channel fluctuated with the increased discharge to depths reaching 2 ft at the front of the culvert model at a discharge rate of 21 cfs. Sediment movement was limited to the start of the channel and had decreased in distance when compared to the movement with the weir.

Figure 4.2. Sediment trial movement showing no movement to the pink rocks.

Discharge calculations showed a mean velocity of 1.5 ft/s (45.7cm/s) and Froude number of only 0.18. *Hjulstrom* (1935) velocity vs. grain size graph indicated that the particle size velocity value used in this experiment was below the threshold for sediment movement. Figure 4.3 is a representation of Hjulstrom's velocity vs. sediment size graph. As a result, a discharge ramp was designed to reduce the upstream eddies and the energy loss at the entrance to the channel.

Experiment trials were repeated with the discharge ramp installed. Sediment started moving at approximately 7 cfs and reached a downstream distance of 8 ft for a discharge of 21 cfs in an elapsed time of 6 hours. Flow depth reduced to 1.25 ft. However, the sediment bed in the immediate vicinity of the road crossing showed no movement. Multiple trials repeating shorter time spans in between increase of flow rates produced the same results. Several trials were attempted over multiple days allowing for potential movement to increase over the previous day's distance. However, the additional distance in movement was minimal with the increase in time over multiple days. Because the laboratory could not operate 24 hours a day unattended, and the sediment movement only traveling short

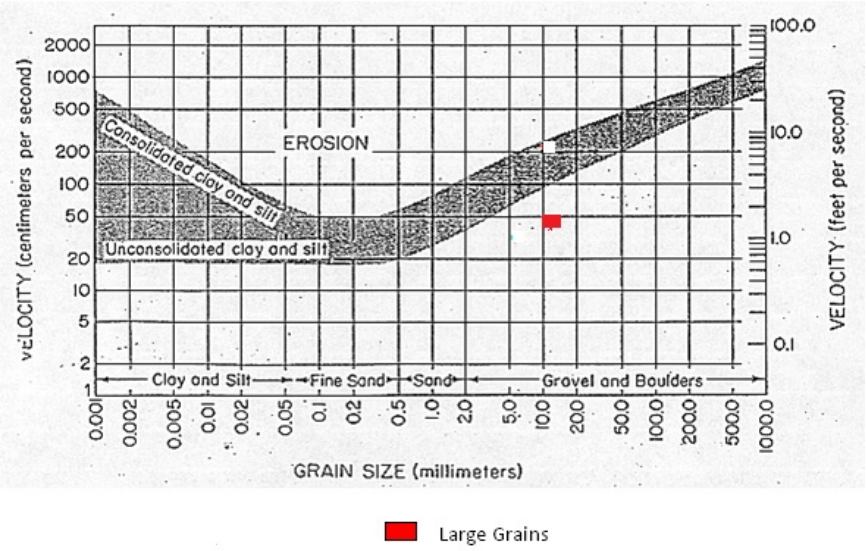

Figure 4.3. Velocity comparison on Huljstrom's diagram (*Vanoni*, 1975)

distances, a second road crossing with culverts was installed 6 ft from the start of the experimental channel. This location placed the culvert models at the downstream edge of the sediment's forward movement discovered in the first series of trials.

4.1.1 Development of Experimental Procedures

Through a series of trials manipulating discharge rates and elapsed time sequences, a psuedo quasi-steady state was developed in the experimental runs. The goal was to produce a constant sediment movement rate toward the culvert model. To achieve this goal a procedure was developed by increasing the pump's electrical power in small increments that in turn increased the discharge rates in small increments. The laboratory team would observe sediment movement looking for a quasi-steady sediment transport rate. The observational techniques in detecting the sediment movement is further explained in the next chapter, Incipient Motion. Ultimately the trial–and–error experimental runs produced a technique that became repeatable for other flow rates and time limits.

The original need of performing over 450 experiments was a controlling factor on time limits for a complete experiment. Techniques developed created total elapsed experimental time limits of approximately 5 hours. Due to the duration of individual experiments, adjustments were made to the number of experiments to a reduced number of 200. The repeatable experimental procedure is listed below in the following subsection. Slight changes were made when the experiments tested the smaller grain size. The changes made to the smaller grain size were only in the starting flow rates.

The research team made dimensional flow calculations relating to sediment size as suggested by *Peterson and Howells* (1973). With a new equivalent flow rate for the smaller grain size as compared to the large grain size, the laboratory team started conducting trial runs to verify sediment movement. After a few trial–and–error runs, the starting flow rate was reduced from 7 cfs to 5 cfs. Data collection for velocity bursts started at 8 cfs and continued through the final flow rate of 12.5 cfs.

4.1.1.1 Large Grain Experimental Procedures

The following list the standard operating procedure the laboratory team followed for each experiment conducted on the large grain sediment movement.

1. Start circulating pump at 24 Hz. Allow water to circulate 15 mins.
2. Slowly bring the pump speed to 32 Hz. Allow the water to stabilize for 15 mins.
3. Increase the pump speed 1 Hz every five mins till 38 Hz is reached. Allow water to stabilize for 15 mins.
4. Take velocity burst measurements for each MicroADV. (3 burst each) (100 samples in 40 seconds).
5. Increase pump speed 1 Hz to 39 Hz. Allow water to stabilize for 15 mins.

6. Take velocity burst measurements for each MicroADV.
7. Repeat this procedure until 42 Hz is reached or culverts become clogged.
   Definition of clog: a clogged culvert constitutes a MicroADV velocity reaching zero. A zero velocity relates to the MicroADV probe being covered with gravel particles.
8. Once culverts clog continue flow at the clogged discharge rate for 1 hr.
9. If no clogging occurs, continue experiment until an experiment time reaches 5 hrs.
10. Turn equipment off: Take pictures of results, survey sediment bed downstream of culvert, make sketch of upstream sediment bed load. Restore sediment bed to proper depths before and after model.

4.1.1.2 Small Grain Experimental Procedures

The following list the standard operating procedure the laboratory team followed for each experiment conducted on the small grain sediment movement.

1. Start circulating pump at 24 Hz. Allow water to circulate 15 mins.
2. Slowly bring the pump speed to 30 Hz. Allow the water to stabilize for 15 mins.
3. Increase the pump speed 1 Hz every five mins till 34 Hz is reached. Allow water to stabilize for 15 mins.
4. Take velocity burst measurements for each MicroADV (3 burst each) (100 samples in 40 seconds).
5. Increase pump speed 1 Hz to 35 Hz. Allow water to stabilize for 15 mins.
6. Take velocity burst measurements for each MicroADV.
7. Repeat this procedure till 37 Hz is reached.
8. Increase pump speed 0.5 Hz to 37.5 Hz. Allow water to stabilize for 15 mins.
9. Take velocity burst measurements for each MicroADV.

10. Increase pump speed to 38 Hz. Allow water to stabilize for 15 mins.
11. Take velocity burst measurements for each MicroADV.
12. Repeat velocity burst measurements every 15 mins for 120 mins.

    Special Note: If the culverts become clogged, stop burst and continue flow for 1 hour.
13. Turn equipment off: Take pictures of results, survey sediment bed downstream of culvert, make sketch of upstream sediment bed load.

Complete experimental times ranged from from 5 to 5.5 hrs. The variance in the overall time is within the start–up procedures for the laboratory, equipment start–up, initial stabilization of the water flow at 24 Hz, and verifying the levelness of the sediment bed. The data collection time for the experiments varied from 3.5 to 4.5 hrs and was dependent on whether or not the culverts clogged. The definition of clog in this project is when the MicroADV probes became covered at the entrance or exit of the culvert barrel. Once a clogged barrel was detected, data acquisition ceased and the discharge was allowed to run for 1-hr. The addition run time was allowed to see if the culverts self–cleaned of continually clogged.

4.1.2 Experiment Matrix

Two categories of experiments were conducted for this project. Category one monitored the sediment movement's interaction with the culverts. Category two experiments created velocity profiles for the length of the experimental channel.

Hydraulic characteristics of the discharge were monitored and recorded as the geometric properties for the culverts and/or slopes were changed throughout the experiments. Geometric properties include the two size ranges of sediment referenced as Large and Small rocks, three different channel slopes, 8 different culvert models, and two different approach angles to the road and culvert models.

- Sediment size ranges are 1/2 to 1 inch (12.7 to 25.4 mm) [Large grain] and 1/4 to 1/2 inch (6.3 to 12.7 mm) [Small grain]. Size ranges are explained further in a subsequent paragraph on sediment type.
- Three different longitudinal slopes were used. The first slope, 0.3% (0.003), represented a virtually level or a flat natural channel. This slope was chosen because it was the lowest slope that allowed for draining when the experiments were shut down. The second slope, 0.6% (0.006), studied the effects of the changing hydraulic properties in the streams currents. The third slope, 1.0% (0.01), represented the steepest slope at which the experiments could be operated with this model set-up.
- Eight culvert models were tested vary in size and geometric shape (Drawings of each are found in Appendix C).
- Culvert models were tested at two different angles with respect to the water flow. The first is a perpendicular approach angle to the water flow and the second being skewed 15° to the water flow direction. Culvert model types and road crossing approach angles are shown in Chapter 3.

A list of experiments performed with respect to sediment size, model type, slope, and approach angle is shown below in Table 4.1. Velocity mapping for the channel was performed for the large rock experiments only. The velocity mapping experiments were performed at speeds that did not induce sediment movement; therefore, the difference in grain size was assumed to have a negligible effect on the velocity profiles. The assumption is deemed valid because the measuring instrument resolution is insufficient to detect the slight difference for such similar grain sizes. Velocity profiles are discussed in Chapter 6.

Not every experiment in the matrix was conducted because as the experimental program proceeded it became evident that those experiments would not contribute additional knowl-

edge. For example, the staggered barrel configuration with the inverts at equal elevations clogged in similar fashions as compared to the multiple 4–in circular culvert model.

Table 4.1: Original Experiment Matrix

SedimentSize	*ModelType*	*Slope*	*Position*
Large Gravel	S4C	0.003, 0.006, 0.01	P
	M4C	0.003, 0.006, 0.01	P
	S6C	0.003, 0.006, 0.01	P
	M6C	0.003, 0.006, 0.01	P
	SR	0.003, 0.006, 0.01	P
	MR	0.003, 0.006, 0.01	P
	SBI	0.003, 0.006, 0.01	P
	SBC	0.003, 0.006, 0.01	P
Large Gravel	S4C	0.003, 0.006	S
	M4C	0.003 , 0.006	S
	S6C	0.003 , 0.006	S
	M6C	0.003 , 0.006	S
	SR	0.003 , 0.006	S
	MR	0.003 , 0.006	S
	SBI	0.003 , 0.006	S
	SBC	0.003 , 0.006	S
Small Gravel	S4C	0.003, 0.006, 0.01	P
	M4C	0.003, 0.006, 0.01	P
	S6C	0.003, 0.006, 0.01	P
	M6C	0.003, 0.006, 0.01	P
	SR	0.003, 0.006, 0.01	P
	MR	0.003, 0.006, 0.01	P
	SBI	0.003, 0.006, 0.01	P
	SBC	0.003, 0.006, 0.01	P
Small Gravel	S4C	0.003, 0.006	S
	M4C	0.003 , 0.006	S
	S6C	0.003 , 0.006	S
	M6C	0.003 , 0.006	S
	SR	0.003 , 0.006	S
	MR	0.003 , 0.006	S
	SBI	0.003 , 0.006	S
	SBC	0.003 , 0.006	S

4.2 Sediment types

During the design test stages of the experiments, an armoring effect was observed with the sediments loaded into the channel and a cohesive clay silt that was on the sediment caused an adhesion between sediment grains. Some of the silty cohesive material was washing from the sediment bed in the channel and creating too much turbidity for observations. A decision was made to clean (wash) the sediment grains and to separate the bed–load into control grain size ranges.

The entire sediment bed was screened to remove grain sizes smaller than 1/2 inch and return the rest to the experiment channel. Grain separation allowed for a control bed-load ranging from 1/2 to 1–in (12.7–25.4 cm). In the process of screening the bed material for the flume, the sediment grains were washed free of all silt and clay materials. Cleaning the sediment grains reduced the turbidity in the circulating system, making observations possible.

Five cubic feet of the nominal 1–in sediment grain was screened and separated into two categories, 1/2 to 1–in and everything < 1/2–in grain size. The sediment grains were stored separately, and the 1/2 to 1–in sediment was reloaded into the flume to the desired sediment bed depth. The remaining sediment grain load was used for recharge during the experimental runs.

Based on the initial experimental design observations, a decision was made to eliminate the larger 2–in sediment grain and to screen the sediment grains remaining from the 1–in grain to create a new control batch. The sediment material remaining from the first separation, grains smaller than 1/2–in were screened to separate an additional size range from 1/4 to 1/2–in. Material passing the 1/4–in screen was considered waste and not used in the experiments. Therefore, giving the researchers two separate sediment ranges required by the research objectives. For experimental purposes the two sediment sizes are

referenced as the large rock (1/2 to 1–in) and small rock (1/4 to 1/2–in) for the remainder of the dissertation.

4.3 Sediment Bed Dimensions

The starting stages of the experimental design, sediment was loaded into the flume to fill the channel to a 6–in depth (0.5 ft). This created a bed–load length of 20 ft before the road crossing equating to 58–ft^3 (2.14 cu. yds.) of material. The amount of material loaded into the flume channel was in excess of 5300 lbs.

Due to the excessive volume and weight of the sediment in the flume, the model design was changed to reduce the volume of material required. The thickness of the sediment bed was changed from 0.5 ft to 0.3 ft. Also, a second road crossing was added closer to the discharge of the head tank. The second road crossing was placed in a location equivalent to a typical sediment transport distance after 5 hours of continuous discharge.

The sediment load placed before the first road crossing model was a control volume of 8.25 ft^3 (eleven 5-gal buckets) weighing approximately 766 lbs. This sediment volume was then spread to a thickness of 0.2 ft across the aluminum screened floor. The corners of the road crossing and side embankments were filled to resemble a natural channel embankment. Figure 4.4 is a photo showing the sediment grains in the corners where the road crossing met the side banks. This sediment was placed in the corners, as shown by the yellow outline in the photograph, before each experimental run to create a gentle slope outwards from the corners to the sediment bed.

The channel section in between the two road crossings was filled with 20 ft^3 of sediment at a depth of 0.3 ft. The weight of the stones between the two road crossings was about 1800 lbs, resulting in a total sediment bed load of $\approx$ 2500 lbs in the experimental channel.

Figure 4.4. Sediment placed in the corners of the stream channel

The sediment load before the first road crossing was controlled by using a measured volume contained in 5–gal bucket increments The large sediment grain load used eleven 5-gal buckets for the perpendicular crossing, and fourteen 5-gal buckets for the skewed crossing. The small grain load used a control amount of twelve 5-gal buckets, and fourteen 5-gal buckets for the skewed model.

4.4 Laboratory Discharge Control

The original design of the experimental channel included a weir at the start of the channel for discharge control. The first weir was 13 inches tall (1–in taller than the 12–in model side bank depth) and extended the entire width of the flume. The length of the weir was 12 inches. In the center of the weir, a suppressed rectangular contracted weir was constructed for fine monitoring of the discharge. The contraction dimensions were $12 \times 12 \times 6$ inches deep. The invert of the contraction was placed at 7 inches above the wooden channel floor creating a 1–in differential in height between invert of the contraction and the top height of the sediment bed. The original contraction of the weir allowed for a maximum flow rate of 7–cfs before the entire weir would engage as a broad–crested weir. A series of checks and balances were set up to check the flow rate through the suppressed rectangle

weir. A second weir, sharp crested, was placed at the end of the flume channel and flow was calculated over the weir and a MicroADV (Sontek flow tracker) was used to measure the flow rates inside of the channel. Flow rates from the head tank were calibrated with equivalent measured depths from a staff gage attached to the head tank.

Calibration of the weirs and validation of the flow trackers were achieved using the known discharge values from the 0.2–cfs submersible pumps. To verify the discharge rates published by the manufacturer of the submersible pumps, a series of bucket tests were performed to clarify the discharge rates.

Discharge rates higher than 7 cfs were unachievable with the configuration of weirs in the experimental channel because of backwater effects encroaching on the weirs and eventually submerging the weirs in the flow. Once the weirs became submerged, the momentum was lost and sediment transport was observed to stop. Subsequently, the weir was removed and discharge was allowed to flow directly into the channel. Even with the free flowing discharge from the head tank into the flume, a severe loss of momentum in the discharge was caused by the drop from the discharge chute into the front of the channel. Maintaining this momentum was the primary reason for the discharge ramp described in Chapter 3.

4.4.1 Head Tank Rating

The discharge from the head tank was rated to produce a stage-discharge chart by using weir controls and MicroADV flow measurements. The head tank was rated for a discharge ranging from 0 to 30 cfs. In practice flows larger than 30 cfs could not be contained in the flume. Figure 4.5 is the discharge rating curve for the head tank.

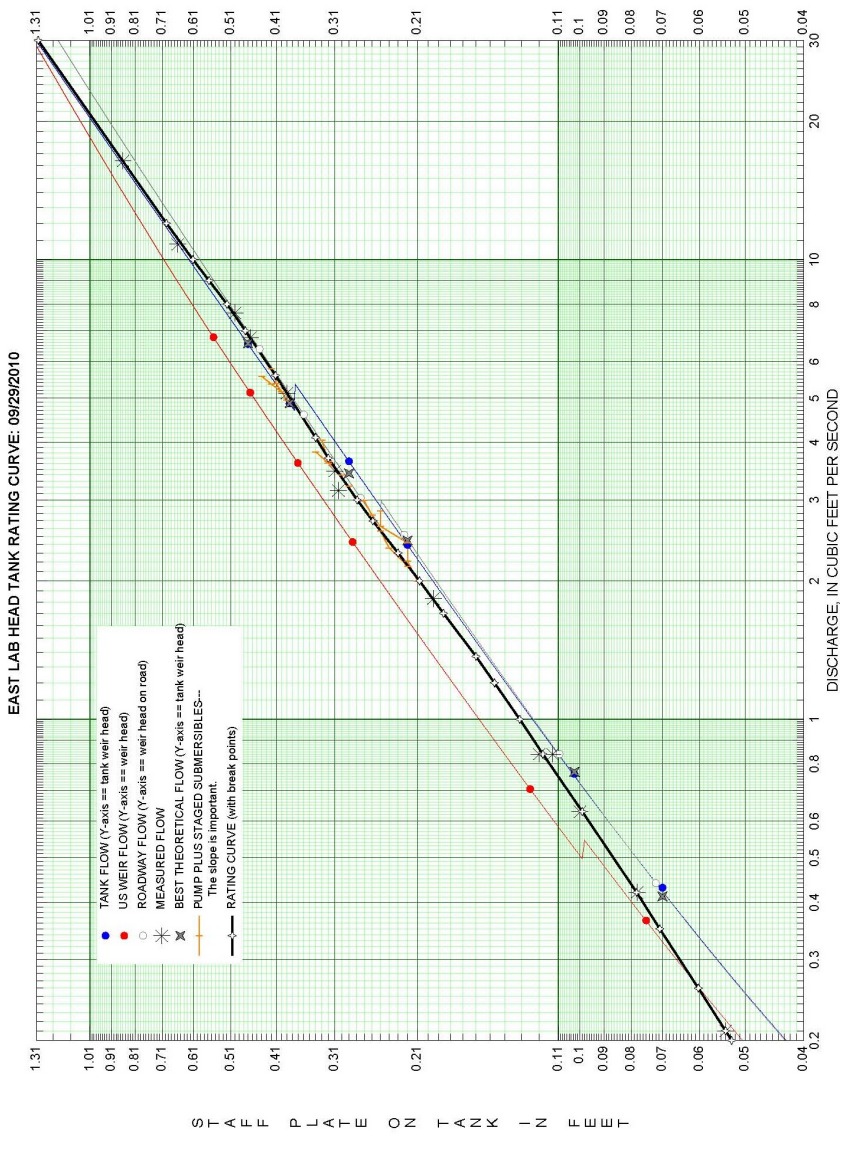

Figure 4.5. Head tank discharge rating curve (courtesy of William H. Asquith)

Chapter 5

Incipient Motion

Sediment transport has been studied for at least the last 100 yrs and has proven to be an elusive subject. Scientists and engineers have developed different methods and ideas to explain how sediment is transported in streams. Three main philosophies have emerged over the years for predicting and explaining sediment transportation: some researchers present a balance in forces, some researchers present an energy exchange from the flow to the sediment, and some researchers present a momentum exchange (*Chien and Wan*, 1999). The ability to predict sediment motion is an important part of predicting erosion rates in streams and rivers, and sediment deposits in lakes and reservoirs (*Cui and Parker*, 2005; *Cui et al.*, 2006; *Wiele et al.*, 2007). Understanding sediment transport is a substantial component for this research; however, the research did not set out to validate any of the sediment transport theories or laws, but to find out how sediment transport is influenced by different culvert types.

In the history of sediment transport, scientists such as *Neill and Yalin* (1969) and *Wilcock* (1988) demonstrated visual observations in their research while defining what and how much movement constitutes incipient motion. *Kramer* (1935) stated four different techniques in observations of sediment motion, and this project used similar techniques to predict incipient motion. The literature contains reports of visual observations of sediment movement and the definitions applied for the difference between no movement, little movement, and continuous movement. One of the best summaries for most of the literature can be found in a recent dissertation published by *Goodridge* (2009).

5.1 Techniques used to Detect Incipient Motion

Two techniques were used in verifying sediment motion, visual observation and monitoring the velocities in the flowing water. Visual observations were obtained through portal holes in the flume along with observations made through glass plates held on the top surface of the water. Sediment grain particles moved in a rolling and sliding motion across the sediment bed load. The movement started at the front of the experimental channel and continued in a dune form down the channel.

Incipient motion was not observed or detected randomly throughout the experimental channel. At the higher flow rates, the final sediment bed in between the upstream and downstream controls showed evidence of scouring in the first layer of sediment particles; however, this randomness was not visually observed or filmed during operations but was discovered after the waters receded in the channel.

5.1.1 Visual Observations

The laboratory team observed the sediment movement while looking for a continuous rate in movement. Visual observations monitored sediment movement looking for multiple grains in motion. When multiple grain movement reduced to single particle movement with time gaps not exceeding 1 minute in between movement and no visual movement; the discharge rates were increased by increasing the axial pump speed in 0.5 Hz increments on the variable speed controller. Further trial-and-error reduced the time gap between movement and no movement to a 20–second-gap for visual movement for single grains. Adjustments were also made in the flow rate by changing to 1 Hz increments every 10 minutes, which provided for multiple grain movements with visual time gaps established between 3 and 20 second-gaps. As the flow rate increased beyond 13 cfs (38 Hz) increases

in discharge were changed to 15 minute increments until a flow rate of approximately 15–16 cfs was achieved. Experimental times continued for approximately 2 hrs at this final discharge rate.

5.1.2 Velocity Monitoring

The second method used to trace the sediment movement was a technique of monitoring the velocity of the flow directly above the sediment bed. Velocities were monitored with a 3-D and 2-D MicroADVs positioned approximately 0.1 ft above the sediment bed. Figure 5.1 is a photograph showing the relationship of the developing dune and the MicroADV probes. In developing the technique, the water flow was reduced to expose the top crest of the dune to verify positioning. The location of the dune was measured and recorded with an equivalent time, which was a part of developing the technique of tracing the sediment dune with the MicroADVs.

Using the live viewing capabilities of the instrument through computer monitors, velocities were monitored for changes in speed. As the sediment bed-load migrated downstream, the MicroADVs were moved in conjunction with the sediment dune movement. Extreme caution was taken when attempting to place the MicroADV over the sediment formation of a dune so as not to influence or interfere with the sediment movement. Careful depth measurements made at the apparent top of the dune were taken in random time and position intervals to coincide with the visual observations of sediment movement. The MicroADV positions were adjusted to coincide with the position of the sediment dune as it grew in size.

Random sampling velocity bursts (100 samples in 40 seconds) were conducted to find the velocity necessary to keep the sediment moving at a visual constant rate. The velocities monitored by the MicroADV ranged from 1.2 to 1.6 ft/s (36.6–48.8 cm/s) at approximately

0.1 ft above the sediment bed. These measured velocities produced the desired sediment movement for the experiments. Through the dynamic function of the sediment motion, the accuracy of following the center of the dune proved to be difficult. Moving the adv manually in increments of 0.5 ft and constantly changing vertical adjustments without disturbing the sediment dune was at best a very slow method and often produced ambiguous and obvious incorrect results. This monitoring technique was eliminated after experiment #10 for the remainder of the experiments.

Figure 5.1. MicroADV's tracking the sediment dune migration

5.2 Comparing Data to the Shields Parameters

Experimental procedures were designed to find hydraulic conditions that would allow sediment movement to continuously occur. Hydraulic and sediment parameters representing the experiments were compared to Shields diagram to verify the visual observations and the measured hydraulic conditions surpassed the threshold for incipient motion. Sed-

iment movement was observed as rolling and sliding actions creating a migrating dune with only the smallest particles experiencing saltation for very short time intervals. Comparing the parameters necessary for incipient motion verifies that the hydraulic conditions produced in the experimental design are close to, or beyond the threshold, for incipient motion.

The following equations listed in the next few paragraphs, Equations 5.1 – 5.8 are used to find the parameters necessary to verify incipent motion on the Shields diagram. Equations 5.1 – 5.4 are used to find the critical limits applicable to a given grain size. Equations 5.5 to 5.8 are used to derive the experimental parameters of incipient motion from the known hydraulic conditions of the experiments. These equations and their definitions are further defined in Chapter 2.

Following the procedures laid out in the literature for applying the Shields diagram, Rouse Reynolds numbers (R_*) (Equation 5.1) were calculated as 3,575 and 1,267 for the large and small grain particles (d_{50}), respectively. The critical tractive shear stress (τ_*) associated with the calculated Rouse numbers found on the Shields diagram was 0.06 (dimensionless). Using the found τ_*, the critical shear stress was then calculated using Equation 5.2, critical shear velocity (u_{*c}) was calculated using Equation 5.3, and the associated critical Reynolds grain numbers Re_{*c} were calculated using Equation 5.4. A summary of the critical values[1] can be found in Table 5.1.

$$R_* = \frac{d_{50}}{\nu}\sqrt{0.1(\frac{\rho_s}{\rho}-1)gd_{50}} \tag{5.1}$$

$$\tau_c = \tau_*(\gamma_s - \gamma)D_s \tag{5.2}$$

$$u_{*c} = \sqrt{\frac{\tau_0}{\rho}} \tag{5.3}$$

[1] Only two experiments are demonstrated, one large rock MR culvert type and one small rock MR culvert type, because all the experiments used the same relative flow rates regardless of the culvert model type, slope, or approach angle. As explained in the experimental setup chapter, only the flow rates were adjusted as the grain particle size changed.

$$Re_{*c} = \frac{u_* d_s}{\nu} \tag{5.4}$$

Known properties from the experiemnts for the sediment grains and hydraulic conditions were as follows; d_{50} for the large rock distribution was 0.0625 ft (19.05mm), d_{50} for the small rock distribution was 0.0313 ft (9.5 mm), specific gravity for the gravel material was 2.66, and the kinematic viscosity (ν) at the median temperature for all the experiments (22 °C) was 1.01×10^{-05} $\frac{ft^2}{s}$. These values were used in the equations to verify observed results to Sheilds parameters for incipient motion.

Using the known experimental parameters listed in the previous paragraph, shear velocity was calculated using Equation 5.5, Shear stress was calculated using Equation 5.6, the Shields parameter τ_* was calculated using Equation 5.7 and the Reynolds grain number was calculated using Equation 5.8. Table 5.1 shows a summary of these calculations. The first section of the table shows the predicted values for the critical limits of incipient motion when using the Shields diagram and a known grain size. The second section shows two parameters in the table, the first are the Shields parameters calculated for the start of the experimental runs, and the second are the Shields parameters for when experimental steady state was achieved.

$$u_* = \sqrt{gR_h S} \tag{5.5}$$

$$\tau_o = u_*^2 \rho \tag{5.6}$$

$$\tau_* = \frac{\tau_o}{(\gamma_s - \gamma) D_s} \tag{5.7}$$

$$R_e* = \frac{u_* d_s}{\nu} \tag{5.8}$$

Table 5.1: Incipient Motion Prediction Values vs. Experimental Values

Prediction Values for Incipient Motion.

Grain Size	Rouse Number (R_*)	Shear Stress (τ_*)	Shear Velocity (u_{*c})	Reynolds Grain No. (R_{e*})	Critical Shear Stress (τ_{*c})
Large	3575	0.06	0.2	1238	0.388
Small	1267	0.06	0.1	619	0.194

Experimental Values for Incipient Motion.

Grain Size	Experiment Time	τ_*	u_*	Re_*	τ_o
Large	Begin	0.064	0.283	1751	0.413
	End	0.08	0.3198	1979	0.53
Small	Begin	0.123	0.278	861	0.398
	End	0.16	0.3153	977	0.51

5.2.1 Modified Shields Diagram

The Shields diagram has been modified through time by different researchers adding their data and their interpretations of sediment movement. One researcher, *Miedema* (2010A), modified the Shields diagram to reflect the critical limits experienced by rolling and sliding grain particles. *Miedema* digitally reproduced the Shields diagram and then added work performed from *Zanke* (2003), *Julien* (1995), *Yalin and Karahan* (1979), *Shields* (1936) and others as added by the listed authors by digitizing their data to the Shield diagram (*Miedema*, 2010A). Through analysis studies of his own and other researchers, *Miedema* created equations predicting sliding and rolling motions for sediment particles. The new equations produced two new curves that modified the location of the original Shields curve on the Shields diagram. As described earilier, the sediment particles moved in a rolling and sliding motion across the sediment bed and dune formation. Figure 5.2 is a copy of the modified Shields diagram as presented by *Miedema* (2010A) with the rolling and sliding curves applied. Sample results from two experiments are plotted verifying the

hydraulic parameters achieved for incipient motion. These results are graphed in Figure 5.2 as lines representing the changing parameters from the start of the experiment through quasi–steady state achieved for the end of the experiments.

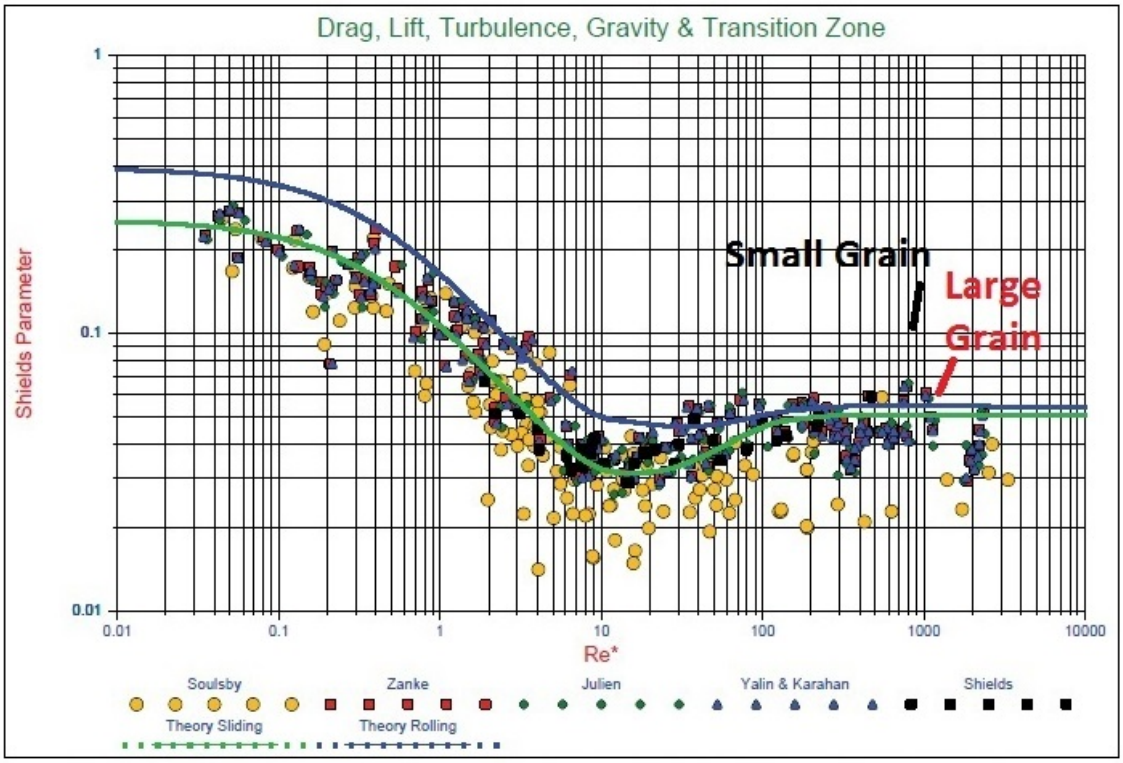

Figure 5.2. Shields diagram as presented by *Miedema* (2010A)

5.3 Summary

The Incipient motion barrier was exceeded (by design) in our experiments. The large grains are closer to the threshold of incipient motion as compared to the smaller grains. This result is reasonable because the experimental techniques were developed using the larger grain materials and the techniques were only slightly adjusted for the smaller grain material. The research wanted to minimize a variance in the experimental procedures

between the two grain sizes, so that the results would reflect the any influence the culvert models might have had on sediment transport rates. Also, the experimental procedures for the small grain materials were introduced to the skew model first. The skew model required slightly higher flow rates to keep the sediment grains moving. In retrospect, the design procedures for the smaller grains should have been tested against the perpendicular model first to find the threshold for continuous movement.

In addition, it should be noted that the smaller particles were more tightly packed when the sediment beds were set up for the experimental runs; therefore, requiring higher tractive forces to introduce incipient motion at the start of the experiments and in the dune formations. Although differences are present in this research experimental techniques, researchers *Gaucher, Marche, and Mahdi* (2010) found similar results that larger tractive forces are needed in tightly packed sediment beds.

Chapter 6

Velocity Profile Mapping

A portion of the experimental program included velocity measurements at three cross-section locations in the flume channel. Measurements were made upstream of and just downstream of the culvert models and in front of the downstream flow control to measure the changes in velocities.

The results of these experiments are interpreted in this chapter, in the context of the research questions and various plausible explanations from the literature. One of the experimental questions asked was "How do the culvert models affect the water profiles over the experimental stream beds with respect to depth, width, and horizontal position of the culvert model?" The conclusions interpreted in this chapter are based on the similarities and differences found in the effects the culvert models had on the flow at each slope. Individual examples shown in the figures are representative of the velocity profiles discussed in each section. Appendix B contains all of the velocity profiles produced for the culvert models at each experimental slope. The velocity profile graphs, in Appendix B, are presented in a ranked order starting from the smallest to largest cross–sectional area, starting with S4C and ending with MR.

6.1 Channel Profile Mapping

Figure 6.1 shows the physical locations for the velocity mapping performed in the channel. There are nine locations where velocities were measured and recorded. The nine locations are divided into three sections along the flow direction and three transverse

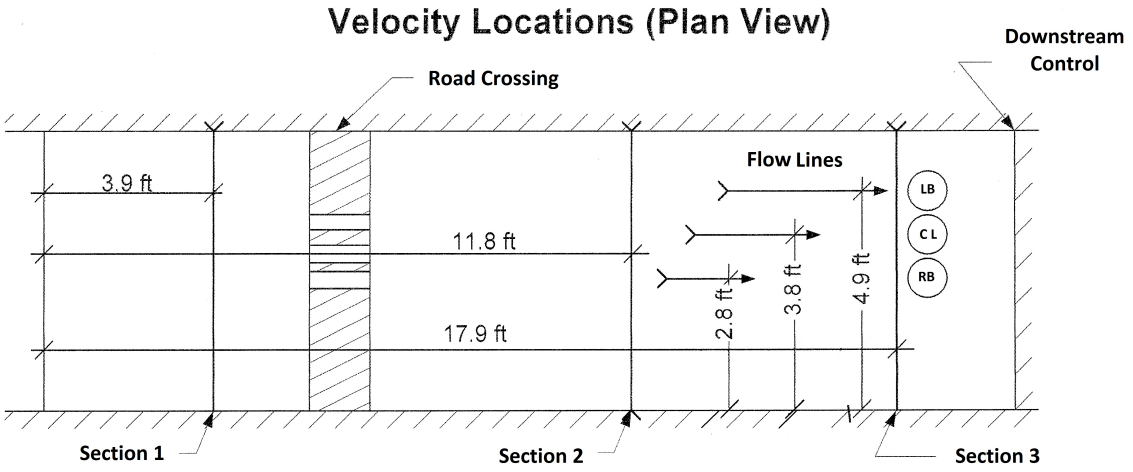

Figure 6.1. Drawing showing the locations for the velocity profile mapping.

positions at each section. The term 'flowline' used in this section of the dissertation refers to a geometric line segment joining stations at the three cross–sections. For example, the centerline stations at each cross–section form the centerline flowline. Similarly a left and right bank flowline are also presented in this interpretation.

6.1.1 Velocity Profile Locations and Development

In this research, observational techniques were described on how the incipient motion was classified. The discharge rate at which noticeable sediment movement began was approximately 7.0 cfs. Such initial movement only disturbed the sediment bed at the leading edge of the sediment bed. After a one hour time period, the materials moved a short distance of $\approx$ 1.0 ft downstream before an armoring effect occurred. Transport movement created a dune with a radius of $\approx$ 1.0 ft in the center of the stream channel. The dune's height was only $\approx$ 0.2 ft.

Knowing the limits of the sediment movement, a channel velocity observation location was designed to construct the depth-velocity profiles before the culvert model. The channel

was divided into three partitions parallel to the flow direction (called flowlines) and divided into three sections transverse to the flow, creating the nine measured locations in an *x*-*y* plane. The transverse position for the flowlines are referred to as Left Bank (LB), Centerline (CL), and Right Bank (RB). The longitudinal locations are referred to as Section 1, 2, and 3, respectively, moving downstream from the start of the stream bed channel (grate) (Figure 6.1).

Velocity measurements were taken at 0.05 ft, 0.1 ft, and then in increments of 0.1 ft to a total depth of 0.7 or 0.8 ft (total depth depended on model type and/or experimental slope). The sediment bed was set as the datum reference point of 0.0 ft. A free board gap was left in between the last velocity measurement and the water surface of $\approx$ 0.2 ft. Measurements in this region were not attempted following the MicroADV manufacturer's specifications for accuracy limits in shallow flows and to avoid any interference with possible wave action on the water surface.

6.1.2 Location Development

The longitudinal locations for the velocity profiles in each section were derived as follows.

- Section 1 was established as the bisector of the distance between any possible sediment movement and the road crossing where the water stage was relatively a constant depth. Depth measurements were taken linearly between the aluminum grate and the road crossing and recorded. At the operating flow rate of 7 cfs, depth measurements were constant for about 1 linear ft and the median distance from the grate was used as the location for Section 1.
- Section 2 was established by dividing the distance between the road crossing and the downstream control in half and then repeating the technique of Section 1 to find a

constant water stage and distance. Again, the measurement location was located in the center of the linear distance and relative constant depth.

- Section 3 was placed an equal distance from the downstream control as Section 1's distance was from the road crossing (2.1 ft).

The developed technique absorbed the structures' effects on the top water surface profile and any backwater effects caused by the control structures. The locations chosen best represented uniform flow conditions in the experimental channel.

The transverse sections were selected with respect to the culvert's position in the channel and the relative equivalent width of the culvert models. The model's design placed the centerline of the middle (or single) culverts in line with the centerline of stream channel, so the research team decided to use the center flowline of the channel as the center measuring location. Left– and Right–bank flowlines were selected as the perpendicular bisector of outer most edge of the widest culvert model. The widest horizontal model type was the three 6–in circular barrels (MR had same horizontal dimension of 6–in). Velocities were measured at the outside edges of the culverts and the center of the channel. The flow line locations were held constant for all three section locations, creating a velocity map of the middle 25% of the channel.

6.2 Velocity Profile Graphical Representations

Data collected during the velocity mapping experiments included water depths and associated velocities for the discharge flow rate of 7.0 cfs ($\pm$ 0.2 cfs). Incremental depth measurements were obtained by the scaling on the holding rods for the MicroADV instruments, and total depths were measured with staff gages. The velocity measurements at each depth were averages of 300 velocity samples over an approximate time of 3 minutes.

Figure 6.2 is a 3-D representation of velocity profiles for the staggered barrel configurations at the 0.3% slope. Slight differences could be detected in the velocity profile maps, mainly with the top velocities showing a faster speed in the staggered barrel configuration. The horizontal axis in the graph, displays both position and velocity magnitude at each respective position.

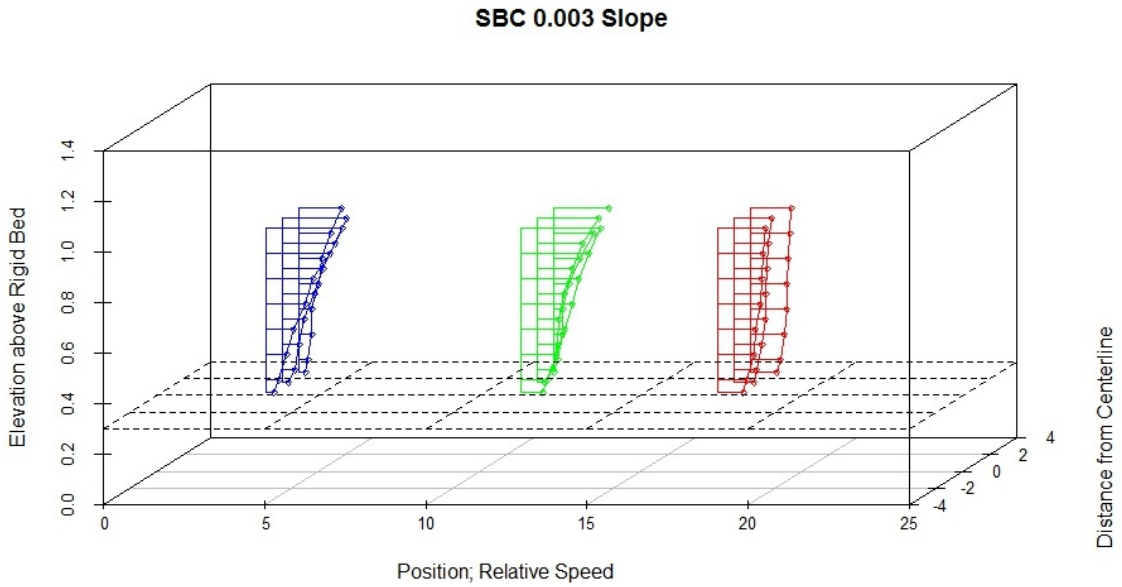

Figure 6.2. 3-d Velocity profile for the staggered barrel culvert model

6.2.1 3–D Graphs used for the Interpretation of Velocity Profile

Using the 3–D plots to compare the culvert models with respect to each other and slope was difficult because slight differences were hard to detect in the plots. The 3–D plots represented an individual model with respect to each position with a profile relatively consistent throughout the total channel. Instead, 2–D graphs were constructed to allow the subtle differences to be more visual and detectable.

Individual velocity profiles at the nine locations were plotted with velocity on the horizontal [abscissa] axis and the depth (elevation) on the vertical [ordinate] axis. The individual graphs were combined by over–laying respective positions to visualize [analyze] the water flow pattern migrating downstream with respect to individual flow lines and at each traverse section in the channel. Table 6.1 is a schematic of the individual velocity profile plots constructed with respect to position and location in the flume. Combination plots are labeled LB, CL, and RB displaying the velocity profiles at the 3 sections (Up, Mid, and Down) simultaneously with respect to flow lines. These plots help interpret the changes in profiles as caused by the road crossing models. Combination plots labeled Section 1, 2, and 3 display the velocity profiles across the section, traverse to the flow, simultaneously. These plots helped interpret changes across the stream's width and were also used to interpret effects of the culvert models.

Table 6.1: Velocity Profile Schematic

Position	$Section1$ $\Downarrow$	$Section2$ $\Downarrow$	$Section3$ $\Downarrow$
Left Bank $\Rightarrow$	Upstream (Up)	Midstream (Mid)	Downstream (Dn)
Centerline $\Rightarrow$	Upstream (Up)	Midstream (Mid)	Downstream (Dn)
Right Bank $\Rightarrow$	Upstream (Up)	Midstream (Mid)	Downstream (Dn)

Figure 6.4 is an example of the individual velocity plots at the nine positions for the SBC Model. The first row was combined to create the Left Bank flowline plot, the second row was combined to create the Center Line flowline plot, and the third row was combined to create the Right Bank flowline plot. The flowline plots then could be analyzed for flow patterns down the length of the channel. The first column could be combined to create the Section 1 plot, column 2 could be combined to create the Section 2 plot, and column 3 could be combined to the create Section 3 plot. The section plots were analyzed for flow patterns changing transverse to the flow direction.

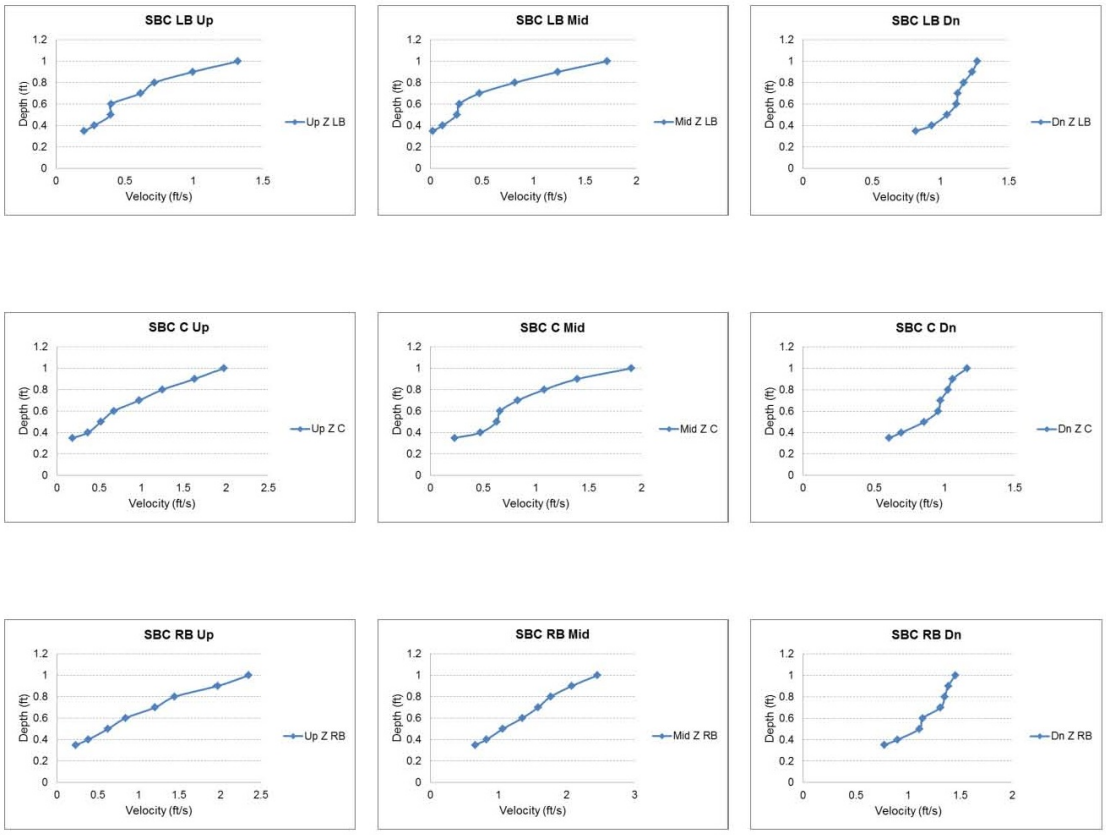

Figure 6.3. Individual velocity profiles for the SBC - 0.003 slope

Individual plots showed the velocity slowed at the sediment bed and magnified in speed for the top third of the flow depth for Sections 1 and 2. Negative velocities are shown on some plots which indicated the presence of eddies and reverse flows at the sediment bed.

Figure 6.4 is a representation of the combination plots for the SBC model. Graphs are shown with respect to flowline and section. The combination plots were used to detect the effects of the culvert model had on the flow patterns within the experimental channel. The upper row of plots in Figure 6.4 are the result of combining along a row of individual plots in Figure 6.4. The lower row in Figure 6.4 are the result of combining along a column of individual plots in Figure 6.4.

The combination plot displayed non-traditional velocity profiles around the culvert models. Section 3 plots showed the first sign of fully developing flow patterns traditionally represented in open channel flow. As a contrast, the combination plots for the 4–in circular multi-barrel culverts are shown in Figure 6.5. Combination plots for all of the recorded velocity profile experiments are presented in Appendix B.

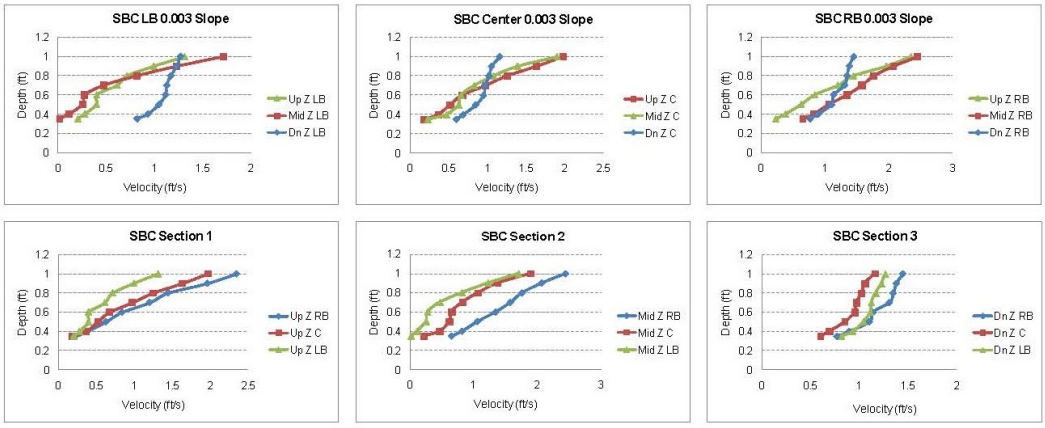

Figure 6.4. Combination velocity profiles for the SBC - 0.003 slope

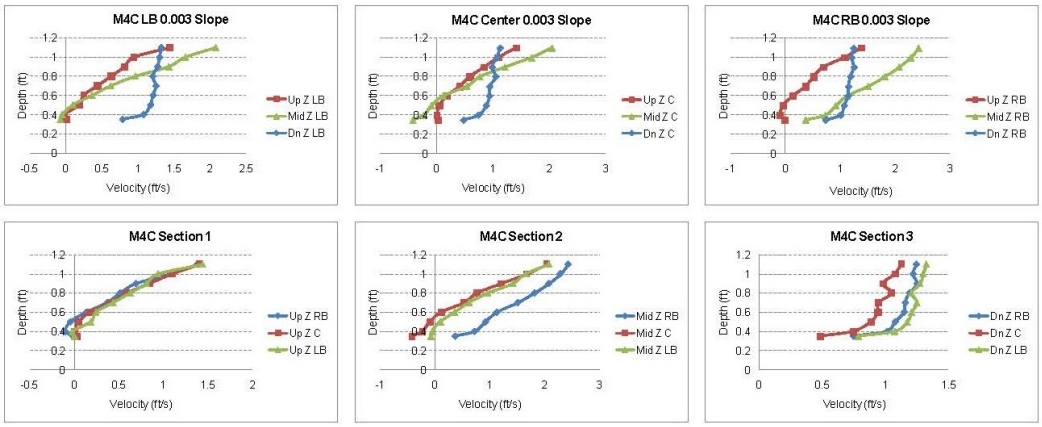

Figure 6.5. Combination velocity profiles for the M4C culvert - slope 0.003

6.3 General Water Flow

6.3.1 Description of Surface Profiles

Flow profile depths measured at various locations were used to describe the water surface profiles. The short nature of the experimental channel and road crossing models created various flow types. Assuming one-dimensional flow, the flow could be described as gradually varied flow before the road crossings, while the flow over the road was rapid varied flow. General classifications of surface water profiles describe the shape of the profiles with reference to normal depth and critical depth. Normal depth is derived from Manning's equation and is solved by nonlinear algebraic equation solver (*Sturm*, 2009). Manning's equation is presented in non-dimensional form for a rectangular channel as Equation 6.1,

$$\frac{AR^{2/3}}{b^{8/3}} = \frac{nQ}{k_n S^{1/2} b^{8/3}} \tag{6.1}$$

Critical depth is calculated by Equation 6.2,

$$y_c = \sqrt[3]{\frac{Q^2}{gB^2}} \tag{6.2}$$

where y_c is critical depth, Q is discharge (flow rate), B is top width, and g is gravitational acceleration.

Total depth measurements for the velocity profile experiments were 1.0 ft ($\pm$0.1 ft) and the calculated critical depth was $\approx$ 0.28 ft. Because the critical depth was 1/4 of the measured depths, and Froude numbers for the experiments were less than one, indicating the flow was sub-critical; the measured depths were used to describe and sketch the water surface profiles in the channel.

Using *Bakhmeteff* (1932) standards, Figure 6.6 is a sketch of the typical water surface profile for the velocity experiments.

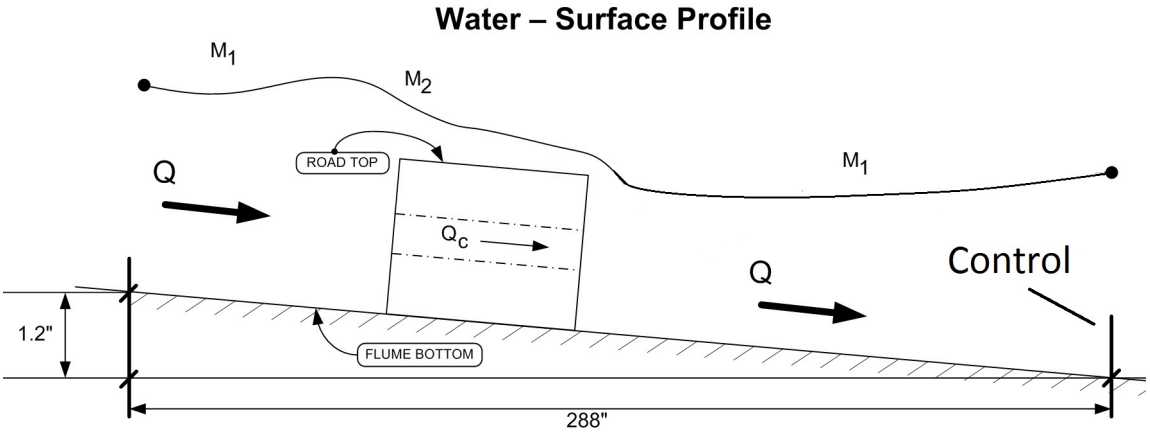

Figure 6.6. Graphical representation of the top surface elevation profile for the velocity profile experiments (not to scale)

The different geometries in the model types had very little effect on the overall surface profile shape at the specified discharge. In the sediment transport experiments, the discharge rates were 1.5 to 2 times larger, then the velocity profile experiments, which changed the top surface elevation profiles as shown in Figure 6.7. Transitions between labeled profile characteristics were slightly more pronounce as compared to the velocity experiments. The flow over the road achieved supercritical flow at the downstream side of the road crossing. The smaller area culverts were able to produced a hydraulic jump, easily detected by the naked eye downstream of the road crossing at the largest flow rates. In some cases due to the backwater effects of the downstream control, two hydraulic jumps were visually observed.

The interpretation of the top surface elevation profiles suggested that the three slopes, 0.3 %, 0.6%, and 1.0 %, were considered mild with relationship to normal depth and critical depth. Channel flow was sub-critical and does not cross through critical depth to reach super-critical flow over the sediment bed. However, supercritical flow was achieved over the tail end of the road crossing. Directly after the road crossing, the surface profiles approached critical depth; however, it was never reached. Because the experiments

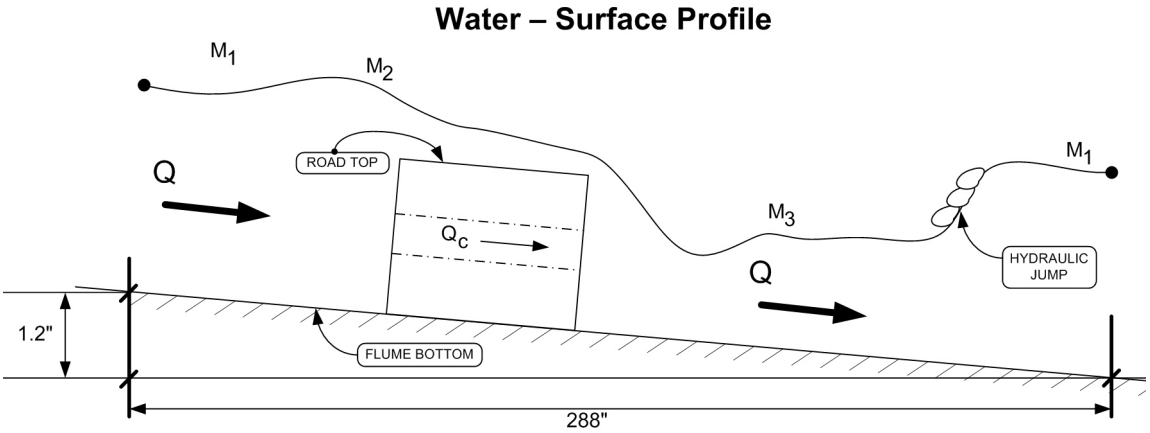

Figure 6.7. Graphical representation of the top surface elevation profile for the sediment transport experiments.

were concerned with flooding conditions at low water crossings, the downstream control produced back–water effects that prevented sustained supercritical flow.

6.3.2 General Observation

The road crossing acted as a speed bump to the flow progressing downstream. The impact of the speed bump depended on the cross–sectional area of the culverts. The smaller area culverts interrupted the flow lines causing eddies, contributing to the back-water effects and increased depths. Adverse currents, both before and after the road crossing were observed and measured near the culvert models and at the stream banks. The speed bump changed a normal convex velocity profile into a concave velocity profile as the culvert areas decreased and the slope increased. The smaller the culvert area, the more the flow lines changed toward supercritical flow over the road crossing and downstream of the road crossing. As the flow lines changed in direction and magnitude, the capacity for sediment transport changed. The reverse currents moved the frictional shear away from the stream bed into the flow field.

6.4 Velocity Profile Interpretation

The interpretation of the profiles assumed that velocity differences are only resolvable to three significant digits. The negative velocities, located at or near the sediment bed, were adverse or secondary water currents that consistently appeared with the smaller cross–sectional area culvert models. The magnitude of these negative velocities were reduced and became positive velocities with increasing cross-sectional areas in the culvert models. As the bed slope increased, these adverse currents decreased in magnitude and did not always occur (not including the skew models).

Chui, Hsiung, and Lin (1978) defined secondary flow as the two vectors of flow that are in the adverse direction to the primary flow. *Bray* (1982) described that some objections occur in how river engineers interpret obstructions in the flow direction, and how obstructions constitute the altering flow direction and these alterations produce secondary currents while some engineers do not recognize secondary currents. In these experiments, adverse flows were detected near the culvert models and channel side banks and bed.

6.4.1 Perpendicular Road Crossing

6.4.1.1 Section Plots Interpreted

Section 1 plots (upstream) show the same relative vertical profile shapes and speed as the water approaches the culvert models with very slight differences in between the models. The velocity profiles were linear in nature (very little curvature), the curvature that was present was concave in nature. The slight concavity in the profile was present in the smaller cross–sectional area models, and as the area increased the shapes progressed towards a linear nature. The increase in slope accentuates the concavity of the vertical profiles for the

smaller culvert cross–sectional areas. At the 0.01% slope the largest culvert cross–sectional (MR), the vertical profiles began to resemble a typical convex velocity profile.

The Section 1 plots demonstrated uniform flow across the flowlines with very little fluctuation in speed from the culvert models. Differences in speed were detected at the sediment bed with the smaller cross-sectional area culverts having a negative to near zero–velocity, where as the larger culvert areas had velocities ≈ 0.4 ft/s.[1] The increase in near bed velocities with respect to cross–section area was observed in all three experimental slopes. The near surface velocities were virtually the same across the culvert models. The higher stream lines were gaining intensity before the over–topping occurs at the road crossing.

Figure 6.8 compares two examples from the batch of Section 1 plots at the 0.003 slope. Figure 6.8a is a representative velocity profile plot for the S4C model. The picture shows how the three transverse profiles are virtually the same and the negative to zero velocities measured at the sediment bed. Figure 6.8b is a representation of a velocity profile plot for the MR model. Here again, the picture shows the three transverse plots virtually the same, and the difference in bed velocities is shown with the near bed velocity ≈ 0.4 ft/s.

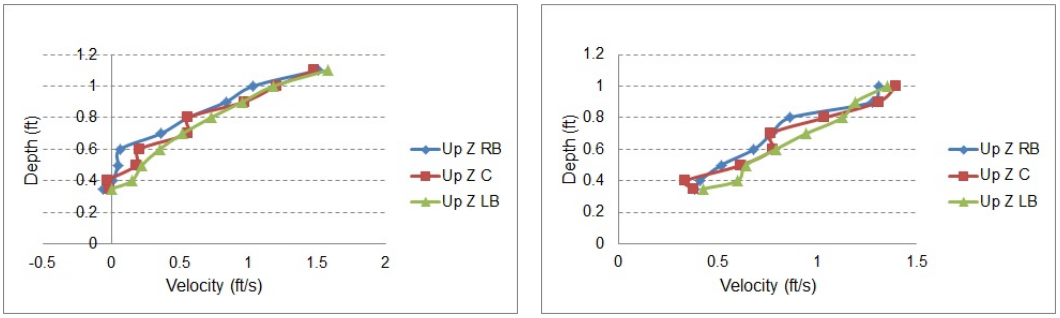

(a) S4C Section 1–0.003 slope **(b)** MR Section 1–0.003 slope

Figure 6.8. Section 1 sample velocity profiles

[1] The lowest measured depth was 0.05 ft above the sediment bed.

Section 2 displays the influence the culvert models had on the stream lines. The vertical profile's shapes were slightly concave to linear in shape for the smaller cross–sectional areas and progress to a linear profile for the larger cross–sectional areas. The larger cross sectional culvert start to show a traditional shaped velocity profile in the lowest 5 measuring points, then a top surface velocity speed was present and reflected in the top 5 measuring stations. The stream lines could be divided into two layers with a breaking point being at about half of the flow depth for the four larger culvert cross–sectional areas.

The Section 2 plots demonstrated less uniformity across the flow lines. The smaller cross–sectional areas showed a decrease in speed at the centerline measurement with faster speeds on the outside flowlines; whereas, the larger cross–sectional areas showed the centerline flow with the faster speed. Negative velocities were more pronounced at the lowest slope and smaller culvert areas near the sediment bed and tend to increase to positive values as the culvert area increases and the slope increased. The intensity of top velocities have increased after the culvert models, reflective of the super-critical flow over the road crossing.

The increase in top surface speeds had virtually doubled as compared to Section 1. The mass of the flow field was dominately shown in the top third of the flow depth.

The magnitude of speed in the top layers decrease as the culvert areas increase. The difference in top surface speeds were decreased from $\approx$ 3 ft/s to 1.75 ft/s at the 0.003 slope. At the larger slope (0.01) the top surface speeds were virtually the same across the culvert models. Differences were detected at the near bed velocities at the 0.01 slope with values increasing with respect to increasing culvert areas.

Figure 6.9 compares two examples from the batch of Section 2 plots. Figure 6.9a is a representation of a velocity profile for the S4C model at the 0.003 slope. The figure shows the negative velocities measured at the center flowline and the center flowline lagging

in speed intensity (The center flowline is shown in red). Figure 6.9b is a representation of a velocity profile for the M6C model at the 0.01 slope. The figure shows the positive velocities near the sediment bed and the separation in stream layers is shown by the typical velocity profile shape in the lower flow depths and the dominated top surface speeds by a linear profile shape in the upper flow depths.

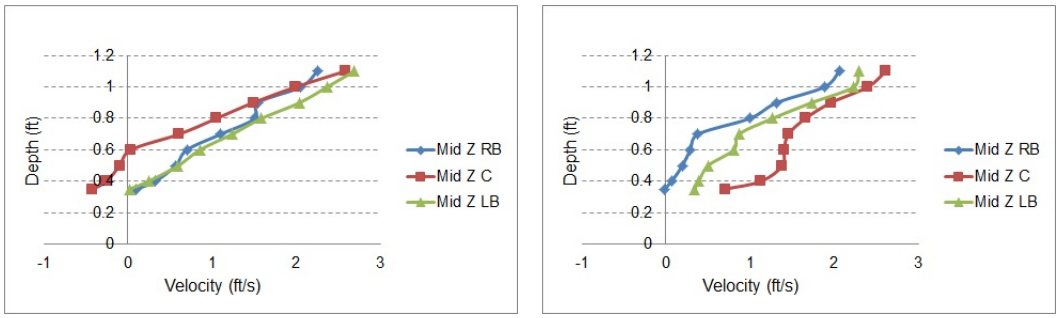

(a) S4C Section 2–0.003 slope **(b)** M6C Section 2–0.01 slope

Figure 6.9. Section 2 sample velocity profiles

Section 3 plots started to show a more conventional velocity profile shape. Fully developed flow patterns were suggested by the velocity profiles with the near bed velocities measured at positive values and top surface velocities being similarly equal across the culvert models, respectively. Velocities appear to be slightly slower at the center flowline when compared to the two outside flowlines, which was attributed more to the function of the flume glass walls and rectangular channel shape, than the resistance coefficients in the experimental channel. As the slope is increased, the velocity profiles represented a more uniform flow across the channel. The culvert model types appeared to have no influence on the velocity profile structure, and there was no evidence of a nearby hydraulic structure being reflected in the data.

Figure 6.10 is a representation of a more conventional velocity profile developed at Section 3 for the SR culvert model and 0.006 slope.

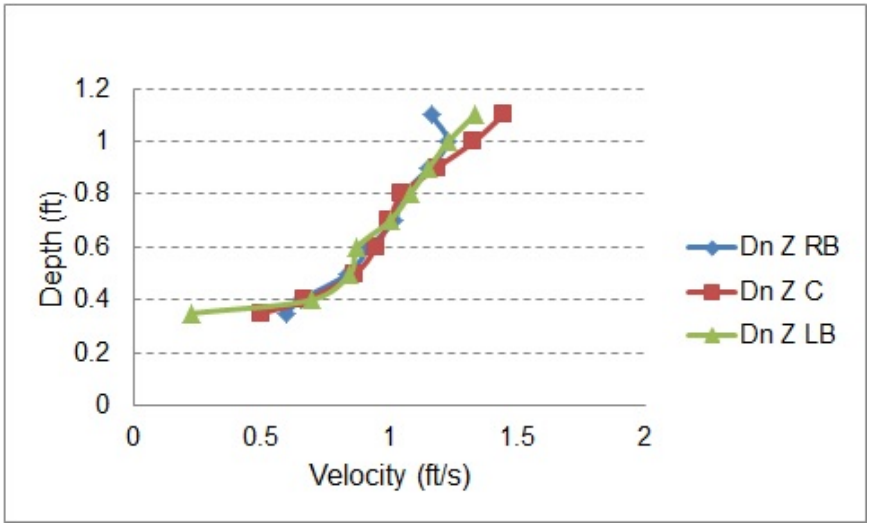

Figure 6.10. Section 3 sample velocity profile demonstrating uniform flow across the channel

6.4.1.2 Flow Line Analysis

Differences in individual model types were easier to detect along a flow line. Near bed velocities were negative or close to zero for the smaller cross–sectional area culverts. The negative values were present before and after the culvert models at Section 1 and 2. The negative values represent adverse currents and/or effects of eddies being created by the structure and channel shape. Differences in top flow patterns were present with an increase in surface speeds at Section 2 when viewed as the same flowline and the other respective sections. The increase in speed was a result of the super–critical flow over the road, and the top surface velocities were shown decreasing as the culvert cross–sectional area increase, with the difference in speed from small to large culvert areas being 1.5 cfs ($\approx$ 1/2 in magnitude).

The presence of the structure is obvious in the flowline plots. The smaller culvert cross–sectional areas presented a profile that was increasing in speed for the top third of the flow field at Section 1, then a further increase was shown at Section 2 after the water

crossed over the model structure, and at Section 3 a more traditional developed profile is represented. The larger culvert cross–sectional areas maintain virtually the same velocity measurements down the length of the channel. Without labels of position on the larger culvert models, it is virtually impossible to guess at the position of the velocity profile. The inability to detect model presence is a desirable outcome. Figure 6.11 shows the nine positional velocity profiles on one graph for the MR model. The velocity profiles are represented in a nice tight configuration, whereas in Figure 6.12 differences can be seen in the nine positional velocity profiles for the S6C model.

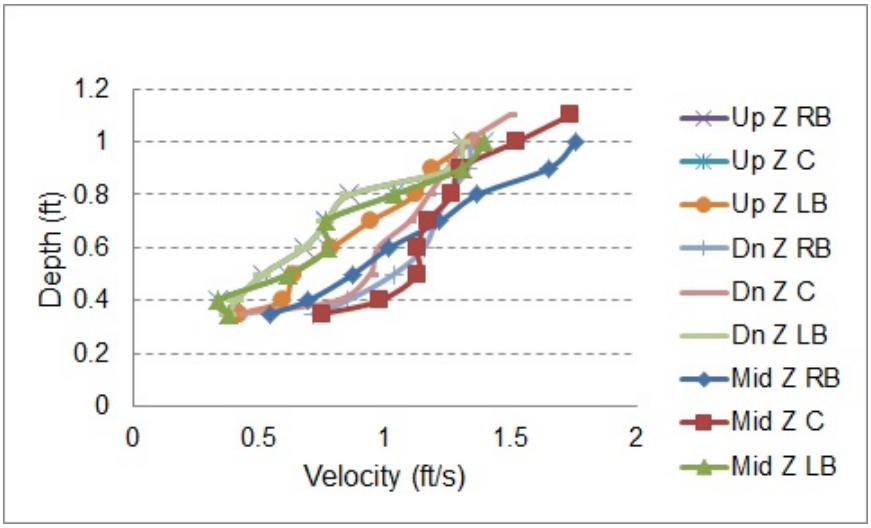

Figure 6.11. Velocity profile comparison down the length of the channel for the MR model

6.4.2 Skew Road Crossing

Part of the research project was to test the change in flow conditions when the culvert was not parallel to the flow centerline. In this project, the skewed road crossing was turned 15° with respect to the center flowline. Figure 6.13 shows the relationship of the skewed culvert models to the water flow.

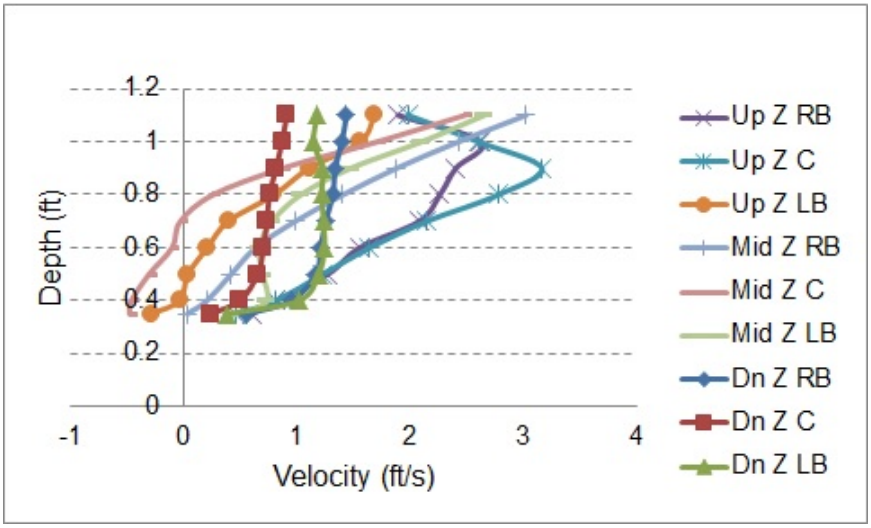

Figure 6.12. Velocity profile comparison down the length of the channel for the S6C model

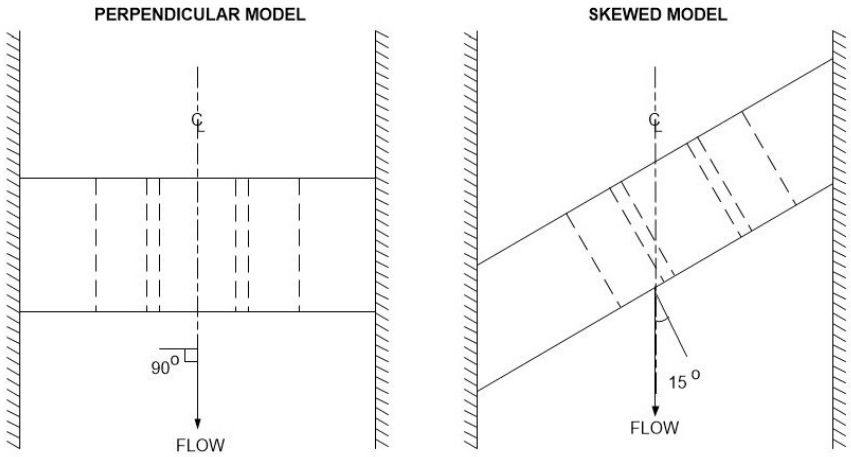

Figure 6.13. Drawing showing the model orientation to the approaching water flow.

6.4.2.1 Section Plots Interpreted

Section 1 plots (upstream) show the very little differences when compared to the parallel culvert models. The plots present the same relative vertical profiles across all three transverse locations indicating a fairly uniform flow patten as the water approached the road crossing within in the same model type. The shape of the velocity profiles were slightly

concave for the smaller culvert cross–sectional areas and progressed to a more linear shape as the cross–sectional area increased.

Velocity magnitudes were also very similar to the parallel models. Negative velocities were measured near the bed for the smaller culvert cross–sectional areas, that progressed to positive values as the cross-sectional area increased. The magnitude of the top surface speeds were similar to the parallel models at $\approx$ 1.25 ft/s. Figure 6.14 compares the M6C culvert model for both the parallel and skewed configurations. The figure demonstrates the similarities for the velocity profiles at Section 1.

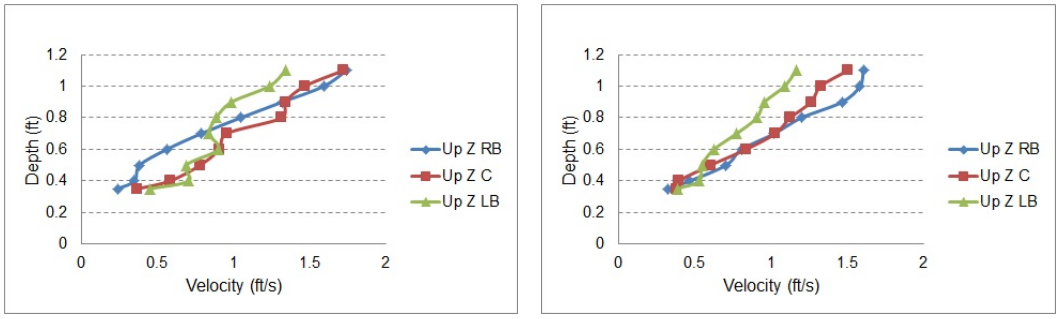

(a) M6C Section 1–0.006 slope parallel model

(b) M6C Section 1–0.006 slope skew model

Figure 6.14. Comparison of velocity profiles at Section 1 for the parallel and skew road crossing

Section 2 was where the effects of the culvert models became presently different from Section 1 and the parallel models. The velocity profiles shape change from concave curves to linear projections as the cross–sectional area increased. The difference in the skew and parallel models were there was also an intensity change in the shape and speed for the velocity profiles across the channel. The Left Bank flowline is linear in nature with a change occurring to a concave curve on the Right Bank. The larger culvert cross–sectional areas produced a conventional shape profile in the lower half of the flow field at the Left and Center flowlines.

The change in profile shape across the channel was explained by the velocity speeds recorded. Negative velocities at the bed were dominant on the Right Bank flowlines; whereas, the Left Bank flowlines produced positive velocity measurements which was different from the parallel models where negative values were consistent across the channel. Negative velocity measurements made for the smaller culvert cross–sectional areas were more intense for the skewed model as compared to the parallel model. The negative values found did change to positive values as the culvert areas increased, except for the Right Bank measurements which remained negative for the culvert models.

The smaller cross-sectional area models produce faster velocities near the surface with a decrease in speed near the sediment bed. As the cross-sectional area increases with the different model types the near bed velocities increase and the top surface velocities decrease. The change in velocity near the surface is $\approx 1.5 ft/s$ between the smallest and largest area culverts. Oscillation in speed is shown from the left bank to the right bank which is an indication of the models position to the flow direction.

The near bed velocities indicate negative values dominated on the right bank. This finding is anticipated because the model is skewed from left to right. The natural oscillation from the left to right bank encourage the formation of reverse eddies in the water flow. The smaller area culverts show negative velocities on both the upstream and downstream side of the road crossing. The larger cross-sectional areas have adverse flows at Section 2 on the right bank side only.

Figure 6.15 compares the S4C and M6C culvert model for both the skewed configurations. Figure 6.15a shows the negative velocities measured in the lower half of the flow field after the culvert models. Figure 6.15b shows the negative velocities in the lower half of the flow field on the Right Bank flow line only.

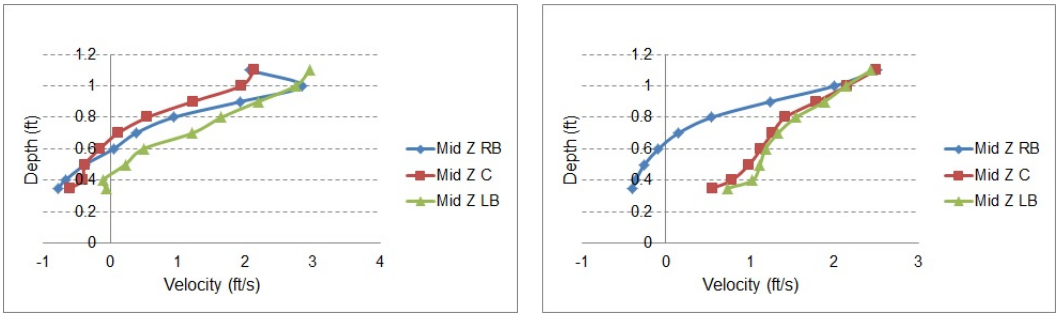

(a) S4C Section 2–0.006 slope skew model

(b) M6C Section 2–0.006 slope skew model

Figure 6.15. Comparison of sample velocity profiles demonstrating differences in cross-sectional culvert area effects

Section 3 plots showed non-uniformity in the flow pattern across the channel. The velocity profile shapes resembled traditional shapes at the center and right bank flowlines. The Left Bank flowline was linear in nature demonstrating a faster top surface speed.

The velocities, demonstrated by the profile shapes, showed a dominance in speed on the Left bank and a slowing trend in speed towards the Right Bank. The single barrel culvert model produced a difference in top surface speed $\approx$ 1.0 cfs across the channel; whereas the multi–barrel models difference was $\approx$ 0.5 cfs. The larger cross–sectional, multi–barrel culverts showed the Left Bank and Center profiles virtually the same, indicating the flow field was migrating towards uniformity across the channel.

Figure 6.16 shows a comparison of a single barrel culvert model, SR, and a multi–barrel culvert model, M6C. The SR culvert model is shown in Figure 6.16a, that demonstrates the speed difference across the channel as well as the Left bank profile supporting a more linear shape; whereas, the M6C culvert, in Figure 6.16b, presents a more traditional profile shape with the Left and Center flowines virtually the same, while the Right bank is lagging in speed intensity.

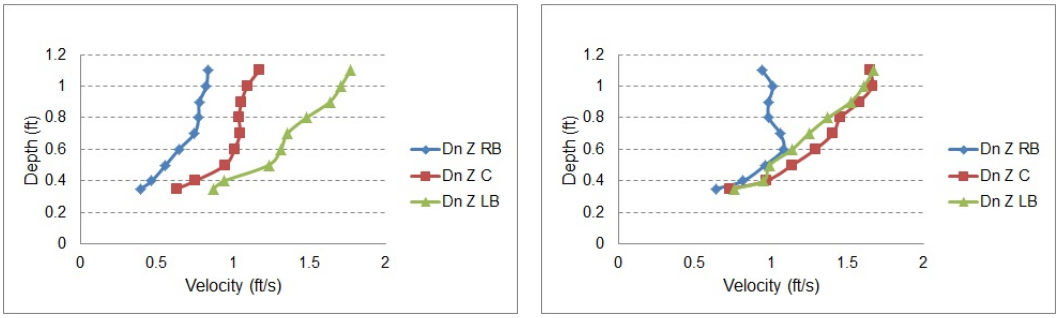

(a) SR Section 3–0.006 slope skew model

(b) M6C Section 3–0.006 slope skew model

Figure 6.16. Comparison of sample velocity profiles demonstrating differences in cross-sectional culvert area effects

6.4.2.2 Flow Line Interpretation

Again, the flowline plots demonstrated the effects of a structure being present. The velocity profile shapes reflected the presence of the culvert models by showing a linearly increased velocity with respect to depth in top half of the flow field at Section 1 and 2. Section 2 showed the fastest top surface speeds that is reflective of the super–critical flow developed over the road crossing.

The differences on the effects of the road crossing on near bed velocities were demonstrated clearly between the three flowlines. The Left Bank flowlines presented negative velocities at the smallest cross-sectional culvert area and quickly changed to positive values with an increase in culvert cross–sectional areas at both Section 1 and Section 2. Section 2 had no negative values measured at the Left Bank flowline. The Center flowlines presented a slight difference with negative measurements consistent at both Section 1 and 2 for all of the culvert models except for the two largest cross sectional areas, M6C and MR model type. The Right Bank flowlines presented additional differences with near zero velocity measurements for the small culvert cross–sectional areas at Section 1 and negative values at Section 2. Here again, the exception were the two largest culvert models.

Figure 6.17 shows the three flowline combination plots produced for the S6C skew model. Differences are shown from the Left Bank flowline to the Right Bank flowline.

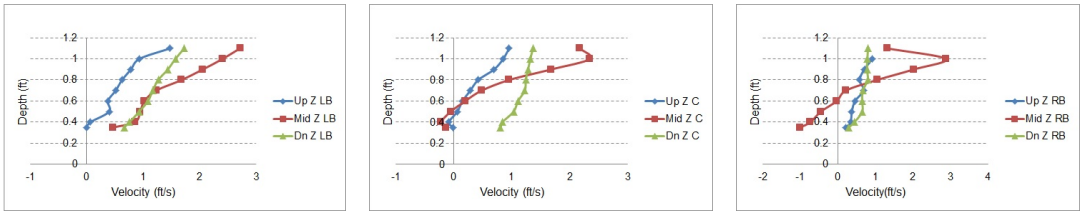

(a) S6C LB–0.006 slope skew model

(b) S6C CL–0.006 slope skew model

(c) S6C RB–0.006 slope skew model

Figure 6.17. Comparison of sample velocity profiles demonstrating differences in the flowline plots

6.5 Comparison to Literature

In 1786, Dubuat stated that one of the hardest problems in hydraulics was to "estimate the velocity of a river of which one knows the width, the depth, and the slope" (*Bray*, 1982; *Rouse and Ince*, 1957). Several theories have been generated over the past 200 years on how to estimate velocity flow in open channels. Secondary currents, shear stress distributions, channel roughness, and geometric shape of the channel affect the velocity distributions through the flow field in the channel. Hydraulic engineers such as Robert Manning created mean velocity equations related to the roughness factors at the boundary. Research in sedimentation studies created resistance equations related to the sediment grain particle sizes and boundary resistance to explain the velocity distribution in channel flow. Turbulent flow theorists, such as Prandtl, developed the theory of dividing the flow field into layers.

Sediment transport is the interaction of the moving fluid and the sediment bed. The shape, size, and type of sediment being transported by the moving fluid has an influence

on the velocity profile. Suspended sediment particles found in the streamlines increase the frictional forces and influence the shear stresses in the flowing fluid. The sediment particle shape and size contribute to the resistant forces applied by the sediment bed to the flowing fluid. The amount of resistance the sediment bed applies to the fluid influences the development of the velocity profile at the bed interface and into the flowlines (*Bray*, 1982; *Bathurst*, 1982). This dissertation evaluated the sediment resistance at the interface of the sediment bed and flowing fluid. The resistance and roughness factors found in the experimental channel were used to predict the velocity profiles in the fluid flow with a stationary sediment bed (incipient motion was not introduced).

6.5.1 Channel Roughness

Water resource engineers have studied hydrology and hydraulics relating to open channel flow for years. Roughness in an open channel is often described as the characteristics of the natural components that make up the channel's sides and bottom, such as vegetation, sediment, debris, and slope. The characteristics, such as sediment particle size (grain size) and shape, that comprises the definition of roughness are used to describe the effects of the water flow at the interface with the channel sediment bed.

Manning's n is an expression of the total roughness as a function of grain size and form resistance. Manning's equation is shown in Equation 6.3 and is used to provide a comparison of the experimental channel roughness (total) to the published tables for Manning's n value,

$$V = \frac{C_1}{n} R^{\frac{2}{3}} S^{\frac{1}{2}} \tag{6.3}$$

By empirically solving Manning's equation for the roughness coefficient n, and using the known geometry and hydraulic data from the velocity experiments; values of 0.107 and 0.058 were calculated for the total roughness at Section 1 and 3, respectively. Rough-

ness value in Section 1 was representative of non-uniform unsteady flow before the road crossing, an unrealistic value that does not represent the function of the channel, but the interaction of the structure. Section 3 was more representative of a uniform and steady flow developing in the channel, and according to the tables for typical n values for natural streams, 0.058 was a realistic.

Manning's roughness coefficient describes the roughness of a channel as a total variable assuming all geometric conditions as a single coefficient. *Einstein and Barbarossa* (1952) defined Mannings n coefficient as two components, grain resistance (n_g) and form resistance (n_f), and presented the relationship as Equation 6.4,

$$n = n_g + n_f \tag{6.4}$$

The roughness coefficients are related to the frictional forces applied by the individual components interacting with the flow. The frictional force applied by the roughness components in the channel can be calculated with traditional friction equations such as Darcy-Weisbach's equation. Sediment transport examines the frictional components applied by the sediment grains to the effects of the flow. The size, shape, and type of sediment grain that make up the sediment bed contribute to the bed or form roughness component of Manning's n.

The velocity profiles in this project considered the grain resistance as related to a sediment size, d_{50}, and the form resistance (n_f) equated to the flow over the side banks plus the sediment bed. Manning's n_f in the experimental channel was mimicked with carpet applied to the channel slopes and glass. [2] A small frictional component existed along the flume walls, however the relationship was mostly negligible at the flow rates used in the experiments. The sediment bed resistance applied to the velocity profiles were caused by

[2] The coefficient of roughness for the carpet was not experimentally found; however, the effects of the carpet were visually detected as described in the Chapter 3.

the grain size of the sediments and were not influenced by the sediment dunes, ripples, or waves because the velocity profiles were conducted with no sediment movement.

6.5.2 Determining the Parameters of the Velocity Equations

6.5.2.1 Grain Size

The literature presents several theories on equivalent grain size measurements to represent bed roughness. Table 6.2 shows values for grain sizes used in the experiments. The table incorporates interpolation of measured sizes to the typical grain size categories as presented in the literature review chapter.

Table 6.2: Grain Size

	LargeRock		
	in	*ft*	*mm*
$d_{(50)}$	0.750	0.063	19.1
$d_{(65)}$	0.825	0.069	21.0
$d_{(84)}$	0.920	0.077	23.3
$d_{(90)}$	0.970	0.081	24.6
	SmallRock		
	in	*ft*	*mm*
$d_{(50)}$	0.375	0.0313	9.5
$d_{(65)}$	0.413	0.0344	10.5
$d_{(84)}$	0.460	0.0383	11.7
$d_{(90)}$	0.485	0.0404	12.3

6.5.2.2 Characterizing the Flow as Hydraulically Smooth or Rough

Two criteria determined whether the flow at the sediment bed was smooth or hydraulically rough. The first was to calculate an equivalent Reynolds number at the sediment bed.

Nikuradse (1933) used equivalent grain size (k_s) to describe the flow above the sediment bed with Equation 6.5,

$$R_{e*} = \frac{u_* k_s}{\nu} \tag{6.5}$$

Re_* is a modified Reynolds number substituting shear velocity (u_*) and grain size (k_s) in the typical Reynold's equation. Incorporating the median values for the experiments of u_* = 0.28 ft/s (0.085 m/s), ν = $1.01 \times 10^{-5} ft^2/s$ and using the d_{50} as grain size (k_s), the values for the large and small sediment Re_* equated to 1,733 and 866, respectively.

Some researchers feel the mean grain size does not represent the resistance factor of the sediment bed, and larger grain sizes should be used (*Leopold, Miller, and Wolman*, 1964). However, the Reynold numbers in these experiments were so large that the grain sizes tested have very little influence on the velocity distribution, and the values were 2–3 orders of magnitude larger than the limit of 70 for hydraulically rough flow.

The second criteria was to calculate the thickness of the viscous layer at the boundary layer. The viscous layer thickness is calculated to find the thickness of the laminar layer using Equation 6.6,

$$\delta_s = 11.6 \frac{\nu}{u_*} \tag{6.6}$$

Nikuradse (1933) described the range which dictates hydraulically smooth, or hydraulically rough flow as a series of limits demonstrated in Figure 6.18. The latter was met with a calculated value of 0.0004 ft for the thickness of the viscous layer, two magnitudes smaller than the grain size. *Nikuradse* (1933) shows if the grain height is larger than six times the viscous layer thickness, then the flow above the sediment is hydraulically rough. Estimating the viscous layer thickness by using 6 times δ_s equates to 0.0024 ft creating a viscous layer one magnitude smaller then the d_{50} grain size used in the experiments. Thus while the thickness of the viscous layer is mathematically obtainable, the viscous layer was

non–existent in the experiments. Hence, the experimental flow regime was fully turbulent, with the turbulent layer interacting at the top of the sediment bed.

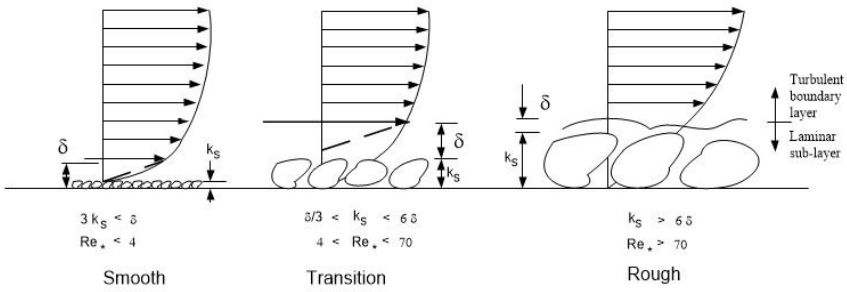

Figure 6.18. Drawing showing the characteristics of hydraulically smooth and rough flow (adapted from *Bartnik and Struzynski* (1996))

6.5.2.3 Viscous Layer Extents

The no-slip boundary is designated by Z_o or y_o in the literature. Finding Z_o can be done by an empirical mathematical calculation derived from known velocity profiles fitting a semi–logarithmic profile. *Nikuradse* (1933) represented Z_o as a function of k_s and the type of flow at the interface of the sediment bed and fluid. Using the parameters presented above for a hydraulically rough flow and the listed k_s d_{65} value from Table 6.2; Z_o was found using Equation 6.7 to be 0.0023 ft (0.70 mm) with respect to the large rock grain size and 0.0011 ft (0.35 mm) for the small rock.

$$Z_o = 0.033 k_s, \tag{6.7}$$

6.6 Resistance Equations

Turbulent velocity distributions are modeled as semi-logarithmic functions assuming uniform flow (*Keulegan*, 1938). Several researchers have developed an equation to explain

the velocity distribution within turbulent flow over sediment beds. These equations assume a semi-logarithmic distribution in the inner turbulent layer and are sometimes carried through to the outer turbulent layer. This dissertation compares the velocity profiles discovered in the velocity profile experiments to several well known semi–logarithmic velocity profiles, and a power equation.

The logarithmic velocity equations demonstrated here are The Law of the Wall developed by *Von Karman* (1931), *Nikuradse* (1933) equation based on equivalent grain size, and a general power law introduced by Prandtl with the power coefficient $n = 1/7$. In addition, three other power coefficients (10, 4, and 2) are represented side by side with Prandtl's value of 7. Table 6.3 list the equations with the respective authors.

Table 6.3: Resistance Equations

$\frac{u}{U_*} = 8.5 + 5.75 \log\left(\frac{y}{k_s}\right)$	Nikuradse
$\frac{u}{U_*} = \frac{1}{k} \ln\left(\frac{z}{z_o}\right)$	Von Karman
$\frac{u}{u_{max}} = \left(\frac{y}{h}\right)^{\frac{1}{7}}$	Prandtl

All of the above equations were developed in uniform flow conditions. Applying these equations to the velocity profile experiments conducted in this research used the measurement stations where uniform flow conditions were assumed. Sediment movement was not engaged during the velocity profiles so not to influence the profile shapes.

A good example of a researchers work matching the literature was *Reichardt* (1951), who derived an equation for the velocity that described the linear profile in the viscous layer, through the transition layer, and into the turbulent layer. His equation was in excellent agreement with the literature on turbulent velocity profiles and the boundary layer theory as presented by *Reichardt* (1951). Additional authors, such as *Wiberg and Smith* (1987)

have used this same velocity profile in their research. Figure 6.19 is a graph of *Reichardt* (1951) equation representing a theoretical velocity profile with turbulent flow.

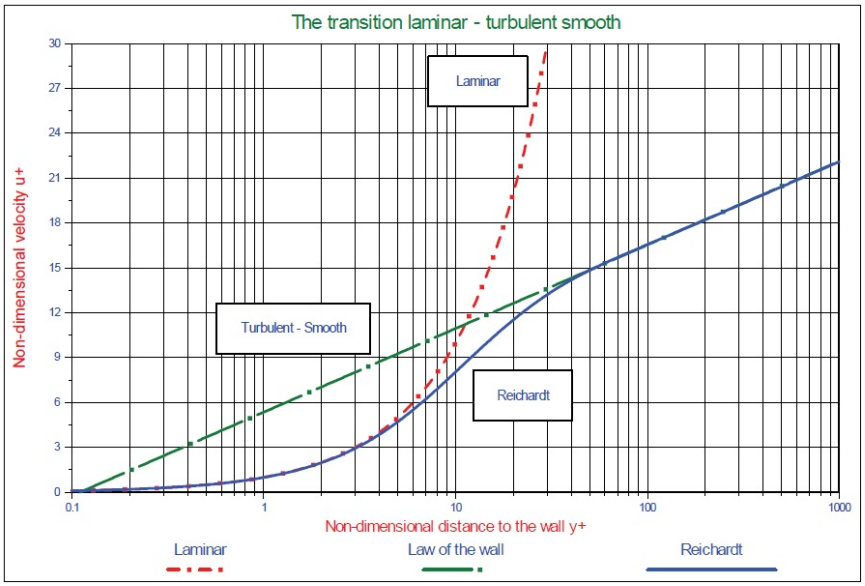

Figure 6.19. The velocity profile from laminar to smooth-turbulent (*Miedema*, 2010A)

Data were chosen from two experiments that represent the two culvert area extremes in the experimental models. The models used were the MR and the M4C configurations. Both were multiple barrel setups used to compare any effects size ratio had on the velocity profiles. The selected data were from Section 1 where the velocity profiles were recorded before the flow interacted with the model structure. Predicted velocity profiles and actual measured velocity profiles were plotted together. Hydraulic parameters collected from the velocity profile experiments used in the demonstrated equations were depth, shear velocity, z_o as proportional to k_s, and k_s as the equivalent grain size d_{50}.

The first demonstration is the Law of the Wall equation. Assumptions made with the Law of the Wall equation was that the profile follows a semi-logarithmic velocity profile in the turbulent layer, the flow is fully developed, and uniform across the cross–section of

the channel. In Figure 6.20, the graph represents the predicted profile from the hydraulic parameters from the MR model tested at the 0.003 slope as the black line. Actual velocity measurements are plotted as the blue line and points for the MR model and the red line and points for the M4C model experiment. These two examples represent the velocity profiles generated upstream of the culvert models before the water engages with the flow over the road top.

The graph clearly shows a difference in the predicted velocity profile and the actual profiles. The Law of the Wall equation assumes uniform flow and the actual profiles are generated in non-uniform flow influenced by the culvert structure. This result is excepted for the flow conditions present in the channel.

Nikuradse's equation is presented second. His equation follows the same assumption as the Law of the Wall with uniform flow conditions. Applying the same hydraulic parameters to Nikuradse's equation, Figure 6.21 shows the predicted velocity profile line in black. Again, the blue line and points are the actual velocities recorded for the MR experiment and the red line and points are the M4C actual velocities measured. Here again, the actual values do not fit to the predicted velocities by the tested equation.

The last comparison between the two sample experiments is with the power law equation. The power law equations used coefficients values of $1/n$ as 10, 7, 4, and 2. *Cheng* (2007) found in his research that the literature only suggests power coefficient of 1/4 to 1/12 and *Chen* (1991) reported that the coefficients have a limited range of valid Reynolds numbers. *Nikuradse* (1933) reports that the coefficients increase from 6 to 10 with increasing Reynolds numbers. Figure 6.22 is a graph showing the relationship of the power coefficients and the two sample experiments. The power coefficient graphs are presented in a descending order with the orange line as the power coefficient 10, followed by the black line, which is Prandtls' Power equation with $n = 7$, down to the purple line with a power

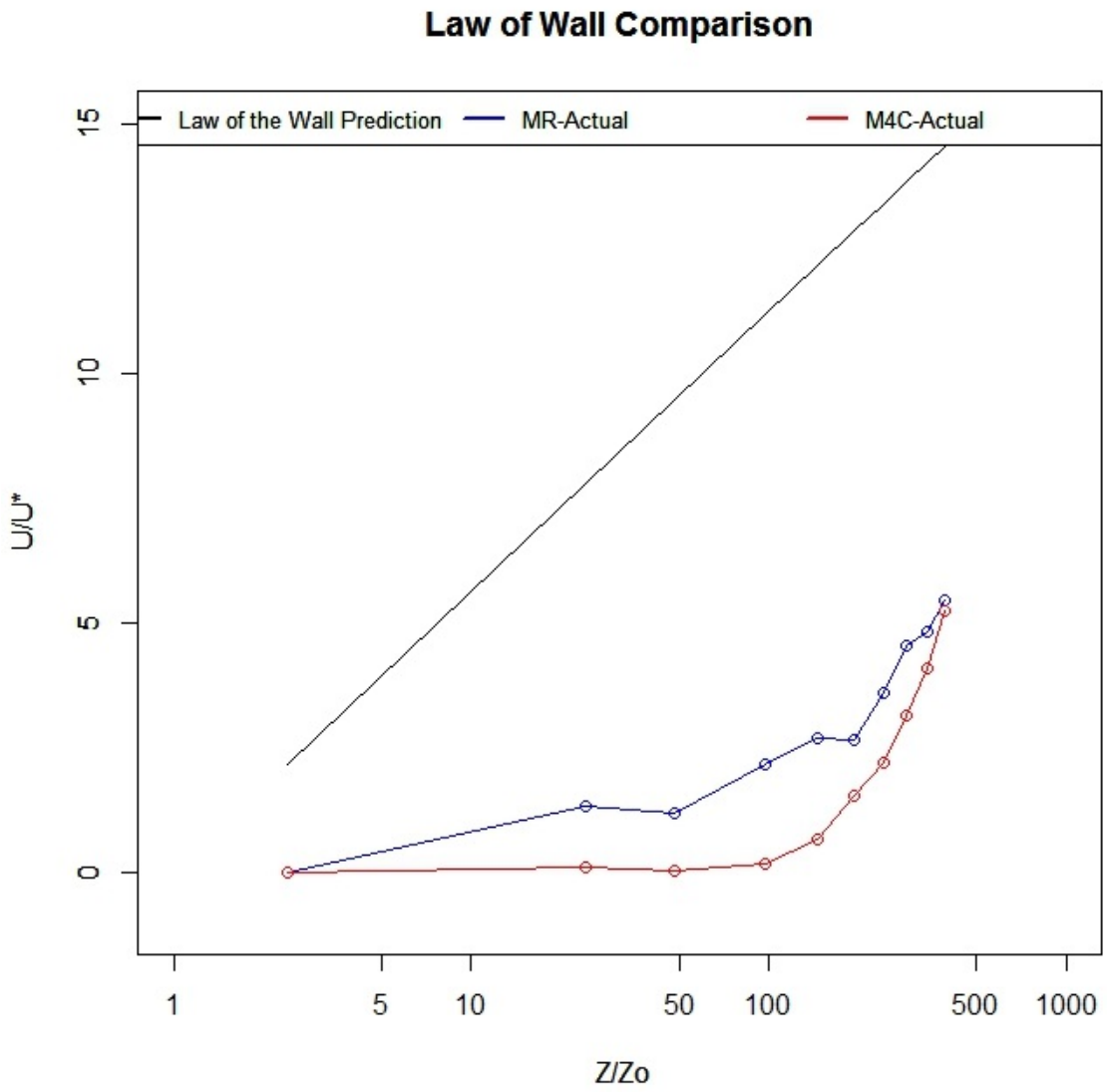

Figure 6.20. Two sample velocity profiles plotted together with the predicted profile by Law of the Wall equation

coefficient of 2. The actual data is shown as blue and red points with their respective color connecting the measured points with lines. In the graph, the two samples have plotted directly on top of each other and are hard to distinguish between the two. The graph is showing the M4C samples as red points and the MR sample as the blue lines connecting

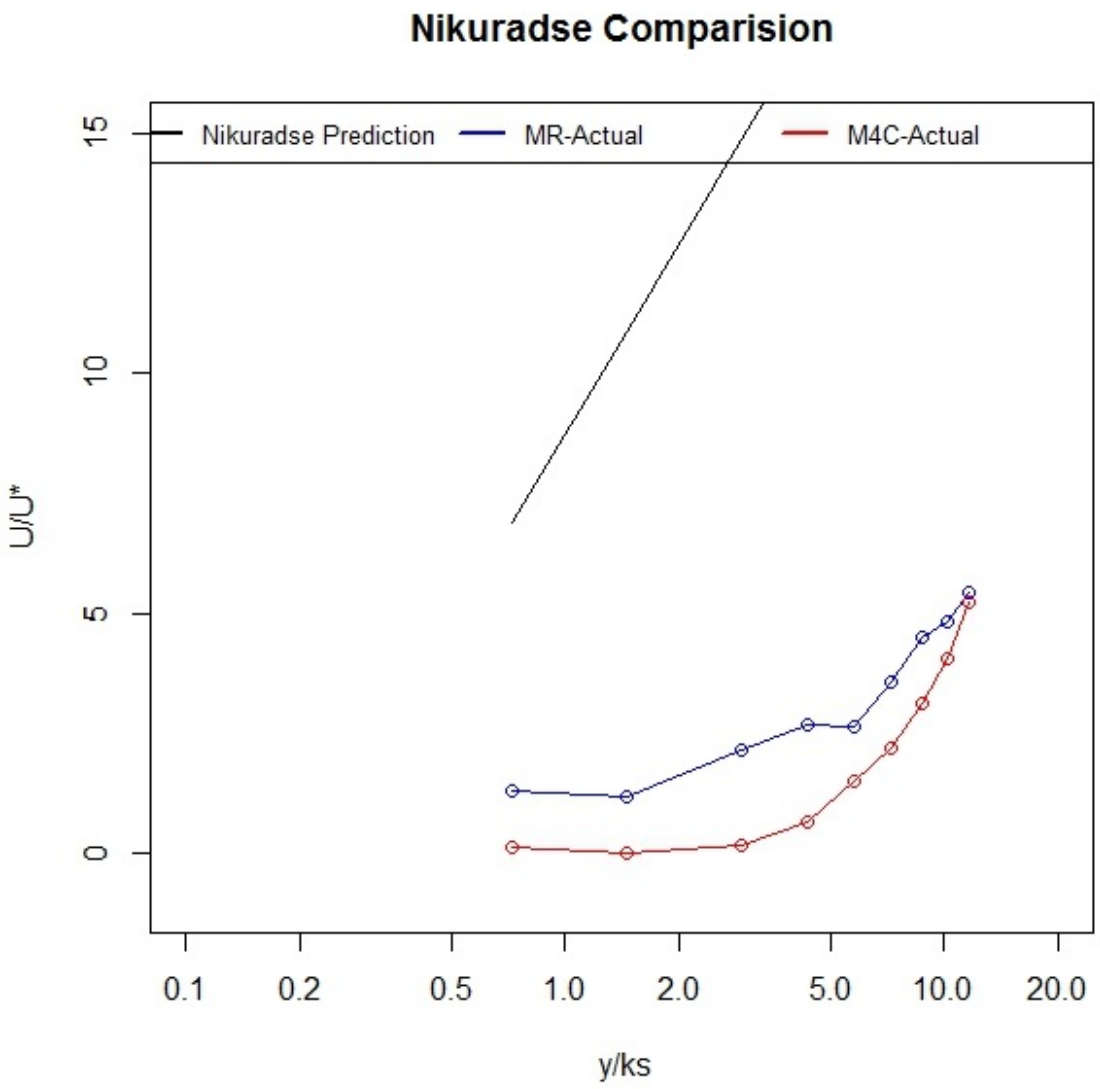

Figure 6.21. Two sample velocity profiles plotted together with the predicted profile by Nikuradse equation

the red points. The actual data is shown plotted below the power coefficient 4 which is outside of the typical ranges found in the literature.

Smart, Duncan, and Walsh (2002) found in their research that the power coefficient could be as low as 2 for large scale bed roughness. In this research, the sediment bed relative roughness height was not large enough to agree with *Smart, Duncan, and Walsh*

(2002), unless the flooded road crossing was used as a single roughness component, then the power coefficient may be reasonable to describe the flow velocities next to a structure. However, accepting the road crossing as a single roughness value would contradict the literature that stated the coefficient values increase with increasing Reynolds numbers and our experiments experienced very large Reynolds numbers around the structure.

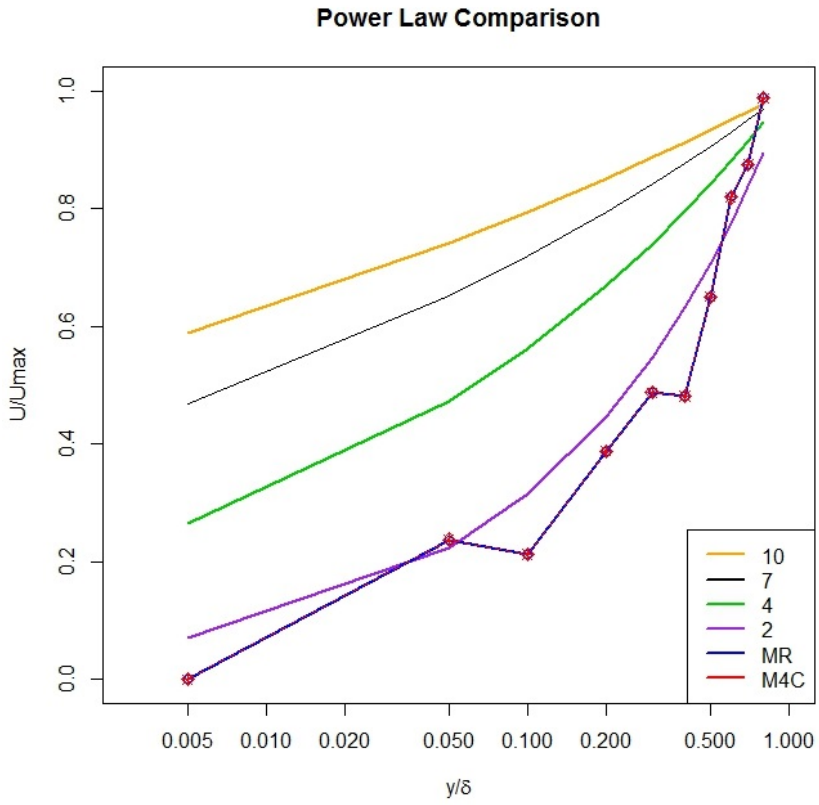

Figure 6.22. Sample velocity profiles plotted together with the predicted profile by the different Power Law coefficients

6.7 Summary

In the experimental channel were mapped velocity profiles to demonstrated the flow characteristics down the length of the channel. The velocity profiles demonstrate how the structure interfered with the flow field. A relationship was shown between the velocity profiles shape and magnitudes and the size of the culvert areas. As the culvert area increased, the structure had less influence on the disruption of the flow field. Common resistance equations were used to describe the velocity field; however, the equations do not match the velocity profiles.

Chapter 7

Sediment Transport

The results presented in this and the next chapter are the author's interpretation of data, video logs, photographs, and hours of observations throughout the 200 recorded experiments. This chapter compares and contrasts the sediment transported in the experiments to prediction equations commonly used in sediment transport. The next chapter will compare the sediment transport through visualized flow patterns shown in pictures, videos, and survey renderings made throughout the experiments. The author recognizes that existing literature applies to uniform flow in open channels that are at steady state and uninterrupted by structures. In this experimental apparatus, the flow patterns were interrupted the road crossing, the discharge is large enough to create flood stages over the road and the culvert flow is a small ratio of the total discharge. Interpretations are based on the literature that, in the author's opinion, were best representative of the collected results.

7.1 Experimental Common Parameters in Results

Results listed within the next few paragraphs are presented in groups with respect to experiments and grain size. The original experimental matrix presented in Chapter 4 is modified to represent the actual experiments conducted with each model and respective slope. Most sediment transport experiments were conducted in groupings of three. Table 7.1 shows the tested sediment size with each culvert model and slope and is divided into individual groups as discussed in the following paragraphs. The individual groups are referred to as large grain, small grain, and skew models in the following discussion.

Table 7.1: Experiment Matrix

Experimental Group	Model Type	Slope	Position
Large Grain	S4C	0.003, 0.01	P
	S6C	0.003, 0.01, 0.006	P
	M4C	0.003, 0.01	P
	SR	0.003, 0.01, 0.006	P
	SBC	0.003, 0.01, 0.006	P
	SBI	0.003, 0.01	P
	M6C	0.003, 0.01, 0.006	P
	MR	0.003, 0.01, 0.006	P
Small Grain	S4C	0.003, 0.006	P
	M4C	0.003, 0.006	P
	S6C	0.003, 0.006	P
	SR	0.003, 0.006	P
	SBI	0.003	P
	SBC	0.003, 0.006	P
	M6C	0.003, 0.006	P
	MR	0.003, 0.006	P
Large Grain & Small Grain	S4C	0.006	Sk
	S6C	0.006	Sk
	M4C	0.006	Sk
	SR	0.006	Sk
	SBC	0.006	Sk
	M6C	0.006	Sk
	MR	0.006	Sk

Goals for the experimental setup were to create an experimental procedure which was repeatable for all experiments. The research team wanted results that were reflective of the culvert models as the dependent variable and the hydraulic conditions as the independent variable. The independent variables such as grain size, flow rates, and slope were as follows. The two grain sizes tested were related to each other with a 1:2 ratio. Mean flow rates are presented in Table 7.2 for each experimental group. The minimum and maximum percentage differences between the mean flow rate and each minimum and maximum flow rate recorded for each grouping is shown. For the majority of the experiments, the flow rates were within a $\pm$ 3% tolerance of the mean flow rates in each individual group. The slopes were 0.003, 0.006, and 0.01.

Table 7.2: Mean Flow Rates Presented for each Experimental Group

Large Grain			
Slope	Qavg (cfs)	Max Q (+)	Min Q (-)
0.003	14.96	2%	2%
0.006	14.81	4%	2%
0.01	15.06	3%	3%
Small Grain			
0.003	12.58	3%	7%
0.006	12.09	2%	4%
Skew Model			
0.006 (Lg)	14.81	3%	3%
0.006 (Sm)	11.8	3%	3%

An exception was in the small grain experiments; where substantial variance was attributed to temperature differences experienced in the laboratory during these experiments. The water temperature was at its highest (78 to 81° F) during the summer months and the daily ambient air temperatures fluctuated from 70° F in the morning to 110° F inside the laboratory by the late afternoon hours. The experimental apparatus started to experience water losses through the wooden channel and the expansion of the glass walls, and the interface of the aluminum framework. The losses were not detected at the start of the small grain experiments during the 0.003 slope; therefore, the flow rates were seen decreasing as experimental time progressed. To overcome the losses, the laboratory team kept a constant flow of fresh water supplied to the reservoir tank. The change in ambient air temperature, and the replenished reservoir allowed the axial pump to work more efficiently suppling a higher flow rate to the last 15 experiments. The correction for the water losses for the last 15 experiments showed a mean flow rate of 12.82 cfs with a minimum and maximum difference in flow rates of 1.5% which the author feels corrected the large difference shown for the experimental group. The flow differences presented in Table 7.2 incorporate the variance across the entire group, not the corrected flow rate variances.

7.2 Sediment Transport vs. Culvert Area

Sediment transport was measured by two methods, a surveying technique and physically measuring the difference between a known sediment volume upstream of the culvert model, before and after each experiment. An additional document written during this research for the technique developed for surveying the before and after sediment volumes downstream of the culvert model was presented in *Dixon* (2011).

The control volume method used the difference between a known 5–gal bucket volume count upstream of the culvert model and the remaining volume upstream of the culvert model as the volume transported through the culverts. The difference in volumes were recorded with the daily experiments. Sediment movement results presented here are based on the known measured volumes not the surveyed volumes presented in *Dixon* (2011) paper.

A trend was detected in the sediment transport volumes. Transported volumes increased with increasing culvert cross–sectional area in the models. In addition, sediment volumes increased as the slope increased in the experiments. Figures 7.1, 7.2, and 7.3 show sediment transport volumes as measured during the experiments for each respective group. The data points represent each experiment conducted with respect to grain size, slope, and model type tested at the given parameters.

The next two figures compare the sediment volumes transported at each slope for each individual model type. The bar graphs show how as the slope increased the sediment volumes increased for each individual model and the graph shows how the sediment volumes increased as cross–sectional areas increased. Experimental runs were conducted in groups of three for each model type. The sediment transported volumes presented were averaged for each model type and then plotted against the relative model type and slope. The model

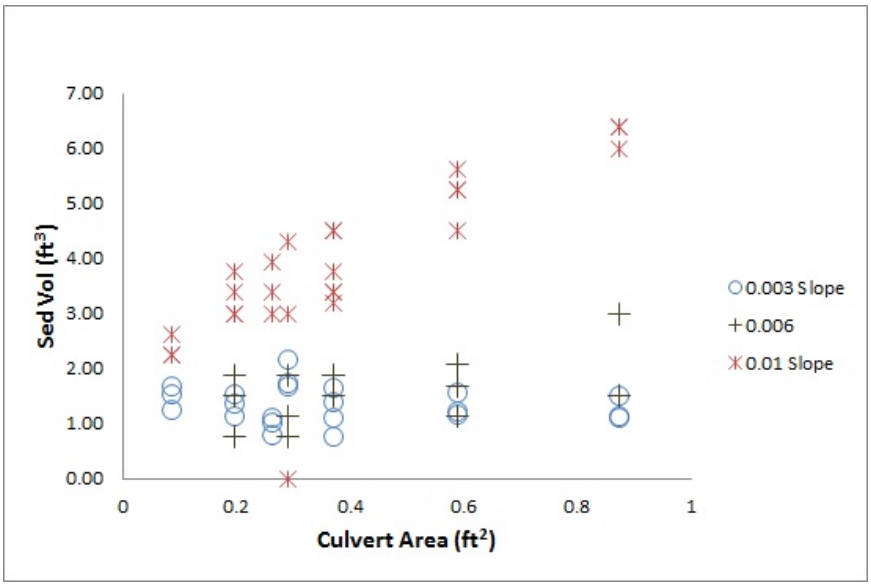

Figure 7.1. Sediment volume vs culvert area for experiments performed with the large grain and all 3 slopes against the perpendicular models

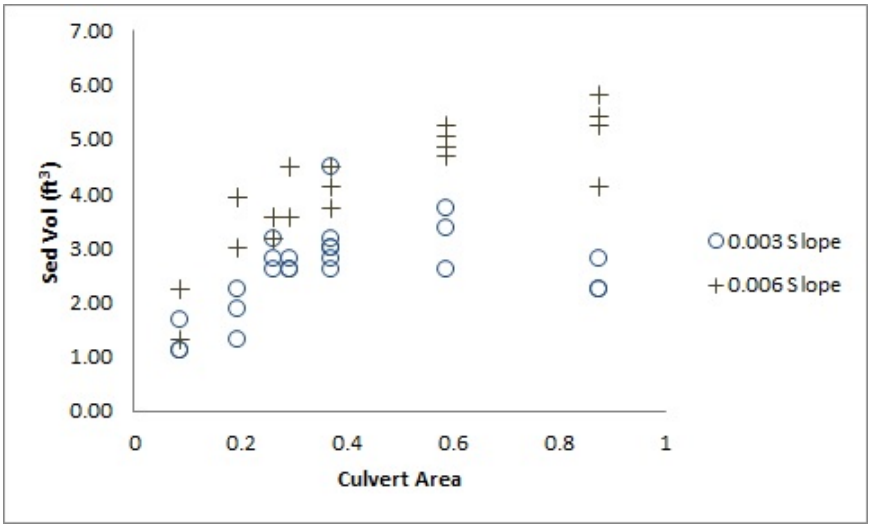

Figure 7.2. Sediment volume vs culvert area for experiments performed with the small grain and 2 slopes against the perpendicular models

types are listed from the smallest culvert cross–sectional area (S4S) to the largest culvert model (MR).

Figure 7.4 shows the experiments conducted with the large sediment, and Figure 7.5 shows the experiments conducted with the small sediment. The data are organized with

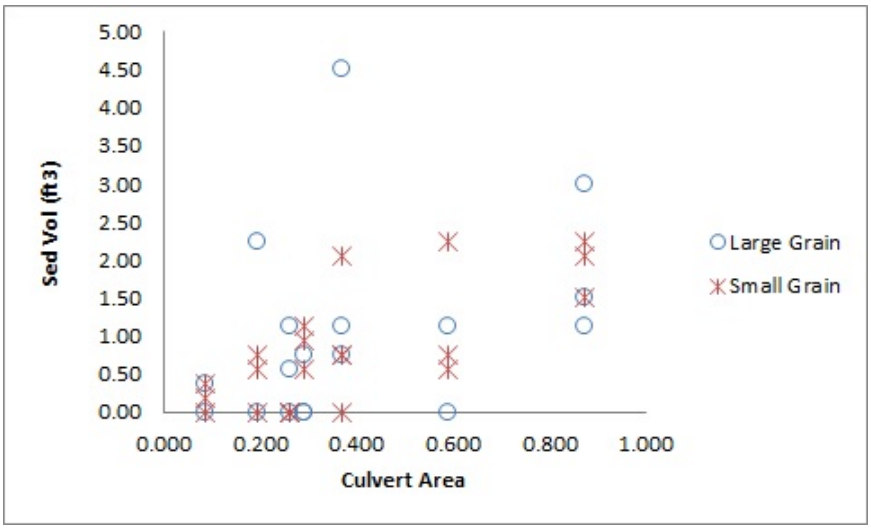

Figure 7.3. Sediment volume vs culvert area for experiments performed with the skewed model and the two grain sizes.

the culvert models on the ordinate axis in order of increasing culvert area vs. sediment transport volumes represented on the abscissa axis. The data are presented with respect to slope along with the experiments performed on the skewed road crossing model. The skew models at the 0.006 slope are shown with a slight decrease in volumes when compared to the same slope and the perpendicular models.

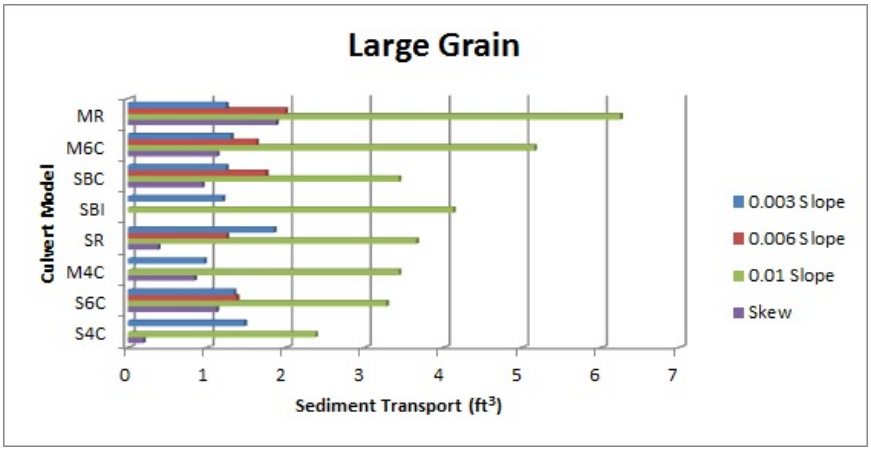

Figure 7.4. A plot of the large grain sediment transported through each model type. Models are listed by increasing area size and each experimental slope.

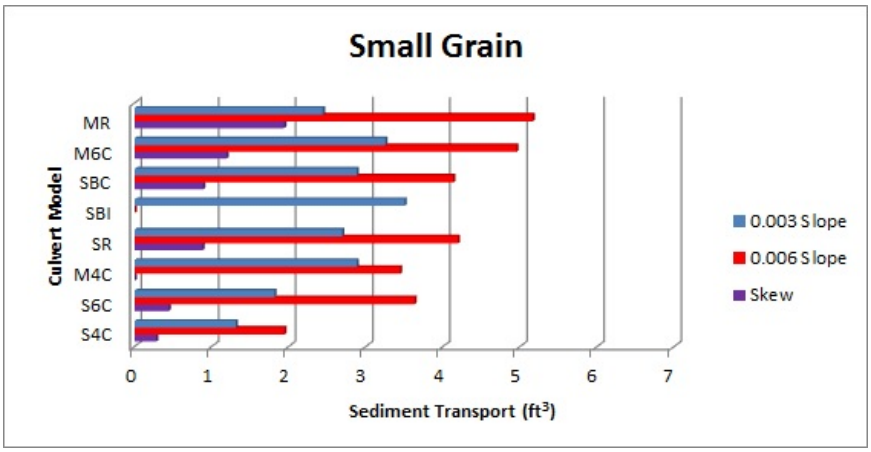

Figure 7.5. A plot of the small grain sediment transported through each model type. Models are listed by increasing area size and each experimental slope.

The trend of the increased sediment volumes with increased culvert area agrees with the analysis of flowlines improving as the culvert area increased as presented in Chapter 6. A further discussion on the flowlines through the culverts is presented in the next chapter.

7.3 Sediment Transport Prediction Equations

The sediment transport equations examined were Shields, Du Boy, Meyer-Peter and Muller, Schoklitsh, and Rottner. These equations contain hydraulic and sediment parameters that were consistent with the parameters provided by these experiments. These equations are for bed-load movements and do not include suspended loads. The experiments presented in this paper did not include suspended loads nor were the sediment grains capable of entrainment. The equations chosen were the most representative and used data parameters similar to our experiments. It is noted that the equations presented were derived in open channel and flume experiments that experienced fully developed uniform flows. The equations presented and compared to in this research predict sediment mass transport rates in terms of volumes per unit width of channels and the actual measured volumes are referred to as transport yield.

7.3.1 Equations Tested

The *Shields* (1936) transport Equation 7.1 is based on incipient motion parameters and is a homogeneous equation that can be used with any set of units. Shields' parameters such as critical shear stress is derived from the Shields diagram.

$$\frac{q_b \gamma_s}{q \gamma S} = 10 \frac{\tau - \tau_c}{(\gamma_s - \gamma) d} \tag{7.1}$$

The *Du Boys* (1879) transport Equation 7.2 is based on balancing the tractive and total resistant forces of the sediment bed causing the sediment particles to move in layers. The thickness of the layers has a relative depth Δ. Through algebraic interpretation and defined constants the resulting equation in U.S. customary units is

$$q_b = \frac{0.173}{d^{3/4}} \tau_o (\tau_o - \tau_c) \tag{7.2}$$

Meyer-Peter and Müller (1948) developed an empirical formula for bed transport for natural streams based on 14+ years of laboratory experiments. The formula in U.S. customary units is Equation 7.3,

$$g_s = \left[0.368 \frac{Q_s}{Q} \left[\frac{(d_{90})^{1/6}}{n_s} \right]^{3/2} D * S - 0.0698 d_m \right]^{3/2} \tag{7.3}$$

where g_s is bed load discharge in lb/sec–ft width, Q_s and Q are the sediment and water discharges, respectively, in ft^3/s, d_{90} is the sediment particle diameter at which 90% of the material is finer (mm), n_s is Manning's roughness value associated with the bed of the stream, D is the depth in ft, S is the slope, and d_m is the mean particle diameter (mm).

The Schoklitsh formula (1935) was based on water discharge. Schoklitsh produced two forms of his equations, one iwas based on unigranular material (Equation 7.4) and the second was based on summing the computed bed–load discharge for each size fraction of sediment particles. The formula used here was the unigranular material formula. The

two sediment sizes tested in this experimental paper were dominated by two grain sizes, 1/2 and 1/4 inch. The chosen formula represents the data most closely than the various size fraction formula. The second equation for computing bed–load discharge was avoided because the mixture of sediment particles tends to produced negative number results for discharge bed loads (*Bureau of Reclamation*, 2006; *Schoklitsch*, 1934),

$$G_s = \frac{86.7}{\sqrt{D}} S^{3/2}(Q - W q_o) \tag{7.4}$$

where G_s is bed-load in lb/s, d is the mean particle size in inches, S is the slope, Q is the water discharge in ft^3/s, W is the channel width in ft, and q_o is the critical discharge at incipient motion in ft^3/s per ft of width. q_o is calculated using

$$q_o = \frac{0.00532d}{S^{4/3}} \tag{7.5}$$

The *Rottner* (1959) Equation 7.6 is based on dimensionless parameters and coefficients,

$$\begin{aligned} q_b =& \gamma_s \left[(\zeta_s - 1) g D^3 \right]^{1/2} \\ & * \left\{ \frac{V}{[\zeta - 1) g D]^{1/2}} \left[0.667 \left(\frac{d_{50}}{D} \right)^{2/3} + 0.14 \right] - 0.778 \left(\frac{d_{50}}{D} \right)^{2/3} \right\}^3 \end{aligned} \tag{7.6}$$

This equation is created through regression analysis based on relative roughness. Rottner's equation is homogeneous and can be used with any set of consistent units.

7.3.2 Prediction Equation Results

Experimental sediment transport was measured by volume after the experimental operations. Measuring buckets were marked in 1/4 increments to measure partial buckets, and when necessary tape down measurements were used to calculate partial bucket volumes between the 1/4 increments. Volumes were then converted into equivalent weight

measurements. Full and partial bucket counts were recorded and weights were converted with a fully air dried sample weight of sediment grains. The large sediment weighed 71.6 lbs/bucket and the small sediment weighed 69.6 lbs/bucket.

Complete tables representing the experimental sediment transport yields and the bed-load equation yields are in Appendix A. Table 7.3 is a sample portion of the large grain sediment experiments used as a referencing tool in the following paragraphs.

The table shows sediment yields transported in lbs per minute per unit width of the channel and the predicted sediment yield is in lbs per minute per unit width. The actual yield is presented as the amount of sediment transport flowing through the culvert models plus any residual sediment in the culvert models and divided by the sediment bed width. The bed-load equations used the experimental parameters to predict sediment transport through the culvert models. The bed-load equations for Shields and Du Boy over predicted the sediment yield through the culverts. The Meyer–Peter and Muller equation failed to predict a positive value for sediment transport, because the ratio of grain size to the roughness factor and the flow depth are too low to produce a positive value (NAN = not a number). The bed-load equations for Schoklitsh and Rottner predicted negative sediment transport values. The negative values are a result of the critical flow equating to a higher value than the actual flow.

As the slope increases, the Shields' and Du Boy's equations predicted transport rates by an increase in magnitude with each sequential increase in slope. Schoklitsh's equation only produced a positive prediction for the large grain at the 0.01 slope, however the results for the 0.01 slope still do not show a correlation to the actual yield.

All of the sediment transport experiments are plotted for each bed-load equation with the predicted yield values plotted on the y-axis and the actual yield values plotted on the x-axis. Figure 7.6 shows the graphs for the results from the Shields and Du Boy equations.

Table 7.3: Sediment Transport Prediction Yield vs. Actual Yield

Experiment	Actual Yield	Shields	DuBoy	Meyer Peter Muller	Schoklitsh	Rottner
#	$\frac{(lb/min)}{ft}$	$\frac{(lb/min)}{ft}$	$\frac{(lb/min)}{ft}$	$\frac{(lb/min)}{ft}$	$\frac{(lb/min)}{ft}$	$\frac{(lb/min)}{ft}$
Slope (0.003)						
1	N/a	1.47	8.04	NAN	-3.55	-74.36
5	0.20	N/a	N/a	NAN	-3.26	N/a
6	0.10	N/a	N/a	NAN	-3.25	N/a
9	0.12	N/a	N/a	NAN	-3.23	N/a
12	0.10	5.34	14.90	NAN	-3.27	-23.53
13	0.11	5.32	14.70	NAN	-3.26	-22.73
14	0.09	4.99	14.07	NAN	-3.26	-22.33
15	0.12	5.39	14.81	NAN	-3.26	-22.76
18	0.15	5.74	15.27	NAN	-3.24	-22.07
19	0.17	5.69	15.38	NAN	-3.23	-23.67
20	0.14	5.97	15.73	NAN	-3.24	-22.35
23	0.10	5.83	15.58	NAN	-3.25	-22.72
24	0.14	5.90	15.72	NAN	-3.25	-22.81
25	0.11	5.58	15.09	NAN	-3.25	-22.46
26	0.12	4.84	13.73	NAN	-3.25	-21.74
27	0.19	5.35	14.81	NAN	-3.26	-23.02
28	0.14	5.02	14.19	NAN	-3.26	-22.62
29	0.16	5.10	14.44	NAN	-3.27	-23.30
30	0.12	4.91	14.08	NAN	-3.27	-23.04
31	0.11	4.63	13.52	NAN	-3.27	-22.53
32	0.21	5.80	15.42	NAN	-3.24	-22.27
33	0.19	6.23	16.26	NAN	-3.24	-22.69
34	0.18	5.94	15.74	NAN	-3.24	-22.65

Shields and Du Boy's graph results, Figures 7.6a, and b respectively, shows an extreme positive bias in the prediction equation results for the sediment transport rates.

In general, the largest slope (0.01) and skew model experiments with the large grain sediment presented a negative sloping trend in the data while the two smaller slopes 0.003 and 0.006 show an increasing slope trend in the predicted data. Examples of these trends are shown in Figure 7.7 and Figure 7.8 with the Shields predicted data vs. actual yield. In the graphs an equal value line ($y = x$) is shown to visually assess any correlation of

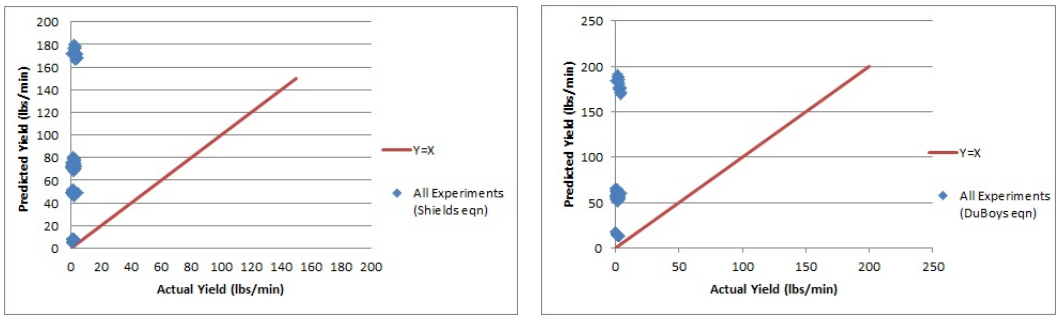

(a) Shields predicted vs actual **(b)** Duboys predicted vs actual

Figure 7.6. Shields and DuBoy sediment transport predictions for all experiments

the predicted vs actual yields. As shown in the graphs, the data cloud is a positive bias relationship to the equal value line. The bed-load equations for DuBoy show a further exaggeration in the distance from the symmetry line.

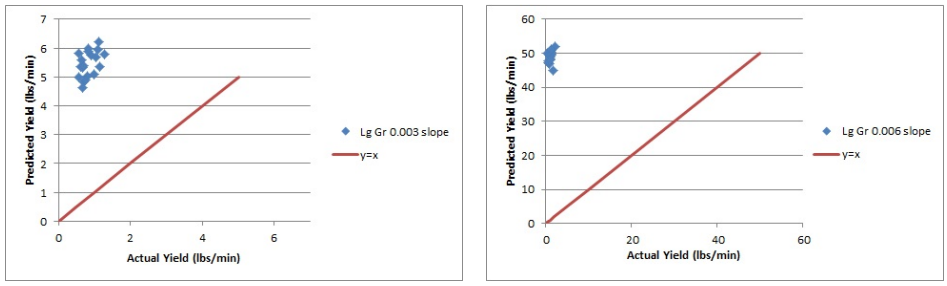

(a) Shields predicted vs actual for 0.003 slope **(b)** Shields predicted vs actual for 0.006 slope

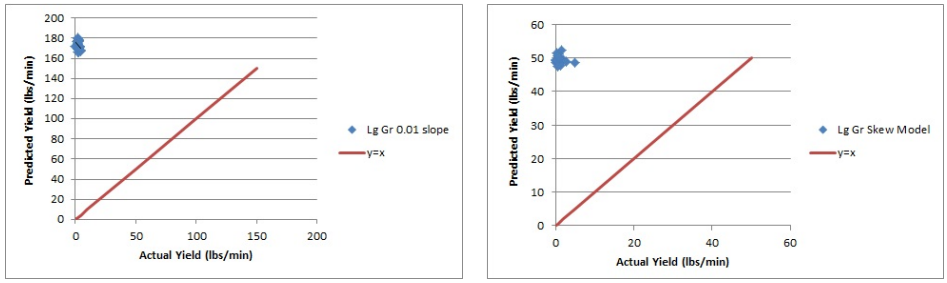

(c) Shields predicted vs actual for 0.01 slope **(d)** Shields predicted vs actual for skew model

Figure 7.7. Shield's sediment transport equation for individual slopes and the large sediment size plotted as predicted yield vs. actual yield

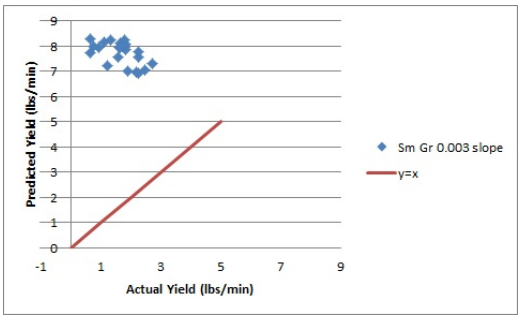

(a) Shields predicted vs actual for 0.003 slope

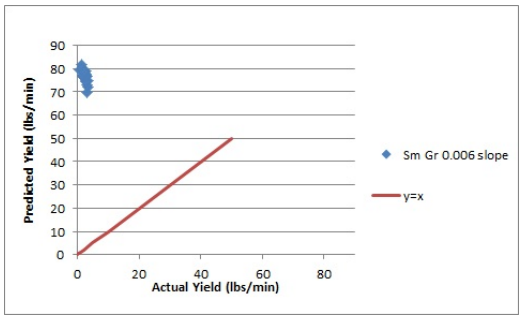

(b) Shields predicted vs actual for 0.006 slope

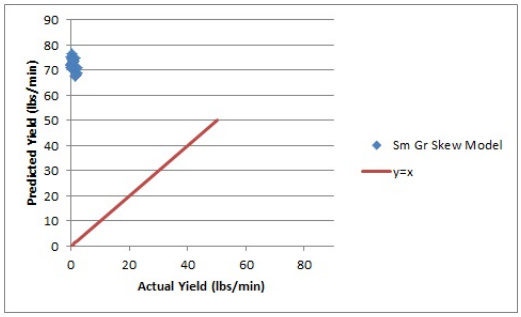

(c) Shields predicted vs actual for skew model

Figure 7.8. Shield's sediment transport equation for individual slopes and the small sediment size plotted as predicted yield vs. actual yield

7.4 Summary

The traditional bed-load equations tested in this experimental paper were developed in flumes or natural streams that experienced uninterrupted flow and stream lines. These experiments conducted in this paper involved sediment transport through a structure with culvert models. The culvert models interfered with the natural stream lines in the discharge. Therefore, it is not surprising the bed-load equations did not predict the actual yielded transport data.

The actual sediment yield transported by the culverts was affected by the cross–sectional area of the culverts. Graphs showed how sediment transport increased with increasing culvert area and increasing slope. Final quantities were affected by the flow patterns approaching and leaving the culvert models. The velocity profiles presented in Chapter 6 agrees with this statement, as the largest culvert areas showed the least amount of interference in the flow patterns and velocity profiles so do the largest culvert areas transport the most sediment. Further discussion on the influence of flow patterns is continued in the next chapter.

Chapter 8

Flow Patterns

This chapter summarizes hours of observations, digital photographs, underwater videos, and quantitative data collection, including flow depths, channel and culvert velocities, and survey renderings of sediment movement. These collected results are used to describe flow patterns and sediment transport patterns approaching and passing through the culvert models. The results are presented as typical patterns of the experiments. These patterns are further classified into results upstream of the culvert and then downstream of the culvert. The following chapter concludes with suggested future studies to quantify the visual observations.

8.1 Experimental Types

Experiments conducted in the research collected two general types of measurements: (1) sediment transport rates and (2) velocity profiles within the channel. A few additional experiments were conducted to test hypothesis developed during the project and to validate findings. Most of these additional experiments were conducted at the end of the scheduled experiment groupings starting at experiment number 190. Experiments 10 and 124 are exceptions that were conducted as part of the main scheduled experiments. The explanations for these additional experiments are presented as appropriate within this chapter.

Most of the the additional experiments were conducted using the SBC model type, with the remainder conducted with the MR Model type. The data for these experiments are

presented in Appendix D. Specific descriptions for the additional experiments are listed below.

Experiments 190–192 were conducted with the culverts clogged manually with large sediment grains. The culverts were packed tightly with large sediment grains to answer two research questions:

- Will the culverts self clean during a normal experimental procedure?
- What is an appropriate flow coefficient for the over the road flow?

The weir coefficient for over the road, was obtained using a plug completely blocking the culverts. Depths were measured before and after the roadway, and an experimentally determined broad–crested weir coefficient was found to be 2.76 for the weir.

Experiments 194–197 were conducted with an increased tailwater depth of 0.33 ft obtained by placing 4–in block traversing the entire width of the flume at the downstream roadway. Experiments 194 and 195 used the MR model whereas 196 and 197 used the SBC model configuration. Experiments were conducted using typical experimental procedures as presented for earlier experiments and the sediment transport was also monitored similar to the typical experiments.

Experiments 198 and 199 were conducted with wingwalls added to the inlet side of the SBC culvert model.

Experiments 200 and 201 were conducted using a decreased tailwater depth obtained by removing the entire center barrel module in the downstream road crossing.

Experiments 202 and 203 were simply velocity profiles conducted at pump speeds of 38 Hz and 41 Hz to determine the center flow line behavior. The upstream sediment bed was removed to avoid interference of sediment with clear water flow.

Experiment 204 (mobile particles) was conducted with the upstream road crossing removed. Sediment transport was monitored for distance and formations without any culvert model. The typical experimental procedure was followed.

8.2 Discharge Patterns

Discharge flow patterns, water surface profiles, water speed, and depths throughout the channel appeared to the naked eye to be about the same in each experiment. The discharge rates were by design similar and produced repeatable symmetrical dune formations upstream of the culvert models. The sediment migrated downstream in a rolling and sliding fashion forming a dune that grew both in volume and height during the experimental run times. The sediment discharge through the culverts was related to solids size, number of barrels, and the downstream hydraulics. Examples of the dune formations are presented first for the upstream development and then the downstream development. The discharge flow patterns experienced very little oscillation from the left to right banks. However, oscillation patterns were detected and measured with the skew models experiments. Skew models did produce a flow pattern as an *S* shape down the length of the flume, where water flowed from the left to the right bank as the flow traversed downstream over the roadway.

8.2.1 Upstream Descriptions to Flow Patterns and Sediment Movement

As the sediment migrated downstream from the grate toward the culvert model, the sediment formed a dune whose shape and location were consistent throughout the experiments. The shape of the dune when viewed from above (plan view) formed a symmetrical parabola with the center vertex pointed downstream. The forward most movement occurred in the center of the channel; consistent with the greatest flow velocities being measured in the

middle of the stream channel. The experimental similarities in the system mimicked natural channels that experience flood conditions. As an example, Figure 8.1 shows a flood that occurred at Flatrock Crossing at Junction, Texas. The picture was taken at the end of the storm event after several hours of flood waters receding.

Figure 8.1. Flood waters receding at Flatrock Crossing at Junction, Texas

Two common features were observed in the dune formations for the experiments. First was the relationship of the ultimate height of the dune upstream of the road model. As the dune formed and migrated towards the culvert models, scouring effects cleaned the sediment bed down to the model floor exposing the aluminum screen. As the dune grew in size, the height of the dune never exceeded a height equivalent to the top of the road crossing deck ($\pm$ a grain height). This height relationship was observed for both sediment grain sizes. During the experiments a hypothesis was proposed. The hypothesis was that the dune's height would only surpass the height of the road crossing if the culvert were clogged with sediment grains. The increased height would be an indication of the transport

efficiency of the culverts and possibly could be used as a guide for maintenance at low water crossings. Special experiments were designed to test this hypothesis by manually clogging the culverts and measuring the height of the dune. Experiments 190–193 examined the hypothesis by randomly changing the sediment build-up in the culverts. Eventually the entire culvert was packed with sediment grains to limit the flow through the culverts. Experiments were performed with the typical experimental procedure and allowed the sediment dune to form naturally. The result refuted the hypothesis and found that the sediment dune did not increase in height past the road height. These experiments demonstrated that dune heights (depths) have a relationship to the road crossing deck height. Figure 8.2 shows a typical view of the height relationship between the large sediment dune and the road crossing. The smaller grain experiments transported higher volumes through the culverts, therefore leaving an eroding center in the dune's top crest. However, the outside widths did not exceed the height of the roadway.

The peak of the dune was consistently the same height across the width of the flume until sediment transport occurred through the culverts. If a large volume of sediment was transported through the culverts, then the sediment dune eroded in the center of the channel leaving the bank side dune at the fully developed height. Examples of such erosion are presented below.

Figure 8.3 is a graph showing the relationship of dune height to the road height for the small sediment grain experiments. The x-axis is the distance from the right bank of the channel to the full width and the y-axis is the height of the sediment dune. Within the figure, the erosion of the dune is seen at the center of the dune with the lower height.

During these experiments with the culverts clogged or completely blocked, the flow pattern would create a cavity in the sediment dune. The dune migrated to the road crossing and sediment started transporting over the top of the model. Flow patterns after solids

Figure 8.2. A photograph showing the sediment dunes height in reference to the road deck

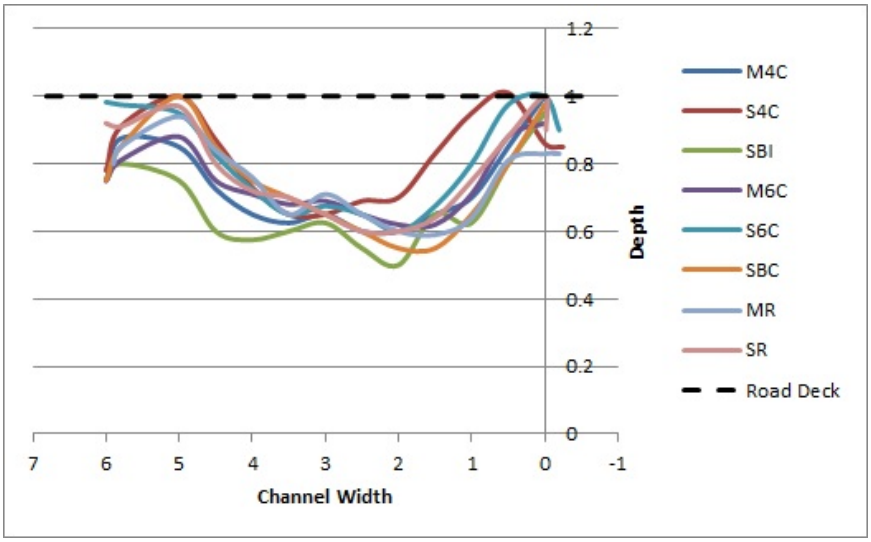

Figure 8.3. A graph of the sediment dune height compared to the road height for the tested culvert models

started moving over the top of the road produced a cavity in the center of the sediment dune at the center of the road crossing (Figure 8.4). Future engineering designs may find this information useful on the placement of future culvert crossing locations. If channels are experiencing clogged culverts and cavities are present in the sediment buildup next to the roadway, in a location other than the location of the existing culverts, the flow patterns would suggest relocating the culvert crossings to the location of the cavity to enhance the natural channel flow patterns. The cavity is an indication of where flow patterns are becoming equalized.

Figure 8.4. Cavity in sediment bed developed by the flow patterns in the channel

The second feature was the distance the dune migrated downstream. Regardless of the culvert size, shape, or bed slope the dune migrated to within 1.0 ft of the culvert model. Once the downstream migration reached this distance, forward progress of the dune stopped and the sediment transport through the culverts became a process of eroding the dune. Erosion started in the center of the channel and proceeded to the model floor while working towards the side banks. The largest erosion and highest transport volumes

occurred in the 0.01-slope experiments. The amount of dune erosion was related to transport quantities through the culverts and the model slope. Once the culverts started to clog and the flow was reduced through the culverts, the upstream dune migration would start up again and continue to move towards the road crossing.

Sediment would transport through the culverts and start to develop a dune on the downstream side of the road crossing. The downstream dune would develop in size and grow from a downstream point, upstream towards the road crossing. As the dune developed, the dune would encroach on the outlet of the culverts and start restricting the flow through the culverts. As the flow decreased, sediment would deposit in the culvert starting from the outlet working towards the entrance of the culvert. Figure 8.5a is a picture taken from the upstream side of a square culvert showing the sediment building at the downstream side. Figure 8.5b is a picture of a circular culvert partially blocked for the entire length. Culverts would clog from the the downstream side to the upstream side until the sediment dune on the upstream side would overcome the entrance and the culverts would become completely clogged (geometric shape did not affect this phenomenon).

(a) Upstream view through a square culvert showing the development of sediment clogging.

(b) Picture of a circular culvert with sediment deposited for the entire length

Figure 8.5. Examples of culverts clogging

Figures 8.6 and 8.7 are graphs that represent the extent of sediment migration downstream towards the culverts model as viewed from the above (plan view). The extent of the migration is shown with respect to the top crest of the sediment dune. The plot extent on the graph is the width and length of the sediment bed upstream of the road crossing. The origin $\{0,0\}$ is located at the beginning of the sediment bed and the model floor at the right bank (looking downstream). The flow direction is the direction of the y-axis.

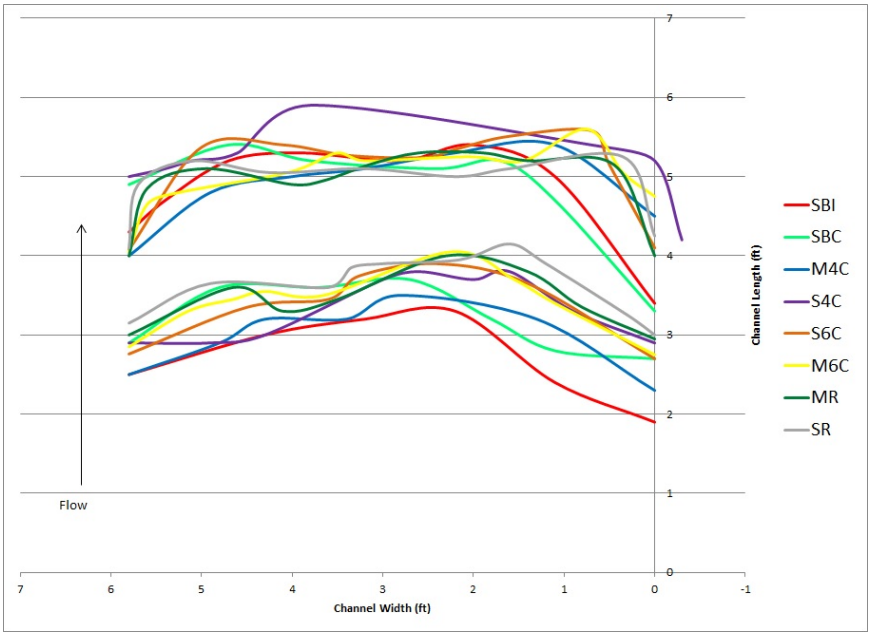

Figure 8.6. A graph of the relative forward progress of the large sediment

Figure 8.6 is a representative example of sediment movement towards the culvert model using the large grains, at slope 0.003. The graph shows the dunes' downstream location of the dune with respect to the road crossing. The location of the forward progress for the S-4-C model depicts the dune crest next to the road crossing, which is true because the S-4-C culvert clogged early in the experimental run. The other culvert models show migration just pass the five-ft marker.

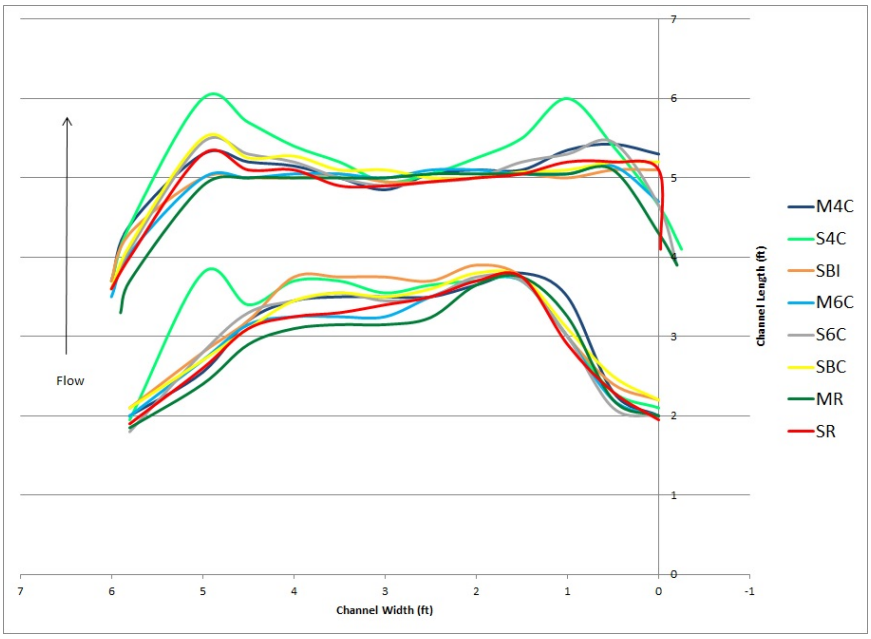

Figure 8.7. A graph of the relative forward progress of the small sediment

Figure 8.7 is a representative example of sediment movement with each culvert model using the small grains, at slope 0.003 downstream distance. The first line in the graph is the upstream edge of the sediment bed and the exposed model floor. The second line is the top ridge of the sediment dune. As the two figures show the crest of the dunes form at ≈ 1 foot location until the culverts become clogged.

Figure 8.8a and b are sample photographs of the sediment dune migration for the large and small grain towards the SBC model type. Similarities in the dune formations upstream of the culvert model are visible in both photographs.

Surficial water flow patterns changed as the sediment dune grew in size. Air bubbles entrained in the flow showed the surface velocity field. The opportunity to use the bubbles as drift tracers to measure velocities was explored using video capture. Velocities were visibly faster in the center of the channel until the sediment dune reached its stopping location before the road crossing. When the dune reached its full height capacity and stopped its forward migration, the channel flow was forced outward to the sides of the

(a) Large grain example **(b)** Small grain example

Figure 8.8. Examples of Sediment dune upstream of the culvert model

flume, and faster velocities were both observed and measured near the banks. The flow behind the dune became tranquil when the dune was at full capacity and size.

Underwater videos captured subtle differences in modes of sediment movement. Some sediments would become entrained in the flow as they passed over the crest of the dune, which caused the sediment grains to jump further downstream; as compared to the original formation of the sediment dune, where grains were rolling and sliding across the sediment bed to create the dune formation.

Some grains were observed trapped in gyres (eddies) and traveling in erratic directions. *Vanoni* (1975) explains dune formations as influenced by the critical shear stresses changing over dunes as compared to comparatively flat sediment beds. *Raudkivi* (1976) and *Rifai and Smith* (1971) explained the sediment movement over dunes as a interaction of pressure, velocity, and shear stress. Figure 8.9 is a sketch of sediment grain patterns along the surface of a dune. The various types of movement are marked with the alphabetic labels.

In these experiments, the sediment dune developed across the entire width of the stream bed and at times moved up onto the side banks that were built in the experimental channel. The shape of the dune produced flow patterns similar to a broad-crested weir, where the

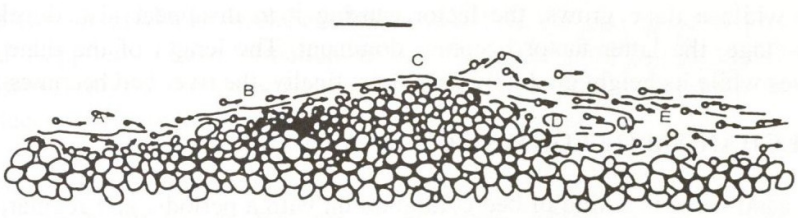

Figure 8.9. Characteristics of sediment movement along the surface of dune (*Chien and Wan*, 1999)

flow was directed over the dune. Sediment motion was anticipated at Froude numbers between 0.5 and 1.0 in sub-critical flow (*Milhous*, 1973). Froude numbers (F_{cs}) estimated at the control datum of the model floor and cross section 1 before the culvert model were ≈ 0.2 indicating sub-critical flow, but did not agree to sediment transport values in the literature. However, by recalculating the terminal Froude number (F_T) for the depth of flow over the sediment dune, the F_T numbers were ≈ 0.7. The Froude numbers calculated for the experiments are listed in Appendix D. The Froude numbers were reported at Bubbler 1, Section 1, Section 2, and Section 3. The Froude numbers fluctuated substantially with respect to location in the channel.

8.3 Velocity Changes in Channel

Experiments were designed to track the movement of the sediment dune with the MicroADV probes monitoring the velocity just above the sediment bed. As the dune moved horizontally and vertically downstream, the probes were moved simultaneously with the dune migration (explained in detail in Chapter 5). A constant water speed of $\approx$ 2–ft/s over the crest of the dune would keep the sediment dune moving downstream until about 1 foot before the culvert model.

During the development of the experimental procedures, the probes located a position in the flow behind the dune where the downstream components of velocity were near zero. Figure 8.10 shows a histogram of velocities recorded where about 40% of the velocity measurements are below 0.2 ft/s. One of the first bins represents a high density of the velocity measurements being less than 0.05 ft/s. This phenomenon where velocity vanishes in the wake of the dune occurred when the dune was fully developed.

Figure 8.11 is a sketch depicting the flow patterns observed and measured around the sediment dune as it grew in size and migrated downstream. The cylindrical object in the sketch represents the near-zero velocity position behind the dune. The importance of this location existing in sediment transportation is because the fall velocities of the sediment grains will easily overcome the horizontal and vertical velocity components applied by the water flow when the sediment grains passed through this region. The sketch in Figure 8.9, shown earlier, show grains flowing with a downward vertical trajectory demonstrating the fall velocities overcoming the horizontal velocities as recorded by interpretations of photography performed by *Jopling* (1961). The curly flow patterns shown in Figure 8.11 in between the dune and culvert model, starting at the perimeter of the flume, were actually helical patterns (horizontal vortex, decreasing radius approaching the culvert) when viewed using the underwater camera. These helical flow patterns contributed to the culvert flow entering at the side edges of the culvert, however, they did not appear to enhance the sediment transport through the culverts from the side parameters of the channel. The helical flows were visible when the sediment dune was fully developed, and when the dune reached the 1–ft position in front of the culverts. Figure 8.12 is a picture taken underwater showing the position of the dune and the inlet of a circular culvert. The helical flow patterns were detected in the underwater videos when the dune became visible in the cameras view.

The main sediment transport came from the sediment bed located in the center of the channel. On the largest slope experiments, solids erosion could extended to the model floor.

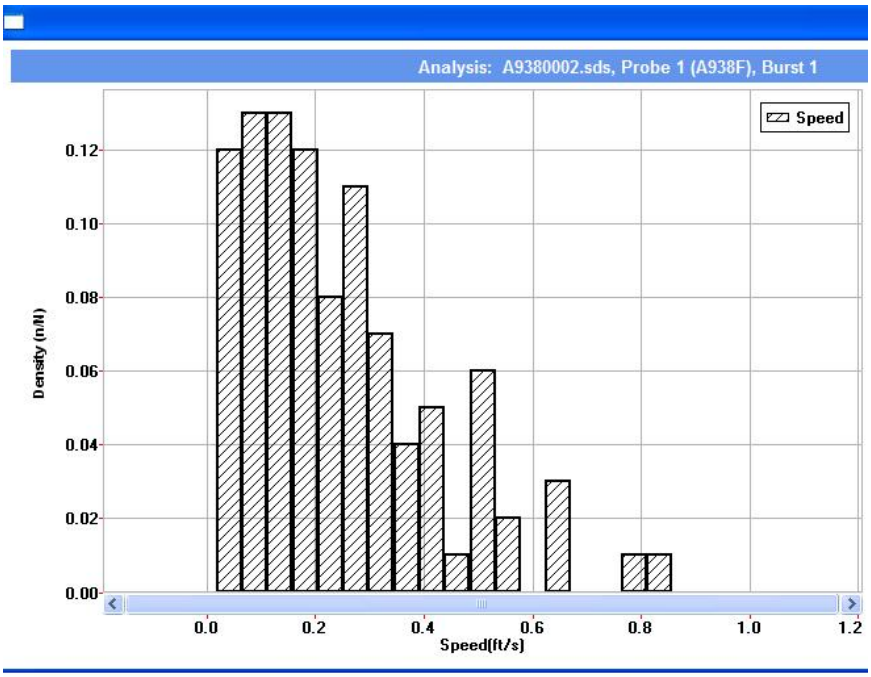

Figure 8.10. Sample velocities measured after a sediment dune

An example of a typical scoured sediment bed can be seen in Figure 8.13. In the picture the sediment bed was still intact at the stream banks on the outside edge.

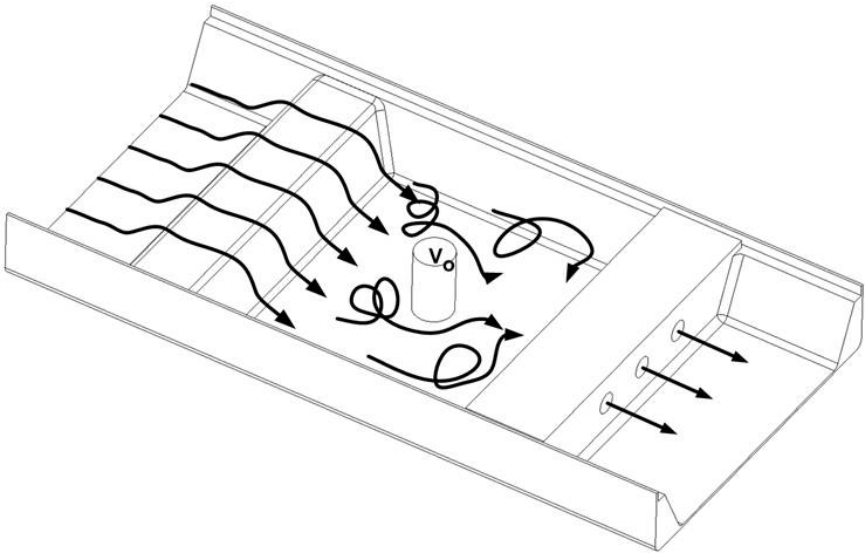

Figure 8.11. Hand sketch showing flow patterns observed in experiments

Figure 8.12. An underwater picture of the dune locations in front of the culvert model

Figure 8.13. Large sediment movement leaving the floor exposed

8.3.1 Culvert Inlet Velocities

Velocities were measured at the center of the inlets and outlets of the culvert barrels at a distance of 0.18 ft from the road structure. Velocity measurements began with the

initial stabilization flow rate of 7.5 cfs, and thereafter with the increase of flow rates every 15 minutes from 12 cfs to the final flow rate ≈ 15 cfs. The range in flow rates allowed the sediment to form a dune while a natural migration occurred towards the culvert model. Measured velocities at the inlet of the culverts were observed to reduce in magnitude as the sediment dune approaches the culvert model.

Figure 8.14 shows velocities measured for the large grain experiments at the 0.003 slope. The decreasing velocities began to be observed at about 60 minutes into the experimental run. This time coincided with the dune location ≈ 2 ft in front of the culvert models. The culvert models clogged at the downstream end of the culverts for the large grain material at the 0.003 slope, with the exception of the Single Rectangular (SR) culvert.

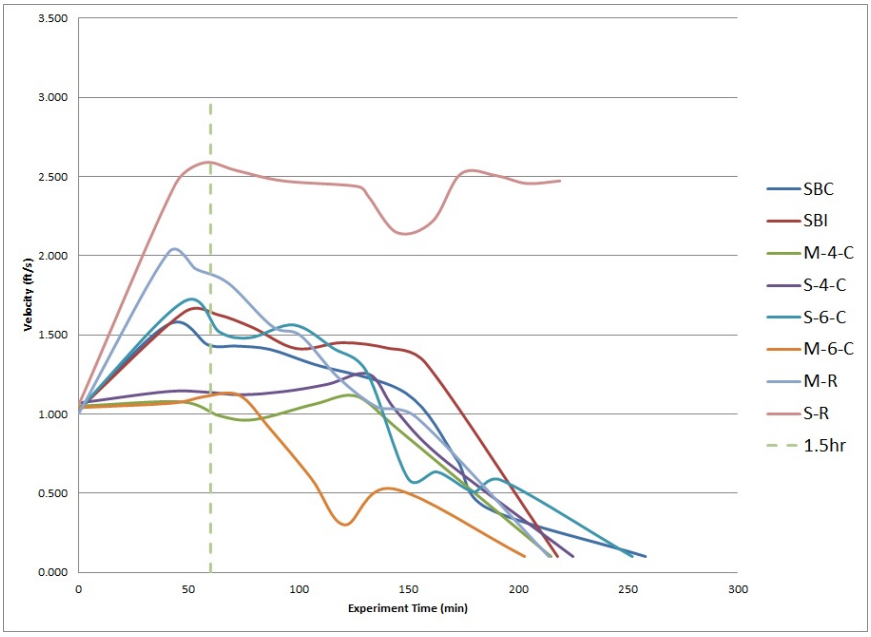

Figure 8.14. Measured velocities at the inlet of the culvert models for the large grain, 0.003 slope experiment

For this group of experiments, the S-R culvert model moved the most amount of sediment grains with the continual eroding of the dune in the center of the channel. Figure 8.15 is a photograph showing how the dune eroded at the center of the channel in line with the

culverts. As a contrast, Figure 8.16 are two pictures of the SBC model that clogged with sediment grains. The pictures are of the upstream (Figure 8.16a) and downstream side of the culvert model (Figure 8.16b).

Figure 8.15. An example on how the sediment dune eroded in the center as transportation continued through the culvert.

(a) Upstream view of the culvert **(b)** Downstream view of the culvert

Figure 8.16. An example of a clogged culvert for the large grain and 0.003 slope experiments

There was a correlation to the volume of sediment debris transported through the culverts and the decreasing velocities at the inlet. The quantity of the sediment bed was a controlled volume for recording purposes and mass balancing. Therefore, when the transport rate exceeded the controlled sediment feed rate to build the dune, the dune would erode in the center of the channel until either the downstream end of the culvert clogged or experimental time ran out. If an unlimited amount of sediment grains were available, the culvert models would most likely have clogged. As described above, the sediment would build up on the downstream side of the culverts and start clogging the culverts from the outlet of the culverts. With the limited supply of sediment bed the dune would erode with time on the upstream side, and the velocities would then increase at the inlet with a smaller dune.

Decreasing velocities at the inlets were observed in all of the models tested at each slopes and grain sizes. Representative velocity-time diagrams for the slope and grain sizes are shown in Figures 8.17a, b using the SBC model. The figure is typical for the velocities measured at the inlet of the culverts.

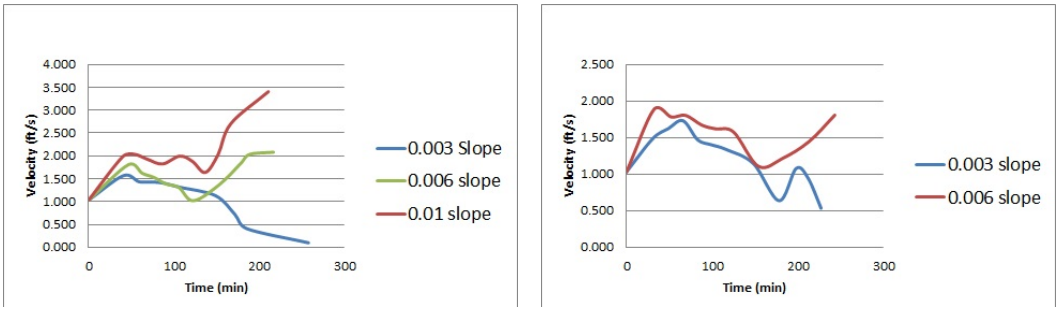

(a) Inlet velocities for the large grain **(b)** Inlet velocities for the small grain

Figure 8.17. Inlet velocities measured for the large and small grains at all slopes tested

8.3.2 Culvert Outlet Velocities

The water speed at the outlets of the culverts was a function of the number of barrels and the upstream head. Exit flow also followed the trend of decreasing speed as the dune approaches the culvert models. Velocities were also reduced at the exit as sediment grains deposit into the culvert barrels. Velocities were measured until the MicroADV probes were covered with sediment grains or the experiment ended. Figures 8.18a and b are typical velocity-time plots for the experiments. Again the results shown are for the SBC model for the large and small grain at the tested slopes.

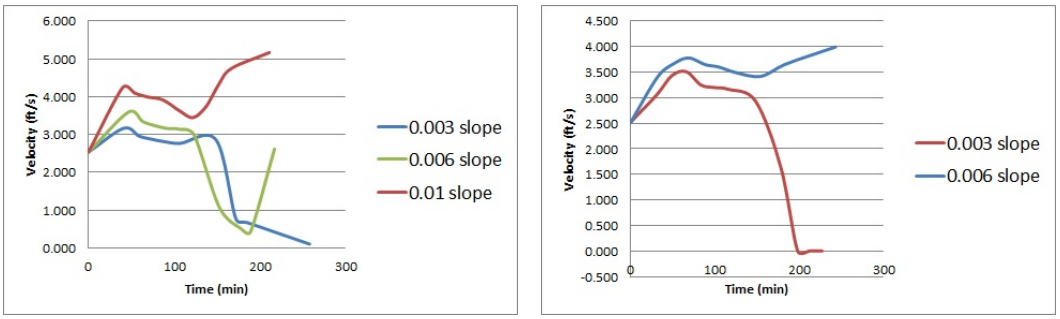

(a) Exit velocities for the large grain **(b)** Exit velocities for the small grain

Figure 8.18. Exit velocities measured for the large and small grains at all slopes tested

8.3.3 Sediment Movement Downstream of Model

Sediment movement downstream of the culverts was a function of the sediment transported through the culvert barrels. The initial sediment bed downstream of the culverts did not show any signs of transport. During the ramp-up of discharge rates the exit of the culvert barrels did experience small amounts of erosion, but were quickly filled in with the solids initially transport through the culverts. Downstream sediment bed scouring did occur at the downstream control with sediment transport through the single culvert,

however this quantity was not measured nor considered part of the experimental transport rates.

As the sediment moved through the culverts, a new sediment dune would form downstream. The linear distance downstream is related to the initial speeds of the exit velocities and the flume slope. The higher slopes had larger Froude numbers that sustained transport further downstream. The distance of transport ranged from 1 ft to 4 ft with respect to the 0.003 and 0.01 slope. Mostly, the higher Froude numbers were associated with scouring evidence in the downstream sediment bed at a distance more than 4 ft from the culvert model to the downstream control. Examples of scouring evidence are shown later in this chapter.

The formation of the dune occurred in the center of the channel. The width of the dune development was related to the width of the culvert barrels and magnitude of the stream eddies. The multi-barrel culverts produced the widest dune widths on the downstream side. Typically, upstream sediment dunes developed with a gentle sloping front edge and a sharp slope on the downstream slope as depicted above in Figure 8.9. The downstream dune formations at the outlet of the culverts were in the opposite sense, with a shape leading edge and gentle trailing edge. Single barrel culverts tended to develop higher dunes and prevented sediment deposits in the barrels until the dune encroached on the exit.

Figure 8.19 shows a picture of a dune developed on the outlet side of the rectangular culvert. The barrel never clogged in the experimental time limit, however the outlet was almost closed by the dune formation. The picture shows how the sediment dune developed towards the culvert barrel and as the dune would overcome the outlet, sediment would deposit in the barrel.

Figures 8.20 and 8.21 show examples of sediment formations formed for the M4C model and the MR model. The examples show the plots generated from surveying the sediment

Figure 8.19. Example of the slope reversal on the downstream sediment dune

movement. Next to the graph is a corresponding photograph representing the sediment formations. The dune formations at the left and right bank appear as if the sediment flowed over the roadway; however, the deposits are from material trapped in eddies in the stream flow. The lighter coloring scheme in the survey plots depict sediment deposits. The tan to yellow color is the original sediment bed elevation. Evidence of scouring is rendered in the survey plots by the lite greenish coloring in the plots.

Figure 8.22 is an example comparing the dune formations for the M6C Model. Figure 8.22a is a representation of the movement and dune formation at the 0.003 slope. Figure 8.22b is a representation of the movement and dune formation at the 0.01 slope. The two pictures show that sediment moved further downstream at the larger slope. The volume increase in sediment transport was related to the increase in slope, but has a more substantial relationship to the depth of the discharge on the downstream side of the culverts. A further explanation in depth is discussed in the next section.

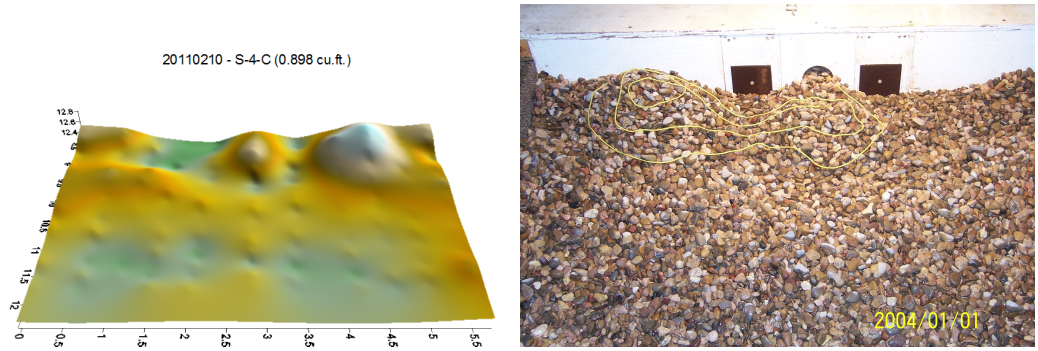

(a) Survey plot **(b)** Digital photograph

Figure 8.20. Example of sediment formation downstream of the culvert with the S4C model

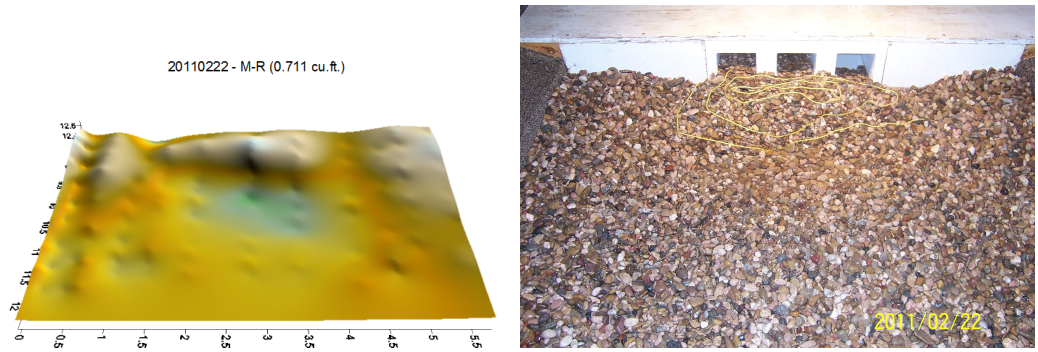

(a) Survey plot **(b)** Digital photograph

Figure 8.21. Example of sediment formation downstream of the culvert with the MR model

8.4 Tailwater Depth Changes

8.4.1 Increased Tailwater Depth

The downstream control depth was increased by building an extension to the top of the road deck. The extension raised the height of the downstream control by 0.33–ft. Figure 8.23 is a photograph of the constructed extension used in the experimental channel.

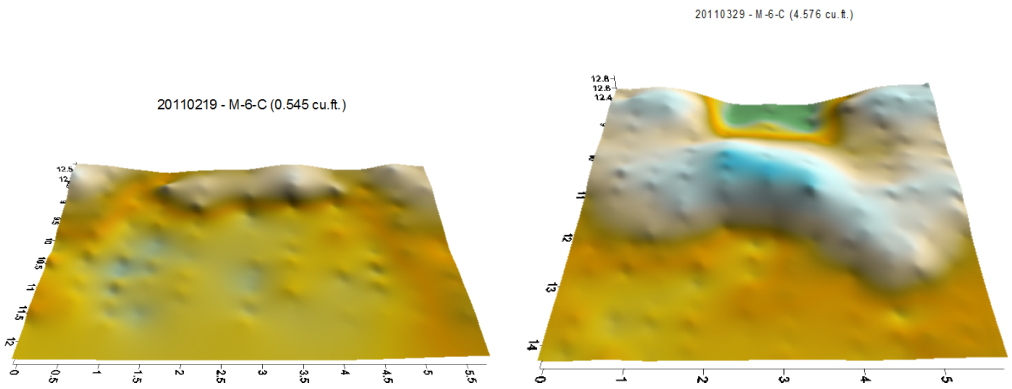

(a) M6C Model at the 0.003 slope **(b)** M6C Model at the 0.01 slope

Figure 8.22. Comparision of sediment transport with respect to slope

Figure 8.23. A picture showing the downstream control's road raised in height

Comparisons were made between this experiment with an increase in depth and a typical experiment. Table 8.1 compares similar discharges used during the experiments along with recorded depth measurements made at each measuring station with the SBC model type installed. The extension increased the depths 10.9%, 25.5%, and 21.3% with respect to Section 1, 2, and 3 in the flume. The increase in depth reduced the supercritical flow over the culvert model road top and changed the water surface to a more tranquil flow.

The increase in depth changed the velocities at both the entrance and exit of the culverts. Figure 8.24 is a graph of the velocities recorded for Experiments 182 and 196. The graph shows the differences in the inlet velocities, Experiment 182 has higher inlet velocities and a large increase in the outlet velocity, whereas Experiment 196 has relatively the same velocities at the inlet and outlet of the culvert. Also in Experiment 196, small decreases in speed are detectable as the sediment dune migrated towards the road crossing. Both experiments followed the typical experimental procedure and time limits.

Table 8.1: Comparison of Depths in Flume for the SBC Model

Date	Exp. No.	Q (ft3/s)	Total Depth (ft)		
			Section 1	Section 2	Section 3
24-Aug-11	182	12.97	1.56	1.08	1.18
2-Dec-11	196	12.44	1.75	1.45	1.50
		% increase	10.9	25.5	21.3

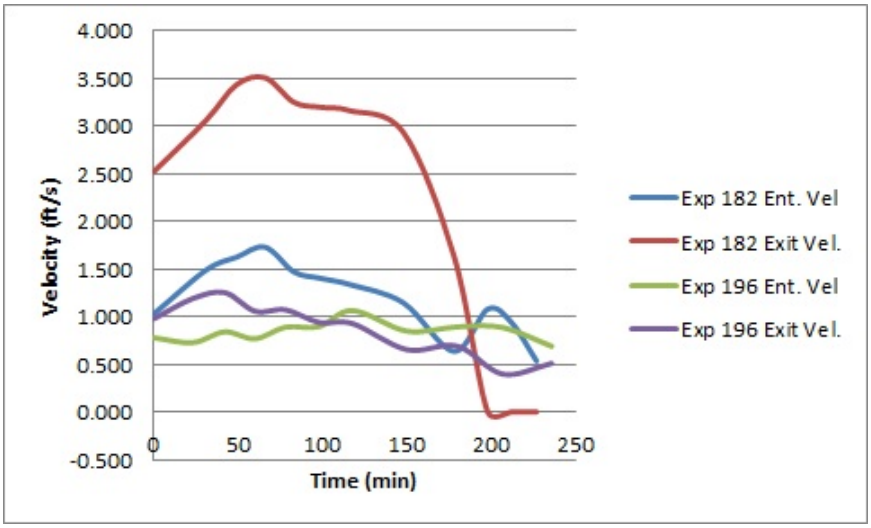

Figure 8.24. Comparison in velocities through the SBC culvert model with an increase in tailwater depth

8.4.1.1 Sediment Transport vs. Depth Change

The increase in depth substantially changed the sediment transport rate for the two tested models; M-R and SBC. The M-R culvert model moved an average of 0.1 ft^3 of sediment and the SBC culvert model moved no detectable amount of sediment through the culvert barrels when the flow depths were increased. The sediment dune formation was similar to the other experiments, but the difference is in the migration pattern. The sediment dune migrated to the culvert model without stopping at the 1–ft position. The dune was encroaching on the inlets of culvert barrels at the end of the experiments.

A small change was made to Experiment 197 by increasing the experiment time by 1.5 hours. The increase in time produced little additional distance with the migrating dune versus Experiment 196. The increase in time, also did not affect the sediment transport rate through the culvert model; again there was not a detectable amount of transport. Figure 8.25 is a picture of the dune development before the culvert model. Notice the encroachment of the dune on the left and center inlets. If the pictures of Experiments 196 and 197 are overlaid on top of each other, there is no visually detectable change in dune formation.

8.4.2 Decrease Tailwater Depth

As a contrast to an increase in depth, Experiments 200 and 201 were conducted by decreasing the downstream depth. The downstream control was disassembled to remove the center module. The removal of the center module allowed an increase in velocity downstream of the first culvert model and a related lowering of the flow depth in the downstream channel. Figure 8.26 is a picture showing the altered downstream control with an increased water flow through the opening.

Figure 8.25. Sediment dune position with larger depths

Figure 8.26. Downstream model altered

Comparisons are made between a typical experiment and this experiment in depth and velocity readings. Table 8.2 compares similar discharges used during the experiments along with recorded depth measurements made at each measuring station with the SBC model type installed. The alteration made in the downstream control decreased the depths by 4.0%, 16.1%, and 21.6% with respect to Section 1, 2, and 3 in the flume when compared to the earlier experiments performed on a SBC model.

The decrease in depth increased the intensity of the super-critical flow over the road crossing producing a hydraulic jump directly after the culvert model shown in Figure 8.27. Comparing the Froude numbers in the two experiments, the numbers changed from 0.29 and 0.26 at Section 2, and 3 respectively, to 0.35 and 0.34 with the decrease in depth. A change of 17% and 23.5% in the Froude number at each respected location.

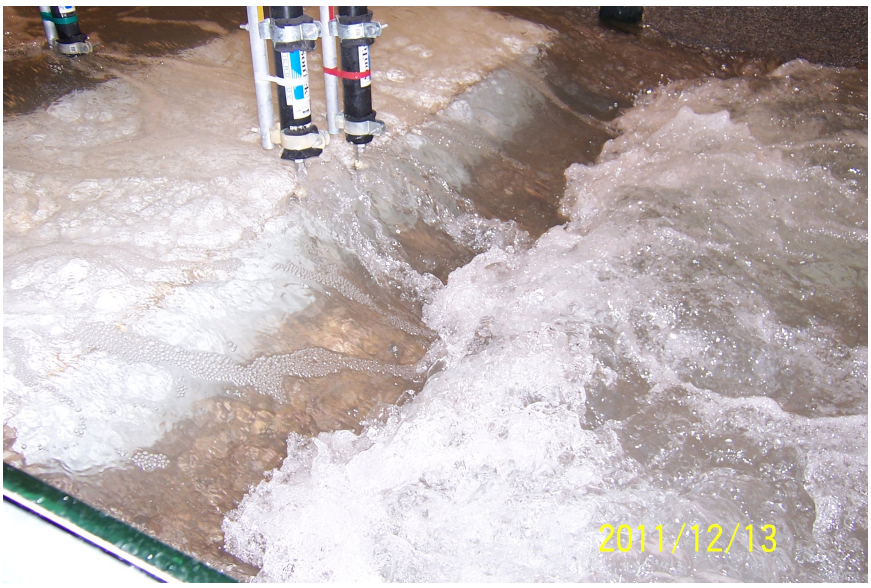

Figure 8.27. Decrease in tailwater depth producing a pronounced hydraulic jump

As anticipated, the decrease in tailwater depth increased the velocities through the culvert model at both the entrance and exit of the culverts. Figure 8.28 is a graph comparing

velocities for Experiments 182 and 201. Experiment 201 shows an increase in both the inlet and outlet sides of the culvert. The outlet velocities show a short decrease in velocity speed at the 60 minute mark, however, the speed becomes constant until about the 180 minute mark where the velocities start to increase again. The measured inlet velocities show very little change in speed throughout the experiment time. The typical experimental timing procedure was followed.

The sediment dune migrated in similar fashions towards the culvert model, and with the increase in speeds, an increase in sediment transport was measured. Experiment 201 was altered a little from normal experimental procedures. Approximately 1.5 hours into the experiment an additional amount of sediment grains was fed into the upstream channel. A total of 2.31 ft^3 of sediment grains was slowly introduced in the upstream flow at the grate divider. The increase in sediment did not slow the velocities in the culvert barrels and actually contributed to a higher flow rate in transport.

Table 8.2: Comparison of Depths in the Flume for the SBC Model.

Date	Exp. No.	Q (ft3/s)	Total Depth (ft)		
			Section 1	**Section 2**	**Section 3**
24-Aug-11	182	12.95	1.56	1.08	1.18
14-Dec-11	201	12.3	1.5	0.93	0.97
		% decrease	-4.00	-16.13	-21.65

8.4.2.1 Photographic Comparison in Sediment Movement

The influence the increase in velocity and the change in Froude number downstream of the culvert model had on the sediment movement and transport rates are shown in Figures 8.29 and 8.30. Side-by-side survey plots and photographs depict the difference in the sediment bed formations.

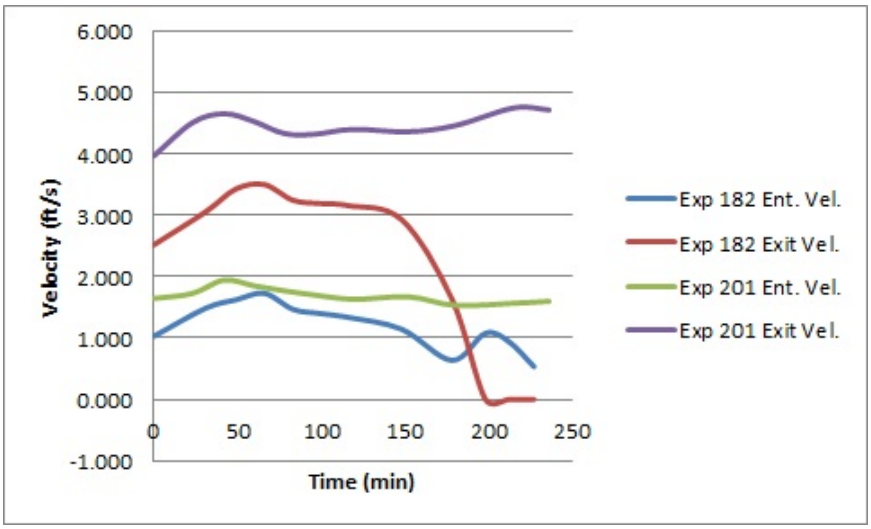

Figure 8.28. Comparison in velocities through the SBC culvert model with a decrease in tailwater depth

Figures 8.29 a and b are of the survey renderings of the sediment bed formation. Figure 8.29a is of Experiment 201 and a distinct difference can be seen when compared to Figure 8.29b in the dune formations. Experiment 201 shows migration of the sediment further downstream with a sediment dune forming at the extent of the survey. Erosion of the sediment bed occurred down to the wooden model floor at approximately 2 ft past the model and for 2 ft of length on both sides of the channel. A smaller dune at the center of the channel was present just in front of the larger dune formation. Experiment 182 shows the typical dune formation at the outlet of the culverts with erosion depressions starting on the outside of the channel. Smaller disturbances are shown in the center of the channel that was more related to the squishing of the center of the bed by the erosion channels.

Figures 8.30 a and b are photographs of Experiments 201 and 182. The photos show the differences in the sediment bed formation. Figure 8.30 is of Experiment 201 and the erosion to the wooden model floor is visibly shown along with the small limited sediment debris in front of the culvert outlets. Figure 8.30 is of Experiment 182 where the sediment

dune is shown at the outlet of the culvert. In the photograph, the dune and the start of the erosion channels are outlined with the yellow string.

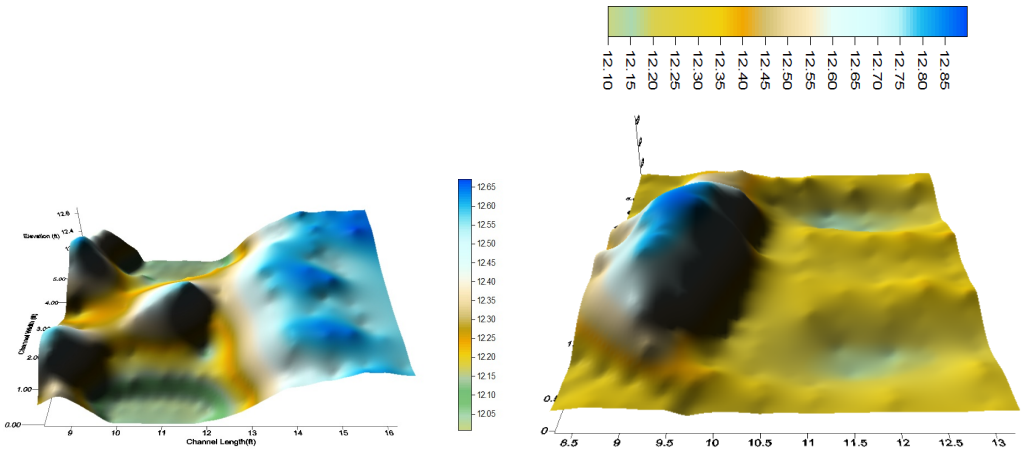

(a) Experiment 201 **(b)** Experiment 182

Figure 8.29. Comparison in sediment bed formation with respect to tailwater depth

(a) Experiment 201 **(b)** Experiment 182

Figure 8.30. Photographs of the differences in sediment bed formations

8.5 Alternate Flow Regime

The experimental apparatus was designed with a downstream control. The downstream control was a single rectangular barrel culvert roadway that experienced the same flooding conditions as the main test models. Recorded depths found in the data show the depth before the two roadways were generally within 0.06 ft with each other, with the larger depth at the upstream station. Experiment 10 presented a contrast to the normal depths and sediment movement as compared to the typical experiments.

Experiment 10 was a special three-day event. The model configuration used the SBC culvert model. The experiment was set up to monitor sediment transport at a higher flow rate and have the flow rate achieved in a shorter time period. The water was stabilized at the 7.5 cfs flow rate as the regular sediment experiments. The flow rate was then increased to $\approx$25 cfs over a 15 min span. The flow was allowed to run for 30 min continuously and then shut down. The results showed a limited amount of transport through the barrels, however the dune had migrated to the roadway and overwhelmed the inlet of the culverts. Clogging appeared to be occurring from the upstream side of the barrels.

The increased flow rate was performed three more times with the same procedure list above for 30-min time limits. The change in downstream sediment structure can be seen in Figure 8.31. Figure 8.31 shows 3-D survey plots of the sediment bed downstream of the culverts. The results showed sediment transport further downstream at each flow event in each consecutive run. However, the formation of the upstream dune occurred differently with respect to the typical experiments. The sediment bed embedded the inlet of the culverts, and each sequential run pushed sediment through the culverts. The increased flow rate produced higher turbulence seen in the water surface as longer waves. The wave action appears to have contributed to the sediment movement between the two roadways. The culvert barrels clogged from upstream to the downstream side and with each sequential

run cleared a little more sediment debris from the culverts. This mode of clogging is in distinct contrast to the typical experiments.

Surveys of the sediment bed can be seen in Figure 8.31 for each test run. Scouring of the first layer of sediment is shown in the first survey plot with a small deposit of sediments at the outlet. The next demonstrates a larger deposit of sediment at the outlet of the culvert and the erosion of the bed has filled in. The last plot shows a much larger deposit of sediments at the culvert outlets and the dune is migrating downstream away from the model.

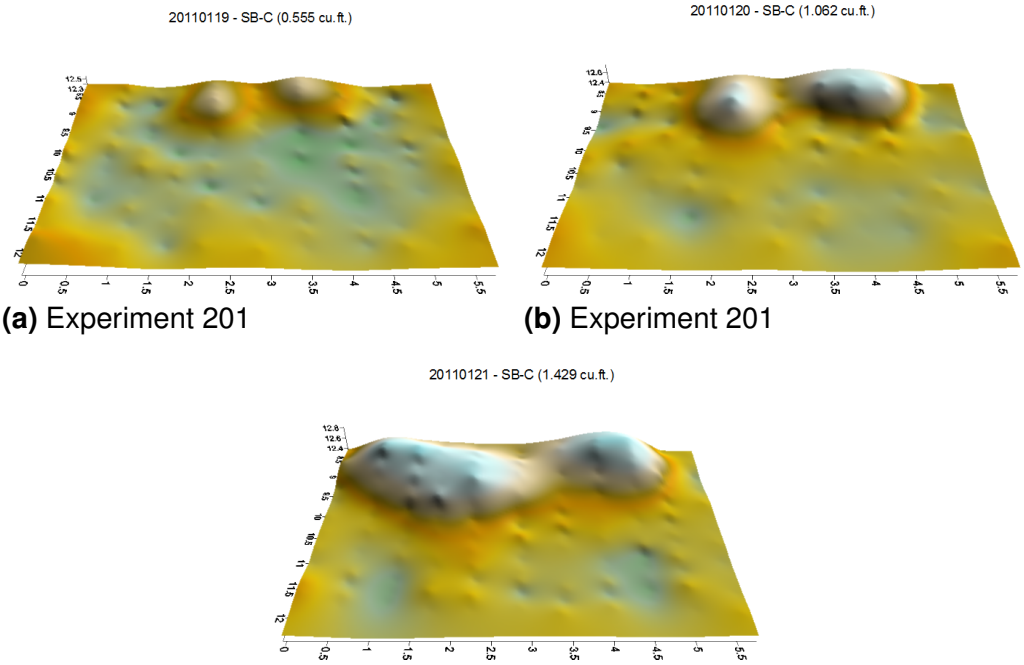

(a) Experiment 201 **(b)** Experiment 201

(c) Experiment 201

Figure 8.31. Survey plots of sediment movement after each large flow event

A difference in ratios between the upstream and downstream depths between a typical experiment and Experiment 10 indicated how tailwater heights affect sediment transport. The water surface slope between measured depths at Sections 1 and 3, demonstrate a

larger difference in depth measurements. This greater difference is related to a difference in pressurized flow between the two sections which contributes to sediment transport.

Differences in depth measurements at Sections 1 and 3 increased from 0.06 to 0.2 ft. In the regular experiments as the time increased the flow depths became stable, and the flow approached a uniform flow throughout the experimental channel. In this special experiment, tailwater depths started to decrease in depth during the short experimental runs.

Examining the hydraulic grade line (HGL) between Section 1 and 3, shows an increase in the HGL line from a 0.004 slope to a 0.014 slope from the typical experiential as compared to this special experiment. The flow rate was 150% of the typical rate, which increased the energy grade line slope by 327%. The typical experiments occurred over a 5 hour time limit from start to finish and this special case occurred over 2.5 hours. The change in flow rate and the change in ratio of depths increased the sediment transport by 300%.

The additional experiments 194–197 and 200–201 support the effects of tailwater depth exhibiting control on solids transport. A summary of the transport rates for the SBC model is presented in Figure 8.33.

8.5.1 Improved Culvert Flow

The efficiency of clear water flow through culverts is improved by changing the edges to the culvert inlet (*Sturm*, 2009). In addition, wingwalls may also be added to improve the flow through culverts (*Herr and Bossy*, 1972; *Yarnell, Nagler, and Woodard*, 1926). The last change to the experimental culverts tested the effect of wingwalls added at the inlet of the culverts. The tested model configuration used the SBC culvert model. Wingwalls were constructed with an approach angle of 45° to the flow. Average flow rates through the culvert improved by 248% for the typical experimental time.

Figure 8.32 is a graph showing the velocity-time diagram with the wingwalls as compared to the equivalent typical experiment (Experiment 182). The velocity graphs are similar for both the entrance and exits of the culverts. The exit velocities show the same decline in velocities as the dune approached the culvert model. The difference in the flow rates was because experiment 182 clogged with sediment grains and recorded no additional flow for the last hour of the experiment. Experiment 198 did not clog, and with the continuous flow through the culvert, the sediment grains that did start to deposit were ultimately flushed through the culvert.

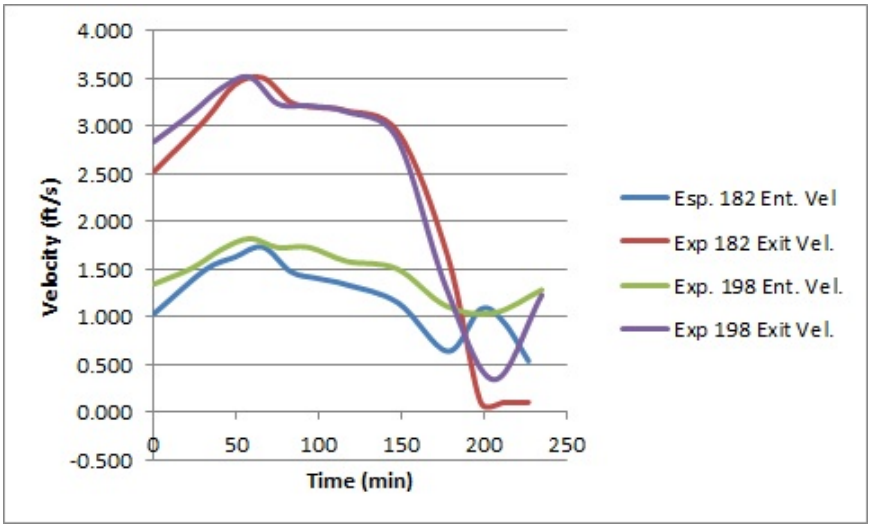

Figure 8.32. Comparison in velocities through the SBC culvert model with a wingwall

Experiment 199 was similar to 198 with the additional of 2.31 ft^3 of sediment grains were slowly introduced to upstream flow 1.5 hours into the experimental run. These extra sediment grains clogged the center barrel. Following experiment protocol, experimental run times were sustained for 1 hour after a culvert is reported clogged. The additional run time in this experiment allowed for the flow to clear the culvert. The author would like to note that if a continuous feed of sediment grains were introduced to the upstream flow, the

culvert barrel would likely have not cleared. However, natural channels do not experience a continuous supply of large sediment grains; therefore, the clearing of the culvert is an acceptable result.

8.6 Summary of Sediment Transport Rates

Figure 8.33 shows the sediment transport yield for all the SBC culvert models at the 0.003 slope. The two largest sediment yields occurred when the wingwall was added to the culvert model. The next largest sediment yield was when the change in tailwater depth was decreased. Changing the tailwater depth produced similar yields when compared to the wingwall. Flow rates were similar in the culvert barrel with the added wing wall and the decreased depth in tailwater.

The added wing wall and the change in tailwater depth experiments did not clog with sediment. The advantage the wingwalls experienced was the ability to flush the sediment debris deposited in the culvert barrel. The dune location position has been presented to show a relationship of movement distance and the model type. With the addition of the wingwall, or change in decreasing tailwater depth; the overall downstream migration of the dune did not penetrate the 1 ft barrier in front of the culvert model.

8.7 Surface Water Comparison

Figures 8.34 and 8.35 are photographs of discharge in the flume. Figures 8.34 a and b show the water surface for the large grain and small grain sediments for the typical experiments. Figure 8.35a is the water surface for the increased downstream depth. Figure 8.35b shows the water surface for the decrease downstream depth. Turbulence was visible in the water surfaces for the different pictures, which assisted in sediment movement

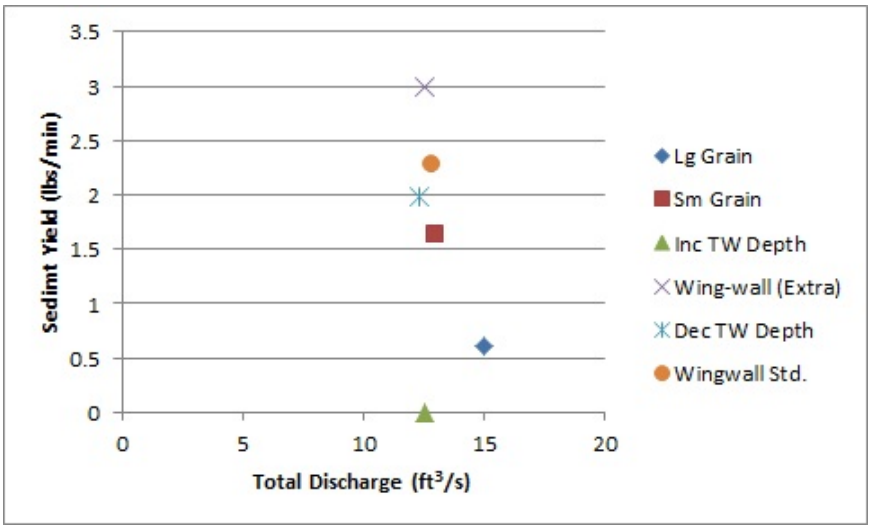

Figure 8.33. Summary graph of the sediment transport volumes through the SBC culvert

below the culvert model. These photographs show the effects the tailwater control had on the water surface, which was related to the sediment discharge patterns.

(a) Large grain example **(b)** Small grain example

Figure 8.34. Examples of the water surface over the large and small grains

(a) Increased tailwater depth **(b)** Decreased tailwater depth

Figure 8.35. Examples of the water surface with an increase and decrease in tailwater depth

8.8 Summary

A series of special experiments were performed throughout the project to test various hypothesis. The main hypothesis was how the tailwater depth affected the flow and transport of solids.

Experiment 10 was a sample of four large flow events in small relative time limits, and the last 12 experiments compared the typical experiment to the additional hypothesis experiments. Figure 8.33 shows these special experiments with the volumes of sediment transport presented as a summary. Transport increases are observed in the addition of wingwalls and the decrease in tailwater depths. The increase in tailwater, which provided for a tranquil flow pattern in the experimental showed no transport volume and the dune migration was not affected by additional run time.

Chapter 9

Conclusions and Recommendations for Future Work

9.1 Discussion And Conclusion

Conclusions in this chapter are based on the authors interpretations of the data collected through the experiments, observations, and the knowledge gained from the literature. The research presented in this paper examined the interaction of sediment mobility and culvert flow. The results presented in this paper are derived from the natural interaction of the sediment grains and the flow field developed around and through the culverts. Typical sediment transport equations are developed for unobstructed flow patterns in open channels. Theories developed for sediment transport rates use various hydraulic conditions and parameters to explain the transport rates, generally in terms of unit widths.

9.1.1 Experimental Findings in Context of Sediment Transport

Incipient motion was surpassed by design in the experiments, allowing the formation of a sediment dune that migrated consistently with the hydraulic conditions developed in the experiments. The sediment volume changes downstream of the culvert were related to the sediment volumes transported through the culverts. Incipient motion downstream of the culverts was negligible, and the stream bed topography changes were in close proximity to the outlets of the culvert barrels. The sediment transport through the culverts formed a dune that grew in size from downstream of the culvert back towards the outlet of the culvert and eventually deposited in the culverts until the culverts became clogged. With an

unlimited sediment supply, sediment yield through the culvert would overcome the culvert storage capacity and completely clog the culverts.

9.1.2 Experimental Findings in Context of Flow patterns

This research has shown how a culvert structure interferes with the flow field and velocity distribution in that flow field is altered. The velocity profiles before and after the culvert structure shows how the structure interferes with the flow patterns by changing or reversing the velocity vectors at various depths. The larger cross-sectional area culverts show the least interference to the velocity profiles and in most cases the structure was virtually undetected. Because sediment transport equations are based on uniform flow conditions, the better the chance of the flow field being undisturbed, the easier the sediment will be allowed to travel in its natural direction downstream.

When culverts are under downstream control, these experiments have demonstrated how sediment transport through culverts is related to the tailwater depth and transport rates are severely under predicted by standard sediment transport equations. Typical sediment transport rates should not be used to predict sediment yields through culverts when the culverts are under outlet control.

With a uniform depth in the experimental channel, and the structure completely flooded, sediment transport rates were undetectable or null through the culvert models. There was a distinct difference in how the sediment bed moved towards the culvert structure with the sediment dune encroaching on the inlet side creating a block aide at the inlet of the culverts. Whereas, when the tailwater depth was decreased therefore creating less influence by the outlet control on the flow rates through the culverts, the sediment transport rates increased over the standard experiments in this paper.

As in clear water analysis of culvert flow, improvements made to the inlet side of the culverts increase culvert flow through the culverts; similar results occurred with the sediment yield increasing through the culverts. The wing wall experiments showed how the improved culvert flow enhanced the sediment yield both through the barrel and the distance sediment traveled downstream.

9.1.3 Experimental Findings in Context of Largest Solids Volume Accommodated

These studies have shown how the culvert area is related to the sediment yield through the culverts. The culverts with the largest area moved the largest sediment yield. At the lowest slope tested (0.003), the sediment yields through the culverts did not vary in quantity, although the visual observation and photographs show how the single barrel culverts and smaller cross-sectional culvert areas would clog completely, whereas the multiple barrel culverts would not. At the two highest slopes, 0.06 and 0.01, the largest culvert areas dominated the sediment yield and the quantities transported through the culverts were ranked in the same order as cross-sectional area.

The staggered barrel configuration did produce an advantage over the other culvert models, as the center barrel clogged with sediment debris and the sediment yield built up on the outlet of the culverts, the two outside barrels were still able to transport clear water flow. In addition, this clear water flow would assist in eroding the top crest of the downstream dune preventing or delaying the dune from building up in the outside barrels. Of course there was a limit to this phenomenon, as the center barrel became overloaded with sediment, the upstream dune migrated to the inlets of the culverts and the culverts began to clog from both the inlet and outlet. Once the upstream dune encroached on the inlets, sediment began to flow through the outside barrels contributing to the downstream

dune. Over time the sediment yield would overcome the capacity of the culvert barrel flow and complete clogging would occur.

The sediment yield through the culverts is related to two properties: (1) Culvert cross-sectional area and (2) Outlet flow control. First, culvert size, these studies have shown how the larger culvert cross-sectional areas moved the largest yield and the geometric shape of the culverts showed no distinction in the transport rates. Second, these studies have shown how the tailwater depth effects the sediment yield in a negative fashion, increased tailwater depth reduces the culvert's ability to transport solids.

9.1.4 Future Research

The author explored a linear regression analysis using similar predicting parameters or hydraulic conditions as the typical sediment transport equations use. The relationship of the predicted yield and the difference in errors showed the relationship to be non-linear. After further thought, the author did not pursue any form of regression analysis nor manipulation of equation fitting with the standard sediment transport equations to the data because the author feels the tailwater depth has a great impact on the sediment yield through the culverts. Further research is needed in discovering the relationship of the tailwater depth, outlet and inlet control to the sediment yield through the culverts.

Further work is needed in exploring the energy and/or momentum exchange as the flow over the road combines with the discharge of the culverts. The loss in energy appears to have a relationship to the sediment travel distance from the outlet of the culverts.

The skewed road crossing changed the flow lines in the flow field and slowed the migration rate of the sediment. This model configuration should be a stand alone study to understand the effects the approach angle has on solids mobility. This research only tested a

small deviation in the approach angle, it is unclear if sediment transport would still occur at larger approach angles.

Studies are still needed on multiple and single barrel culverts at low slopes below 0.5%. Single barrel culverts tend to operate better as pressurized flow when compared to multiple barrel culverts at the lower slopes.

References

The author does not directly cite selected bibliographic entries within the main body of this dissertation—These entries are identified the †. These uncited entries are listed here because each was consulted by the author during the process of completing this dissertation and are included for archival purposes and potential use by others.

†Ackers, P. and White, W.R., (1973) Sediment transport: new approach and analysis. Journal of the Hydraulics Division, American Society of Civil Engineers, Vol. 99, No. HY11, pp. 2041–2060.

†Afzalimehr, H., and Anctil, F., (1999) Velocity distribution and shear velocity behavior of decelerating flows over a gravel bed. Canada. Journal of Civil Engineering. Vol. 26, pp. 468–475.

Alan, A.M.Z., and Kennedy, J.F. (1969). Friction factors for flow in sand-bed channels. Journal Hydraulic Division, American Society Civil Engineers, 95 HY6, pp. 1973–1992.

†Bagnold, R.A., (1966) An approach to the sediment transport problems from general physics. U.S. Geological Survey Professional Paper 422–5.

Bakhmeteff, B.A., (1932) Hydraulics of open channels. 1st edition, McGraw-Hill Book Company, New York, pp 329.

†Barry, J.J., Buffington, J.M. and King, J.G., (2004) A general power equation for predicting bedload transport rates in gravel bed rivers. Water Resources Research, Vol. 40, W10401, 22 p.

Bates, K., B. Barnard, B. Heiner, J.P. Klavas, and P.D. Powers, (2003) Fish passage design at road culverts. Washington Department of Fish and Wildlife, Olympia.

Bathurst, J.C., (1982) Theoretical aspects of flow resistance. In: Gravel-bed Rivers (ed. by R.D. Hey, J.C. Bathurst and C.R. Thorne), John Wiley and Sons, New York, USA, pp 83–108.

Bartnik, Wojciech, Struzynski, Andrzej, (1996) Measurements of basic velocity fluctuation characteristic in rough stream bed. Zeszyty Naukowe Agricultural University of Cracow., No. 16, pp 19–30, [Polish].

†Bergeron, N.E., and Abrahams, A.D., (1992) Estimating shear velocity and roughness length from velocity profiles. Water Resource Research, Vol. 28, No. 8, pp. 2155–2158.

Branson, F.A. and Reid, E.H. and Society for Range Management, (1981) Rangeland hydrology. Range science series 2nd edition, Kendall/Hunt Pub. Co. 340 p..

Bray, D.I., (1979) Estimating average velocity in gravel-bed rivers. Journal of the Hydraulic Division. American Society of Civil Engineers, Vol. 105, No. HY9, pp. 1103–1123.

Bray, D.I., (1982) Flow resistance in gravel-bed rivers. In: R.D. Hey, J.C. Bathurst and C.R. Thorne (Editors), Gravel-Bed Rivers: Fluvial Processes, Engineering and Management. Wiley, New York, pp. 109–137.

†Brownlie, W.R., (1981) Prediction of flow depth and sediment discharge in open channels. W.M. Keck Laboratory of Hydraulics and Water Resources, Report No. KH–R–43A, California Institute of Technology, Pasadena, California.

Bureau of Reclamation, (2006) Erosion and sedimentation manual. U.S. Department of the Interior, Bureau of Reclamation, Technical Service Center, Sedimentation and River Hydraulics Group, Denver, CO.

Chen, C.I., (1991) Unified theory on power laws for flow resistance. Journal of Hydraulic Engineering-American Society of Civil Engineers, Vol. 117, No. 3, pp. 371–389.

Cheng, N.S., (2007) Power-law index for velocity profiles in open channel flows. Advances in Water Resources, Vol. 30, No. 8, August. pp. 1775–1784.

Chien, N. and Wan Z.H., (1999) Mechanics of sediment transport. American Society of Civil Engineering Press.

†Chiu, C.L., and McSparran, J.E., (1966) Effect of secondary flow on sediment transport. Journal of the Hydraulics Division, American Society of Civil Engineers, Vol. 92, No. HY5, September, pp. 57–70.

†Chiu, C.L., Hsiung, D.E., Lin, H.C. (1978) Three dimensional open channel flow. Journal of the Hydraulics Division, American Society of Civil Engineers, Vol. 104, No. Hy6, August, pp. 1119–1136.

†Ciray, C., (1967) On secondary current. In Proceedings of the Twelfth Congress of the International Association for Hydraulic Research, Fort Collins, Colorado. Vol. 1, September, pp. 408–414.

Chow, V.T., (1959) Open channel hydraulics. McGraw-Hill, New York, USA. 680 p.

†Clauser, F.H., (1956) The turbulent boundary layer. Advance Applied Mechanics. 4, pp. 1–51.

Coleman, N.L. (1981) Velocity profiles with suspended sediment. Journal of Hydraulic Research, Vol. 19, No. 3, pp. 211–229.

Coleman, N.L. (1986) Effects of suspended sediment on the open-channel distribution. Water Resources Research, AGU, Vol. 22, No. 10, pp. 1377–1384.

Coles, Donald, (1956) The law of the wake in the turbulent boundary layer. Journal of Fluid Mechanics, Vol. 1, pp. 191–226.

Cui, Y.T., G. Parker, C. Braudrick, W.E. Dietrich, and B. Cluer, (2006) Dam removal express assessment models (DREAM). Part 1: Model Development and Validation, Journal of Hydraulic Research, Vol. 44, No. 3, pp. 291–307.

Cui, Y.T. and G. Parker, (2005) Numerical model of sediment pulses and sediment-supply disturbances in mountain rivers. Journal Hydraulic Engineering, American Society of Civil Engineers, Vol. 131, No. 8, pp. 646–656.

Dey, S., and U. Raju, (2002) Incipient motion of gravel and coal beds. Sadhana, Vol. 27, NO. 5, pp. 559–568.

Dixon, Jeremy, (2012) A relation between select hydraulic properties and sediment transport volume through experimental culvert configurations and techniques for measuring sediment transport volumes. Master Thesis,Texas Tech University, Lubbock, Texas.

Du Boys, Paul, (1879) Le rhone et les rivieres a lit affouillable. Annales des Ponts et Chaussees Vol. 18, NO. 5, pp. 141–195.[French].

Einstein, H.A., (1950) The bed load function for sediment transport in open channel flow. U.S. Department of Agriculture Soil Conservation Technical Bulletin No. 1026.

Einstein, H.A., and N.L. Barbarossa, (1952) River channel roughness. Transactions of the American Society of Civil Engineers, Vol. 117, pp. 1121–1132.

Elliott, J.G., (2002) Bed-material entrainment potential. Roaring Fork River at Basalt, Colorado: U.S. Geological Survey Water-Resources Investigations Report 02–4223, 33 p.

Engelund, F., and Hansen, E., (1967) A monograph on sediment transport in alluvial streams. Technisk Vorlag, Copenhagen, Denmark.

†Gaucher, J., Marche, C., and Mahdi, T., (2010) Experimental investigation of the hydraulic erosion of noncohesive compacted soils. Journal of Hydraulic Engineers, American Society of Civil Engineering, Vol. 136, NO. 11, pp. 901–913.

Gilbert, G.K., (1914) Transportation of debris by running water. Professional Paper No. 86, United States Geological Survey.

Goodridge, W.H., (2009) Sediment transport impacts upon culvert hydraulics. Ph.D. Thesis, Utah State University, Logan, Utah.

†Grass, A.J., (1971) Structural features of turbulent flow over smooth and rough boundaries. Journal of Fluid Mechanics, Vol. 50, pp. 233–255.

Guo, Junke, and Julien, Pierre Y., (2001) Turbulent velocity profiles in clear water and sediment laden flows. Journal of Hydraulic Research, Vol. 39, No. 1.

Guo, Junke (2002) Hunter rouse and shields diagram. Advances in Hydraulic and Water Engineering, Vol. 2, pp. 1096–1098.

Guy, H.P., Simons, D.B., and Richardson, E.V. (1966) Summary of alluvial channel data from flume experiments. U.S. Geological Survey Professional Paper 462-1, pp. 1556–1561.

Haderlie, G. and Tullis, B. (2008) Hydraulics of multibarrel culverts under inlet control. Journal of Irrigation and Drainage Engineering, Vol. 134, No. 4, pp. 507–514.

Hadley, R.F., and Schumm, S.A., (1961) Sediment sources and drainage-basin characteristics in upper Cheyenne River basin. U.S. Geological Survey Water–Supply Paper 1531–B.

Handbook of Culvert and Drainage Practice. (1948) Published by Armco Drainage and Metal Products, Inc. Middleton, Ohio. pp. 470

Henderson, F.M., (1966) Open channel flow. New York, MacMillan, 522 p.

Hydraulic Charts for the Selection of Highway Culverts, L.A. Herr and H.G. Bossy, HEC No. 5, Hydraulics Branch, Bridge Division, Office of Engineering, FHWA, Washington, D.C. 20590, 1965.

Capacity Charts for the Hydraulic Design of Highway Culverts, Lester A. Herr and Herbert G. Bossy, Hydraulic Engineering Circular (HEC) No. 10, Hydraulics Branch, Bridge Division, Office of Engineering, FHWA, Washington, D.C. 20590, November 1972.

Hydraulic Design of Improved Inlets for Culverts, L.J. Harrison, J.L. Morris, J.M. Normann and F.L. Johnson, HEC No. 13, Hydraulics Branch, Bridge Division, Office of Engineering, FHWA, Washington, D.C. 20590, August 1972.

Hey, R.D., (1979) Flow resistance in gravel-bed rivers. Journal of the Hydraulics Division. American Society of Civil Engineers, Vol. 105, NO. 4, pp. 365–379.

†Hey, R.D., (1979) Flow resistance in gravel-bed rivers. Journal of Hydraulics Division, American Society of Civil Engineers, Vol. 107, NO. 7, pp. 899–918.

Hinze, J.O., (1975) Turbulence. 2nd edition, McGraw-Hill series in mechanical engineering. New York: McGraw-Hill. x, 790 p.

Hjulstrom, F, (1935) The morphological activity of rivers as illustrated by River Fyris. Bulletin of the Geological Institute, Uppsala, Vol. 25, ch. 3.

Julien, P., (1995) Erosion and sedimentation. Cambridge University Press.

†Jopling A.V., (1961) An experimental study on the mechanics of bedding. Ph.D. Dissertation, Harvard University.

Johnson, J.W., (1943) Laboratory investigation of bed-load transportation and bed roughness. U.S. Department of Agriculture Report SCS–TP–50.

Keulegan, Garbis H., (1938) Laws of turbulent flow in open channels. Research Paper RP 1151, National Bureau of Standard, Journal of Research, Vol. 21: pp 701–741.

†King, J.G., Emmett, W.W., Whiting, P.J., Kenworthy, R.P., and Barry, J.J., (2004) Sediment transport data and related information for selected coarse-bed streams and rivers in Idaho. Department of Agriculture, Forest Service, Rocky Mountain Research Station, USA. 31 p.

Kironoto, B.A. and Graf, W.H., (1995) Turbulence characteristics in rough non-uniform open-channel flow. Proceedings of the ICE. Instn Civil Engineers, Water Maritime and Energy, Vol. 112, pp. 336–348.

Kramer, H., (1935) Sand mixtures and sand movement in fluvial models. Transactions of American Society of Civil Engineers, Vol. 100, NO. 1909, pp. 798–838.

Kummu, Matti, (2002) Roughness characteristics and velocity profile in vegetated and nonvegetated channel. Master Thesis, Helsinki University of Technology.

Leopold, L.B., J.P. Miller, and M. Gordon Wolman, (1964) Fluvial processes in geomorphology. Dover Publications, New York.

Limerinos, J.T. (1970) Determination of the Manning coefficient from measured bed roughness in natural channels. U.S. Geological Survey, Water Supply Paper 1898–B, 47 p.

Liu, Z., (2001) Sediment transport. Laboratoriet for Hydraulik og Havnebygning, Institut for Vand, Jord og MiljÃÿteknik, Aalborg Universitet. 33 p.

Lovera, F., and J.F. Kennedy. (1960) Factors for flat-bed flows in sand channels. Journal of Hydraulics Division Vol. 95 (HY4 Proceedings Paper 6678) pp. 1227–1234.

Mays, Larry W., (2005) Water resources engineering. John Wiley and Sons, Inc., 842 p.

Meyer-Peter, E., and Müller, R., (1948) Formulas for bed load transport, proceedings. The Second Meeting of the International Association for Hydraulic Structures Research, Stockholm, pp. 39–64.

Meyer-Peter, E., Favre, H., and Einstein, H.A., (1934) Neuere versuchsresultate Ãijber den geschiebetrieb. Schweizerische Bauzeitung, 103 (13), ZÃijrich, Switzerland, pp. 147–150. [German].

Miedema, S., (2010A) Constructing the Shields curve: Part A fundamentals of the sliding, rolling and lifting. Miedema, S.A., Constructing the Shields curve, a new theoretical approach and its applications. WODCON XIX, Beijing China, September 2010. Copyright Dr. S.A. Miedema Mechanisms for the Entrainment of Particles. Journal of Dredging Engineering, Vol. 12, No. 1, January 2012.

†Milhous, R.T., (1973) Sediment transport in a gravel-bottomed stream, Ph.D. Thesis, Department of Civil Engineering, Oregon State University, U.S.A., 232 p.

†Muskatirovic, J., (2005) Prediction of sediment transport in gravel-bed rivers at the watershed scale for the purpose of assessing river restoration activities. Center for Ecohydraulic Research. Boise, University of Idaho, USA.

†Muskatirovic, J., and Goodwin, P., (2003) On the prediction of sediment transport in gravel bed rivers: examples from streams in central Idaho. XXX IAHR Congress of the International Association for Hydraulic Research, Thessaloniki, Greece.

†Nagy, H.M., (2002) Prediction of sediment load concentration in rivers using artificial neural network model. Journal of Hydraulic Engineering, American Society of Civil Engineers, Vol. 128, No. 6, pp. 588–595.

Neill, C.R., and M. Yalin, (1969) Quantitative definition of beginning of bed movement. Proc. American Society of Civil Engineers 95 (HY1): pp. 585–588.

Nezu, I., and Nakagawa, H., (1993) Turbulence in open channel flows. IAHR Monograph, Balkema, Rotterdam, The Netherlands.

Nikuradse, J., (1933) "Stromungsgesetze in rauhen Rohren". Forschung auf dem Gebiete des Ingenieurwesens. Forschungsheft 361. VDI Verlag, Berlin, Germany [German]). (English translation: Laws of flow in rough pipes, NACA TM 1292, (1950).

Obermiller, Clark, (2012) A laboratory study of incipient motion. Geology Senior Thesis, Texas Tech University, Lubbock, Texas.

†Parker, G., (1990) Surface-based bed load transport relation for gravel rivers. Journal of Hydraulics Research, Vol. 28, No. 4, pp. 501–518.

Peterson, A.W. and Howells, R.F. (1973) A compendium of solids transport data for mobile boundary channels. Technical report, Inland Waters Directorate, Envrionment Canada.

Potter, Merle C., Wiggert, and David C., (1997) Mechanics of fluids. Pearson Education Canada, 862 p.

Raudkivi, A.J., (1976) Loose boundary hydraulics. 2nd ed. Pregamon Press, p. 397

Reichardt, H. (1951) Vollstandige Darstellung der Turbulenten Geswindigkeitsverteilung in Glatten Leitungen. Zum Angew. Math. Mech., Vol. 3, No. 7, pp. 208–219.[German].

Reynolds, Osborne (1883) An experimental investigation of the circumstances which determine whether the motion of water shall be direct or sinuous, and of the law of resistance in parallel channels. Philosophical Transactions of the Royal Society 174, pp. 935–982.

Richards, K.S., (1982) Rivers: form and processes in alluvial channels. Methuen, 358 p.

Rifai, M.F. and K.V.H. Smith. (1971) Flow over triangular elements simulating dunes. Journal of Hydraulic Division, American Society of Civil Engineering, Vol. 97, No. Hy7, pp. 963–976.

†Robert, A., (1990) Boundary roughness in coarse-grained channels. Progress in Physical Geography, Vol. 27, pp. 42–70.

Rottner, J., (1959) A formula for bedload transportation. La Houille Blanche, Vol. 14, No. 3, pp. 285–307.

Rouse, H., (1939) An analysis of sediment transportation in the light of fluid turbulence. Soil Conservation Service Report No. SCS–TP–25, U.S. Department of Agriculture, Washington, D.C.

Rouse, Hunter, and Ince, Simon, (1957) History of hydraulics. Iowa City: Iowa Institute of Hydraulic Research.

Schlichting, H., (1968) Boundary-layer theory. 6th edition, McGraw-Hill series in mechanical engineering, New York: McGraw-Hill. xxii, 817 p.

Schoklitsch, A., (1934) Der geschiebetrieb und die geschiebefracht, Wasserkraft und Wasserwirtschujl, Vol. 29, No. 4, pp. 37–43.

Schumm, S.A., and Hadley, R.F., (1957) Arroyos and the semiarid cycle of erosion. American Journal of Science, Vol. 255, pp. 161J–174.

Shields, A., (1936) Application of similarity principles and turbulence research to bed load movement. California Institute of Technology, Pasadena (translated from German).

Simons, Daryl B., and Richardson Everett V., (1966) Resistance to flow in alluvial channels. Geological Survey Professional Paper 422–J, Physiolographic and hydraulic studies of rivers, 61 p.

Smart, G.M., M.J. Duncan, and J.M. Walsh, (2002) Relatively rough flow resistance equations. Journal of Hydraulic Engineering, American Society of Engineers, Vol. 128, NO. 6, pp. 568-578.

†Stevens, H.H., and C.T. Yang, (1989) Computer programs for 13 commonly used sediment transport formulas. U.S. Geological Survey Water Resources Investigation Report pp. 89–4026.

Straub, L.G., (1935) Missouri river report. House Document 238, Appendix XV, Corps of Engineers, U.S. Dept. of the Army to 73rd U.S. Congress, 2nd Session, 1156 p.

Sturm, T.W., (2009) Open channel hydraulics. 2nd edition, McGraw-Hill, New York, 493 p.

Vanoni, V.A., ed. (1975) Sedimentation engineering. American Society of Civil Engineers Task Committee for the Preparation of the Manual on Sedimentation of the Sedimentation Committee of the Hydraulics Division (reprinted 1977).

Von Karman, Theodore, (1931) Mechanical similitude and turbulence. Tech Mem NACA No. 611, 21 p.

Von Karman, Theodore, (1934) Turbulence and skin friction. Journal of the Aeronautical Sciences, Vol. 1, No. 1, pp. 1–20.

Wargo, R.S. and Weisman, R.N. (2006) A comparison of single-cell and multicell culverts for stream crossings. Journal of the American Water Resources Association, Vol. 42, NO. 4, pp. 989–995.

†White, C.M., (1940) The equilibrium of grains on the bed of an alluvial channel. Proceedings of the Royal Society of London, Series A, Vol. 174, pp. 332–338.

White, F.M., (1979) Fluid mechanics. McGraw-Hill, New York, 701 p.

Wiberg, P.L., and J.D. Smith, (1987) Calculations of the critical shear stress for motion of uniform and heterogeneous sediments. Water Resources Research 23(8): pp. 1471–1480.

Wiele, S.M., Wilcock, P.R. and Grams, P.E., (2007) Reach-averaged sediment routing model of a canyon river. Water Resource Research, Vol. 43, NO. W02425.

Wilcock, P.R., (1988) Methods for estimating the critical shear stress of individual fractions in mixed-size sediment. Water Resources Research 24 (7): pp. 1127–1135.

Yalin, MS., and E. Karahan, (1979) Inception of sediment transport. Journal of the Hydraulics Division, American Society of Civil Engineers, Vol. 105, No. HYII, pp. 1433–1443.

†Yang, C.T., (1972) Unit stream power and sediment transport. Journal of the Hydraulics Division 98 (HY10 Proceeding Paper 9295), pp. 1805–1826.

†Yang, C.T., (1973) Incipient motion and sediment transport. Journal of the Hydraulics Division 99 (HY10), pp. 1679–1704.

Yang, C.T., (1996) Sediment transport theory and practice. The McGraw-Hill Companies, Inc., New York (reprint by Krieger Publishing Company, Malabar, Florida, 2003).

†Yarnell, David L., Floyd A. Nagler, and Sherman M. Woodard, (1926) Flow of water through culverts. University of Iowa, Iowa City, Iowa, U.S.A.

Zanke, U.C., (2003) On the influence of turbulence on the initiation of sediment motion. International Journal of Sediment Research, Vol. 18, No. 1, pp. 17–31.

Appendix A
Sediment Yield: Actual vs. Predicted

Exp.	Actual Yield	Shields	DuBoy	Meyer Peter Muller	Schoklitsh	Rottner
#	$\frac{(lb/min)}{ft}$	$\frac{(lb/min)}{ft}$	$\frac{(lb/min)}{ft}$	$\frac{(lb/min)}{ft}$	$\frac{(lb/min)}{ft}$	$\frac{(lb/min)}{ft}$
Large Grain						
Slope (0.003)						
1	N/a	1.47	8.04	NAN	-3.55	-74.36
5	0.20	N/a	N/a	NAN	-3.26	N/a
6	0.10	N/a	N/a	NAN	-3.25	N/a
9	0.12	N/a	N/a	NAN	-3.23	N/a
12	0.10	5.34	14.90	NAN	-3.27	-23.53
13	0.11	5.32	14.70	NAN	-3.26	-22.73
14	0.09	4.99	14.07	NAN	-3.26	-22.33
15	0.12	5.39	14.81	NAN	-3.26	-22.76
18	0.15	5.74	15.27	NAN	-3.24	-22.07
19	0.17	5.69	15.38	NAN	-3.23	-23.67
20	0.14	5.97	15.73	NAN	-3.24	-22.35
23	0.10	5.83	15.58	NAN	-3.25	-22.72
24	0.14	5.90	15.72	NAN	-3.25	-22.81
25	0.11	5.58	15.09	NAN	-3.25	-22.46
26	0.12	4.84	13.73	NAN	-3.25	-21.74
27	0.19	5.35	14.81	NAN	-3.26	-23.02
28	0.14	5.02	14.19	NAN	-3.26	-22.62
29	0.16	5.10	14.44	NAN	-3.27	-23.30
30	0.12	4.91	14.08	NAN	-3.27	-23.04
31	0.11	4.63	13.52	NAN	-3.27	-22.53
32	0.21	5.80	15.42	NAN	-3.24	-22.27
33	0.19	6.23	16.26	NAN	-3.24	-22.69
34	0.18	5.94	15.74	NAN	-3.24	-22.65
Slope (0.01)						
38	0.00	171.49	183.86	NAN	0.10	-23.05
39	0.35	173.83	182.99	NAN	0.19	-22.27

Exp.	Actual Yield	Shields	DuBoy	Meyer Peter Muller	Schoklitsh	Rottner
40	0.47	177.70	187.66	NAN	0.23	-22.13
41	0.64	168.48	169.60	NAN	0.23	-21.04
42	0.77	167.74	171.00	NAN	0.19	-21.57
43	0.70	167.23	169.32	NAN	0.20	-21.36
44	0.64	171.35	174.95	NAN	0.23	-21.39
45	0.63	172.20	176.66	NAN	0.23	-21.51
46	0.67	172.32	176.09	NAN	0.25	-21.36
47	0.44	177.95	188.55	NAN	0.23	-22.20
48	0.35	177.58	187.37	NAN	0.23	-22.12
49	0.40	177.20	188.25	NAN	0.21	-22.35
52	0.46	165.82	176.94	NAN	0.04	-23.24
53	0.39	166.43	175.58	NAN	0.07	-22.83
54	0.49	177.59	185.03	NAN	0.27	-21.65
55	0.28	180.22	191.21	NAN	0.26	-22.09
56	0.31	179.48	188.84	NAN	0.27	-21.87
57	0.25	176.73	188.25	NAN	0.20	-22.46
60	0.53	178.34	180.96	NAN	0.35	-20.74
61	0.54	176.44	176.66	NAN	0.36	-20.36
62	0.39	169.28	175.64	NAN	0.16	-22.07
65	0.39	170.02	174.67	NAN	0.20	-21.67
66	0.42	171.08	175.24	NAN	0.22	-21.50
67	0.35	170.10	174.92	NAN	0.20	-21.70
68	0.50	170.47	171.66	NAN	0.26	-20.95
69	0.34	175.09	181.28	NAN	0.25	-21.63
Slope (0.006)						
70	0.08	49.89	62.54	NAN	-2.20	-22.32
71	0.21	49.46	62.76	NAN	-2.23	-22.86
72	0.15	49.37	62.40	NAN	-2.22	-22.71
73	0.18	48.74	61.09	NAN	-2.22	-22.46
74	0.23	50.15	61.94	NAN	-2.18	-21.71
75	0.15	46.99	59.19	NAN	-2.26	-22.88
78	0.27	44.97	56.74	NAN	-2.30	-23.20
79	0.17	48.27	60.19	NAN	-2.22	-22.29
80	0.38	51.88	62.76	NAN	-2.11	-20.67
82	0.21	49.60	62.10	NAN	-2.21	-22.32
83	0.09	47.14	59.69	NAN	-2.27	-23.08
84	0.11	47.71	60.39	NAN	-2.26	-22.98
85	0.17	48.02	61.19	NAN	-2.26	-23.22

Exp.	Actual Yield	Shields	DuBoy	Meyer Peter Muller	Schoklitsh	Rottner
86	0.21	50.89	63.12	NAN	-2.17	-21.76
87	0.21	51.21	62.41	NAN	-2.14	-21.04
Large Grain Skew Model						
91	0.22	47.83	59.55	NAN	-2.23	-22.27
92	0.34	49.36	62.31	NAN	-2.22	-22.66
93	0.18	49.36	61.26	NAN	-2.20	-21.99
94	N/a	49.03		NAN	-2.23	-22.68
95	0.00	48.63	62.20	NAN	-2.26	-23.28
96	0.09	49.60	63.02	NAN	-2.23	-22.88
101	0.00	49.21	62.85	NAN	-2.24	-23.16
102	0.23	52.23	65.23	NAN	-2.16	-21.89
104	0.15	50.09	62.42	NAN	-2.19	-22.07
105	N/a	48.57		NAN	-2.24	-22.88
107	0.12	51.06	64.36	NAN	-2.19	-22.38
108	0.08	50.64	63.12	NAN	-2.18	-21.99
109	0.44	48.89	62.51	NAN	-2.25	-23.23
113	0.00	49.42	64.98	NAN	-2.28	-24.25
114	0.03	51.55	66.27	NAN	-2.21	-23.08
115	0.13	50.08	63.33	NAN	-2.21	-22.62
116	N/a	50.93		NAN	-2.18	-22.19
117	0.06	50.64	63.81	NAN	-2.20	-22.42
Start Small Grain						
Small Grain Skew Model						
118	0.00	75.38	56.61	NAN	-0.45	-4.17
119	N/a	74.14	N/a	NAN	-0.49	-4.36
120	0.00	72.34	55.31	NAN	-0.51	-4.40
121	0.31	72.55	57.13	NAN	-0.55	-4.67
122	0.16	76.64	58.04	NAN	-0.45	-4.24
123	N/a	80.51	N/a	NAN	-0.40	-4.16
125	0.48	71.89	53.05	NAN	-0.45	-4.05
126	1.90	71.05	52.68	NAN	-0.47	-4.11
127	0.64	70.10	52.43	NAN	-0.49	-4.21
128	0.49	73.90	56.35	NAN	-0.49	-4.35
129	0.00	72.04	55.71	NAN	-0.53	-4.52
130	0.62	72.90	56.10	NAN	-0.51	-4.45
131	0.00	70.92	53.30	NAN	-0.49	-4.25
132	0.49	74.83	55.42	NAN	-0.43	-4.05
133	0.42	74.50	55.31	NAN	-0.44	-4.08

Exp.	Actual Yield	Shields	DuBoy	Meyer Peter Muller	Schoklitsh	Rottner
134	1.41	74.75	55.86	NAN	-0.44	-4.13
135	2.07	69.03	51.81	NAN	-0.51	-4.26
136	1.65	67.87	51.07	NAN	-0.53	-4.30
137	1.29	67.64	51.07	NAN	-0.54	-4.34
138	0.95	74.62	56.35	NAN	-0.46	-4.24
139	0.81	73.41	55.84	NAN	-0.49	-4.33
140	0.45	73.55	55.71	NAN	-0.48	-4.29
Parallel Model						
Slope (0.006)						
141	3.09	69.61	52.68	NAN	-0.52	-4.34
142	3.48	71.82	53.57	NAN	-0.47	-4.16
143	3.26	72.86	53.79	NAN	-0.44	-4.03
144	3.35	74.73	55.31	NAN	-0.43	-4.04
146	2.71	77.74	58.19	NAN	-0.42	-4.10
147	2.09	76.16	57.97	NAN	-0.46	-4.28
148	2.63	78.88	58.19	NAN	-0.38	-3.94
149	2.45	78.17	57.41	NAN	-0.38	-3.91
150	2.25	77.13	57.52	NAN	-0.42	-4.07
151	2.66	77.14	57.52	NAN	-0.42	-4.07
152	2.96	76.46	56.52	NAN	-0.41	-3.99
153	2.85	74.98	55.86	NAN	-0.44	-4.09
154	2.99	76.50	56.30	NAN	-0.40	-3.95
155	2.77	74.46	55.53	NAN	-0.44	-4.11
156	2.95	76.51	57.07	NAN	-0.42	-4.08
157	2.37	78.98	59.66	NAN	-0.42	-4.16
158	1.80	76.70	58.30	NAN	-0.45	-4.26
159	2.21	78.86	59.77	NAN	-0.42	-4.19
160	0.78	79.28	60.80	NAN	-0.44	-4.30
161	1.32	81.49	62.31	NAN	-0.41	-4.23
162	1.33	79.91	61.26	NAN	-0.43	-4.28
163	2.08	79.12	58.98	NAN	-0.39	-4.03
164	1.90	77.21	58.64	NAN	-0.44	-4.25
165	2.13	78.46	59.32	NAN	-0.42	-4.17
Slope (0.003)						
166	1.78	7.97	13.91	NAN	-1.66	-4.27
167	1.23	7.24	13.52	NAN	-1.71	-4.78
168	1.84	7.85	13.90	NAN	-1.67	-4.42
169	0.95	7.95	14.11	NAN	-1.68	-4.57

Exp.	Actual Yield	Shields	DuBoy	Meyer Peter Muller	Schoklitsh	Rottner
170	0.67	7.73	13.88	NAN	-1.69	-6.53
171	0.67	8.28	14.30	NAN	-1.67	-4.37
172	2.71	7.31	13.39	NAN	-1.69	-4.48
173	1.82	8.07	13.42	NAN	-1.60	-3.47
174	1.80	8.08	13.42	NAN	-1.60	-3.47
175	2.25	7.56	12.96	NAN	-1.61	-3.47
176	1.92	7.03	12.52	NAN	-1.62	-3.54
177	2.27	7.78	13.19	NAN	-1.61	-3.51
178	1.13	8.16	13.56	NAN	-1.61	-3.55
179	0.77	8.00	13.50	NAN	-1.62	-3.69
180	1.33	8.27	13.69	NAN	-1.61	-3.60
181	1.81	8.24	13.59	NAN	-1.60	-3.49
182	1.64	8.12	13.44	NAN	-1.60	-3.44
183	1.72	7.98	13.37	NAN	-1.61	-3.52
184	2.46	7.05	12.46	NAN	-1.61	-3.42
185	2.20	6.99	12.39	NAN	-1.61	-3.37
186	2.27	6.91	12.31	NAN	-1.61	-3.36
187	1.60	7.94	13.42	NAN	-1.62	-3.65
188	1.57	7.57	13.10	NAN	-1.63	-3.68
189	1.66	7.94	13.42	NAN	-1.62	-3.65
194	0.04	10.56	16.95	NAN	-1.65	-4.57
195	0.06	10.69	17.04	NAN	-1.65	-4.52
196	0.00	10.98	17.26	NAN	-1.64	-4.42
197	0.00	11.08	17.33	NAN	-1.63	-4.38
198	2.28	5.85	13.42	NAN	-1.61	-2.16
199	2.99	7.78	13.37	NAN	-1.63	-3.79
200	2.36	4.09	12.64	NAN	-1.64	-1.15
201	1.98	6.51	12.23	NAN	-1.91	-3.75

Appendix B
Velocity Profiles

The velocity profile plots presented here are the combination plots for both the section and flow line combination plots as described in Chapter 6. The Flowline plots are shown in the first row and the Section plots are shown in the second row for each model type and respected slope. Skew model velocity plots are shown in the last grouping. The profiles were created with a constant flow rate of 7.0 cfs and incipient motion of the sediment bed was not engaged.

Sediment Bed 0.003 Slope

Single 4” Circular Barrel

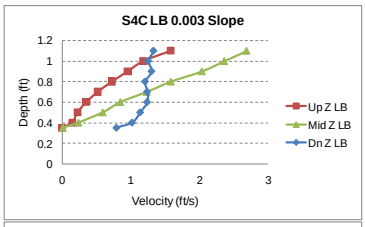

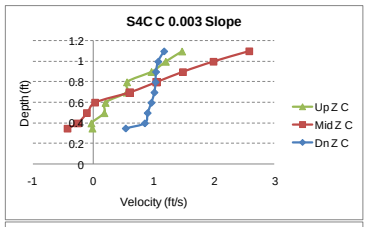

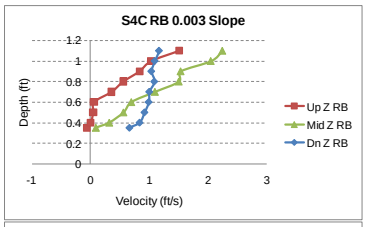

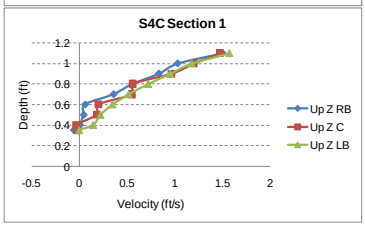

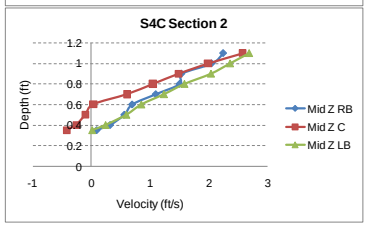

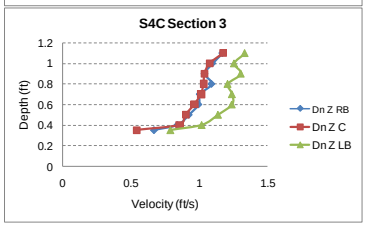

Single 6” Circular Barrel

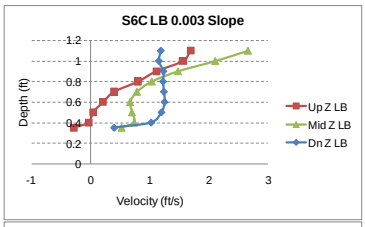

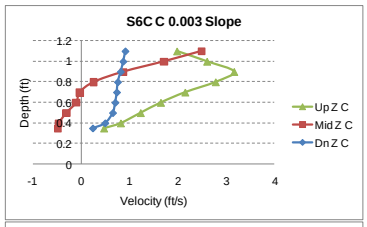

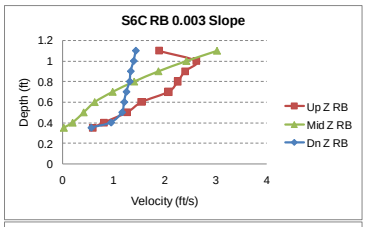

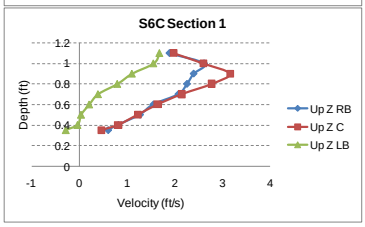

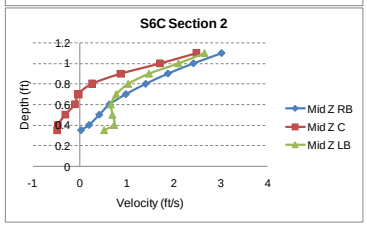

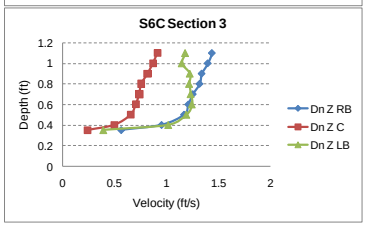

Multiple 4” Circular Barrel

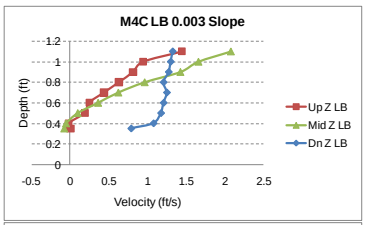

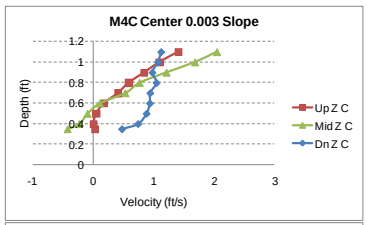

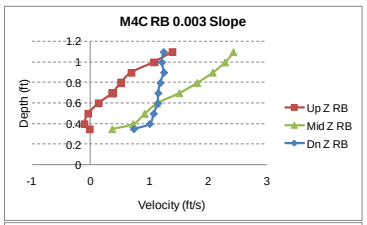

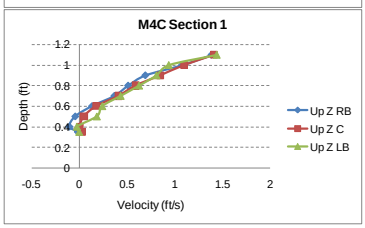

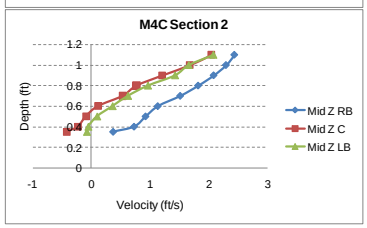

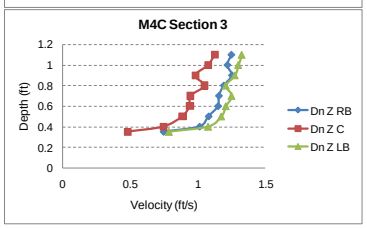

Single Rectangular Barrel

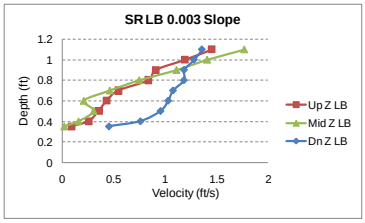

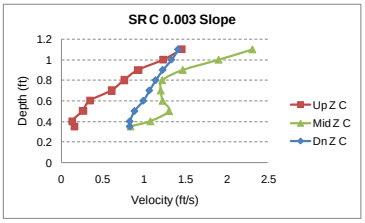

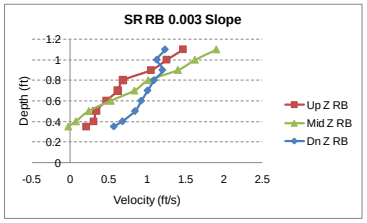

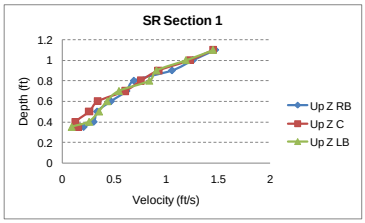

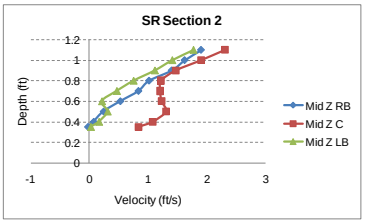

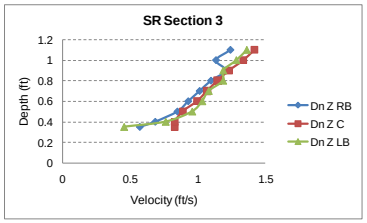

Staggered Barrel Circular (crowns matching)

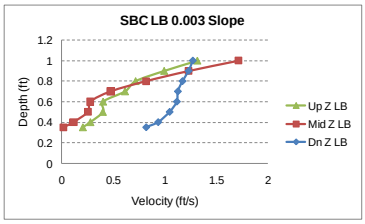

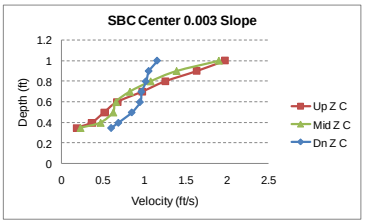

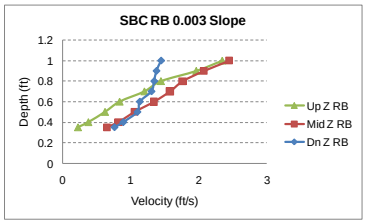

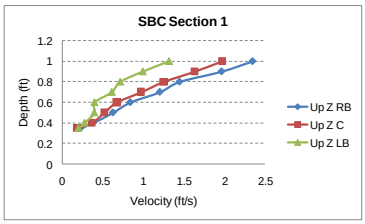

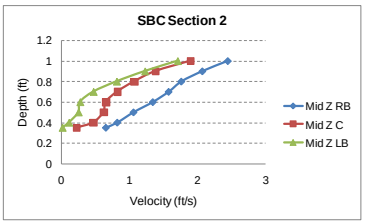

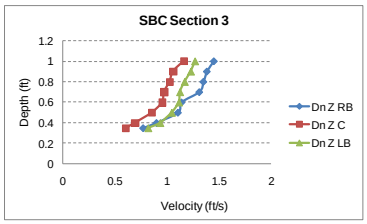

Multiple 6” Circular Barrel

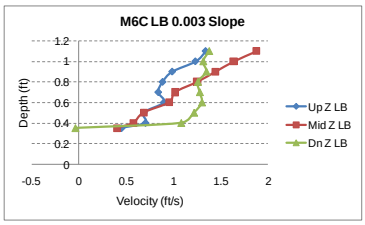

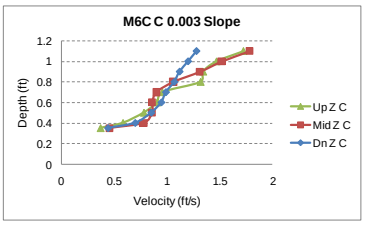

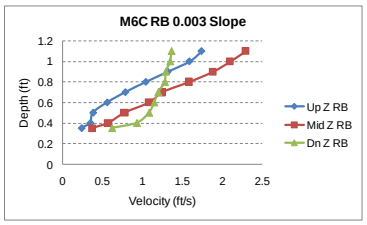

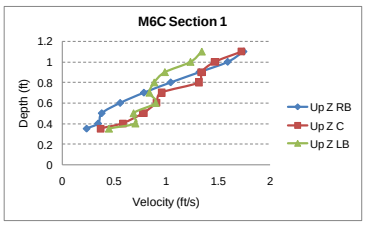

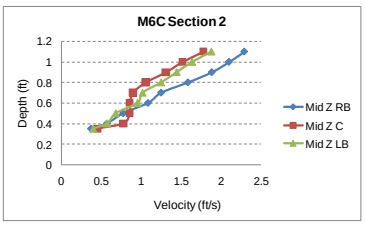

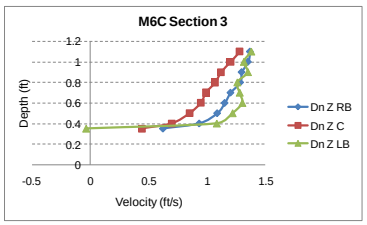

Multiple Rectangular Barrel

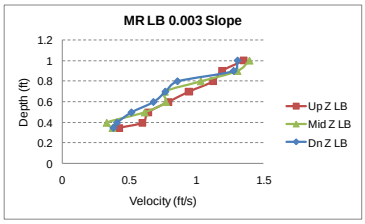

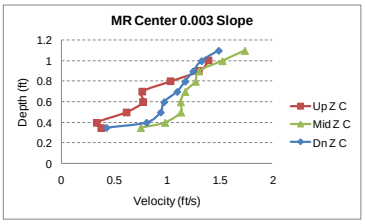

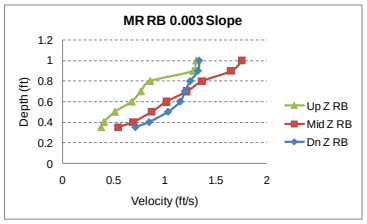

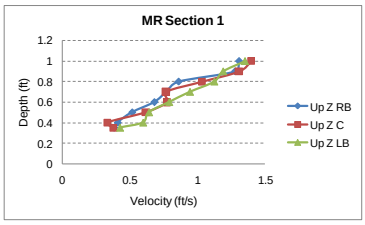

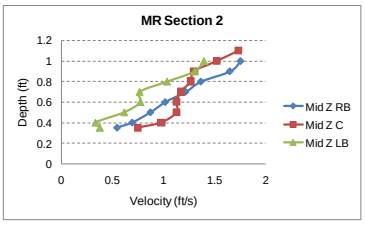

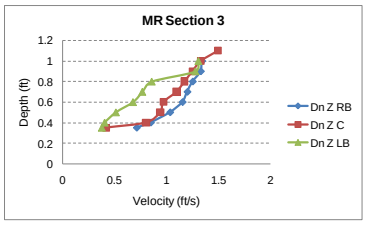

Sediment Bed 0.006 Slope

Single 6” Circular Barrel

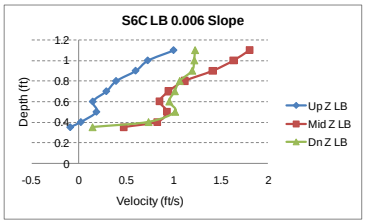

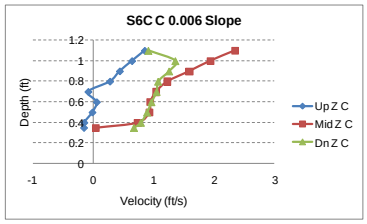

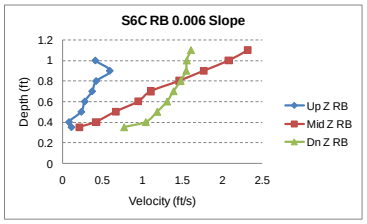

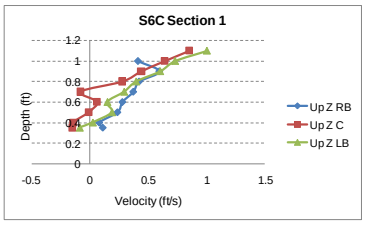

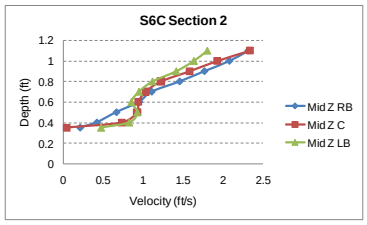

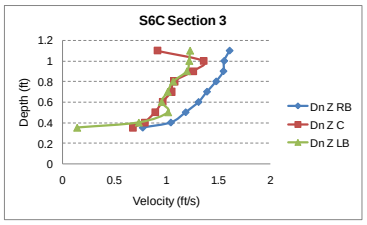

Single Rectangular Barrel

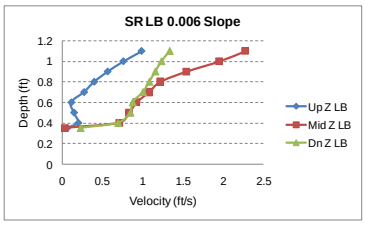

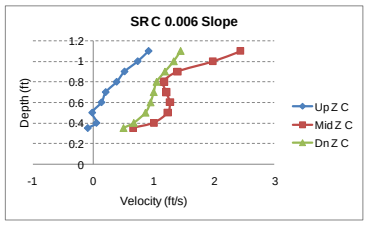

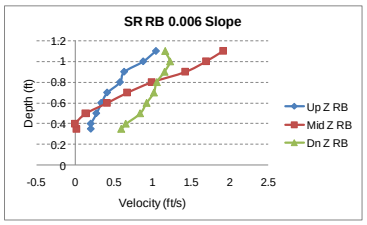

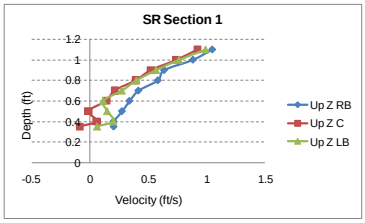

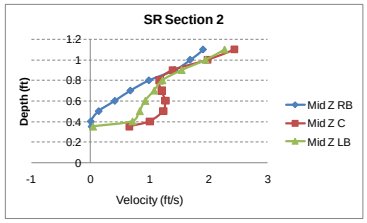

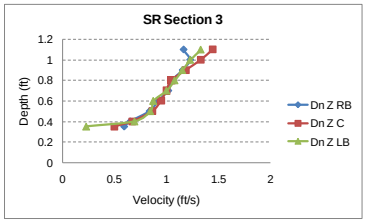

Multiple 6” Circular Barrel

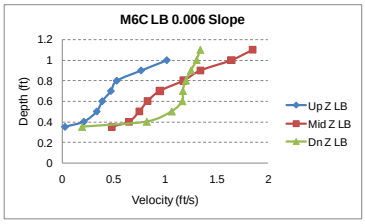

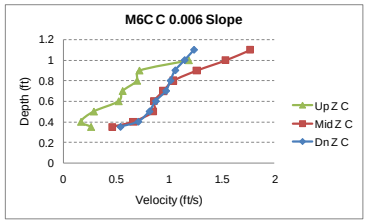

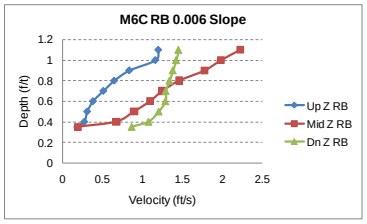

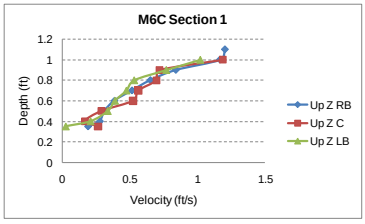

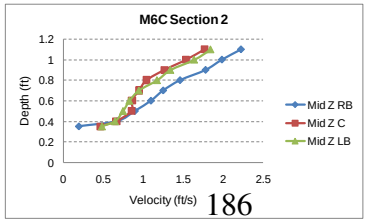

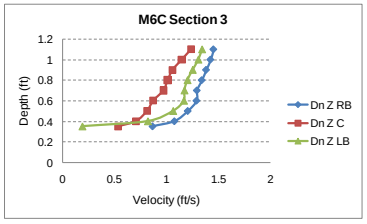

Multiple Rectangular Barrel

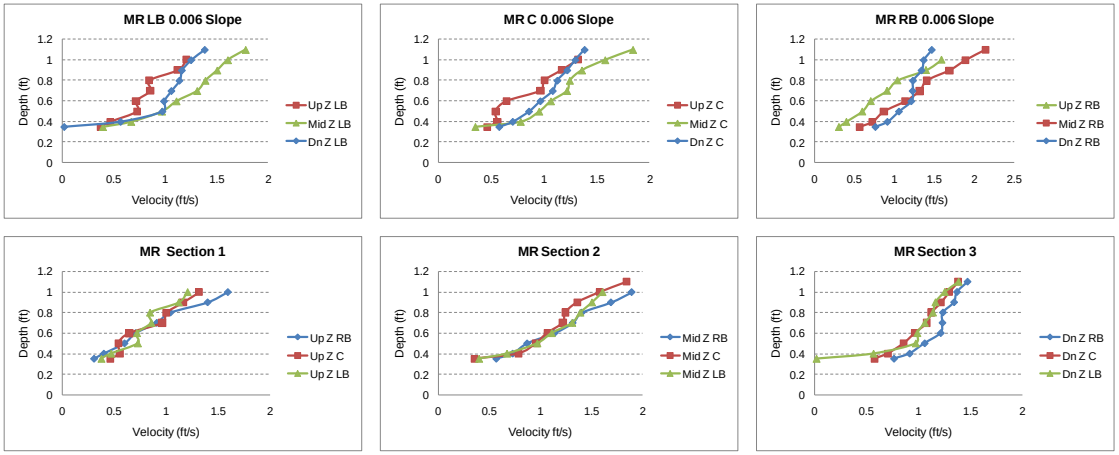

Sediment Bed 0.01 Slope

Single 4” Circular Barrel

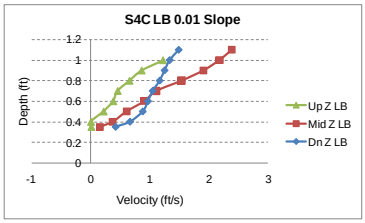

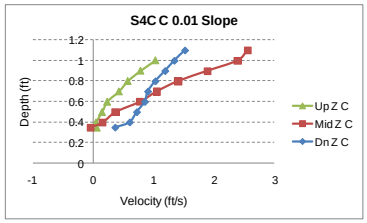

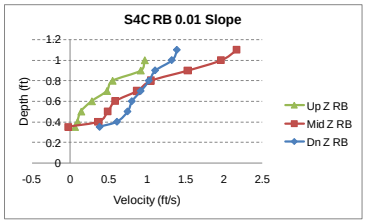

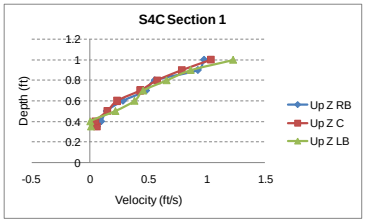

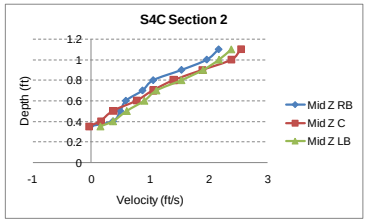

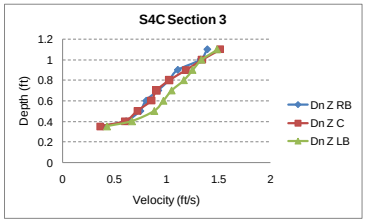

Single 6” Circular Barrel

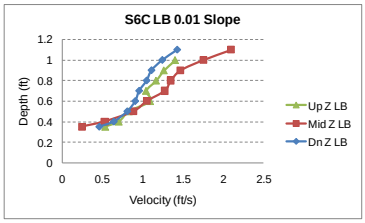

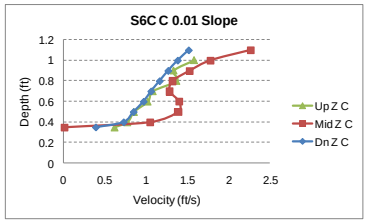

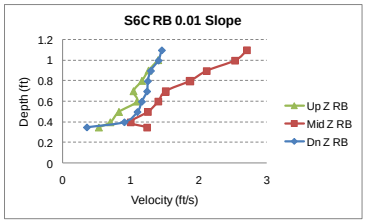

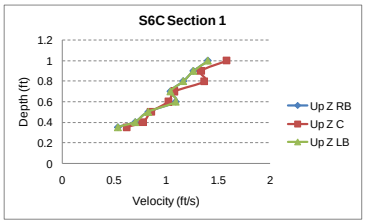

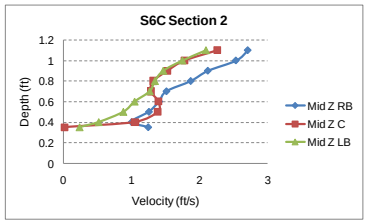

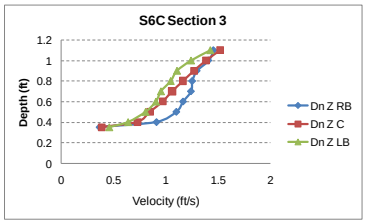

Multiple 4” Circular Barrel

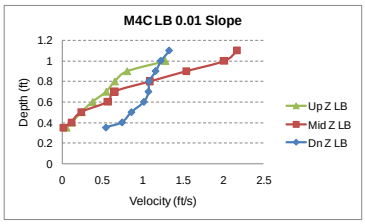

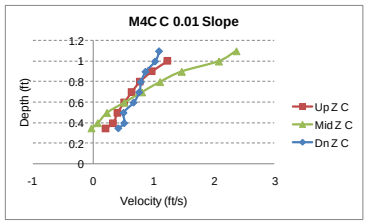

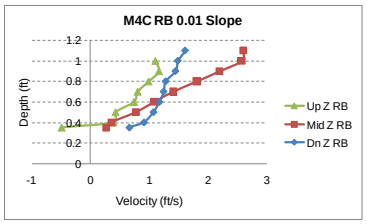

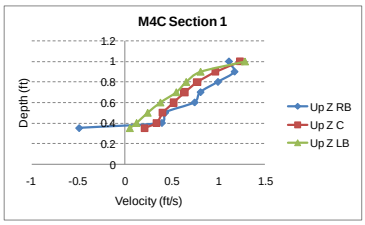

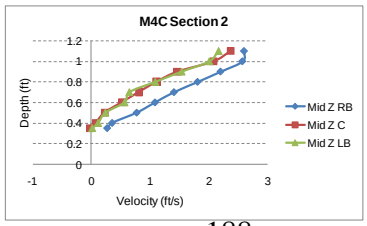

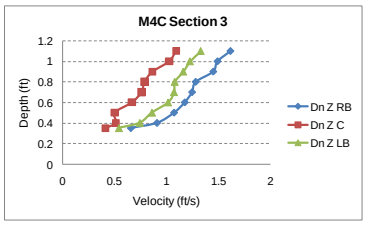

Single Rectangular Barrel

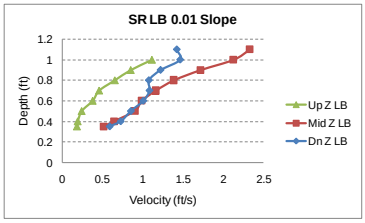

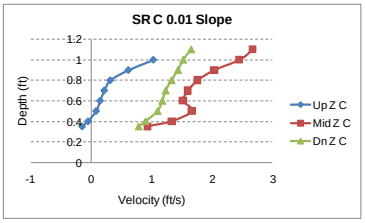

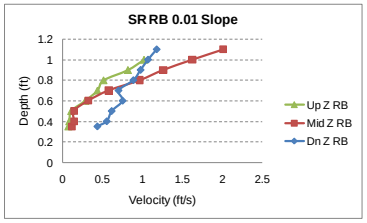

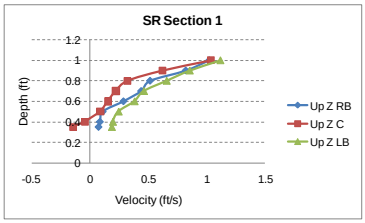

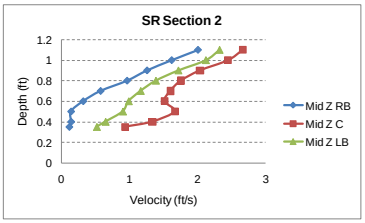

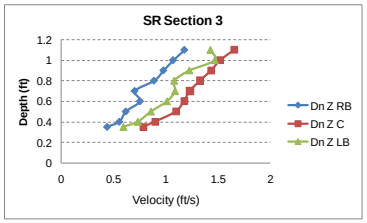

Staggered Barrel Circular (crowns matching)

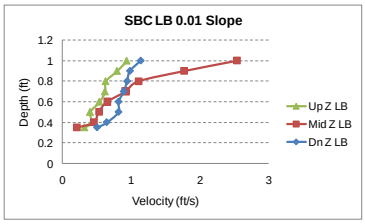

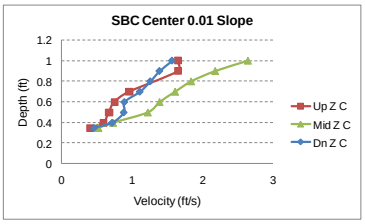

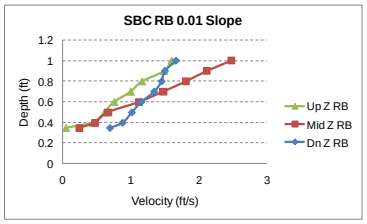

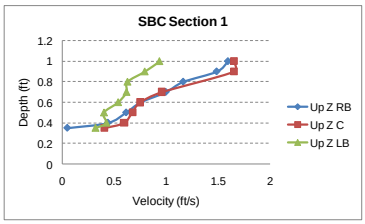

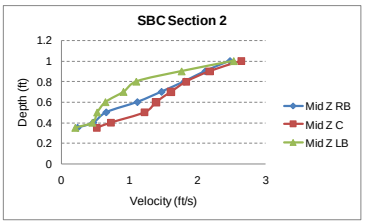

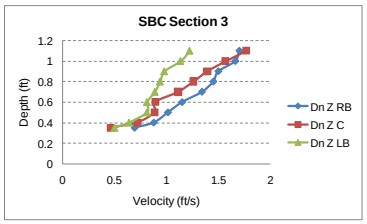

Staggered Barrel Circular (inverts matching)

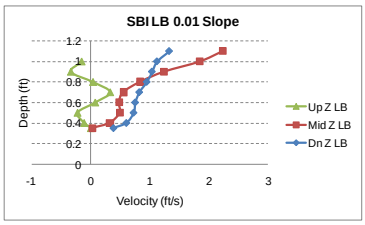

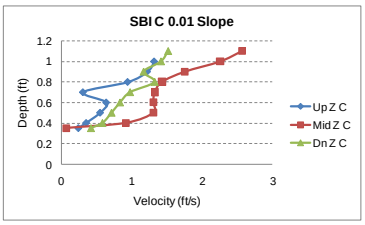

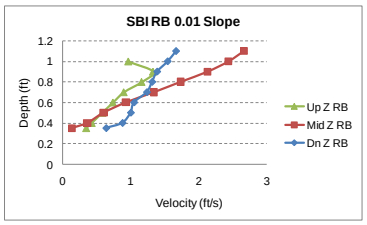

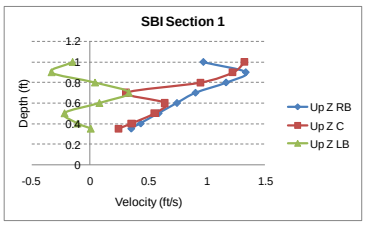

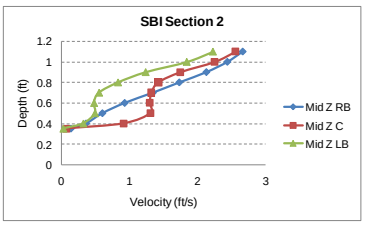

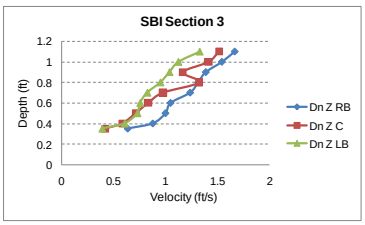

Multiple 6” Circular Barrel

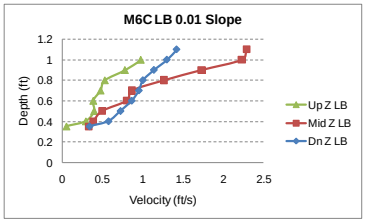

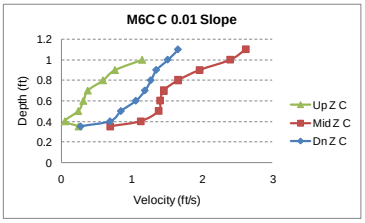

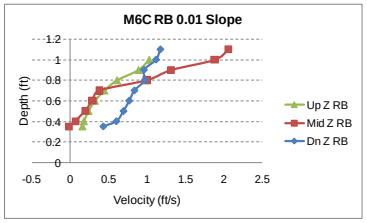

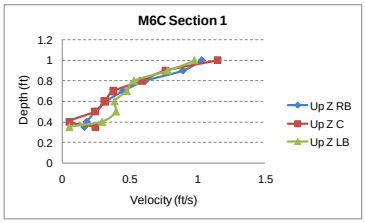

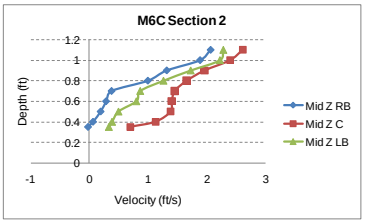

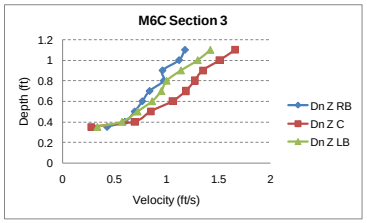

Mulitple Rectangular Barrel

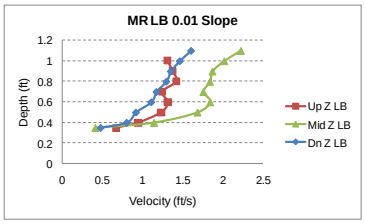

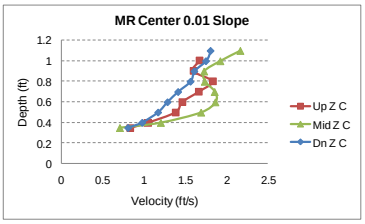

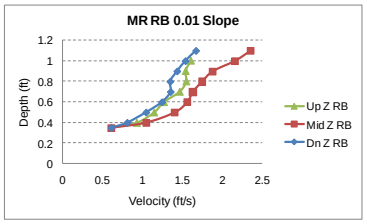

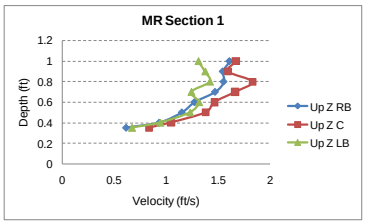

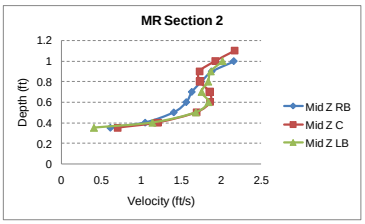

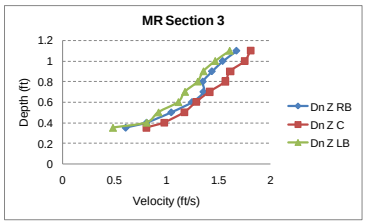

Sediment Bed Skew

Single 4” Circular Barrel

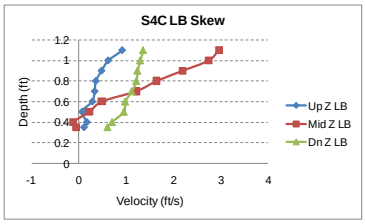

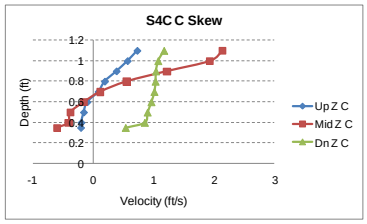

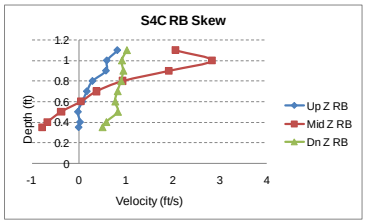

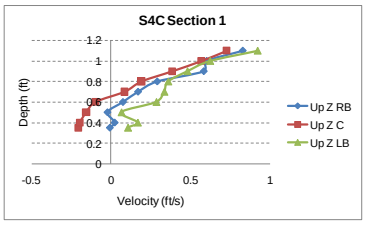

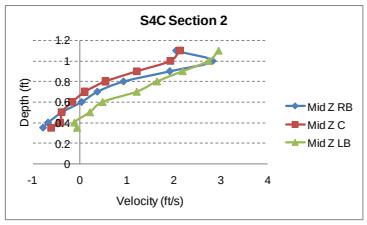

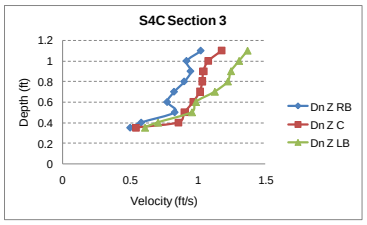

Single 6” Circular Barrel

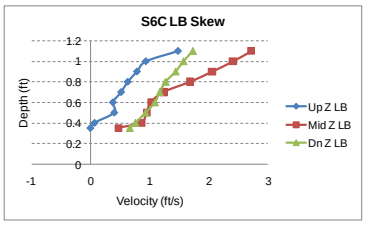

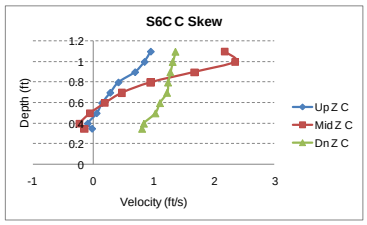

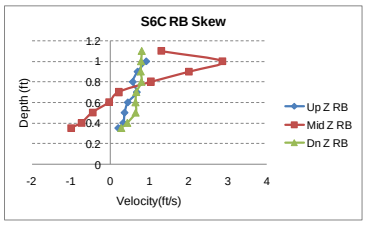

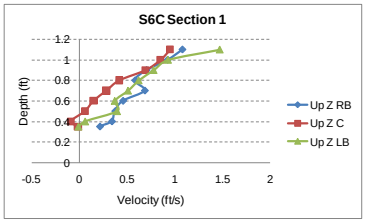

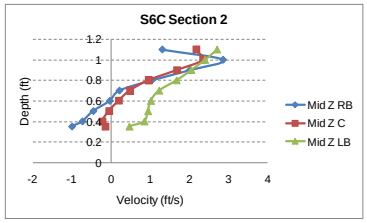

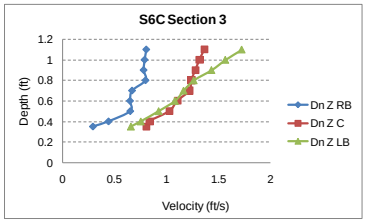

Multiple 4” Circular Barrel

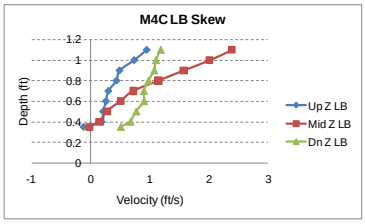

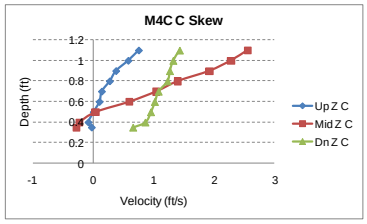

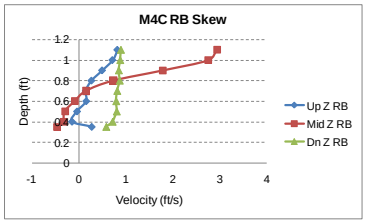

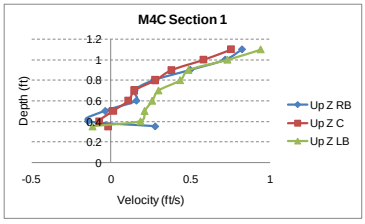

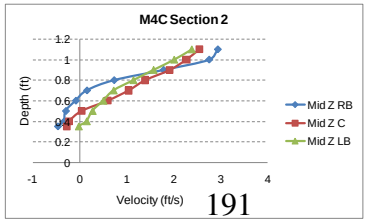

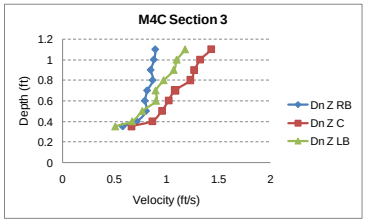

Single Rectangular Barrel

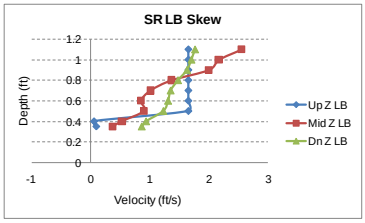

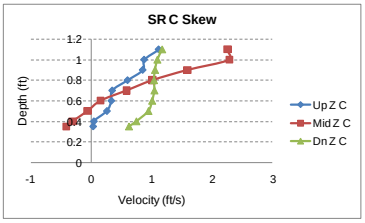

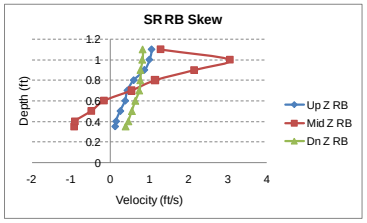

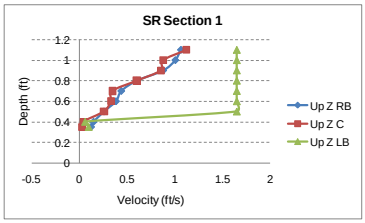

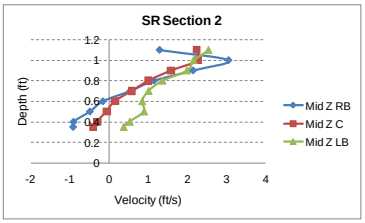

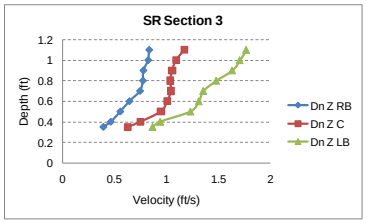

Staggered Barrel Circular (crowns matching)

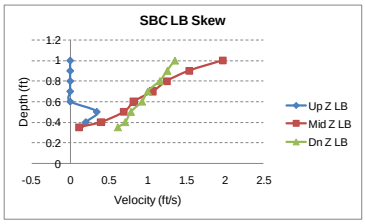

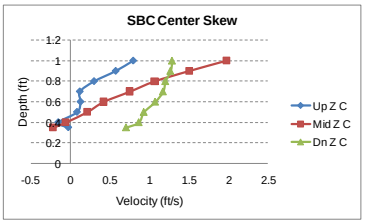

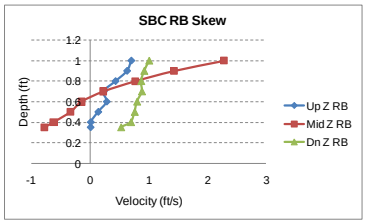

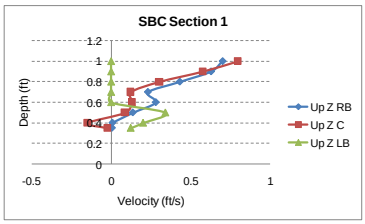

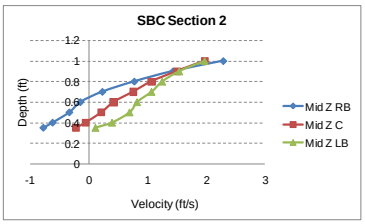

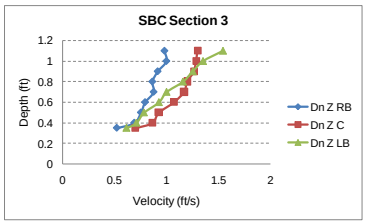

Multiple 6” Circular Barrel

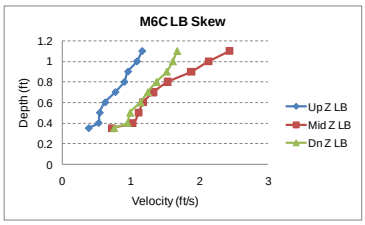

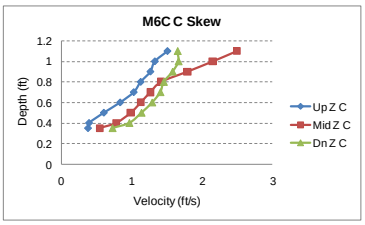

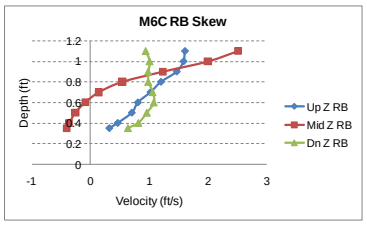

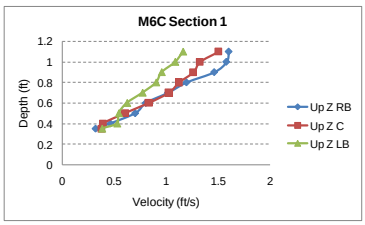

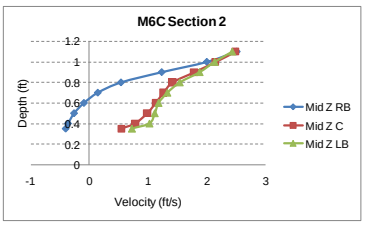

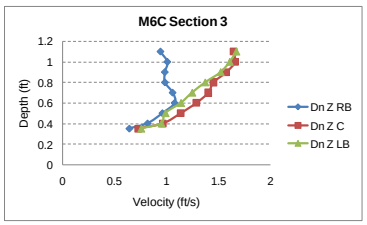

Multiple Rectangular Barrel

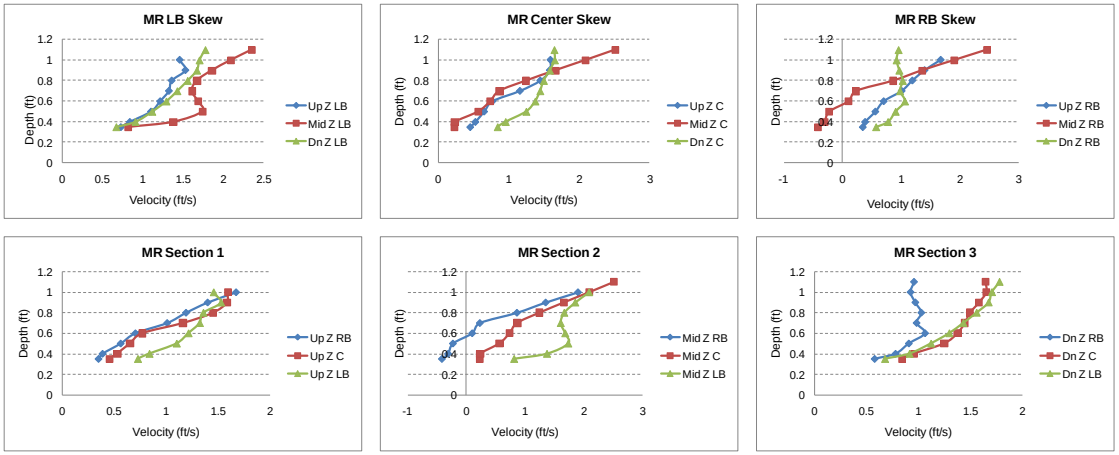

Appendix C
Culvert Models

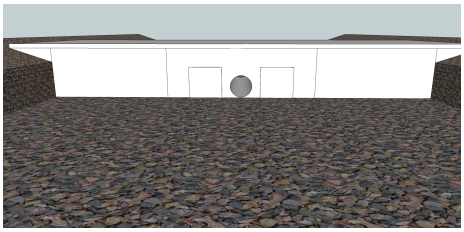

(a) Single 4 inch circular barrel

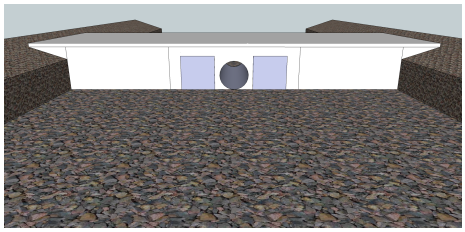

(b) Single 6 inch circular barrel

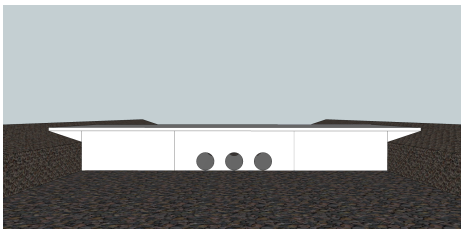

(c) Multiple 4 inch circular barrel

(d) Single Rectangular

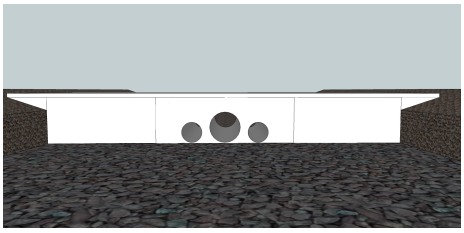

(e) Staggered Barrel (inverts matching)

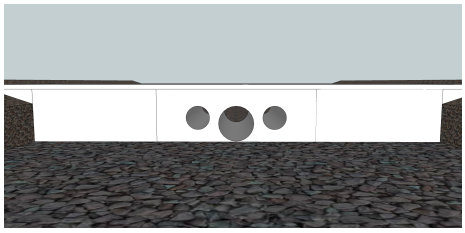

(f) Staggered Barrel (crowns matching)

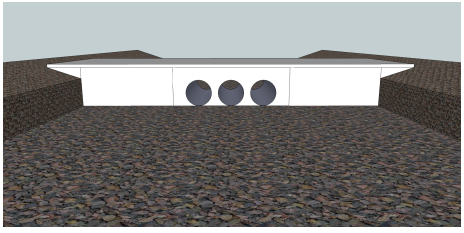

(g) Multiple 6 inch circular barrel

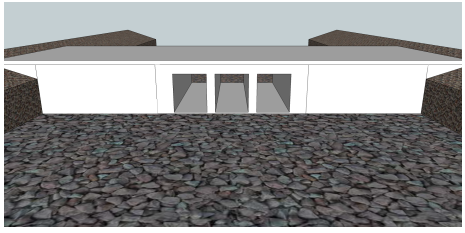

(h) Multiple Rectangular

Figure C.1. Culvert models tested in the experiments (*Dixon*, 2011)

Appendix D
Data Summary – Critical Values

Data shown herein are the time–average summary values calculated from the last 2–hrs of each experimental run. The last two hours of the experiments are considered to have reached steady state. Values shown are the authors interpretations of the critical values used in calculations for this research, many calculated values on the downstream side of the structure are not shown because they do not represent the interactions of the water flow and sediment movement with the culvert models.

Missing data are shown by $---$and means "Data not Collected" in the experiments. The velocity profile experiments are listed in order of performance along with the sediment transport experiments. The velocity profile experiments did not collect the same data; therefore, the velocity profile experiments are filled in as such. In addition, data collection methods by hand changed in the first 10 experiments and the electronic data collectors suffered a power loss which corrupted the first 30 days of data; therefore the data is represented as shown and a few experiments did not collect data as shown because of building power outages, or catastrophic model failures in the experimental channel. Lastly, some table locations present nr (Not Recorded) which are human mistakes in failing to record the physical measurements such as sediment transport volume data or water depth.

Expermental Hydraulic Data Part A

						Discharge					Section 1				Section 2		Section 3	
Date	**Exp. No.**	**Time**	**Model**	**Slope (ft/ft)**	**Position**	**Total (ft^3/s)**	**Culvert (ft^3/s)**	**Over the Road (ft^3/s)**	**Water Temp (°C)**	**Viscosity (ft^2/s) (10-5)**	**Depth (Nail) (ft)**	**Depth (Bubbler) (ft)**	**Area (Nail) (ft^2)**	**Area (Bubbler) (ft^2)**	**Depth (ft)**	**Area (ft^2)**	**Depth (ft)**	**Area (ft^2)**
16-Dec-10	VP		SB-I	0.003	P	—	—	—	18.7	1.09	—	—	—	—	—	—	—	—
20-Dec-10	1	3:29	SB-I	0.003	P	9.71	1.16	8.55	20.0	1.05	1.26	1.24	8.28	8.13	—	—	0.90	5.95
22-Dec-10	2	3:12	SB-I	0.003	P	13.89	0.97	12.92	18.7	1.09	—	—	—	—	—	—	—	—
28-Dec-10	3	1:36	SB-I	0.003	P	14.43	0.85	13.58	20.3	1.05	—	—	—	—	—	—	—	—
30-Dec-10	4	2:45	SB-I	0.003	P	14.95	0.64	14.31	20.7	1.04	—	—	—	—	—	—	—	—
4-Jan-11	5	2:11	SB-I	0.003	P	14.87	0.78	14.09	19.6	1.06	—	—	—	—	—	—	—	—
6-Jan-11	6	2:52	SB-C	0.003	P	14.97	1.07	13.90	19.2	1.07	—	—	—	—	—	—	—	—
7-Jan-11	7	3:19	SB-C	0.003	P	15.91	0.98	14.93	18.7	1.09	—	—	—	—	—	—	—	—
10-Jan-11	8	2:33	SB-C	0.003	P	15.20	0.99	14.22	19.5	1.07	—	—	—	—	—	—	—	—
18-Jan-11	9	3:06	SB-C	0.003	P	15.28	0.93	14.35	19.5	1.07	—	—	—	—	—	—	—	—
19-Jan-11	10	Special	SB-C	0.003	P	—	—	—	19.5	1.07	—	—	—	—	—	—	—	—
21-Jan-11	11	VP	SB-C	0.003	P	—	—	—	19.2	1.07	—	—	—	—	—	—	—	—
24-Jan-11	12	1:59	SB-I	0.003	P	14.65	0.90	13.75	18.7	1.09	1.56	1.64	10.62	11.22	1.17	8.79	1.26	8.76
25-Jan-11	13	2:23	M-4-C	0.003	P	14.86	0.72	14.14	19.5	1.07	1.55	1.63	10.56	11.14	1.17	8.78	1.26	8.73
27-Jan-11	14	2:15	M-4-C	0.003	P	14.86	0.67	14.19	19.0	1.08	1.53	1.59	10.36	10.89	1.19	8.92	1.26	8.73
28-Jan-11	15	2:28	M-4-C	0.003	P	14.89	0.72	14.18	19.0	1.08	1.56	1.63	10.60	11.18	1.15	8.57	1.27	8.81
31-Jan-11	16	VP	M-4-C	0.003	P	—	—	—	19.0	1.08	—	—	—	—	—	—	—	—
1-Feb-11	17	VP	S-4-C	0.003	P	—	—	—	19.0	1.08	—	—	—	—	—	—	—	—
5-Feb-11	18	2:43	S-4-C	0.003	P	15.20	0.28	14.93	17.7	1.12	1.58	1.65	10.75	11.36	1.14	8.56	1.27	8.85
7-Feb-11	19	2:31	S-4-C	0.003	P	15.28	0.24	15.04	17.2	1.13	1.58	1.66	10.78	11.41	1.16	8.71	1.29	9.01
10-Feb-11	20	2:20	S-4-C	0.003	P	15.20	0.27	14.94	16.8	1.14	1.59	1.68	10.88	11.54	1.15	8.61	1.28	8.88
11-Feb-11	21	VP	M-6-C	0.003	P	—	—	—	16.5	1.15	—	—	—	—	—	—	—	—
12-Feb-11	22	VP	S-6-C	0.003	P	—	—	—	18.0	1.11	—	—	—	—	—	—	—	—
14-Feb-11	23	3:10	S-6-C	0.003	P	15.03	0.57	14.46	17.7	1.12	1.59	1.67	10.85	11.48	1.16	8.68	1.27	8.80
15-Feb-11	24	2:54	S-6-C	0.003	P	15.03	0.41	14.62	18.0	1.11	1.59	1.68	10.86	11.54	1.17	8.74	1.27	8.84
16-Feb-11	25	3:20	S-6-C	0.003	P	15.03	0.49	14.54	18.7	1.09	1.57	1.65	10.67	11.29	1.14	8.53	1.25	8.71
17-Feb-11	26	2:45	M-6-C	0.003	P	14.97	1.01	13.96	18.2	1.10	1.51	1.58	10.24	10.75	1.15	8.57	1.24	8.58
18-Feb-11	27	2:10	M-6-C	0.003	P	14.79	1.23	13.56	18.3	1.10	1.56	1.63	10.60	11.18	1.20	8.96	1.27	8.82
19-Feb-11	28	2:16	M-6-C	0.003	P	14.79	1.41	13.38	19.0	1.08	1.53	1.60	10.39	10.94	1.16	8.66	1.23	8.52
21-Feb-11	29	2:26	M-R	0.003	P	14.62	1.76	12.86	19.3	1.07	1.54	1.61	10.47	11.04	1.20	8.97	1.26	8.72
22-Feb-11	30	2:26	M-R	0.003	P	14.62	1.98	12.64	19.7	1.06	1.53	1.59	10.36	10.89	1.21	9.04	1.27	8.80
23-Feb-11	31	2:34	M-R	0.003	P	14.67	0.84	13.83	19.5	1.07	1.50	1.57	10.16	10.67	1.19	8.90	1.23	8.50
24-Feb-11	32	2:42	S-R	0.003	P	15.17	1.01	14.15	19.2	1.07	1.58	1.66	10.77	11.42	1.18	8.80	1.25	8.69
25-Feb-11	33	2:27	S-R	0.003	P	15.19	1.02	14.17	18.6	1.09	1.62	1.70	11.05	11.74	1.20	9.02	1.29	8.95
28-Feb-11	34	2:24	S-R	0.003	P	15.11	0.76	14.34	19.2	1.07	1.59	1.68	10.88	11.54	1.20	9.00	1.28	8.92
1-Mar-11	35	VP	S-R	0.003	P	—	—	—	19.5	1.07	—	—	—	—	—	—	—	—
2-Mar-11	36	VP	M-R	0.003	P	—	—	—	19.5	1.07	—	—	—	—	—	—	—	—
Change Slopes																		
5-Mar-11	37	VP	M-R	0.01	P	—	—	—	19.5	1.07	—	—	—	—	—	—	—	—
7-Mar-11	37B	VP	S-R	0.01	P	—	—	—	17.3	1.13	—	—	—	—	—	—	—	—
9-Mar-11	38	2:34	S-R	0.01	P	14.74	1.32	13.42	17.2	1.13	1.54	1.62	10.50	11.09	1.14	8.04	1.20	8.31
10-Mar-11	39	2:18	S-R	0.01	P	14.97	1.33	13.65	19.2	1.07	1.57	1.62	10.67	11.06	1.17	8.29	1.23	8.51
21-Mar-11	40	2:27	S-R	0.01	P	15.11	1.48	13.62	19.0	1.08	1.58	1.64	10.80	11.22	1.14	8.00	1.26	8.75
22-Mar-11	41	2:38	M-R	0.01	P	15.11	3.05	12.06	20.0	1.05	1.55	1.56	10.53	10.60	1.17	8.23	1.27	8.80
23-Mar-11	42	2:12	M-R	0.01	P	14.97	3.67	11.30	19.5	1.07	1.50	1.56	10.19	10.65	1.14	8.06	1.24	8.57
24-Mar-11	43	2:16	M-R	0.01	P	15.01	3.27	11.73	19.7	1.06	1.50	1.56	10.14	10.60	1.13	7.97	1.23	8.51
25-Mar-11	44	2:10	M-6-C	0.01	P	15.11	2.42	12.69	19.7	1.06	1.54	1.58	10.50	10.79	1.22	8.63	1.25	8.69

Expermental Hydraulic Data Part A

Date	Exp. No.	Time	Model	Slope (ft/ft)	Position	Total (ft^3/s)	Culvert (ft^3/s)	Over the Road (ft^3/s)	Water Temp (°C)	Viscosity (ft^2/s) (10-5)	Depth (Nail) (ft)	Depth (Bubbler) (ft)	Area (Nail) (ft^2)	Area (Bubbler) (ft^2)	Depth (ft)	Area (ft^2)	Depth (ft)	Area (ft^2)
28-Mar-11	45	2:12	M-6-C	0.01	P	15.11	2.51	12.60	19.3	1.07	1.56	1.59	10.60	10.85	1.20	8.54	1.25	8.69
29-Mar-11	46	2:13	M-6-C	0.01	p	15.14	2.33	12.81	20.5	1.04	1.55	1.59	10.54	10.83	1.16	8.16	1.27	8.85
30-Mar-11	47	2:15	S-6-C	0.01	P	15.09	0.92	14.17	20.5	1.04	1.57	1.64	10.68	11.25	1.13	7.98	1.24	8.58
31-Mar-11	48	2:15	S-6-C	0.01	P	15.11	0.93	14.18	19.8	1.06	1.55	1.64	10.51	11.21	1.14	8.03	1.22	8.42
1-Apr-11	49	2:14	S-6-C	0.01	P	15.04	0.92	14.11	19.2	1.07	1.59	1.64	10.86	11.24	1.17	8.23	1.25	8.64
2-Apr-11	50	VP	S-6-C	0.01	P	—	—	—	19.2	1.07	—	—	—	—	—	—	—	—
2-Apr-11	51	VP	M-6-C	0.01	P	—	—	—	19.2	1.07	—	—	—	—	—	—	—	—
6-Apr-11	52	1:56	M-4-C	0.01	P	14.54	1.04	13.50	20.2	1.05	1.53	1.59	10.38	10.86	1.14	8.01	1.19	8.23
7-Apr-11	53	2:01	M-4-C	0.01	P	14.65	0.92	13.73	20.1	1.05	1.53	1.58	10.37	10.81	1.11	7.77	1.24	8.62
8-Apr-11	54	2:07	M-4-C	0.01	P	15.21	1.01	14.20	20.1	1.05	1.58	1.63	10.76	11.13	1.17	8.26	1.26	8.72
11-Apr-11	55	2:07	S-4-C	0.01	P	15.18	0.37	14.80	20.1	1.05	1.60	1.65	10.93	11.34	1.15	8.08	1.26	8.76
12-Apr-11	56	2:14	S-4-C	0.01	P	15.21	0.36	14.85	20.1	1.05	1.58	1.64	10.81	11.26	1.09	7.68	1.24	8.58
13-Apr-11	57	2:21	S-4-C	0.01	P	15.01	0.34	14.66	20.1	1.05	1.56	1.64	10.64	11.24	1.17	8.28	1.25	8.64
14-Apr-11	58	VP	S-4-C	0.01	P	—	—	—	20.1	1.05	—	—	—	—	—	—	—	—
14-Apr-11	59	VP	M-4-C	0.01	P	—	—	—	20.1	1.05	—	—	—	—	—	—	—	—
18-Apr-11	60	2:14	SB-I	0.01	P	15.45	1.46	13.98	19.2	1.07	1.57	1.61	10.69	11.00	1.18	8.35	1.26	8.79
19-Apr-11	61	2:13	SB-I	0.01	P	15.48	1.53	13.95	20.2	1.05	1.49	1.59	10.11	10.85	1.24	8.78	1.26	8.75
20-Apr-11	62	2:18	SB-I	0.01	P	14.89	1.39	13.51	20.2	1.05	1.52	1.58	10.29	10.81	1.15	8.12	1.22	8.42
21-Apr-11	63	VP	SB-I	0.01	P	—	—	—	20.2	1.05	—	—	—	—	—	—	—	—
22-Apr-11	64	VP	SB-C	0.01	P	—	—	—	20.7	1.04	—	—	—	—	—	—	—	—
25-Apr-11	65	2:18	SB-C	0.01	P	15.00	1.59	13.42	20.7	1.04	1.54	1.58	10.48	10.78	1.24	8.81	1.26	8.79
26-Apr-11	66	2:22	SB-C	0.01	P	15.07	1.62	13.46	20.1	1.05	1.55	1.58	10.54	10.80	1.18	8.31	1.25	8.64
29-Apr-11	67	2:24	SB-C	0.01	P	15.00	1.53	13.47	19.8	1.06	1.54	1.58	10.44	10.79	1.19	8.46	1.27	8.84
2-May-11	68	2:24	M-6-C	0.01	P	15.18	1.77	13.41	18.8	1.09	1.53	1.57	10.38	10.68	1.21	8.56	1.26	8.72
3-May-11	69	2:20	S-6-C	0.01	P	15.15	0.89	14.26	18.7	1.09	1.55	1.61	10.51	11.01	1.15	8.12	1.20	8.27
Change Slope																		
4-May-11	70	2:30	S-6-C	0.006	P	14.89	0.70	14.20	18.7	1.09	1.52	1.60	10.33	10.96	1.22	8.63	1.24	8.64
10-May-11	71	2:19	S-6-C	0.006	P	14.73	0.69	14.04	21.7	1.01	1.55	1.61	10.58	10.98	1.28	9.15	1.26	8.73
11-May-11	72	2:43	S-6-C	0.006	P	14.76	0.71	14.05	22.1	1.00	1.54	1.60	10.48	10.94	1.22	8.67	1.24	8.61
12-May-11	73	2:26	M-6-C	0.006	P	14.77	1.06	13.71	21.0	1.03	1.51	1.59	10.25	10.82	1.19	8.45	1.26	8.74
13-May-11	74	2:24	M-6-C	0.006	P	15.06	0.93	14.13	20.7	1.03	1.53	1.60	10.40	10.90	1.21	8.58	1.26	8.75
14-May-11	75	1:59	M-6-C	0.006	P	14.53	0.87	13.66	20.0	1.05	1.52	1.56	10.27	10.63	1.15	8.14	1.22	8.46
16-May-11	76	VP	M-6-C	0.006	P	—	—	—	20.2	1.05	—	—	—	—	—	—	—	—
16-May-11	77	VP	S-6-R	0.006	P	—	—	—	20.2	1.05	—	—	—	—	—	—	—	—
16-May-11	78	1:27	M-R	0.006	P	14.30	2.41	11.89	20.2	1.05	1.47	1.53	9.94	10.39	1.15	8.08	1.24	8.56
17-May-11	79	2:21	M-R	0.006	P	14.77	2.11	12.66	20.2	1.05	1.52	1.57	10.32	10.73	1.20	8.52	1.25	8.71
18-May-11	80	2:07	M-R	0.006	P	15.46	1.40	14.05	20.7	1.03	1.55	1.61	10.51	10.98	1.21	8.62	1.28	8.95
18-May-11	81	VP	M-R	0.006	P	—	—	—	22.5	0.99	—	—	—	—	—	—	—	—
18-May-11	82A	VP	S-R	0.006	P	—	—	—	22.5	0.99	—	—	—	—	—	—	—	—
19-May-11	82	2:19	S-R	0.006	P	14.87	1.02	13.85	21.5	1.01	1.56	1.60	10.59	10.92	1.19	8.45	1.25	8.70
20-May-11	83	2:20	S-R	0.006	P	14.50	1.01	13.48	21.7	1.01	1.48	1.57	10.03	10.68	1.13	7.94	1.21	8.37
21-May-11	84	2:37	S-R	0.006	P	14.57	1.02	13.55	21.2	1.02	1.50	1.58	10.16	10.75	1.13	7.94	1.24	8.63
23-May-11	85	2:22	SB-C	0.006	P	14.53	1.17	13.36	22.3	0.99	1.51	1.59	10.26	10.83	1.17	8.28	1.23	8.55
24-May-11	86	2:20	SB-C	0.006	P	15.11	0.99	14.12	22.3	0.99	1.52	1.61	10.28	11.01	1.17	8.25	1.25	8.65
25-May-11	87	2:24	SB-C	0.006	P	15.31	1.02	14.29	22.5	0.99	1.50	1.60	10.12	10.95	1.18	8.33	1.24	8.56
26-May-11	88	VP	SB-C	0.006	P	—	—	—										
Large Grain Skew Model																		
27-May-11	89	TRIAL	M-R	0.006	S	—	—	—	22.0	1.01	—	—	—	—	—	—	—	—

Expermental Hydraulic Data Part A

Date	Exp. No.	Time	Model	Slope (ft/ft)	Position	Total (ft^3/s)	Culvert (ft^3/s)	Over the Road (ft^3/s)	Water Temp (°C)	Viscosity (ft^2/s) (10-5)	Depth (Nail) (ft)	Depth (Bubbler) (ft)	Area (Nail) (ft^2)	Area (Bubbler) (ft^2)	Depth (ft)	Area (ft^2)	Depth (ft)	Area (ft^2)
27-May-11	90	TRIAL	M-R	0.006	S	—	—	—	22.0	1.01	—	—	—	—	—	—	—	—
31-May-11	91	1:47	M-R	0.006	S	14.74	1.65	13.09	23.5	0.97	1.51	1.57	10.26	10.67	1.12	7.92	1.25	8.69
1-Jun-11	92	2:19	M-R	0.006	S	14.77	2.33	12.44	24.2	0.96	1.49	1.60	10.06	10.94	1.09	7.65	1.22	8.41
2-Jun-11	93	1:41	M-R	0.006	S	14.93	2.36	12.58	24.0	0.96	1.53	1.59	10.38	10.84	1.14	8.02	1.29	8.96
6-Jun-11	94	2:11	S-R	0.006	S	14.74	1.09	13.65	23.7	0.97	1.54	1.59	10.48	10.89	1.02	7.13	1.23	8.52
6-Jun-11	95	2:05	S-R	0.006	S	14.57	1.08	13.49	24.0	0.96	1.51	1.60	10.25	10.93	1.01	7.01	1.23	8.49
7-Jun-11	96	2:20	S-R	0.006	S	14.74	0.90	13.84	23.5	0.97	1.49	1.61	10.06	11.00	1.12	7.91	1.25	8.67
7-Jun-11	97	VP	S-R	0.006	S	—	—	—	23.5	0.97	—	—	—	—	—	—	—	—
7-Jun-11	98	VP	M-R	0.006	S	—	—	—	23.5	0.97	—	—	—	—	—	—	—	—
8-Jun-11	99	VP	M-6-C	0.006	S	—	—	—	23.5	0.97	—	—	—	—	—	—	—	—
8-Jun-11	100	VP	S-6-C	0.006	S	—	—	—	23.5	0.97	—	—	—	—	—	—	—	—
8-Jun-11	101	2:35	S-6-C	0.006	S	14.64	0.68	13.96	23.5	0.97	1.48	1.61	10.02	10.99	0.98	6.76	1.19	8.22
9-Jun-11	102	2:36	S-6-C	0.006	S	15.18	0.67	14.52	24.6	0.95	1.56	1.64	10.62	11.21	1.03	7.15	1.23	8.52
9-Jun-11	103	2:06	M-6-C	0.006	S	14.53	1.61	12.93	24.6	0.95	1.51	1.57	10.22	10.71	1.11	7.79	1.25	8.66
10-Jun-11	104	1:58	M-6-C	0.006	S	14.97	1.44	13.53	25.0	0.94	1.53	1.60	10.42	10.95	1.11	7.82	1.25	8.69
10-Jun-11	105	2:26	M-6-C	0.006	S	14.66	1.60	13.06	25.2	0.93	1.51	1.59	10.25	10.86	1.07	7.49	1.21	8.39
13-Jun-11	106	2:43	SB-C	0.006	S	14.91	0.93	13.98	25.0	0.94	1.51	1.57	10.22	10.72	1.05	7.37	1.21	8.35
13-Jun-11	107	2:24	SB-C	0.006	S	14.97	0.74	14.23	25.2	0.93	1.54	1.63	10.47	11.13	1.06	7.44	1.26	8.78
14-Jun-11	108	2:28	SB-C	0.006	S	15.03	0.74	14.29	25.0	0.94	1.56	1.61	10.59	11.01	1.10	7.72	1.27	8.87
14-Jun-11	109	2:43	SB-C	0.006	S	14.60	0.67	13.93	25.0	0.94	1.49	1.60	10.07	10.96	1.05	7.34	1.23	8.52
15-Jun-11	110	VP	SB-C	0.006	S	—	—	—	25.1	0.94	—	—	—	—	—	—	—	—
16-Jun-11	111	VP	M-4-C	0.006	S	—	—	—	25.7	0.92	—	—	—	—	—	—	—	—
16-Jun-11	112	VP	S-4-C	0.006	S	—	—	—	25.7	0.92	—	—	—	—	—	—	—	—
16-Jun-11	113	2:22	S-4-C	0.006	S	14.40	0.32	14.07	25.7	0.92	1.54	1.63	10.43	11.19	0.96	6.62	1.23	8.50
17-Jun-11	114	3:29	S-4-C	0.006	S	14.84	0.32	14.52	25.2	0.93	1.57	1.65	10.70	11.31	1.00	6.94	1.23	8.49
20-Jun-11	115	2:21	M-4-C	0.006	S	14.84	0.89	13.94	25.5	0.93	1.53	1.61	10.42	11.03	1.03	7.18	1.24	8.57
21-Jun-11	116	2:20	M-4-C	0.006	S	15.01	0.91	14.10	25.6	0.92	1.52	1.62	10.30	11.08	1.11	7.80	1.23	8.51
22-Jun-11	117	2:18	M-4-C	0.006	S	14.93	0.92	14.00	25.6	0.92	1.54	1.62	10.47	11.08	1.04	7.29	1.23	8.55
Start Small Grain Small Grain Skew Model																		
5-Jul-11	118	1:45	M-4-C	0.006	S	12.00	0.92	11.08	27.5	0.89	1.46	1.53	9.83	10.38	0.96	6.62	1.14	7.81
6-Jul-11	119	2:15	M-4-C	0.006	S	11.80	0.93	10.87	27.5	0.89	1.42	1.53	9.53	10.38	0.96	6.65	1.15	7.90
6-Jul-11	120	2:16	M-4-C	0.006	S	11.69	0.92	10.78	27.5	0.89	1.48	1.51	9.97	10.25	0.97	6.70	1.13	7.73
7-Jul-11	121	1:54	S-4-C	0.006	S	11.48	0.33	11.15	27.3	0.89	1.44	1.54	9.71	10.43	0.91	6.25	1.13	7.73
7-Jul-11	122	1:47	S-4-C	0.006	S	12.00	0.33	11.67	27.2	0.89	1.49	1.55	10.10	10.52	0.94	6.44	13.18	101.72
8-Jul-11	123	1:34	S-4-C	0.006	S	12.21	0.34	11.88	27.5	0.89	1.49	1.58	10.04	10.81	0.91	6.26	1.17	8.06
11-Jul-11	124	SP VP	M-6-C	0.006	S	—	—	—	28.2	0.87	—	—	—	—	—	—	—	—
11-Jul-11	125	1:48	M-6-C	0.006	S	11.96	1.76	10.20	28.2	0.87	1.39	1.48	9.32	10.01	1.01	7.00	1.15	7.90
12-Jul-11	126	1:50	M-6-C	0.006	S	11.88	1.76	10.11	28.8	0.86	1.42	1.48	9.49	9.97	1.02	7.06	1.16	7.94
12-Jun-11	127	1:49	M-6-C	0.006	S	11.75	1.76	10.00	28.7	0.86	1.42	1.47	9.52	9.95	1.00	6.96	1.16	7.94
13-Jul-11	128	1:46	S-6-C	0.006	S	11.80	0.74	11.06	28.6	0.87	1.44	1.53	9.68	10.35	0.97	6.68	1.17	8.03
13-Jul-11	129	1:48	S-6-C	0.006	S	11.59	0.73	10.86	28.6	0.87	1.48	1.52	9.99	10.29	0.95	6.57	1.13	7.77
14-Jul-11	130	1:52	S-6-C	0.006	S	11.67	0.74	10.93	28.6	0.87	1.47	1.52	9.90	10.33	0.95	6.59	1.17	8.02
14-Jul-11	131	1:47	SB-C	0.006	S	11.76	1.21	10.55	28.2	0.87	1.44	1.49	9.71	10.04	0.99	6.90	1.14	7.81
15-Jul-11	132	2:22	SB-C	0.006	S	12.08	1.24	10.84	28.2	0.87	1.44	1.51	9.70	10.26	0.96	6.67	1.15	7.88
15-Jul-11	133	2:47	SB-C	0.006	S	12.05	1.24	10.81	28.2	0.87	1.43	1.51	9.61	10.25	0.98	6.80	1.16	7.99
16-Jul-11	134	2:16	SB-C	0.006	S	12.01	1.26	10.75	28.2	0.87	1.44	1.52	9.69	10.30	1.01	7.04	1.18	8.10
18-Jul-11	135	1:41	M-R	0.006	S	11.67	2.38	9.29	28.6	0.87	1.39	1.47	9.27	9.88	1.01	7.04	1.14	7.78

Expermental Hydraulic Data Part A

Date	Exp. No.	Time	Model	Slope (ft/ft)	Position	Total (ft^3/s)	Culvert (ft^3/s)	Over the Road (ft^3/s)	Water Temp (°C)	Viscosity (ft^2/s) (10-5)	Depth (Nail) (ft)	Depth (Bubbler) (ft)	Area (Nail) (ft^2)	Area (Bubbler) (ft^2)	Depth (ft)	Area (ft^2)	Depth (ft)	Area (ft^2)
19-Jul-11	136	1:56	M-R	0.006	S	11.59	2.34	9.25	29.3	0.86	1.38	1.46	9.21	9.81	1.00	6.94	1.14	7.81
19-Jul-11	137	1:48	M-R	0.006	S	11.55	2.51	9.04	29.2	0.86	1.38	1.46	9.24	9.81	1.01	7.04	1.13	7.77
20-Jul-11	138	1:50	S-R	0.006	S	11.92	1.03	10.89	29.2	0.86	1.45	1.53	9.73	10.35	0.97	6.70	1.17	8.03
20-Jul-11	139	1:48	S-R	0.006	S	11.79	1.02	10.77	29.2	0.86	1.47	1.52	9.95	10.30	0.95	6.59	1.13	7.76
21-Jul-11	140	1:57	S-R	0.006	S	11.83	1.01	10.82	28.6	0.87	1.47	1.52	9.88	10.29	0.96	6.61	1.15	7.93
Parallel Model																		
22-Jul-11	141	2:04	M-R	0.006	P	11.63	2.40	9.24	28.6	0.87	1.41	1.48	9.45	9.98	1.06	7.39	1.17	8.06
23-Jul-11	142	2:20	M-R	0.006	P	11.87	2.79	9.08	29.2	0.86	1.42	1.49	9.55	10.07	1.05	7.37	1.18	8.12
25-Jul-11	143	2:35	M-R	0.006	P	12.01	3.03	8.98	29.7	0.85	1.45	1.49	9.74	10.09	1.07	7.49	1.20	8.29
25-Jul-11	144	2:41	M-R	0.006	P	12.08	3.03	9.05	29.7	0.85	1.46	1.51	9.82	10.25	1.06	7.40	1.19	8.18
26-Jul-11	145	2:45	S-R	0.006	P	12.22	1.20	11.02	29.7	0.85	1.52	1.58	10.33	10.76	1.09	7.69	1.18	8.11
27-Jul-11	146	2:34	S-R	0.006	P	12.15	1.16	11.00	29.0	0.86	1.46	1.55	9.88	10.54	1.12	7.86	1.18	8.10
27-Jul-11	147	2:38	S-R	0.006	P	11.94	1.12	10.82	29.0	0.86	1.49	1.55	10.07	10.51	1.09	7.68	1.17	8.08
28-Jul-11	148	2:39	S-R	0.006	P	12.33	1.13	11.20	28.8	0.86	1.49	1.55	10.11	10.53	1.11	7.78	1.18	8.11
29-Jul-11	149	2:36	SB-C	0.006	P	12.33	1.41	10.93	28.7	0.86	1.51	1.54	10.24	10.46	1.09	7.67	1.19	8.22
30-Jul-11	150	2:35	SB-C	0.006	P	12.15	1.38	10.78	28.7	0.86	1.45	1.54	9.77	10.47	1.08	7.54	1.17	8.09
31-Jul-11	151	2:37	SB-C	0.006	P	12.15	1.44	10.72	29.2	0.86	1.47	1.54	9.89	10.47	1.10	7.74	1.17	8.04
1-Aug-11	152	2:33	M-6-C	0.006	P	12.19	2.07	10.12	28.5	0.87	1.46	1.53	9.81	10.37	1.06	7.40	1.19	8.22
1-Aug-11	153	2:39	M-6-C	0.006	P	12.05	2.03	10.01	28.5	0.87	1.47	1.52	9.94	10.30	1.08	7.54	1.18	8.16
2-Aug-11	154	2:37	M-6-C	0.006	P	12.23	2.11	10.12	28.5	0.87	1.47	1.52	9.94	10.35	1.06	7.44	1.18	8.15
3-Aug-11	155	2:37	M-6-C	0.006	P	12.01	1.95	10.06	28.5	0.87	1.45	1.51	9.75	10.27	1.05	7.32	1.19	8.20
3-Aug-11	156	2:45	M-6-C	0.006	P	12.12	2.03	10.09	29.0	0.86	1.48	1.53	9.98	10.42	1.03	7.22	1.18	8.17
4-Aug-11	157	2:34	S-6-C	0.006	P	12.15	0.77	11.38	29.6	0.85	1.50	1.57	10.16	10.68	1.12	7.86	1.18	8.11
5-Aug-11	158	2:35	S-6-C	0.006	P	11.98	0.67	11.31	29.0	0.86	1.49	1.55	10.10	10.55	1.08	7.55	1.17	8.06
6-Aug-11	159	2:45	S-6-C	0.006	P	12.12	0.77	11.35	29.0	0.86	1.50	1.57	10.16	10.69	1.08	7.58	1.16	8.01
7-Aug-11	160	2:37	S-4-C	0.006	P	12.05	0.31	11.74	29.0	0.86	1.54	1.58	10.45	10.79	1.06	7.43	1.14	7.83
8-Aug-11	161	2:38	S-4-C	0.006	P	12.19	0.33	11.87	29.5	0.85	1.52	1.60	10.32	10.94	1.12	7.85	1.20	8.30
8-Aug-11	162	2:37	S-4-C	0.006	P	12.08	0.32	11.76	29.5	0.85	1.54	1.59	10.45	10.84	1.05	7.35	1.17	8.09
9-Aug-11	163	2:39	M-4-C	0.006	P	12.26	0.89	11.37	29.5	0.85	1.49	1.56	10.04	10.61	1.08	7.60	1.17	8.03
10-Aug-11	164	2:36	M-4-C	0.006	P	12.01	0.91	11.10	29.5	0.85	1.48	1.55	10.00	10.58	1.12	7.91	1.19	8.19
10-Aug-11	165	2:35	M-4-C	0.006	P	12.12	0.91	11.20	29.5	0.85	1.49	1.56	10.08	10.65	1.11	7.77	1.18	8.16
Changed Slope																		
11-Aug-11	166	2:46	M-4-C	0.003	P	12.08	0.82	11.26	29.5	0.85	1.51	1.59	10.21	10.82	1.08	7.61	1.17	8.04
12-Aug-11	167	3:18	M-4-C	0.003	P	11.47	0.79	10.68	29.2	0.86	1.48	1.57	10.02	10.66	1.03	7.19	1.14	7.83
13-Aug-11	168	2:22	M-4-C	0.003	P	11.93	0.84	11.09	29.2	0.86	1.50	1.59	10.13	10.82	1.06	7.43	1.18	8.10
15-Aug-11	169	2:44	S-4-C	0.003	P	11.80	0.29	11.51	28.7	0.86	1.51	1.60	10.23	10.90	1.06	7.38	1.17	8.07
15-Aug-11	170	2:36	S-4-C	0.003	P	11.73	0.29	11.44	28.7	0.86	1.54	1.58	10.46	10.82	1.05	7.36	1.16	8.00
16-Aug-11	171	2:35	S-4-C	0.003	P	12.05	0.27	11.78	28.7	0.86	1.54	1.61	10.47	10.98	1.07	7.46	1.17	8.08
17-Aug-11	172	2:34	SB-I	0.003	P	11.76	1.15	10.62	28.7	0.86	1.47	1.56	9.94	10.61	1.09	7.67	1.18	8.12
17-Aug-11	173	2:33	SB-I	0.003	P	12.96	1.10	11.85	28.7	0.86	1.51	1.56	10.22	10.62	1.08	7.59	1.18	8.12
18-Aug-11	174	2:35	SB-I	0.003	P	12.95	1.13	11.83	29.0	0.86	1.47	1.56	9.96	10.62	1.12	7.87	1.19	8.21
19-Aug-11	175	2:35	M-6-C	0.003	P	12.84	1.19	11.66	28.6	0.87	1.50	1.54	10.12	10.43	1.10	7.76	1.18	8.16
20-Aug-11	176	2:07	M-6-C	0.003	P	12.67	1.17	11.50	28.6	0.87	1.48	1.51	9.99	10.25	1.06	7.40	1.16	7.95
21-Aug-11	177	2:18	M-6-C	0.003	P	12.84	0.93	11.91	28.6	0.87	1.49	1.55	10.06	10.53	1.06	7.38	1.17	8.06
22-Aug-11	178	2:34	S-6-C	0.003	P	12.88	0.58	12.30	28.6	0.87	1.51	1.57	10.21	10.68	1.10	7.76	1.17	8.09
22-Aug-11	179	2:38	S-6-C	0.003	P	12.70	0.65	12.05	28.6	0.87	1.52	1.56	10.30	10.66	1.08	7.57	1.17	8.07
23-Aug-11	180	2:37	S-6-C	0.003	P	12.84	0.67	12.18	28.2	0.87	1.52	1.57	10.32	10.73	1.08	7.60	1.19	8.18
23-Aug-11	181	2:43	SB-C	0.003	P	12.96	0.85	12.10	28.7	0.86	1.48	1.57	10.02	10.69	1.07	7.52	1.18	8.12

Expermental Hydraulic Data Part A

Date	Exp. No.	Time	Model	Slope (ft/ft)	Position	Total (ft^3/s)	Culvert (ft^3/s)	Over the Road (ft^3/s)	Water Temp (°C)	Viscosity (ft^2/s) (10-5)	Depth (Nail) (ft)	Depth (Bubbler) (ft)	Area (Nail) (ft^2)	Area (Bubbler) (ft^2)	Depth (ft)	Area (ft^2)	Depth (ft)	Area (ft^2)
24-Aug-11	182	2:39	SB-C	0.003	P	12.99	0.90	12.08	28.7	0.86	1.49	1.56	10.09	10.63	1.08	7.54	1.18	8.14
24-Aug-11	183	2:22	SB-C	0.003	P	12.87	0.90	11.98	28.7	0.86	1.49	1.56	10.09	10.61	1.08	7.57	1.18	8.11
25-Aug-11	184	1:46	M-R	0.003	P	12.81	1.04	11.76	28.7	0.86	1.45	1.51	9.74	10.22	1.11	7.77	1.18	8.11
25-Aug-11	185	1:35	M-R	0.003	P	12.84	1.05	11.79	28.7	0.86	1.44	1.50	9.67	10.19	1.11	7.79	1.18	8.13
26-Aug-11	186	1:32	M-R	0.003	P	12.85	1.27	11.57	28.7	0.86	1.45	1.50	9.75	10.16	1.06	7.42	1.17	8.03
26-Aug-11	187	2:32	S-R	0.003	P	12.73	0.81	11.92	29.2	0.86	1.51	1.56	10.23	10.62	1.08	7.60	1.16	8.01
27-Aug-11	188	2:35	S-R	0.003	P	12.63	0.93	11.69	29.2	0.86	1.50	1.54	10.16	10.49	1.04	7.26	1.14	7.82
29-Aug-11	189	2:37	S-R	0.003	P	12.73	0.93	11.81	29.2	0.86	1.49	1.56	10.05	10.62	1.06	7.40	1.17	8.02
Weir Coefficient																		
1-Nov-11	190	3:00	M-R	0.003	P	12.87	—	—	22.0	1.01	—	—	—	—	—	—	—	—
3-Nov-11	191	3:00	M-R	0.003	P	12.81	—	—	22.0	1.01	—	—	—	—	—	—	—	—
7-Nov-11	192	3:00	M-R	0.003	P	12.84	—	—	22.0	1.01	—	—	—	—	—	—	—	—
Additional Flow Regime																		
29-Nov-11	193	3:00	M-R	0.003	P	12.85	—	—	22.0	1.01	—	—	—	—	—	—	—	—
30-Nov-11	194	2:40	M-R	0.003	P	12.22	0.49	11.74	20.0	1.05	1.69	1.74	11.65	11.99	1.45	10.45	1.49	10.56
1-Dec-11	195	2:35	M-R	0.003	P	12.30	0.51	11.79	20.0	1.05	1.69	1.74	11.66	12.03	1.46	10.56	1.50	10.66
2-Dec-11	196	2:38	SBC	0.003	P	12.44	0.45	11.99	20.0	1.05	1.70	1.75	11.75	12.10	1.45	10.49	1.50	10.66
3-Dec-11	197	3:47	SBC	0.003	P	12.50	0.49	12.01	21.0	1.03	1.70	1.75	11.73	12.13	1.46	10.56	1.50	10.66
5-Dec-11	198	2:40	SBC	0.003	P	12.84	2.66	10.18	21.0	1.03	1.50	1.56	10.14	10.62	1.09	7.63	1.18	8.15
9-Dec-11	199	2:49	SBC	0.003	P	12.55	2.24	10.31	21.0	1.03	1.54	1.56	10.49	10.60	1.07	7.51	1.18	8.12
13-Dec-11	200	2:35	SBC	0.003	P	12.42	4.20	8.22	21.0	1.03	1.49	1.52	10.06	10.30	0.86	5.82	0.96	6.38
14-Dec-11	201	2:38	SBC	0.003	P	12.30	4.13	8.17	21.0	1.03	1.48	1.50	9.98	10.12	0.93	6.38	0.97	6.48

Expermental Hydraulic Data Part B

	Velocity at each section				Froude No. (F_{cs})				Terminal Froude (F_T)		Hydraulic Radius				
Exp. No.	**Section 1 (Nail) (ft/s)**	**Section 1 (Bubbler) (ft/s)**	**Section 2 (ft/s)**	**Section 3 (ft/s)**	**Nail 1** (Dimensionless)	**Nail 2** (Dimensionless)	**Nail 3** (Dimensionless)	**Bubbler 1** (Dimensionless)	**Nail 1** (Dimensionless)	**Bubbler 1** (Dimensionless)	**Nail (1) (ft)**	**Bubbler 1 (ft)**	**Nail 2 (ft)**	**Nail 3 (ft)**	**Bubbler 2 (ft)**
VP	—	—	—	—	—	—	—	—	—	—	—	—	—	—	—
1	0.54	0.55	—	0.76	0.09	—	0.14	0.09	0.58	0.56	0.89	0.90	NAN	0.75	0.75
2	—	—	—	—	—	—	—	—	—	—	—	—	—	—	—
3	—	—	—	—	—	—	—	—	—	—	—	—	—	—	—
4	—	—	—	—	—	—	—	—	—	—	—	—	—	—	—
5	—	—	—	—	—	—	—	—	—	—	—	—	—	—	—
6	—	—	—	—	—	—	—	—	—	—	—	—	—	—	—
7	—	—	—	—	—	—	—	—							
8	—	—	—	—	—	—	—	—	—	—	—	—	—	—	—
9	—	—	—	—	—	—	—	—	—	—	—	—	—	—	—
10	—	—	—	—	—	—	—	—	—	—	—	—	—	—	—
11	—	—	—	—	—	—	—	—	—	—	—	—	—	—	—
12	1.38	1.31	1.67	1.67	0.19	0.27	0.26	0.18	0.64	0.54	1.03	1.07	0.04	0.94	0.96
13	1.41	1.33	1.69	1.70	0.20	0.28	0.27	0.18	0.66	0.56	1.02	1.06	0.04	0.94	0.96
14	1.43	1.36	1.67	1.70	0.21	0.27	0.27	0.19	0.71	0.60	1.01	1.04	0.04	0.94	0.95
15	1.40	1.33	1.74	1.69	0.20	0.29	0.26	0.18	0.66	0.56	1.02	1.06	0.04	0.95	0.96
16	—	—	—	—	—	—	—	—	—	—	—	—	—	—	—
17	—	—	—	—	—	—	—	—	—	—	—	—	—	—	—
18	1.41	1.34	1.78	1.72	0.20	0.29	0.27	0.18	0.64	0.54	1.03	1.08	0.04	0.95	0.97
19	1.36	1.29	1.76	1.69	0.19	0.29	0.26	0.18	0.61	0.52	1.03	1.07	0.04	0.96	0.98
20	1.40	1.32	1.77	1.71	0.20	0.29	0.27	0.18	0.62	0.52	1.04	1.09	0.04	0.95	0.97
21	—	—	—	—	—	—	—	—	—	—	—	—	—	—	—
22	—	—	—	—	—	—	—	—	—	—	—	—	—	—	—
23	1.39	1.31	1.73	1.71	0.19	0.28	0.27	0.18	0.61	0.52	1.04	1.09	0.04	0.95	0.96
24	1.38	1.30	1.72	1.70	0.19	0.28	0.27	0.18	0.62	0.52	1.04	1.09	0.04	0.95	0.97
25	1.41	1.33	1.76	1.72	0.20	0.29	0.27	0.18	0.65	0.55	1.03	1.07	0.04	0.94	0.95
26	1.46	1.39	1.75	1.74	0.21	0.29	0.28	0.20	0.74	0.63	1.00	1.03	0.04	0.93	0.94
27	1.40	1.32	1.65	1.68	0.20	0.27	0.26	0.18	0.65	0.55	1.02	1.06	0.04	0.95	0.96
28	1.42	1.35	1.71	1.74	0.20	0.28	0.28	0.19	0.69	0.59	1.01	1.05	0.04	0.92	0.94
29	1.40	1.32	1.63	1.68	0.20	0.26	0.26	0.18	0.67	0.57	1.01	1.05	0.04	0.94	0.95
30	1.41	1.34	1.62	1.66	0.20	0.26	0.26	0.19	0.69	0.59	1.01	1.04	0.04	0.95	0.96
31	1.44	1.38	1.65	1.72	0.21	0.27	0.27	0.19	0.74	0.63	0.99	1.03	0.04	0.92	0.93
32	1.41	1.33	1.72	1.74	0.20	0.28	0.27	0.18	0.64	0.53	1.04	1.08	0.04	0.94	0.95
33	1.37	1.29	1.68	1.70	0.19	0.27	0.26	0.17	0.59	0.49	1.06	1.10	0.04	0.96	0.98
34	1.39	1.31	1.68	1.69	0.19	0.27	0.26	0.18	0.61	0.51	1.04	1.09	0.04	0.96	0.97
35	—	—	—	—	—	—	—	—	—	—	—	—	—	—	—
36	—	—	—	—	—	—	—	—	—	—	—	—	—	—	—
Change Slope															
37	—	—	—	—	—	—	—	—	—	—	—	—	—	—	—
37B	—	—	—	—	—	—	—	—	—	—	—	—	—	—	—
38	1.40	1.33	1.83	1.77	0.20	0.30	0.29	0.18	0.67	0.56	1.02	1.06	0.05	0.91	0.92
39	1.40	1.35	1.80	1.76	0.20	0.29	0.28	0.19	0.64	0.58	1.03	1.06	0.05	0.92	0.92
40	1.40	1.35	1.89	1.73	0.20	0.31	0.27	0.19	0.63	0.56	1.04	1.07	0.05	0.94	0.93
41	1.44	1.43	1.83	1.72	0.20	0.30	0.27	0.20	0.68	0.67	1.02	1.02	0.05	0.95	0.94
42	1.47	1.41	1.86	1.75	0.21	0.31	0.28	0.20	0.75	0.65	0.99	1.03	0.05	0.93	0.94
43	1.48	1.42	1.88	1.76	0.21	0.31	0.28	0.20	0.76	0.67	0.99	1.02	0.05	0.92	0.94
44	1.44	1.40	1.75	1.74	0.20	0.28	0.27	0.20	0.68	0.63	1.02	1.04	0.05	0.94	0.94

Expermental Hydraulic Data Part B

	Velocity at each section				Froude No. (F_{cs})				Terminal Froude (F_T)		Hydraulic Radius				
Exp. No.	**Section 1 (Nail) (ft/s)**	**Section 1 (Bubbler) (ft/s)**	**Section 2 (ft/s)**	**Section 3 (ft/s)**	**Nail 1** (Dimensionless)	**Nail 2** (Dimensionless)	**Nail 3** (Dimensionless)	**Bubbler 1** (Dimensionless)	**Nail 1** (Dimensionless)	**Bubbler 1** (Dimensionless)	**Nail (1) (ft)**	**Bubbler 1 (ft)**	**Nail 2 (ft)**	**Nail 3 (ft)**	**Bubbler 2 (ft)**
45	1.43	1.39	1.77	1.74	0.20	0.28	0.27	0.20	0.67	0.62	1.02	1.04	0.05	0.94	0.94
46	1.44	1.40	1.86	1.71	0.20	0.31	0.27	0.20	0.68	0.63	1.02	1.04	0.05	0.95	0.93
47	1.41	1.34	1.89	1.76	0.20	0.31	0.28	0.18	0.65	0.56	1.03	1.07	0.05	0.93	0.93
48	1.44	1.35	1.88	1.80	0.20	0.31	0.29	0.19	0.68	0.56	1.02	1.07	0.05	0.91	0.92
49	1.39	1.34	1.83	1.74	0.19	0.30	0.28	0.18	0.61	0.56	1.04	1.07	0.05	0.93	0.92
50	—	—	—	—	—	—	—	—	—	—	—	—	—	—	—
51	—	—	—	—	—	—	—	—	—	—	—	—	—	—	—
52	1.40	1.34	1.82	1.77	0.20	0.30	0.29	0.19	0.68	0.60	1.01	1.04	0.05	0.90	0.91
53	1.41	1.35	1.89	1.70	0.20	0.32	0.27	0.19	0.69	0.61	1.01	1.04	0.04	0.93	0.91
54	1.41	1.37	1.84	1.74	0.20	0.30	0.27	0.19	0.64	0.58	1.04	1.06	0.05	0.94	0.93
55	1.39	1.34	1.88	1.73	0.19	0.31	0.27	0.18	0.61	0.55	1.05	1.07	0.05	0.94	0.93
56	1.41	1.35	1.98	1.77	0.20	0.33	0.28	0.19	0.63	0.56	1.04	1.07	0.04	0.93	0.93
57	1.41	1.34	1.81	1.74	0.20	0.30	0.27	0.18	0.65	0.55	1.03	1.07	0.05	0.93	0.92
58	—	—	—	—	—	—	—	—	—	—	—	—	—	—	—
59	—	—	—	—	—	—	—	—	—	—	—	—	—	—	—
60	1.45	1.41	1.85	1.76	0.20	0.30	0.28	0.20	0.66	0.61	1.03	1.05	0.05	0.94	0.93
61	1.53	1.43	1.76	1.77	0.22	0.28	0.28	0.20	0.80	0.64	0.99	1.04	0.05	0.94	0.93
62	1.45	1.38	1.83	1.77	0.21	0.30	0.28	0.19	0.72	0.62	1.00	1.04	0.05	0.91	0.92
63	—	—	—	—	—	—	—	—	—	—	—	—	—	—	—
64	—	—	—	—	—	—	—	—	—	—	—	—	—	—	—
65	1.43	1.39	1.70	1.71	0.20	0.27	0.27	0.20	0.69	0.63	1.02	1.04	0.05	0.94	0.92
66	1.43	1.40	1.81	1.74	0.20	0.29	0.28	0.20	0.67	0.63	1.02	1.04	0.05	0.93	0.92
67	1.44	1.39	1.77	1.70	0.20	0.29	0.27	0.19	0.69	0.62	1.01	1.04	0.05	0.95	0.93
68	1.46	1.42	1.77	1.74	0.21	0.28	0.27	0.20	0.71	0.66	1.01	1.03	0.05	0.94	0.93
69	1.44	1.38	1.87	1.83	0.20	0.31	0.29	0.19	0.68	0.59	1.02	1.05	0.05	0.90	0.91
Change Slope															
70	1.44	1.36	1.73	1.72	0.21	0.28	0.27	0.19	0.71	0.59	1.00	1.05	0.05	0.93	0.93
71	1.39	1.34	1.61	1.69	0.20	0.25	0.27	0.19	0.65	0.58	1.02	1.05	0.05	0.94	0.92
72	1.41	1.35	1.70	1.71	0.20	0.27	0.27	0.19	0.67	0.59	1.02	1.05	0.05	0.93	0.92
73	1.44	1.37	1.75	1.69	0.21	0.28	0.27	0.19	0.73	0.61	1.00	1.04	0.05	0.94	0.93
74	1.45	1.38	1.76	1.72	0.21	0.28	0.27	0.19	0.70	0.61	1.01	1.04	0.05	0.94	0.93
75	1.41	1.37	1.79	1.72	0.20	0.29	0.27	0.19	0.71	0.63	1.00	1.03	0.05	0.92	0.91
76	—	—	—	—	—	—	—	—	—	—	—	—	—	—	—
77	—	—	—	—	—	—	—	—	—	—	—	—	—	—	—
78	1.44	1.38	1.77	1.67	0.21	0.29	0.26	0.20	0.78	0.67	0.98	1.01	0.05	0.93	0.91
79	1.43	1.38	1.73	1.70	0.21	0.28	0.27	0.19	0.71	0.63	1.00	1.03	0.05	0.94	0.92
80	1.47	1.41	1.79	1.73	0.21	0.29	0.27	0.20	0.70	0.61	1.02	1.05	0.05	0.96	0.94
81	—	—	—	—	—	—	—	—	—	—	—	—	—	—	—
82A	—	—	—	—	—	—	—	—	—	—	—	—	—	—	—
82	1.40	1.36	1.76	1.71	0.20	0.28	0.27	0.19	0.65	0.60	1.02	1.05	0.05	0.94	0.92
83	1.45	1.36	1.83	1.73	0.21	0.30	0.28	0.19	0.76	0.62	0.98	1.03	0.05	0.91	0.91
84	1.43	1.36	1.83	1.69	0.21	0.30	0.27	0.19	0.73	0.61	0.99	1.03	0.05	0.93	0.91
85	1.42	1.34	1.75	1.70	0.20	0.29	0.27	0.19	0.71	0.60	1.00	1.04	0.05	0.93	0.93
86	1.47	1.37	1.83	1.75	0.21	0.30	0.28	0.19	0.74	0.59	1.00	1.05	0.05	0.93	0.93
87	1.51	1.40	1.84	1.79	0.22	0.30	0.28	0.19	0.78	0.61	0.99	1.05	0.05	0.93	0.93
88	—	—	—	—	—	—	—	—	—	—	—	—	—	—	—

Expermental Hydraulic Data Part B

	Velocity at each section				Froude No. (F_{cs})				Terminal Froude (F_T)		Hydraulic Radius				
Exp. No.	**Section 1 (Nail) (ft/s)**	**Section 1 (Bubbler) (ft/s)**	**Section 2 (ft/s)**	**Section 3 (ft/s)**	**Nail 1** (Dimensionless)	**Nail 2** (Dimensionless)	**Nail 3** (Dimensionless)	**Bubbler 1** (Dimensionless)	**Nail 1** (Dimensionless)	**Bubbler 1** (Dimensionless)	**Nail (1) (ft)**	**Bubbler 1 (ft)**	**Nail 2 (ft)**	**Nail 3 (ft)**	**Bubbler 2 (ft)**
Large Grain Skew Model															
89	—	—	—	—	—	—	—	—	—	—	—	—	—	—	—
90	—	—	—	—	—	—	—	—	—	—	—	—	—	—	—
91	1.44	1.38	1.86	1.70	0.21	0.31	0.27	0.19	0.75	0.66	1.00	1.03	0.05	0.94	0.92
92	1.47	1.35	1.93	1.76	0.21	0.33	0.28	0.19	0.81	0.61	0.98	1.05	0.04	0.91	0.93
93	1.44	1.38	1.86	1.67	0.21	0.31	0.26	0.19	0.73	0.64	1.01	1.04	0.05	0.96	0.93
94	1.41	1.35	2.07	1.73	0.20	0.36	0.27	0.19	0.70	0.62	1.02	1.04	0.04	0.92	0.92
95	1.42	1.33	2.08	1.72	0.20	0.37	0.27	0.19	0.74	0.60	1.00	1.05	0.04	0.92	0.92
96	1.46	1.34	1.86	1.70	0.21	0.31	0.27	0.19	0.80	0.60	0.98	1.05	0.05	0.93	0.95
97	—	—	—	—	—	—	—	—	—	—	—	—	—	—	—
98	—	—	—	—	—	—	—	—	—	—	—	—	—	—	—
99	—	—	—	—	—	—	—	—	—	—	—	—	—	—	—
100	—	—	—	—	—	—	—	—	—	—	—	—	—	—	—
101	1.46	1.33	2.16	1.78	0.21	0.39	0.29	0.19	0.81	0.60	0.98	1.05	0.04	0.90	0.93
102	1.43	1.35	2.12	1.78	0.20	0.37	0.28	0.19	0.69	0.58	1.03	1.07	0.04	0.92	0.94
103	1.42	1.36	1.87	1.68	0.20	0.31	0.26	0.19	0.75	0.64	1.00	1.03	0.04	0.93	0.93
104	1.44	1.37	1.92	1.72	0.20	0.32	0.27	0.19	0.72	0.62	1.01	1.05	0.04	0.94	0.93
105	1.43	1.35	1.96	1.75	0.21	0.33	0.28	0.19	0.75	0.62	1.00	1.04	0.04	0.91	0.93
106	1.46	1.39	2.02	1.78	0.21	0.35	0.29	0.20	0.77	0.66	1.00	1.03	0.04	0.91	0.93
107	1.43	1.35	2.01	1.71	0.20	0.34	0.27	0.19	0.71	0.59	1.01	1.06	0.04	0.94	0.92
108	1.42	1.36	1.95	1.69	0.20	0.33	0.26	0.19	0.69	0.61	1.02	1.05	0.04	0.95	0.91
109	1.45	1.33	1.99	1.71	0.21	0.34	0.27	0.19	0.80	0.60	0.99	1.05	0.04	0.92	0.93
110	—	—	—	—	—	—	—	—	—	—	—	—	—	—	—
111	—	—	—	—	—	—	—	—	—	—	—	—	—	—	—
112	—	—	—	—	—	—	—	—	—	—	—	—	—	—	—
113	1.38	1.29	2.18	1.69	0.20	0.39	0.27	0.18	0.69	0.55	1.01	1.07	0.04	0.92	0.92
114	1.39	1.31	2.14	1.75	0.20	0.38	0.28	0.18	0.66	0.55	1.03	1.07	0.04	0.92	0.93
115	1.42	1.34	2.07	1.73	0.20	0.36	0.27	0.19	0.72	0.60	1.01	1.05	0.04	0.93	0.92
116	1.46	1.35	1.95	1.76	0.21	0.33	0.28	0.19	0.75	0.60	1.00	1.06	0.04	0.92	0.93
117	1.43	1.35	2.05	1.75	0.20	0.35	0.28	0.19	0.71	0.60	1.01	1.06	0.04	0.93	0.92
Start Small Grain															
Small Grain Skew Model															
118	1.22	1.16	1.81	1.54	0.18	0.33	0.25	0.16	0.71	0.59	0.97	1.01	0.04	0.86	0.89
119	1.24	1.14	1.77	1.49	0.18	0.32	0.25	0.16	0.78	0.58	0.95	1.01	0.04	0.87	0.89
120	1.17	1.14	1.75	1.51	0.17	0.31	0.25	0.16	0.66	0.60	0.98	1.00	0.04	0.86	0.88
121	1.18	1.10	1.84	1.49	0.17	0.34	0.25	0.16	0.71	0.55	0.96	1.01	0.04	0.86	0.87
122	1.19	1.14	1.86	1.29	0.17	0.34	0.21	0.16	0.64	0.56	0.99	1.02	0.04	1.33	0.87
123	1.22	1.13	1.95	1.52	0.18	0.36	0.25	0.16	0.67	0.52	0.98	1.04	0.04	0.88	0.89
124															
125	1.28	1.19	1.71	1.51	0.19	0.30	0.25	0.17	0.86	0.66	0.93	0.98	0.04	0.87	0.89
126	1.25	1.19	1.68	1.50	0.19	0.29	0.25	0.17	0.80	0.67	0.94	0.98	0.04	0.87	0.89
127	1.24	1.18	1.69	1.48	0.18	0.30	0.24	0.17	0.79	0.67	0.94	0.98	0.04	0.87	0.89
128	1.22	1.14	1.77	1.47	0.18	0.32	0.24	0.16	0.74	0.58	0.96	1.01	0.04	0.88	0.89
129	1.16	1.13	1.76	1.49	0.17	0.32	0.25	0.16	0.65	0.59	0.98	1.00	0.04	0.86	0.89
130	1.18	1.13	1.77	1.46	0.17	0.32	0.24	0.16	0.67	0.58	0.97	1.00	0.04	0.88	0.88
131	1.21	1.17	1.70	1.51	0.18	0.30	0.25	0.17	0.73	0.65	0.96	0.98	0.04	0.86	0.89
132	1.25	1.18	1.81	1.53	0.18	0.33	0.25	0.17	0.75	0.62	0.96	1.00	0.04	0.87	0.90

Expermental Hydraulic Data Part B

	Velocity at each section				Froude No. (F_{cs})				Terminal Froude (F_T)		Hydraulic Radius				
Exp. No.	**Section 1 (Nail) (ft/s)**	**Section 1 (Bubbler) (ft/s)**	**Section 2 (ft/s)**	**Section 3 (ft/s)**	**Nail 1** (Dimensionless)	**Nail 2** (Dimensionless)	**Nail 3** (Dimensionless)	**Bubbler 1** (Dimensionless)	**Nail 1** (Dimensionless)	**Bubbler 1** (Dimensionless)	**Nail (1) (ft)**	**Bubbler 1 (ft)**	**Nail 2 (ft)**	**Nail 3 (ft)**	**Bubbler 2 (ft)**
133	1.25	1.18	1.77	1.51	0.18	0.32	0.25	0.17	0.77	0.62	0.95	1.00	0.04	0.88	0.90
134	1.24	1.17	1.71	1.48	0.18	0.30	0.24	0.17	0.75	0.60	0.96	1.00	0.04	0.89	0.90
135	1.26	1.18	1.66	1.50	0.19	0.29	0.25	0.17	0.86	0.68	0.93	0.97	0.04	0.86	0.89
136	1.26	1.18	1.67	1.48	0.19	0.29	0.25	0.17	0.89	0.69	0.92	0.97	0.04	0.86	0.88
137	1.25	1.18	1.64	1.49	0.19	0.29	0.25	0.17	0.86	0.69	0.92	0.97	0.04	0.86	0.89
138	1.23	1.15	1.78	1.48	0.18	0.32	0.24	0.16	0.73	0.59	0.96	1.01	0.04	0.88	0.89
139	1.19	1.14	1.79	1.52	0.17	0.32	0.25	0.16	0.67	0.59	0.98	1.00	0.04	0.86	0.89
140	1.20	1.15	1.79	1.49	0.17	0.32	0.24	0.16	0.69	0.60	0.97	1.00	0.04	0.87	0.88
Parallel Model															
141	1.23	1.17	1.57	1.44	0.18	0.27	0.24	0.17	0.81	0.67	0.94	0.98	0.04	0.88	0.89
142	1.24	1.18	1.61	1.46	0.18	0.28	0.24	0.17	0.79	0.66	0.95	0.99	0.04	0.89	0.90
143	1.23	1.19	1.60	1.45	0.18	0.27	0.23	0.17	0.75	0.66	0.96	0.99	0.04	0.90	0.90
144	1.23	1.18	1.63	1.48	0.18	0.28	0.24	0.17	0.73	0.63	0.97	1.00	0.04	0.89	0.91
145	1.18	1.14	1.59	1.51	0.17	0.27	0.24	0.16	0.73	0.63	0.97	1.00	0.04	0.89	0.91
146	1.23	1.15	1.55	1.50	0.18	0.26	0.24	0.16	0.72	0.58	0.97	1.02	0.05	0.89	0.89
147	1.19	1.14	1.55	1.48	0.17	0.26	0.24	0.16	0.66	0.57	0.99	1.02	0.04	0.89	0.89
148	1.22	1.17	1.58	1.52	0.18	0.27	0.25	0.17	0.67	0.59	0.99	1.02	0.04	0.89	0.90
149	1.20	1.18	1.61	1.50	0.17	0.27	0.24	0.17	0.64	0.60	1.00	1.01	0.04	0.90	0.90
150	1.24	1.16	1.61	1.50	0.18	0.27	0.24	0.17	0.75	0.59	0.96	1.01	0.04	0.89	0.89
151	1.23	1.16	1.57	1.51	0.18	0.26	0.25	0.16	0.72	0.59	0.97	1.01	0.04	0.88	0.90
152	1.24	1.18	1.65	1.48	0.18	0.28	0.24	0.17	0.74	0.61	0.97	1.01	0.04	0.90	0.90
153	1.21	1.17	1.60	1.48	0.18	0.27	0.24	0.17	0.70	0.62	0.98	1.00	0.04	0.89	0.90
154	1.23	1.18	1.64	1.50	0.18	0.28	0.24	0.17	0.71	0.62	0.98	1.01	0.04	0.89	0.90
155	1.23	1.17	1.64	1.46	0.18	0.28	0.24	0.17	0.74	0.62	0.96	1.00	0.04	0.90	0.90
156	1.21	1.16	1.68	1.48	0.18	0.29	0.24	0.17	0.69	0.60	0.98	1.01	0.04	0.89	0.90
157	1.20	1.14	1.55	1.50	0.17	0.26	0.24	0.16	0.65	0.55	0.99	1.03	0.05	0.89	0.89
158	1.19	1.14	1.59	1.49	0.17	0.27	0.24	0.16	0.65	0.57	0.99	1.02	0.04	0.88	0.88
159	1.19	1.13	1.60	1.51	0.17	0.27	0.25	0.16	0.65	0.55	0.99	1.03	0.04	0.88	0.89
160	1.15	1.12	1.62	1.54	0.16	0.28	0.25	0.16	0.59	0.53	1.01	1.04	0.04	0.86	0.89
161	1.18	1.12	1.55	1.47	0.17	0.26	0.24	0.16	0.62	0.51	1.00	1.05	0.04	0.90	0.89
162	1.16	1.12	1.64	1.49	0.16	0.28	0.24	0.16	0.59	0.52	1.01	1.04	0.04	0.89	0.89
163	1.22	1.16	1.61	1.53	0.18	0.27	0.25	0.16	0.68	0.57	0.98	1.02	0.04	0.88	0.89
164	1.20	1.14	1.52	1.47	0.17	0.25	0.24	0.16	0.68	0.56	0.98	1.02	0.05	0.90	0.89
165	1.20	1.14	1.56	1.49	0.17	0.26	0.24	0.16	0.67	0.56	0.99	1.03	0.04	0.89	0.90
Change Slope															
166	1.18	1.12	1.59	1.50	0.17	0.27	0.25	0.16	0.64	0.53	1.00	1.04	0.04	0.88	0.90
167	1.15	1.08	1.60	1.47	0.17	0.28	0.24	0.15	0.65	0.52	0.98	1.03	0.04	0.86	0.89
168	1.18	1.10	1.60	1.47	0.17	0.27	0.24	0.15	0.65	0.52	0.99	1.04	0.04	0.89	0.90
169	1.15	1.08	1.60	1.46	0.17	0.28	0.24	0.15	0.62	0.50	1.00	1.04	0.04	0.88	0.89
170	0.90	0.92	1.27	1.17	0.16	0.27	0.24	0.15	0.57	0.51	1.01	1.04	0.04	0.88	0.89
171	1.15	1.10	1.62	1.49	0.16	0.28	0.24	0.15	0.58	0.50	1.01	1.05	0.04	0.89	0.90
172	1.18	1.11	1.53	1.45	0.17	0.26	0.24	0.16	0.68	0.55	0.98	1.02	0.04	0.89	0.90
173	1.27	1.22	1.71	1.59	0.18	0.29	0.26	0.17	0.68	0.60	1.00	1.03	0.04	0.89	0.90
174	1.30	1.22	1.65	1.58	0.19	0.27	0.25	0.17	0.75	0.60	0.98	1.03	0.05	0.90	0.90
175	1.27	1.23	1.65	1.57	0.18	0.28	0.26	0.18	0.70	0.63	0.99	1.01	0.04	0.89	0.90
176	1.27	1.24	1.71	1.59	0.18	0.29	0.26	0.18	0.72	0.66	0.98	1.00	0.04	0.87	0.89
177	1.28	1.22	1.74	1.59	0.18	0.30	0.26	0.17	0.71	0.62	0.98	1.02	0.04	0.88	0.90

Expermental Hydraulic Data Part B

	Velocity at each section				Froude No. (F_{cs})				Terminal Froude (F_T)		Hydraulic Radius				
Exp. No.	**Section 1 (Nail) (ft/s)**	**Section 1 (Bubbler) (ft/s)**	**Section 2 (ft/s)**	**Section 3 (ft/s)**	**Nail 1** (Dimensionless)	**Nail 2** (Dimensionless)	**Nail 3** (Dimensionless)	**Bubbler 1** (Dimensionless)	**Nail 1** (Dimensionless)	**Bubbler 1** (Dimensionless)	**Nail (1) (ft)**	**Bubbler 1 (ft)**	**Nail 2 (ft)**	**Nail 3 (ft)**	**Bubbler 2 (ft)**
178	1.26	1.21	1.66	1.59	0.18	0.28	0.26	0.17	0.68	0.58	1.00	1.03	0.04	0.89	0.89
179	1.23	1.19	1.68	1.57	0.18	0.28	0.26	0.17	0.65	0.58	1.00	1.03	0.04	0.88	0.89
180	1.24	1.20	1.69	1.57	0.18	0.29	0.25	0.17	0.65	0.57	1.00	1.03	0.04	0.89	0.89
181	1.29	1.21	1.72	1.60	0.19	0.29	0.26	0.17	0.73	0.59	0.98	1.03	0.04	0.89	0.90
182	1.29	1.22	1.72	1.60	0.19	0.29	0.26	0.17	0.71	0.60	0.99	1.03	0.04	0.89	0.90
183	1.28	1.21	1.70	1.59	0.18	0.29	0.26	0.17	0.71	0.60	0.99	1.02	0.04	0.89	0.90
184	1.32	1.25	1.65	1.58	0.19	0.28	0.26	0.18	0.80	0.68	0.96	1.00	0.04	0.89	0.90
185	1.33	1.26	1.65	1.58	0.20	0.28	0.26	0.18	0.82	0.69	0.96	0.99	0.04	0.89	0.90
186	1.32	1.26	1.73	1.60	0.19	0.30	0.26	0.18	0.80	0.69	0.96	0.99	0.04	0.88	0.90
187	1.24	1.20	1.67	1.59	0.18	0.28	0.26	0.17	0.66	0.59	1.00	1.03	0.04	0.88	0.89
188	1.24	1.20	1.74	1.61	0.18	0.30	0.27	0.17	0.68	0.61	0.99	1.02	0.04	0.86	0.89
189	1.27	1.20	1.72	1.59	0.18	0.29	0.26	0.17	0.71	0.59	0.98	1.03	0.04	0.88	0.89
Weir Cefficient															
190	—	—	—	—	—	—	—	—	—	—	—	—	—	—	—
191	—	—	—	—	—	—	—	—	—	—	—	—	—	—	—
192	—	—	—	—	—	—	—	—	—	—	—	—	—	—	—
Additional Flow Regime															
193	—	—	—	—	—	—	—	—	—	—	—	—	—	—	—
194	1.05	1.02	1.17	1.16	0.14	0.17	0.17	0.14	0.42	0.39	1.10	1.12	0.05	1.08	1.09
195	1.05	1.02	1.16	1.15	0.14	0.17	0.17	0.14	0.42	0.39	1.10	1.12	0.05	1.09	1.09
196	1.06	1.03	1.19	1.17	0.14	0.17	0.17	0.14	0.42	0.39	1.10	1.13	0.05	1.09	1.10
197	1.07	1.03	1.18	1.17	0.14	0.17	0.17	0.14	0.42	0.39	1.10	1.13	0.05	1.09	1.10
198	1.27	1.40	1.68	1.58	0.18	0.28	0.26	0.22	0.69	0.60	0.99	0.96	0.04	0.89	0.90
199	1.20	1.18	1.67	1.55	0.17	0.28	0.25	0.17	0.61	0.59	1.02	1.02	0.04	0.89	0.90
200	1.22	1.63	2.11	1.92	0.18	0.40	0.35	0.29	0.68	0.63	0.98	0.91	0.04	0.73	0.73
201	1.23	1.22	1.93	1.90	0.18	0.35	0.34	0.18	0.71	0.71	0.98	0.99	0.04	0.74	0.73

Expermental Hydraulic Data Part C

Exp. No.	Shear Velocity (U_*)	Shear Stress (τ_o) (lbs/ft^2)	Shields Parameter (τ_*) (Dimensionless)	Critical Shear Stress (τ_c) (lbs/ft^2)	Reynolds Grain Number (Re_*)	Sediment Transport Yield (ft^3)	Area Culvert (ft^2)	Culvert Clog
VP	—	—	—	—	—	—	0.371	VP
1	0.29	0.45	0.07	0.39	1753.40	nr	0.371	No
2	—	—	—	0.39	—	nr	0.371	No
3	—	—	—	0.39	—	nr	0.371	Yes
4	—	—	—	0.39	—	nr	0.371	Yes
5	—	—	—	0.39	—	1.64	0.371	Yes
6	—	—	—	0.39	—	1.11	0.371	Yes
7	—	—	—	0.39	—	nr	0.371	Yes
8	—	—	—	0.39	—	nr	0.371	No
9	—	—	—	0.39	—	1.38	0.371	No
10	—	—	—	0.39	—	nr	0.371	VP
11	—	—	—	0.39	—	nr	0.371	VP
12	0.32	0.53	0.08	0.39	1840.11	0.76	0.371	Yes
13	0.32	0.53	0.08	0.39	1869.50	1.02	0.262	Yes
14	0.32	0.52	0.08	0.39	1837.11	0.80	0.262	Yes
15	0.32	0.53	0.08	0.39	1854.86	1.09	0.262	Yes
16	—	—	—	—	—	—	—	—
17	—	—	—	—	—	—	—	—
18	0.32	0.54	0.08	0.39	1799.10	1.54	0.087	Yes
19	0.32	0.53	0.08	0.39	1779.65	1.66	0.087	Yes
20	0.32	0.54	0.08	0.39	1777.26	1.23	0.087	Yes
21	—	—	—	—	—	—	—	—
22	—	—	—	—	—	—	—	—
23	0.32	0.54	0.08	0.39	1805.87	1.14	0.196	Yes
24	0.32	0.54	0.08	0.39	1825.11	1.52	0.196	Yes
25	0.32	0.53	0.08	0.39	1844.50	1.37	0.196	Yes
26	0.32	0.52	0.08	0.39	1795.19	1.21	0.589	Yes
27	0.32	0.53	0.08	0.39	1821.20	1.55	0.589	Yes
28	0.32	0.52	0.08	0.39	1839.80	1.16	0.589	Yes
29	0.32	0.53	0.08	0.39	1863.49	1.50	0.875	Yes
30	0.32	0.52	0.08	0.39	1871.66	1.14	0.875	Yes
31	0.32	0.51	0.08	0.39	1840.18	1.09	0.875	Yes
32	0.32	0.54	0.08	0.39	1886.49	2.16	0.292	No
33	0.33	0.55	0.08	0.39	1870.37	1.74	0.292	No
34	0.32	0.54	0.08	0.39	1893.92	1.66	0.292	Yes
35	—	—	—	—	—	—	—	—
36	—	—	—	—	—	—	—	—

Expermental Hydraulic Data Part C

Exp. No.	(U_*)	(τ_o) (lbs/ft^2)	(τ_*) (Dimensionless)	(τ_c) (lbs/ft^2)	(Re_*)	STY (ft^3)	Area (ft^2)	Clog
Change Slope								
37	—	—	—	—	—	—	—	—
37B	—	—	—	—	—	—	—	—
38	0.58	1.76	0.27	0.39	3226.92	0.00	0.292	No
39	0.58	1.75	0.27	0.39	3404.66	3.00	0.292	No
40	0.59	1.77	0.27	0.39	3390.31	4.31	0.292	No
41	0.57	1.70	0.26	0.39	3415.91	6.38	0.875	No
42	0.57	1.71	0.26	0.39	3357.98	6.38	0.875	No
43	0.57	1.70	0.26	0.39	3382.67	6.00	0.875	No
44	0.58	1.72	0.27	0.39	3405.50	5.25	0.589	No
45	0.58	1.73	0.27	0.39	3380.30	5.25	0.589	No
46	0.58	1.73	0.27	0.39	3475.77	5.63	0.589	No
47	0.59	1.77	0.27	0.39	3524.03	3.75	0.196	No
48	0.59	1.77	0.27	0.39	3453.22	3.00	0.196	No
49	0.59	1.77	0.27	0.39	3424.43	3.38	0.196	No
50	—	—	—	—	—	—	—	—
51	—	—	—	—	—	—	—	—
52	0.58	1.73	0.27	0.39	3445.68	3.38	0.262	Yes
53	0.58	1.72	0.27	0.39	3440.70	3.00	0.262	Yes
54	0.58	1.76	0.27	0.39	3477.41	3.94	0.262	No
55	0.59	1.78	0.28	0.39	3500.20	2.25	0.087	No
56	0.59	1.78	0.27	0.39	3491.41	2.63	0.087	No
57	0.59	1.77	0.27	0.39	3489.01	2.25	0.087	No
58	—	—	—	—	—	—	—	—
59	—	—	—	—	—	—	—	—
60	0.58	1.75	0.27	0.39	3397.10	4.50	0.371	No
61	0.58	1.73	0.27	0.39	3444.53	4.50	0.371	No
62	0.58	1.72	0.27	0.39	3441.07	3.38	0.371	No
63	—	—	—	—	—	—	—	—
64	—	—	—	—	—	—	—	—
65	0.58	1.72	0.27	0.39	3470.05	3.38	0.371	No
66	0.58	1.72	0.27	0.39	3439.31	3.75	0.371	No
67	0.58	1.72	0.27	0.39	3405.49	3.19	0.371	No
68	0.58	1.71	0.26	0.39	3299.28	4.50	0.589	No
69	0.58	1.75	0.27	0.39	3336.27	3.00	0.196	No
Change Slope								
70	0.45	1.04	0.16	0.39	2580.04	0.75	0.196	No
71	0.45	1.05	0.16	0.39	2786.47	1.88	0.196	No
72	0.45	1.04	0.16	0.39	2810.95	1.50	0.196	No
73	0.45	1.03	0.16	0.39	2717.50	1.69	0.589	Yes
74	0.45	1.04	0.16	0.39	2725.19	2.06	0.589	Yes
75	0.45	1.02	0.16	0.39	2649.04	1.13	0.589	Yes
76	—	—	—	—	—	—	—	—
77	—	—	—	—	—	—	—	—
78	0.44	1.00	0.16	0.39	2626.43	1.50	0.875	Yes
79	0.45	1.03	0.16	0.39	2657.89	1.50	0.875	Yes
80	0.45	1.05	0.16	0.39	2731.90	3.00	0.875	No
81	—	—	—	—	—	—	—	—
82A	—	—	—	—	—	—	—	—
82	0.45	1.04	0.16	0.39	2780.67	1.88	0.292	No
83	0.45	1.03	0.16	0.39	2758.64	0.75	0.292	No
84	0.45	1.03	0.16	0.39	2737.87	1.13	0.292	No
85	0.45	1.04	0.16	0.39	2828.47	1.50	0.371	Yes
86	0.45	1.05	0.16	0.39	2845.60	1.88	0.371	Yes
87	0.45	1.04	0.16	0.39	2839.38	1.88	0.371	Yes
88	—	—	—	—	—	—	—	—
Large Grain Skew Model								
89	—	—	—	—	—	—	—	—
90	—	—	—	—	—	—	—	—
91	0.45	1.02	0.16	0.39	2870.60	1.50	0.875	Yes
92	0.45	1.04	0.16	0.39	2927.25	3.00	0.875	Yes
93	0.45	1.04	0.16	0.39	2917.22	1.13	0.875	Yes
94	0.45	1.04	0.16	0.39	2892.77	nr	0.292	No
95	0.45	1.04	0.16	0.39	2926.32	0.00	0.292	No
96	0.45	1.05	0.16	0.39	2903.55	0.75	0.292	No
97	—	—	—	—	—	—	—	—
98	—	—	—	—	—	—	—	—
99	—	—	—	—	—	—	—	—
100	—	—	—	—	—	—	—	—

Expermental Hydraulic Data Part C

Exp. No.	(U_*)	(τ_o) **(lbs/ft^2)**	(τ_*) **(Dimensionless)**	(τ_c) **(lbs/ft^2)**	(Re_*)	**STY (ft^3)**	**Area (ft^2)**	**Clog**
101	0.45	1.05	0.16	0.39	2902.26	0.00	0.196	No
102	0.45	1.06	0.16	0.39	2984.95	2.25	0.196	No
103	0.45	1.03	0.16	0.39	2935.82	0.75	0.589	
104	0.45	1.04	0.16	0.39	2990.47	1.13	0.589	Yes
105	0.45	1.04	0.16	0.39	3013.71	nr	0.589	Yes
106	0.45	1.03	0.16	0.39	2967.75	8.25	0.371	
107	0.45	1.06	0.16	0.39	3041.17	1.13	0.371	Yes
108	0.45	1.05	0.16	0.39	2997.07	0.75	0.371	No
109	0.45	1.04	0.16	0.39	2991.37	4.50	0.371	Yes
110	—	—	—	—	—	—	—	—
111	—	—	—	—	—	—	—	—
112	—	—	—	—	—	—	—	—
113	0.45	1.06	0.16	0.39	3080.28	0.00	0.087	No
114	0.46	1.07	0.17	0.39	3059.02	0.38	0.087	No
115	0.45	1.05	0.16	0.39	3031.25	1.13	0.262	Yes
116	0.45	1.05	0.16	0.39	3069.26	nr	0.262	Yes
117	0.45	1.05	0.16	0.39	3069.08	0.56	0.262	Yes
Start Small Grain								
Small Grain Skew Model								
118	0.44	1.00	0.31	0.19	3097.17	0.00	0.262	No
119	0.44	1.00	0.31	0.19	3097.60	nr	0.262	No
120	0.44	0.99	0.31	0.19	3082.74	0.00	0.262	No
121	0.44	1.01	0.31	0.19	3102.86	0.38	0.087	No
122	0.44	1.01	0.31	0.19	3113.22	0.19	0.087	No
123	0.45	1.03	0.32	0.19	3143.93	nr	0.087	No
124	—	—	—	—	—	—	—	—
125	0.44	0.98	0.30	0.19	3126.58	0.56	0.589	No
126	0.43	0.97	0.30	0.19	3158.16	2.25	0.589	No
127	0.43	0.97	0.30	0.19	3155.17	0.75	0.589	No
128	0.44	1.00	0.31	0.19	3165.58	0.56	0.196	No
129	0.44	1.00	0.31	0.19	3158.15	0.00	0.196	No
130	0.44	1.00	0.31	0.19	3162.75	0.75	0.196	No
131	0.44	0.98	0.30	0.19	3129.71	0.00	0.371	No
132	0.44	1.00	0.31	0.19	3154.79	0.75	0.371	No
133	0.44	0.99	0.31	0.19	3153.43	0.75	0.371	No
134	0.44	1.00	0.31	0.19	3159.54	2.06	0.371	No
135	0.43	0.97	0.30	0.19	3111.30	2.25	0.875	No
136	0.43	0.96	0.30	0.19	3138.01	2.06	0.875	No
137	0.43	0.96	0.30	0.19	3138.02	1.50	0.875	No
138	0.44	1.00	0.31	0.19	3202.09	1.13	0.292	No
139	0.44	1.00	0.31	0.19	3196.40	0.94	0.292	No
140	0.44	1.00	0.31	0.19	3158.16	0.56	0.292	No
Parallel Model								
141	0.43	0.97	0.30	0.19	3122.08	4.13	0.875	Yes
142	0.44	0.98	0.30	0.19	3168.95	5.25	0.875	No
143	0.44	0.98	0.30	0.19	3208.73	5.44	0.875	No
144	0.44	0.99	0.31	0.19	3227.79	5.81	0.875	Yes
145	0.44	0.99	0.31	0.19	3227.79	nr	0.292	
146	0.44	1.01	0.31	0.19	3223.14	4.50	0.292	No
147	0.44	1.01	0.31	0.19	3220.33	3.56	0.292	No
148	0.44	1.01	0.31	0.19	3222.97	4.50	0.292	No
149	0.44	1.01	0.31	0.19	3213.99	4.13	0.371	No
150	0.44	1.01	0.31	0.19	3215.49	3.75	0.371	No
151	0.44	1.01	0.31	0.19	3215.54	4.50	0.371	No
152	0.44	1.00	0.31	0.19	3166.82	4.88	0.589	No
153	0.44	1.00	0.31	0.19	3159.57	4.88	0.589	No
154	0.44	1.00	0.31	0.19	3164.64	5.06	0.589	No
155	0.44	1.00	0.31	0.19	3155.66	4.69	0.589	No
156	0.44	1.01	0.31	0.19	3210.32	5.25	0.589	No
157	0.45	1.03	0.32	0.19	3277.26	3.94	0.196	No
158	0.44	1.02	0.31	0.19	3224.49	3.00	0.196	No
159	0.45	1.03	0.32	0.19	3240.41	3.94	0.196	No
160	0.45	1.03	0.32	0.19	3251.79	1.31	0.087	No
161	0.45	1.04	0.32	0.19	3306.08	2.25	0.087	No
162	0.45	1.04	0.32	0.19	3295.00	2.25	0.087	No
163	0.44	1.02	0.32	0.19	3269.83	3.56	0.262	No
164	0.44	1.02	0.31	0.19	3266.17	3.19	0.262	No
165	0.45	1.02	0.32	0.19	3273.50	3.56	0.262	No
Change Slope								

Expermental Hydraulic Data Part C

Exp. No.	(U_*)	(τ_o) **(lbs/ft^2)**	(τ_*) **(Dimensionless)**	(τ_c) **(lbs/ft^2)**	(Re_*)	**STY (ft^3)**	**Area (ft^2)**	**Clog**
166	0.32	0.52	0.16	0.19	2328.78	3.19	0.262	Yes
167	0.32	0.51	0.16	0.19	2289.32	2.63	0.262	Yes
168	0.32	0.52	0.16	0.19	2301.32	2.81	0.262	Yes
169	0.32	0.52	0.16	0.19	2307.94	1.69	0.087	No
170	0.32	0.52	0.16	0.19	2301.35	1.13	0.087	No
171	0.32	0.52	0.16	0.19	2314.02	1.13	0.087	No
172	0.31	0.51	0.16	0.19	2285.24	4.50	0.371	No
173	0.31	0.51	0.16	0.19	2285.93	3.00	0.371	Yes
174	0.31	0.51	0.16	0.19	2286.22	3.00	0.371	No
175	0.31	0.50	0.16	0.19	2244.71	3.75	0.589	No
176	0.31	0.50	0.15	0.19	2229.74	2.63	0.589	Yes
177	0.31	0.51	0.16	0.19	2252.16	3.38	0.589	Yes
178	0.32	0.51	0.16	0.19	2264.30	1.88	0.196	No
179	0.31	0.51	0.16	0.19	2262.65	1.31	0.196	No
180	0.32	0.51	0.16	0.19	2268.46	2.25	0.196	No
181	0.32	0.51	0.16	0.19	2291.61	3.19	0.371	Yes
182	0.31	0.51	0.16	0.19	2287.00	2.81	0.371	Yes
183	0.31	0.51	0.16	0.19	2284.61	2.63	0.371	Yes
184	0.31	0.50	0.15	0.19	2253.68	2.81	0.875	Yes
185	0.31	0.49	0.15	0.19	2250.89	2.25	0.875	Yes
186	0.31	0.49	0.15	0.19	2248.30	2.25	0.875	Yes
187	0.31	0.51	0.16	0.19	2286.22	2.63	0.292	No
188	0.31	0.51	0.16	0.19	2275.47	2.63	0.292	No
189	0.31	0.51	0.16	0.19	2286.04	2.81	0.292	No
Weir Coefficient								
190	—	—	—	—	—	—	—	—
191	—	—	—	—	—	—	—	—
192	—	—	—	—	—	—	—	—
Alternate Flow Regime								
193	—	—	—	—	—	—	—	—
194	0.33	0.56	0.17	0.19	1956.76	0.08	0.875	No
195	0.33	0.56	0.17	0.19	1958.62	0.11	0.875	No
196	0.33	0.56	0.17	0.19	1963.07	0.00	0.371	No
197	0.33	0.56	0.17	0.19	2002.71	0.00	0.371	No
198	0.30	0.48	0.15	0.19	1846.09	3.94	0.371	No
199	0.31	0.51	0.16	0.19	1907.49	5.44	0.371	No
200	0.30	0.45	0.14	0.19	1797.94	3.94	0.371	No
201	0.31	0.49	0.15	0.19	1873.97	3.38	0.371	No

Appendix E
Generic Data Tables

Tables listed here supply generic data used throughout the calculations where necessary.

Area of Culverts (ft^2)		
Shape	Single-B	Multi-B
4–in Cir	0.087	0.262
6–in Cir	0.196	0.589
6×7–in Sq.	0.292	0.875
SB	N/A	0.371

Sediment Properties	
ρ_s	5.16 slug/ft3
γ_s	166 lbs/ft3
d_{50} lg	0.0625 ft
d_{50} sm	0.03125 ft

Incipient Motion Critical Values		
Shields (τ_*)	0.06	Lg & Sm Grain
Du Boys (τ_c)	0.05	Lg Grain
Du Boys (τ_c)	0.03	Sm Grain

5–Gallon Bucket			
Small Grain	71.6 lbs	Density Small	93.00 lbs/ft^3
Large Grain	69.6 lbs	Density Large	90.4 lbs/ft^3